Collective dynamics of solid-state spin chains and ensembles in quantum information processing



Yuting Ping
Hertford College

Thesis submitted for the degree of
Doctor of Philosophy
at the
University of Oxford
Michaelmas Term 2012

Collective dynamics of solid-state spin chains and ensembles in quantum information processing

Yuting Ping
Hertford College, University of Oxford
Michaelmas Term 2012

Abstract of thesis submitted for the degree of Doctor of Philosophy

This thesis is concerned with the collective dynamics in different spin chains and spin ensembles in solid-state materials. The focus is on the manipulation of electron spins, through spin-spin and spin-photon couplings controlled by voltage potentials or electromagnetic fields. A brief review of various systems is provided to describe the possible physical implementation of the ideas, and also outlines the basis of the adopted effective interaction models.

The first two ideas presented explore the collective behaviour of non-interacting spin chains with external couplings. One focuses on mapping the identical state of spin-singlet pairs in two currents onto two distant, static spins downstream, creating distributed entanglement that may be accessed. The other studies a quantum memory consisting of an array of non-interacting, static spins, which may encode and decode multiple flying spins. Both chains could effectively 'enhance' weak couplings in a cumulative fashion, and neither scheme requires active quantum control. Moreover, the distributed entanglement generated can offer larger separation between the qubits than more conventional protocols that only exploit the tunnelling effects between quantum dots. The quantum memory can also 'smooth' the statistical fluctuations in the effects of local errors when the stored information is spread.

Next, an interacting chain of static spins with nearest-neighbour interactions is introduced to connect distant end spins. Previously, it has been shown that this approach provides a cubic speed-up when compared with the direct coupling between the target spins. The practicality of this scheme is investigated by analysing realistic error effects via numerical simulations, and from that perspective relaxation of the nearest-neighbour assumption is proposed.

Finally, a non-interacting electron spin ensemble is reviewed as a quantum memory to store single photons from an on-chip stripline cavity. It is then promoted to a full quantum processor, with major error effects analysed. [*word count*: 298]

Acknowledgements

I am extremely grateful to my supervisors Dr. Brendon W. Lovett and Dr. Simon C. Benjamin for their guidance, encouragement, support and friendship throughout my D.Phil. studies, and also for proof-reading this thesis. In addition, I would like to particularly thank Prof. John H. Jefferson and Dr. Erik M. Gauger for many stimulating and enjoyable discussions, as well as for the important contributions they made to this thesis. Without these people, it would have been an impossible task to complete my research projects on time.

Furthermore, I gratefully acknowledge the contributions to this thesis by Dr. Avinashi Kolli, Dr. Janus H. Wesenberg, Dr. Hugo Cable, and Prof. Kai Bongs. My fellow graduate students Yuchiro Matsuzaki, Tom Close, Marcus Schaffry, Nikesh Dattani, George Knee, and Kieran Higgins also deserve a special mention for sharing interesting discussions: It has been really inspirational working in the QuNaT group.

I am highly indebted to my parents for their support under all circumstances and funding my studies, and wish to express my sincere gratitude to them. I would also like to thank all my friends, with whom I have spent fun time together during my studies here in Oxford. This has made my past three years so wonderfully enjoyable. In particular, thank you Weina, for your love and support.

I gratefully acknowledge Hertford College for the Carreras senior scholarship and funding me to attend the SUSSP67 summer school (which should also be acknowledged for providing me the bursary) and the CMMP11 conference. The same goes to the Vice-Chancellors' Fund to aid me for the past three months. I also thank the Department of Materials for providing the necessary equipment and workspace, and funding me to attend the QSPICE II workshop. The various skills workshops organized by the department have also been very useful for my research.

Contents

1 Motivation and outline **1**
1.1 Motivation . . . 1
1.2 Outline . . . 3

2 Introduction to quantum information processing (QIP) **5**
2.1 Basics of quantum computation (QC) . . . 5
2.1.1 Units - quantum bits (qubits) . . . 5
2.1.2 Quantum logic gates . . . 7
2.1.3 Quantum algorithms . . . 9
2.1.4 Applications in QIP . . . 11
2.2 Notion of entanglement . . . 12
2.2.1 Non-local correlations . . . 13
2.2.2 Measurement-based QC . . . 15
2.3 Decoherence and fault-tolerant QIP . . . 16
2.3.1 Quantum noise . . . 17
2.3.2 Quantum error corrections . . . 19
2.3.3 Modelling open quantum systems . . . 21
2.4 Summary . . . 22

3 Potential architectures for QIP implementation **23**
3.1 Photonic, atomic, and molecular . . . 24
3.1.1 Photonic — quantum optics . . . 24
3.1.2 Atomic — ion traps, optical lattice for cold atoms . . . 25
3.1.3 Molecular — nuclear magnetic resonance (NMR) . . . 27
3.2 Solid-state spins . . . 28
3.2.1 Quantum dots (QDs) . . . 29
3.2.2 Impurities and defects . . . 35
3.2.3 Endohedral fullerenes . . . 40
3.2.4 Free electrons . . . 42
3.2.5 Beyond spins . . . 45
3.3 Summary . . . 47

4 Spin chains and ensembles **49**
4.1 Electron spin-spin interactions . . . 50
4.1.1 Exchange mechanism: Heisenberg and XY models . . . 50
4.1.2 Magnetic dipole-dipole interaction . . . 60
4.2 Electron spin-photon coupling . . . 66
4.3 Spin chains and their implementations . . . 68
4.3.1 Non-interacting spin chain with external coupling . . . 68
4.3.2 Interacting spin chain . . . 70
4.4 Spin ensemble coupled to stripline cavity . . . 72
4.5 Summary . . . 74

5 Passive generator for distributed spin-entanglement **75**
5.1 Motivation . . . 75
5.2 Set-up, model and basic results . . . 77
5.2.1 Attractor . . . 78
5.2.2 Convergence . . . 79
5.3 Generalizations . . . 81
5.4 Decoherence . . . 85
5.4.1 Static spins . . . 85
5.4.2 Flying spins . . . 87
5.5 Splitting efficiency . . . 88
5.6 Other models . . . 90
5.7 Conclusion . . . 90

6 Coherent and passive spin-chain quantum memory **93**
6.1 Set-up, model and basic results . . . 93
6.1.1 Memory size scales with coupling strength . . . 98
6.1.2 Coupling mismatch between encoding and decoding . . . 99
6.2 Decoherence of static spins . . . 100
6.3 Generalizations to multiple flying qubits . . . 102
6.3.1 Collective 1-spin down-flip distributions . . . 102
6.3.2 $(0, 0)^{\text{th}}$ 2-spin down-flip distribution . . . 110
6.4 Variations in coupling strengths . . . 113
6.5 Conclusion . . . 115

7 Spin-chain quantum to classical channel transition in diamond **117**
7.1 Background . . . 117
7.2 Practicality for fault tolerance . . . 119
7.2.1 Two-round protocol . . . 120
7.2.2 Meeting the fault-tolerance thresholds . . . 122
7.3 Quantum to classical channel transition . . . 125
7.4 Beyond nearest-neighbour couplings . . . 131
7.5 Coupling disorder . . . 132
7.6 Conclusion . . . 133

8 Measurement-based spin-ensemble quantum information processor 135
8.1 Motivation, set-up and model . . . 135
8.2 Single qubit operations in dual-rail encoding . . . 138
8.2.1 X rotations . . . 139
8.2.2 Z rotations . . . 140
8.3 Measurement-assisted entanglement . . . 140
8.4 Major errors . . . 143
8.4.1 Type I measurement error . . . 144
8.4.2 Type II measurement error . . . 150
8.4.3 Cavity photon leakage . . . 151
8.5 Read-out scheme . . . 152
8.6 Conclusion . . . 154

9 Summary and outlook 155

Bibliography 157

List of Figures

2.1 Qubit representation on Bloch sphere 6
2.2 Examples of graph states 15

3.1 Electronic qubit in trapped ion: Simplified level structure 26
3.2 Exchange process for single electron spins in coupled, lithographically defined quantum dots (QDs) 30
3.3 Coulomb blockade and spin blockade effects in gated QDs 31
3.4 Transitions between valence & conduction bands of self-assembled QDs 32
3.5 Spin qubit in self-assembled QDs: Simplified level structure 33
3.6 Physical and simplified level structures of NV^- centre in diamond . . 38
3.7 Endohedral fullerenes and nanotube 'peapod' structures 41
3.8 Quantum point contact (QPC) and electron transport in gated semiconducting quantum wires 43

4.1 Electrons with Coulombic interactions. 51
4.2 Effective spin-photon exchange coupling in cavity quantum electrodynamics (QED) through two-photon Raman processes 66

5.1 Illustration of singlet splitter with three QDs 76
5.2 Scheme of passive generator for distributed, static entanglement . . . 77
5.3 Convergence to attractor state 81
5.4 Degree of entanglement produced by generator (XY model) 83
5.5 Effects of round-to-round coupling disorder 84
5.6 Decoherence of static spins 87
5.7 Effects of splitting inefficiency 89
5.8 Degree of entanglement produced by generator (Heisenberg) 90

6.1 Illustration of quantum memory chain 94
6.2 Coupling mismatch between encoding and decoding 99
6.3 Decoherence in memory spins: Spreading to 'smooth' fluctuations . . 101
6.4 Collective one-spin down-flip distributions 108
6.5 Comparison of analytical results with simulations 110
6.6 Memory storage of entangled pairs 113
6.7 Storing multiple qubits and effects of round-to-round coupling disorder 114
6.8 Effects of site-to-site coupling disorder 115

7.1 Illustration of coupled spin chain 'wiring' in diamond 118
7.2 Practicality of fault tolerance 123
7.3 Decoherence for $N = 3$ chain 126
7.4 T_1 processes for $N = 15$ chain 127
7.5 T_1 processes for different chain lengths 128
7.6 Quantum to classical channel transition 129
7.7 Beyond nearest-neighbour couplings 131
7.8 Effects of coupling disorder 133

8.1 Electron spin ensemble quantum processor 135
8.2 Single qubit rotations for logical collective qubits in spin ensemble . . 139
8.3 Measurement-assisted entanglement between ensemble modes 141
8.4 Fidelity of entangling operation 147
8.5 Degree of entanglement with appropriate metric 148
8.6 Probability of reaching end of protocol 150
8.7 Modified entangling circuit to tackle cavity photon leakage 152
8.8 Read-out procedures 153

List of Publications

The research chapters in this thesis are based on the following publications (or preprints):

1. *Practicality of spin chain wiring in diamond quantum technologies.* Y. Ping, B. W. Lovett, S. C. Benjamin, and E. M. Gauger. Physical Review Letter **110** 100503 (2013). [Chapter 7]

2. *A coherent and passive one dimensional quantum memory.* Y. Ping, J. H. Jefferson, and B. W. Lovett. arXiv: 1208.4828 (In Review, 2013). [Chapter 6]

3. *Measurement-based quantum computing with a spin ensemble coupled to a stripline cavity.* Y. Ping, E. M. Gauger, and S. C. Benjamin. New Journal of Physics **14** 013030 (2012). [Chapter 8]

4. *Generating distributed entanglement from electron currents.* Y. Ping, A. Kolli, J. H. Jefferson, and B. W. Lovett. New Journal of Physics **13** 103004 (2011). [Chapter 5]

Chapter 1

Motivation and outline

1.1 Motivation

With its foundations laid down in the late 1920s, quantum mechanics has stimulated huge advances in various fields of science and technology over the past few decades. Its accurate predictions about the behaviour of physical systems at the fundamental level have made digital electronics and photonics possible, and these have transformed our world into the modern day Information Age.

The whole of society now relies heavily on information technology across all sectors. In addition, many innovative business models in the past decade [1, 2, 3], as well as valuable progress in scientific research [4, 5], have been largely associated with the ever-increasing information processing power of computers. It was mainly the ability to fabricate smaller and smaller microchips that made the fast growth in computing power possible, which in turn promoted the advancement in those two essential elements that fuel economic development and social progress. Yet, as the components are now reaching nanoscale dimensions, quantum effects (such as quantum tunnelling) start to become dominant, and we have to take these into account in the design of any information processor [see also Sec. 2.1.2]. Indeed, over

the past few years computer manufacturers have already shifted their focus from trying to make chips smaller onto producing multi-core processors in order to boost the information processing power via parallel computation.

On the other hand, if somehow we manage to harness those quantum effects, we can actually employ an alternative model of computing based on the most fundamental aspects of quantum theory [6]. The resulting quantum information processors can efficiently perform certain important tasks, in which the classical computers we encounter every day have fundamental limitations [7]. It was the influence of *Feynman*'s vision [8] supported by *Deutsch*'s insight [9] into the quantum version of *Church-Turing* thesis [10] underpinning universal information processing that started to draw researchers' attention to this possibility in the late 1980s. Since then, the theory of quantum information processing (QIP) in an abstract mathematical language has been formulated [7]. Furthermore, there have been various proposals for the candidate architectures of such devices, as well as a number of proof-of-concept experimental demonstrations [7]. However, the ultimate goal of building a scalable quantum computer remains a challenge, due to the undesirable loss of phase information (namely, decoherence [see Sec. 2.3]) from the fragile quantum systems into the surrounding environment. As a result, we have been witnessing an enormous amount of research efforts into the field, together with the associated impressive progress [7].

Owing to the silicon-based manufacturing expertise accumulated in the latter half of the last century, many researchers have been working on solid-state QIP implementations, and so does this thesis. We shall consider the basic element to be the spin (an intrinsic degree of freedom[1]) of an electron or a nucleus, though other solid-state quantum information carriers are also possible [11]. The quantum

[1]The spin state of an elementary particle contributes towards its total angular momentum, and that of an electron or nucleus can be associated with *Zeeman* or hyperfine splittings in energy levels [12]. Throughout this thesis, we shall take the reduced *Planck* constant $\hbar = 1$ [12].

systems are usually controlled by electromagnetic fields (or photons) and electric potentials. One particular problem is that the best achievable interaction strengths for manipulating a single spin can be very weak, with strengths smaller than the spin decoherence rates [see Chapter 3]. Therefore, the main theme of this thesis is the theoretical study of collective dynamics in different spin chains and spin ensembles, with potential enhancement effects for solid-state QIP. Moreover, we find that some schemes can also reduce the required level of active quantum control, which would otherwise introduce additional errors and impose further challenges. We investigate different aspects of quantum information processors, with the hope of bringing the powerful emerging technologies closer into reality.

1.2 Outline

We begin this thesis with an introduction to the QIP field in Chapters 2 (concepts) and 3 (implementation), followed by Chapter 4 addressing formalisms for spin chains, ensembles, the related interaction models and their potential realization, providing the basis for analysis in later research chapters [see List of Publications].

Original research work starts from Chapter 5, where a novel scheme is presented to connect two distant, static electron spins using spin-entangled currents in two separate channels [13, 14], making it easier to access the entanglement resource. By using currents rather than just a single spin, the scheme could work with weak interaction strengths as a result of the collective enhancement. This entanglement generation device does not require active quantum control. Moreover, the spatial separation between the static electrons can be higher than that achieved by only exploiting the tunnelling effects between quantum dots.

In Chapter 6, we propose a coherent one-dimensional quantum memory based on a non-interacting spin chain. The quantum state of multiple flying spins can be

coherently transferred to the memory in a sequential manner, and then may be read out similarly. Again, active quantum control is not required during the quantum information storage and retrieval processes. The collective enhancement here is to 'smooth' the statistical fluctuations of local error effects in the memory, in addition to the ability of coping with weak interaction strengths.

Proceeding to Chapter 7, we encounter recent literature on quantum state transfer through a spin-chain channel at *room temperature* [15, 16, 17], which provides a cubic speed-up in the transfer time as compared to the case with direct dipolar interactions between two distant spins. In the language of diamond defects, we numerically investigate realistic error effects in the system, and show that decoherence (in particular, physical dephasing) limits the channel capacity significantly. We thus re-purpose the channel for the distribution of finite levels of entanglement: This would enable QIP in a distributed architecture through distillation protocols [see Sec. 2.2]. In this case, we demonstrate that the impractical restriction to nearest-neighbour couplings employed by previous studies [15, 16, 17] can be lifted without a significant penalty in performance. Recent research also shows that mediation via spin ensembles may further enhance the connection between distant spins [18].

Finally, in Chapter 8 we turn a holographic (electron) spin-ensemble quantum memory [19] into a full processor. The ensemble spins can collectively store quantum information for longer time, which was suggested by earlier researchers [20, 21, 22, 23]. We integrate a recent quantum measurement technology [24] into the memory system, and suggest a scheme to perform full QIP with the device.

Each research chapter focuses on an independent topic, and we thus summarize the main results and discuss areas for future work in their own conclusions. These schemes either illustrate alternative, new ideas or re-purpose earlier studies to allow realistic noise effects, making further steps towards closing the gap between theory and experiment. We conclude this thesis in Chapter 9 with some further remarks.

Chapter 2

Introduction to quantum information processing (QIP)

We now start the thesis with a general introduction to the basic QIP concepts, the source of its unique advantages over classical computing, and the main hurdles that any quantum information technology needs to overcome.

2.1 Basics of quantum computation (QC)

By analogy to classical computation, QIP employs the quantum version of units, gates, logic and algorithms, which are illustrated below.

2.1.1 Units - quantum bits (qubits)

The basic unit of information in QIP is a quantum binary digit or a *qubit*, which models a two-level physical system. The mathematical notation for the two levels

are

$$|0\rangle = \begin{pmatrix} 1 \\ 0 \end{pmatrix} \qquad \text{and} \qquad |1\rangle = \begin{pmatrix} 0 \\ 1 \end{pmatrix}, \tag{2.1}$$

which can represent, e.g., the two linear polarization states of a photon, two appropriate energy levels of an atom, the two orthogonal spin states of an electron [12].

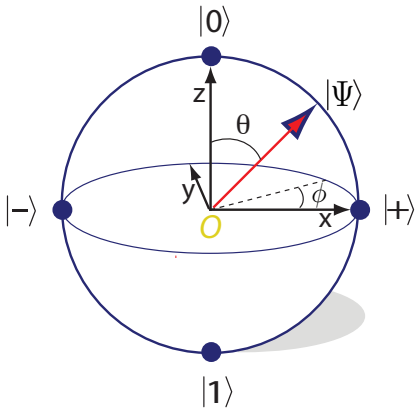


Figure 2.1: The Bloch sphere (picture courtesy of Dr. Erik M. Gauger [193]) for the visualisation of the general qubit state $|\Psi\rangle = a\,|0\rangle + b\,|1\rangle$, which can also be written as $|\Psi\rangle = e^{i\psi}(\cos\frac{\theta}{2}\,|0\rangle + e^{i\phi}\sin\frac{\theta}{2}\,|1\rangle)$ by a change of variables. The global phase ψ can always be ignored as it does not have any effect on the measurement statistics, and the states are equivalent. Therefore, the parameter set (θ, ϕ) is sufficient for the characterization of any qubit state. Here, $|\pm\rangle := (|0\rangle \pm |1\rangle)/\sqrt{2}$.

Interestingly, in a quantum system the general qubit state can take any linear superposition of the individual states of the two levels, being

$$|\Psi\rangle = a\,|0\rangle + b\,|1\rangle = \begin{pmatrix} a \\ b \end{pmatrix} \quad \text{with} \quad |a|^2 + |b|^2 = 1. \tag{2.2}$$

When this qubit is measured in the computational basis $\{|0\rangle, |1\rangle\}$, the measurement outcome can be either $|0\rangle$ with probability $|a|^2$ or $|1\rangle$ with probability $|b|^2$ [12]; conservation of the total probability is ensured by the unit sum condition in Eq. 2.2. The general qubit state $|\Psi\rangle$ can also be visualized on the so-called *Bloch* (or *Poincaré*)

sphere as shown in Fig. 2.1 [7].

To represent more information, qubits are combined by the operation of tensor product [25], e.g., a two-qubit state can be written as

$$|\Psi_1\rangle \bigotimes |\Psi_2\rangle = \begin{pmatrix} a_1 \\ b_1 \end{pmatrix} \bigotimes \begin{pmatrix} a_2 \\ b_2 \end{pmatrix} = \begin{pmatrix} a_1 \begin{pmatrix} a_2 \\ b_2 \end{pmatrix} \\ b_1 \begin{pmatrix} a_2 \\ b_2 \end{pmatrix} \end{pmatrix} = \begin{pmatrix} a_1 a_2 \\ a_1 b_2 \\ b_1 a_2 \\ b_1 b_2 \end{pmatrix}. \tag{2.3}$$

Note that even without any explicit reference to quantum mechanics, evidence that coherent superposition states do exist has recently been demonstrated by the experimental violation [26] of the *Leggett-Garg* inequality [27].

2.1.2 Quantum logic gates

Just like classical information processing, in the circuit model quantum gates are required to perform quantum logic on the qubits to accomplish QIP tasks. All quantum gates correspond to unitary operations on the target qubits, and are thus reversible. Mathematically, an n-qubit gate is represented by a $2^n \times 2^n$ unitary matrix acting on the 2^n-dimensional state vector of the qubits; the tensor product operation takes two gates respectively on n and m qubits to an $(n+m)$-qubit gate [7].

Single qubit gates can be visualized by pure rotations on the Bloch sphere [see Fig. 2.1], e.g., the *Pauli* operators

$$\sigma_x = \begin{pmatrix} 0 & 1 \\ 1 & 0 \end{pmatrix} \qquad \sigma_y = \begin{pmatrix} 0 & -i \\ i & 0 \end{pmatrix} \qquad \sigma_z = \begin{pmatrix} 1 & 0 \\ 0 & -1 \end{pmatrix} \tag{2.4}$$

rotate a qubit on the sphere by π radians around the x, y or z axis, respectively. While σ_x is the quantum version of the classical NOT gate, the other two do not

have analogs in classical computation [7]. In fact, in quantum mechanics rotation about any axis through an arbitrary angle on the Bloch sphere is possible, and in principle the complete set corresponds to an infinite number of gates. Nonetheless, it can be proven that each gate in this set can be efficiently approximated (to a good accuracy) by *finite* applications of a suitable phase gate, such as the $\frac{\pi}{8}$-gate $R(\pi/4)$, and the *Hadamard* gate H, where

$$R(\pi/4) = \begin{pmatrix} 1 & 0 \\ 0 & e^{i\frac{\pi}{4}} \end{pmatrix}, \qquad \mathsf{H} = \frac{1}{\sqrt{2}} \begin{pmatrix} 1 & 1 \\ 1 & -1 \end{pmatrix}, \tag{2.5}$$

with the latter being another unique operation in the quantum regime mapping $|0(1)\rangle \longrightarrow |+(-)\rangle$ [7]. For solid-state spins, it is usually sufficient to be able to rotate a single qubit around two independent axes of the Bloch sphere, where the rotation angle could be controlled by pulse timing [see Chapter 3]: Combining a set of three such rotations through the *Euler* decomposition allows one to recover any single qubit operation [28].

Together with any entangling two-qubit gate, they [Eq. 2.5 and either gate in Eq. 2.6] form a universal set of quantum gates that can be adopted to carry out all quantum algorithms [29]. Examples of such entangling operations include the Controlled-NOT and the Controlled-Phase gates,

$$C_{\mathrm{NOT}} = \begin{pmatrix} 1 & 0 & 0 & 0 \\ 0 & 1 & 0 & 0 \\ 0 & 0 & 0 & 1 \\ 0 & 0 & 1 & 0 \end{pmatrix}, \qquad C_{\mathrm{Phase}} = \begin{pmatrix} 1 & 0 & 0 & 0 \\ 0 & 1 & 0 & 0 \\ 0 & 0 & 1 & 0 \\ 0 & 0 & 0 & -1 \end{pmatrix}, \tag{2.6}$$

which can be transformed to each other by suitable single qubit gates. A couple of basic results concerning the entangling gates are as follows: Three C_{NOT} gates

in alternating directions constitute the SWAP gate that swaps the states of two qubits, and an appropriate combination of three C_{NOT} and four $\pm\frac{3\pi}{8}-$gates acting on three qubits can give us the quantum equivalence of the *Toffoli* gate [29]. The latter can implement all *Boolean* logic in classical circuits, even though many of the classical gates are irreversible (e.g., the AND, OR, XOR gates). Therefore, all classical computation can be simulated efficiently by quantum circuits, while the reverse is intuitively regarded infeasible (but without any formal proof) as there exist quantum algorithms with (as yet) no efficient classical analogs [7].

Note that in the quantum world changing the order of gate operations usually gives us different results, e.g., $\sigma_z \mathsf{H} \neq \mathsf{H}\sigma_z$. This quantum non-commutative effect is an example of violation in classical logic, and has to be considered in the design of information processors when the dimensions reach nanoscale.

At the end of any quantum algorithm, the read-out processes are realized by measurement in an appropriate basis; this action generally destroys the coherent superpositions of the qubits. Take $|\Psi\rangle$ from Eq. 2.2 for example, measurement in the basis $\{|0\rangle, |1\rangle\}$ yields $|0\rangle$ with probability $|\langle 0|\Psi\rangle|^2 = |a|^2$ or $|1\rangle$ with probability $|\langle 1|\Psi\rangle|^2 = |b|^2$, where $\langle \bullet| \equiv |\bullet\rangle^\dagger$ denotes the Hermitian conjugate (H.c.) of $|\bullet\rangle$. The state then remains $|0\rangle$ or $|1\rangle$ depending on the measurement outcome, until any subsequent interaction occurs with the qubit [12].

2.1.3 Quantum algorithms

Due to the superposition principle in quantum mechanics, a single qubit can encode a large amount of information into the two parameters forming a two-dimensional space as opposed to a classical bit 0 or 1. Yet, this advantage soon disappears when we consider how to access the information [30], for which a large number of measurements is required to precisely determine the values of the parameters due to

the probabilistic nature of measurement results. In that case, the same algorithm must be executed many times to get many copies of the same final state, since copying of an arbitrary unknown state is forbidden in quantum mechanics by the *no-cloning* theorem [31]: This diminishes the potential of QC. Powerful algorithms in QIP that provide advantages over their classical counterparts thus mainly involve some clever encoding and measurement tricks, and exploit the potential interference effects enabled by relative phases.

The first such algorithm was discovered by Deutsch in 1985 [9] to determine whether a target function $f : |x\rangle\,|y\rangle \longrightarrow |x\rangle\,|f(x) \oplus y\rangle$ is constant ($f(0) = f(1)$) or balanced ($f(0) \neq f(1)$). Starting with Hadamard transforms on the initial state $|0\rangle\,|1\rangle$ which results in $|+\rangle\,|-\rangle$, f is then implemented to give us

$$\frac{(-1)^{f(0)}}{2}(|0\rangle + (-1)^{f(0)\oplus f(1)}\,|1\rangle)\,|-\rangle\,. \tag{2.7}$$

A single measurement on the first qubit in the basis $\{|+\rangle,\ |-\rangle\}$ will thus yield the required information about whether $f(0) \oplus f(1)$ equals 0 (for constant f) or 1 (for non-constant f) because of the $\oplus$ (+ modulo 2) operation. Therefore, only a single implementation of the function f is needed for our purpose, as opposed to the classical case of two evaluations of f.

This algorithm was later generalized by Deutsch with *Jozsa* to account for the n-qubit case where we have $f : |\boldsymbol{x}\rangle\,|y\rangle \longrightarrow |x\rangle\,|f(\boldsymbol{x}) \oplus y\rangle$ with an n-dimensional vector $\boldsymbol{x}$. Again, measurement on the first n qubits after one f enquiry is sufficient for a correct answer [32]. Classically, to solve this problem with absolute confidence $(2^{n-1} + 1)$ f enquiries are required. Even if we adopt probabilistic approaches, a constant k evaluations of f are still needed for a high probability ($\geqslant 1 - \frac{1}{2^{k-1}}$) of correct judgement [7]. Therefore, this quantum boost in computational speed is phenomenal when f takes much more time or is much more difficult to be implemented

than other gate operations.

Although the Deutsch-Jozsa algorithm may have little applicational value, it has inspired many other algorithms. It actually belongs to a wider family of algorithms that correspond to the solutions of different special cases of the *Hidden Subgroup* problem [7], among which there is the famous *Shor*'s factoring algorithm making efficient factorization of large numbers possible [33]. It also inspired the *Grover*'s search algorithm which provides a quadratic speed-up for searching an unsorted database [34]; this advantage over classical computation is considerable for databases with huge sizes. These two revolutionary algorithms in QIP that make the use of quantum Fourier transforms are of great practical values and implications once they are realized. Furthermore, there have also been discoveries of many other quantum algorithms [35, 36].

2.1.4 Applications in QIP

Aside from the factoring and searching abilities, QIP also has many other applications in the real world. For instance, the current security of data transmission [37] is based on the mathematical assumption that factoring large numbers in a timely fashion is a pratically impossible task, which seems plausible since no efficient factoring scheme in classical computation has yet been found. However, resting on this assumption for the communication security in the entire banking and military industries is rather unpleasant. Moreover, if a quantum computer were in place, this security can be easily breached due to its powerful factoring capability. But in return, QIP can also ensure secure communication against any third party eavesdropping through quantum key distribution [38, 39, 40, 41, 42], which results from the fact that measurement destroys coherent superpositions of qubits. Implementation of such networks and some protocols have been demonstrated in the past few

years [43, 44, 45, 46, 47, 48, 49]. In addition, some quantum cryptographic devices are already commercially available, although at this stage they are primarily aimed at institutions where the security of data transmission is crucial [50]. As the technology matures, lower cost quantum cryptographic networks are expected to be in place in the near future.

As another example, by exploiting the entanglement property of small-scale systems, highly sensitive measurements on physical parameters can be achieved by quantum metrology in QIP, which enables better precisions than conventional limits [51, 52, 53]. Applications include high resolution measurement in optical phases [54] and magnetic field strength variations [55], the sensitive detection of gravitational waves, and so on. Accurate phase measurement is important for determining the position, distance, acceleration in nanoscale dimensions, while small variations in field strengths can be used to discover impurity properties, *et cetera* [56].

The greatest power of all in QIP would perhaps be its capability in simulating quantum systems efficiently [8, 57, 58]. Classical simulation of the behaviour of an n-qubit system requires tracking the evolutions of the 2^n parameters [see Eq. 2.3], and thus results in an exponential slowdown as the system size n increases. This obstacle can be overcome by genuine quantum simulations on a quantum computer once it is in place. It would be of great significance in scientific research where experiments are time-consuming and costly for the target quantum system: Quantum simulations can be applied to suggest properties of the target object prior to experimental verifications.

2.2 Notion of entanglement

Thus far, we have encountered the basics in QIP, where we have seen the important roles of quantum superposition and entanglement. But, what is entanglement?

2.2.1 Non-local correlations

In 1935, *Einstein, Podolsky and Rosen* illustrated a peculiar feature about the *Bell* states through a thought experiment [59]. It was later referred as the famous *EPR* paradox and has since provoked philosophical controversies around local realism and counterfactual definiteness in quantum mechanics [60]. We shall not go into any details of such issues, but instead focus on the original thought experiment and its implications for practical purposes.

Take the singlet Bell state $|S\rangle := (|01\rangle - |10\rangle)/\sqrt{2}$ for example, suppose the two qubits are separated to distant parties (Alice and Bob) each of whom possesses one of them. In that case, neither Alice nor Bob has any knowledge of the states of their individual qubits. However, if now Alice measures her qubit with a result, say $|0\rangle_A$, thus collapsing the two-qubit state into the state $|0_A 1_B\rangle$, she immediately gains the information about Bob's state being in $|1\rangle_B$ for certainty even before any communication with Bob. This is rather intriguing since the two qubits shared by Alice and Bob are not interacting, yet an action on one immediately changes the state of the other. It seems as though information could travel faster than the speed of light via such states[1]. This is known as the EPR paradox [59]. Note that the argument is equally valid for the other three triplet Bell states, namely $|T_0\rangle := (|01\rangle + |10\rangle)/\sqrt{2}$ and $|T_\pm\rangle := (|00\rangle \pm |11\rangle)/\sqrt{2}$.

It was Bell who then first suggested in his 1964 seminal paper that the Bell states exhibit correlation which is to a higher degree than any that can be seen in the classical world [61]. In fact, through his famous Bell's inequality or the variants like the *CHSH* inequality [62], such non-local correlations exist in any quantum state that is able to violate the inequality [63] up to the *Cirel'son* bound [64] (attained by the Bell states). These peculiar correlations between two or more qubits that are

[1]Statistically, Bob cannot tell the difference between what Alice did and a random measurement. Thus, this does not allow instantaneous transmission of information between Alice and Bob.

unseen classically are referred as *entanglement* [65] in quantum mechanics.

It is actually this property of entanglement that makes QIP so powerful. All quantum algorithms and hence the applications involve this phenomenon through the entangling two-qubit gates. We can even teleport qubits in absence of quantum channels if Bell states are available [66, 67]. But, entanglement has to be generated and dissipated during the implementation of any algorithm, and it cannot be created by *local operations and classical communications* (LOCC) alone [7]. Therefore, a challenge in QIP is the ability to generate entanglement between initially separable qubits. In view of this, entanglement is regarded as an essential *resource* in QIP.

In an effort to quantify entanglement for practical QIP tasks, there have been a number of proposals for entanglement measures [65], such as the *Wootters concurrence* $\mathcal{C} \in [0,1]$ [68] or *entanglement of formation* $\mathrm{E}_F \in [0,1]$ for two-qubit states [69]. All entanglement measures are monotones in that they are zero for separable states (expressible in tensor product forms) and equal to one for the Bell states, while LOCC can not increase their values [65]. Therefore, they are essentially equivalent. In particular, the entanglement of formation E_F represents the number of Bell pairs needed to prepare a single copy of the bipartite state in question through LOCC only [69]. For states with positive E_F values, one can apply distillation protocols to a required number of copies ($\sim 1/\mathrm{E}_F$) of the target state using only LOCC, to enhance the degree of entanglement for a single copy of the state which is purified to be maximally entangled at the end [70, 71, 72, 73, 74, 75]. There also exists probabilistic single-copy distillation protocols for states with E_F values higher than some threshold [76]. These methods are also connected to quantum error-correction codes to overcome quantum noise [77, 76], which are to be introduced in Sec. 2.3.

One interesting property of entanglement is that when two qubits are maximally entangled with $\mathrm{E}_F = 1$, they can not be simultaneously entangled to any other qubit to any degree, i.e. quantum entanglement is monogamous [78].

2.2.2 Measurement-based QC

Notably, entanglement naturally exists between interacting quantum systems at certain points of time, and can be created through controlled interactions between the target qubits. In 2001, *Raussendorf* and *Briegel* suggested a novel way of utilizing entanglement to perform QIP tasks with measurement-based quantum computation (MBQC), an alternative but equivalent paradigm to the circuit model for QIP tasks [79, 80].

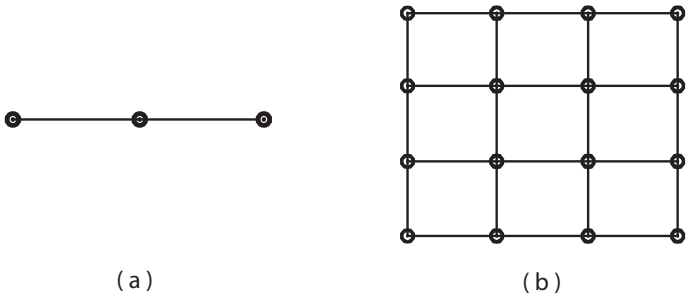


Figure 2.2: Examples for graphical representations of graph states: Each node represents a $|+\rangle$ state and each line corresponds to a C_{Phase} gate applied to the two nodes it connects. (a) A one dimensional 3-qubit chain in MBQC representing the 3-qubit state of $(|000\rangle + |001\rangle + |010\rangle + |100\rangle - |011\rangle + |101\rangle - |110\rangle + |111\rangle)/2\sqrt{2}$; (b) A 4×4 two dimensional cluster state — a lattice of qubits.

The key element in MBQC or one-way QC is a cluster state, which is some large entangled resource, mathematically represented as a graph with nodes connected by lines [see Fig. 2.2]. Once a cluster state of a sufficient size is constructed, the only requirement for executing a quantum algorithm is purely single qubit measurement which are taken successively from one end (left) to the other (right): Errors during the execution of algorithms can all be dealt with at the end [79]. Moreover, in creating this entangled resource, one can also tolerate complete failures which are simply disgarded from the cluster state, by using different degrees of freedom to grow and store the graph state [81]. Therefore, taking errors such as decoherence into account, MBQC scales better than controlled interactions.

The major task for the physical realization is then to scalably create such a sufficiently large, entangled resource, which is to be consumed during the implementation of any QIP task. Basic MBQC involving four photons has been experimentally performed with an implementation of the Grover's search algorithm [82]. Over the years, there have also been quite a few novel proposals for the scalable creation of cluster states [83, 84, 85, 86, 87, 88, 89, 90, 91, 92]. In addition, a new framework for MBQC beyond the cluster-state model has also been suggested recently, with experimental demonstrations of the Deutsch algorithm [93].

Furthermore, the distributed architectures[2] adopted in Refs. [83, 84] also have the advantage that unwanted direct interactions can be avoided and hence the difficulty in practical quantum control is reduced. Due to their inherently distributed nature, the cluster states generated can also be directly used to perform distributed QIP tasks such as quantum cryptography through applying single qubit operations only.

2.3 Decoherence and fault-tolerant QIP

Let us turn to the challenges along the way towards the realization of QIP. The main obstacle is the naturally-occurring process of decoherence which leads to loss of phase information and changes of the superposition states [7]. This follows from the fact that any quantum system constantly interacts with its surrounding environment. The good news is that we can implement various quantum error-correction codes (QECC) to account for the errors from the environment [7] as we do in classical computation; there is thus no need for error-free QIP. The challenge, however, remains at meeting the fault-tolerance threshold for universal QC at $\sim 10^2 - 10^4$ gate operations before a single error could occur so that feasible QECC can be carried out with-

[2] Earlier schemes for the generation of distributed cluster states via photon detection on spin qubits exist [94, 95], but they did not take into account of the realistic error of photon loss.

out compromising the scalability of the physical system [see Sec. 2.3.2] [96, 97, 98]. This essentially sets the condition for suitable candidates of qubits, whose coherence time must be sufficiently long when compared to their typical gate operation times. Meanwhile, the architecture must be such that probability of errors in gate operations are sufficiently low, which normally requires good quantum control techniques.

2.3.1 Quantum noise

The noise introduced into any quantum system by the surrounding environment can be arbitrary. Simple examples are those represented by the Pauli operators [Eq. 2.4], corresponding to the bit-flip (σ_x), the phase-flip (σ_z) and the combination of bit and phase-flip (σ_y) errors. Together with the Identity $\mathbb{1}$ (error-free), they form the basis of error operators on a single qubit. An error could be any linear combination of the basis operators, such as the general *depolarizing* error channel which consists of all four basis operators with equal weight [7]. Yet, upon measurement the effect of any error can be categorized into one of the four basis operators, which can be corrected by an appropriate QECC [7]. Therefore, unlike analog computing, the power of QIP does *not* diminish through the introduction of continuous errors.

To take account of errors in general, we need to adopt the density matrix and quantum operation formalism from Ref. [7]: The density matrix or density operator of the qubit described by Eq. 2.2 can be expressed as

$$\rho = |\Psi\rangle \langle\Psi| = \begin{pmatrix} |a|^2 & ab^* \\ a^*b & |b|^2 \end{pmatrix}, \tag{2.8}$$

which describes a pure state with $\mathrm{Tr}(\rho^2) = 1$ for the trace operation Tr. Note that $\mathrm{Tr}(\rho) = 1$ for any density matrix by the conservation of total probability. With

general Pauli errors acting on the qubit, the state becomes

$$\rho_{\boldsymbol{\epsilon}} = (1-\epsilon)\,|\Psi\rangle\langle\Psi| + \sum_{\alpha=x,y,z} \epsilon_\alpha \sigma_\alpha\,|\Psi\rangle\langle\Psi|\,\sigma_\alpha, \tag{2.9}$$

where ϵ_α denotes the occurrence probability of the corresponding error, and we have $\epsilon = \sum_\alpha \epsilon_\alpha$. Eq. 2.9 generally represents a mixed state $\big($with $\mathrm{Tr}(\rho_{\boldsymbol{\epsilon}}^2) < 1\big)$, and once the coherences off the diagonal in Eq. 2.8 are lost the state becomes a classical mixture as $\rho_{\mathrm{cm}} = |a'|^2\,|0\rangle\langle 0| + |b'|^2\,|1\rangle\langle 1|$ [7].

The general density operator for a qubit [Eq. 2.8] can also be re-written as

$$\rho = \frac{1}{2}\big(\mathbb{1} + \sum_{\alpha=x,y,z} r_\alpha \sigma_\alpha\big), \tag{2.10}$$

where $r_\alpha = \mathrm{Tr}(\sigma_\alpha \rho)$. This provides a natural one-to-one mapping to the Bloch sphere picture, with coordinate $\boldsymbol{r} = (r_x, r_y, r_z)$ for the state ρ. Mixed states correspond to points inside the sphere, where the completely mixed state sits on the origin O in Fig. 2.1 [7]. Again, tensor product operations can be applied to combine qubits.

More generally, beyond a single qubit the density matrix of a quantum system can be expressed as $\rho = \sum_i p_i\,|\psi_i\rangle\langle\psi_i|$, where the probabilities p_i of being in particular states $|\psi_i\rangle\langle\psi_i|$ sum to one. This is distinct from a statistical mixture, since coherences can potentially exist. Ref. [7] provides more detailed treatment of the density matrix and quantum operation formalism, together with the generalized measurement theory, which this thesis shall not be concerned with. We shall, however, note that to measure an observable $\mathcal{O}$ with eigenvalues $\{\mathcal{O}_n\}$ the result will be n with probability $\Pr(\mathcal{O}_n) = \mathrm{Tr}\,(P_n\rho)$, where P_n is the projection operator onto the corresponding eigenspace; the state then becomes $\rho' = P_n\rho P_n/\Pr(\mathcal{O}_n)$ for subsequent evolution [7].

2.3.2 Quantum error corrections

We now briefly look at some examples of quantum error corrections. Like their classical counterparts, QECC are implemented through the introduction of redundancy. The simplest QECC are for either the bit-flip or the phase-flip errors on the general qubit state $|\Psi\rangle = a\,|0\rangle + b\,|1\rangle$ in Eq. 2.2, through introducing another two qubits in the $|0\rangle$ state [7]. By two successive applications of C_{NOT} gates, $|\Psi\rangle$ is transformed to the state $|\Psi'\rangle = a\,|000\rangle + b\,|111\rangle$, which is protected against a single bit-flip error via the 3-qubit bit-flip code (*majority voting*).

The implementation of the code is as follows: First, we detect the position of the error (if any) by legitimate measurement processes through distinguishable projection operatiors:

$$\begin{aligned} P_0 &:= |000\rangle\langle 000| + |111\rangle\langle 111| \\ P_1 &:= |100\rangle\langle 100| + |011\rangle\langle 011| \\ P_2 &:= |010\rangle\langle 010| + |101\rangle\langle 101| \\ P_3 &:= |001\rangle\langle 001| + |110\rangle\langle 110| \end{aligned} \tag{2.11}$$

where the measurement results are obtained through the actions of these operators on the 3-qubit state, which does *not* change after the measurement. Depending on the result, with P_i corresponding to error on the i^{th} qubit (and 0 means error-free), we then apply σ_x gate on the affected qubit to recover the initial state $|\Psi'\rangle$. Finally, application of C_{NOT} gates gives us back the original qubit state $|\Psi\rangle$, separated from the other two $|0\rangle$ qubits [7].

The success of such recovery requires that the error rate is much smaller than unity, and that the errors are uncorrelated. Similarly, we can implement the 3-qubit phase-flip code if we apply Hadamard gates to transform $|\Psi'\rangle$ into the basis $\{|+\rangle, |-\rangle\}$ [7]; in 1998 demonstration of this code with liquid-state nuclear magnetic

resonance was achieved, as the first experimental QECC implementation [99].

Through more redundancy, one can implement QECC capable of correcting an arbitrary error on a single qubit. The first such scheme was discovered by Shor in 1995 with his 9-qubit concatenation code, based on the 3-qubit bit-flip and phase-flip codes [100]. Since then, QECC with other approaches that can accomplish the same goal, but with less redundancy, have been discovered. Examples are the *Steane*'s 7-qubit code [101], and the *Laflamme*'s 5-qubit code [102] that uses the least redundancy possible, both of which were later generalized to the *CSS* codes [103, 104] and further to the stabilizer codes [105]. There have also been newer QECC proposals involving topological QC [106] and the assistance of quantum entanglement [107]. Ref. [108] provides more detailed development of QECC over the last decade. Furthermore, noticeable experimental progress in QECC has also been observed with different physical systems [109, 110, 111, 112, 113, 114, 115].

It was the discovery of these codes that can take care of errors which made fault-tolerant QIP possible. Currently, the best QECC (surface codes [116]) can tackle depolarizing noise with an error rate up to 18.5% for a quantum memory, assuming perfect gate operations and measurement on the qubits [117]. When noise from all sources are taken into account, the general error threshold that could be tolerated for QIP stands at a few percent, if all qubits can interact with each other at the same error rate [118, 119]. More realistically, when this last assumption is relaxed and each qubit can only interact with a few others *locally*, the error threshold from *each source* has been improved from 0.75% in 2007 [120, 121] to the recent $1.1 - 1.4\%$, using better decoding techniques [98]. Note that these numbers are the threshold values, and for a real quantum computer lower error rates would be required for realistic resource overheads (ideally at least tens times lower) [116]. Whenever relevant [see Chapter 7], we shall use 1% as the benchmark for the fault-tolerant error target.

2.3.3 Modelling open quantum systems

In this section, we shall introduce the main methods for modelling errors. There is no genuinely isolated quantum system in practice, apart from the Universe as a whole. If some quantum system has extremely weak interactions with the surrounding environment, we could regard it as isolated to a good approximation and thus subject to unitary evolution governed by the Schrödinger equation [Eq. 4.1] [12], at least for a certain amount of time. Beyond this error-free period or in the case where the interactions are not negligible, we must model it as an open quantum system whose evolution is no longer unitary. This is normally regarded as a *Markovian* process and the state of the system $\rho(t)$ evolves according to the quantum master equation[3]

$$\frac{d}{dt}\rho(t) = \mathcal{L}\rho(t) = -i[H,\rho] + \sum_k \gamma_k (A_k \rho A_k^\dagger - \frac{1}{2}A_k^\dagger A_k \rho - \frac{1}{2}\rho A_k^\dagger A_k), \tag{2.12}$$

where the *Lindblad* operators A_k's can be any orthonormal basis set of operators in the quantum *Liouville* space for the system and correspond to the interactions with the surrounding environment at the respective rates γ_k [122]. The commutator term $-i[H,\rho] := -i(H\rho - \rho H)$ with the appropriate Hamiltonian H, represents the unitary evolution part. Here, the super-operatior $\mathcal{L}$ in Eq. 2.12 is an example of quantum operations [7].

Meanwhile, under certain circumstances where we are only interested in the initial and final states without explicit reference to the intermediate details [see Sec. 5.3], it is easier to use an alternative yet equivalent approach: We couple the target system $\rho_t^{(i)}$ with another ancilla system ρ_a via the tensor product operation, forming a larger and to a good approximation, closed system, which is then subject to unitary evolution U for some time. We can recover the final state $\rho_t^{(f)}$ of the

[3]This equation is applied in Chapters 5 – 7 for general decoherence processes.

target system by the partial trace operation Tr_a over the ancilla system, i.e.,

$$\rho_t^{(f)} = \mathrm{Tr}_a[U(\rho_t^{(i)} \bigotimes \rho_a)U^\dagger], \tag{2.13}$$

which gives the correct measurement statistics [7].

In any case, good control ability over the target quantum objects is usually needed in QIP; certain quantum control techniques can be applied appropriately [123]. Due to the various approximations adopted and the error sources in presence, perfect results are extremely difficult to obtain. In practice, the term *fidelity* F is used, between the evolved state ρ and the desired state σ, where

$$F(\rho, \sigma) = \mathrm{Tr}\left(\sqrt{\sqrt{\rho}\sigma\sqrt{\rho}}\right), \tag{2.14}$$

to determine the effectiveness of the control processes [124]. Symmetric in its two arguments, the fidelity $F \in [0, 1]$ indicates the closeness of the two states compared, with "1" indicating the perfect match. To link to the error thresholds (i.e., maximum allowed error probability) introduced in Sec. 2.3.2, the more relevant metric is F^2 which denotes the probability of measuring ρ being in the state σ.

2.4 Summary

In this chapter, we have described the essential ingredients for QC with a few potentially very important applications. There have been many great achievements in the QIP field within the last two decades, and in the following chapter we shall briefly describe the major architectures proposed for the physical implementation of QIP devices.

Chapter 3

Potential architectures for QIP implementation

The fact that technological advances in the semiconductor area put the universal Turing machine into reality, has inspired many researchers in the QIP field to seek suitable materials for implementing QC [7]. Now, having become familiar with the principal concepts and obstacles in QIP, let us review the prominent proposals of candidate architectures and their significant progress since the inception of the very idea. We shall focus on solid-state spins for the development of later chapters in this thesis. However, other physical systems will also be mentioned, not only because of the crucial advances achieved but the analogy that could be drawn to the solid-state version. On top of that, hybrid approaches employing different degrees of freedom can make solid-state spins even more powerful for QIP tasks [125].

3.1 Photonic, atomic, and molecular

3.1.1 Photonic — quantum optics

Photons, or quanta of light [126, 127], can be utilized to encode qubits in a number of ways: The polarization of a photon is a natural two-level system, or alternatively two optical modes of another kind (such as spatial paths after a beam splitter, presence and absence in a cavity, or two different frequency modes, *etc.*) provide other realizations [128]. Single qubit operations on photon polarization states are straightforward with appropriate arrangement of conventional birefringent waveplates [129]. In addition, polarizing beam splitters can be adopted to convert between polarization and path encoding schemes for photon qubits [130].

Besides single qubit rotations, universal optical QIP also requires the ability to efficiently implement an entangling gate (e.g., the C_{NOT}) for at least one of the encoding schemes. This is a major challenge for photons since they do not interact with each other and only very weakly with the environment in free space (or optical fibres). Non-linearity in the optical *Kerr* effect was then considered for entangling path-encoded qubits, yet no materials can produce large enough cross-Kerr phase shifts for this purpose [128]. In 2001, *Knill, Laflamme* and *Milburn* (KLM) discovered an alternative, probabilistic approach to realize the C_{NOT} gate on polarization-encoded qubits, with only simple *linear* optical circuits as well as single photon sources and detectors [131]. However, this measurement-induced C_{NOT} gate requires redundancy, and a high success probability ($> 95\%$) demands a huge resource overhead ($> 10^4$ photon pairs per C_{NOT} gate) despite further development in the scheme [130], raising the serious issue of non-scalability. MBQC [see Sec. 2.2.2], on the other hand, can tolerate complete failures in the creation of cluster states [79, 81] and can thus be probabilistic for the purposes of creating entanglement. This alternative paradigm was later adopted to significantly reduce the resource overhead

by $3-4$ orders of magnitude [132, 133] (with proof-of-concept experimental demonstrations [82, 134, 135]), revitalising the remarkable KLM scheme [130].

The difficulty in efficiently entangling photons is accompanied by the great advantage of the qubits being largely decoherence free at any temperature. This makes photons an ideal candidate for quantum communications, connecting distant qubits of another degree of freedom. Nevertheless, the problem of photon loss, together with the necessity of scalable, indistinguishable single photon sources and high-efficiency photon detectors, remain the challenging aspects of reaching the fault-tolerant error threshold $\sim 10^{-2} - 10^{-4}$ for universal optical QIP [136], although tremendous progress has been demonstrated in addressing these issues with novel solid-state materials (source, detector) and integrated optics (low photon loss) [130].

3.1.2 Atomic — ion traps, optical lattice for cold atoms

Atomic energy levels of individual trapped ions (or atoms) [137] are also suitable for QIP, the idea of which was pioneered by *Cirac* and *Zoller* in 1995 [138]. Various laser cooling techniques, together with appropriately arranged electric and magnetic fields, are required to provide the spatial confinement so that spectroscopy can be applied to access the small energy scales [137]. This means that such QIP architectures could only be implemented in the laboratory, due to the low temperature requirement.

Here, a qubit can be represented by either two hyperfine levels (associated with the nuclear spin states) in the stable ground state of a trapped ion, or the composite of the electronic ground state and an optically excited level [see Fig. 3.1]. The ground state can be populated through *optical pumping* as dictated by the selection rules, while transitions between the corresponding two levels are achieved via laser pulses of the correct frequencies [137]; other irrelevant levels can hence be ignored.

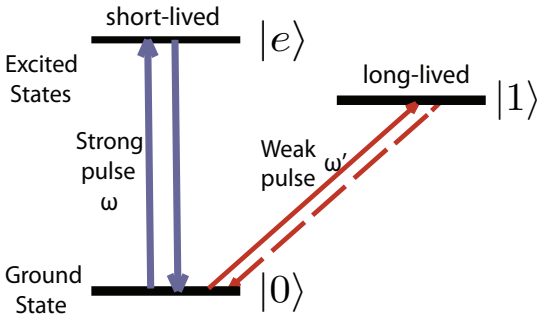


Figure 3.1: Three relevant energy levels of a trapped ion for the optically accessible electronic qubit, which is encoded in the ground state $|0\rangle$ and the metastable (dark) level $|1\rangle$. Allowed transitions (indicated by arrows) are excited respectively by the simultaneous strong and weak laser pulses of appropriate frequencies. The state $|0\rangle$ is distinguished from the dark state $|1\rangle$ by fluorescence detection due to the short-lived level $|e\rangle$.

By combining pulses of suitable durations, any single qubit gate on the hyperfine qubit can be implemented [137], and has been achieved with an error occurrence below the fault-tolerant threshold ($\sim 10^{-4}$) [139]. Single qubit operations on the optically accessible degree of freedom in any selected ion within a linear chain has also been experimentally demonstrated [140].

The entangling $C_{\rm NOT}$ gate proposed in Ref. [138] requires the mediation of the lowest phonon state (quantized motional degree of freedom), with external laser pulses. This Cirac-Zoller scheme was experimentally demonstrated in 2003 [141]; furthermore, an alternative route to preparing a Bell state was also achieved with a fidelity $F > 97\%$ [142]. Since then, appreciable experimental advancements have been witnessed [143]. One advantange of trapped ion qubits is that they exhibit long coherence time, with more than ten minutes observed for the hyperfine qubit [144] and at least 20 s for the electronic case [145]. However, coupling to the motional degree of freedom limits the speed of the entangling operations, and it also makes the implementation much more difficult as the size of the ion traps grows [146] (and current experiments are restricted to 14 qubits [147]). Proposals for scaling up the one-

dimensional geometry mainly explore arrays of individual trap zones, each accommodating a few ions [146, 148]; one would either physically move the ions between zones, or could adopt the distributed architecture mentioned in Sec. 2.2.2 [146].

Alternatively, neutral atoms trapped in cavities [149, 150, 151] or in an *optical lattice* [152, 153, 154, 155] can also be employed for QIP. Notably, for an internal degree of freedom of the cold atoms in an optical lattice, effective spin exchange models [156, 157] with fully tunable parameters could be realized [158]. Moreover, in presence of a magnetic field gradient, single sites could be selectively and coherently manipulated with microwave pulses [159]. This provides a substitute testbed for many solid-state QIP proposals involving spin exchange interactions [see Sec. 4.1.1].

3.1.3 Molecular — nuclear magnetic resonance (NMR)

QIP can also be carried out based on the well-proven technology of nuclear magnetic resonance (NMR) [28], where the qubits are encoded in the spin states of inequivalent atomic nuclei in a molecule; a sample with a large number of the identical, independent molecules is required for signal amplification, while an average over the ensemble is taken for computational purposes [160, 161]. Single qubit operations and the read-out processes can be accomplished by sequences of radio-frequency pulses [28], while an entangling gate is mediated via electrons in the chemical bonds [162]. In this way, liquid-state NMR has witnessed the earliest triumphs in implementing small-scale quantum algorithms, such as the Deutsch algorithm [163], 7-qubit Shor's factorization of 15 [164] and high-fidelity QECC for three ($F = 0.93$) [165] and five qubits ($F = 0.75$) [166].

Despite these huge successes, QIP with conventional liquid-state NMR has a fundamental limit on its scalability ($\sim$ 10 qubits), due to the restricted number of distinct nuclei on any molecule and (more crucially) the highly mixed nature of the

ensemble-averaged pseudo-pure states [167, 168]. It is, however, suggested that solid-state NMR QC can be scaled somewhat further due to much larger polarization [169].

3.2 Solid-state spins

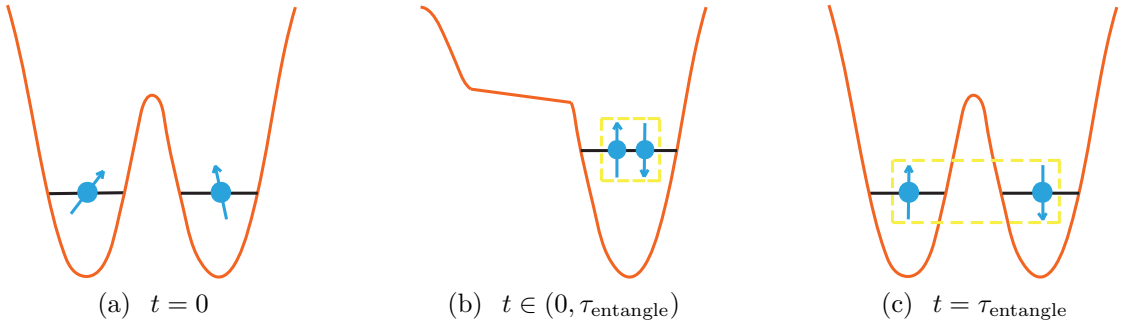
Solid-state qubits can take different forms, including charge, spin and others [11]. Our focus is on spin qubits which can be realized in a variety of ways, such as a single electron spin confined in a *quantum dot*, the electron or nuclear spin hosted by an impurity in silicon or diamond, or that exhibited by a *fullerene* caging an atom or ion, and even the spin of a free electron [125]. Throughout the rest of this thesis (unless stated otherwise), we identify the spin-up state $|\uparrow\rangle$ with the qubit state $|0\rangle$, and spin down $|\downarrow\rangle$ with $|1\rangle$; both are projections in $S_z = \frac{1}{2}\sigma_z$ for spin-1/2 particles [12]. We shall review the basic properties of these qubits, which are envisaged to fit into the interaction models to be introduced in Chapter 4.

We point out the two decoherence channels that are of particular importance for solid-state spins, namely, relaxation and dephasing [28]. The relaxation process arises when the qubit state $|1\rangle$ decays to $|0\rangle$ associated with energy dissipation, and is characterized by the relaxation (or decay) time T_1. The energy-conserving dephasing channel occurs due to the loss of phase coherence [off-diagonal terms in Eq. 2.8], and is characterized by the coherence (or dephasing) time T_2. One contribution for the T_2 process is pure dephasing, which is equivalent to the phase-flip error σ_z introduced in Sec. 2.3.1. Each process can be modelled by the Lindblad master equation [Eq. 2.12] for the corresponding operator $A_1 = \begin{pmatrix} 0 & 1 \\ 0 & 0 \end{pmatrix}$ or $A_2 = \sigma_z$ with rate $\gamma_i = 1/T_i$ $(i = 1, 2)$ [122]. The T_2 time is typically much shorter than T_1, and is limited by $T_2 \leq 2T_1$ since relaxation automatically generates a dephasing [88, 170].

3.2.1 Quantum dots (QDs)

Generally speaking, there are two different types of semiconductor quantum dots (QDs) useful for QIP, both of which can confine electronic states with quantized energy levels in all three spatial dimensions (on the nanometre scale) [125, 171, 172]. The first proposal for QIP with QDs was raised by *Loss* and *DiVincenzo* in 1998, where a qubit is encoded in the single electron spin in each *lithographically* defined QD; a universal set of qubit operations was suggested [173]. To obtain such a QD, miniature gate electrodes are deposited on a quantum well heterostructure (e.g., AlGaAs/GaAs) that already traps a two-dimensional electron gas (2DEG) [see Fig. 3.8(a)] [174, 175]. Electrical potentials are then applied to provide the confinement in further dimensions, and also control the number of electrons in the QD [176, 177]. This technique allows fabricating QDs of the desired lateral shapes, sizes and arrangement, including to position a number of QDs side-by-side [see Fig. 3.8] [171]. In addition, it is also readily compatible with the mature integrated semiconductor technology [171]. However, current experiments are typically conducted at electron temperature T $\sim$ 150 mK in a dilution refrigerator [174].

Single qubit gates for this kind of QDs have been implemented (on the nanosecond timescale) through electron spin resonance (ESR [178]) driven magnetically [179] and electrically [180, 181], and in certain scenarios by exploring the spin-orbit (SO [175]) coupling effect [182, 183]. The simplest two-qubit entangling gate is based on the *exchange* process [see Fig. 3.2], which requires virtual tunnelling of the spins between neighbouring QDs [see Sec. 4.1.1] [173]. This idea has been exploited to coherently manipulate a two-spin qubit in the basis $\{|S\rangle, |T_0\rangle\}$ in a double QD (i.e., two coupled QDs) [184]. Furthermore, by combining an inter-dot exchange process with single qubit operations, *Brunner* and co-workers have recently entangled two separately addressable single-spin qubits (with one spin in each of the two

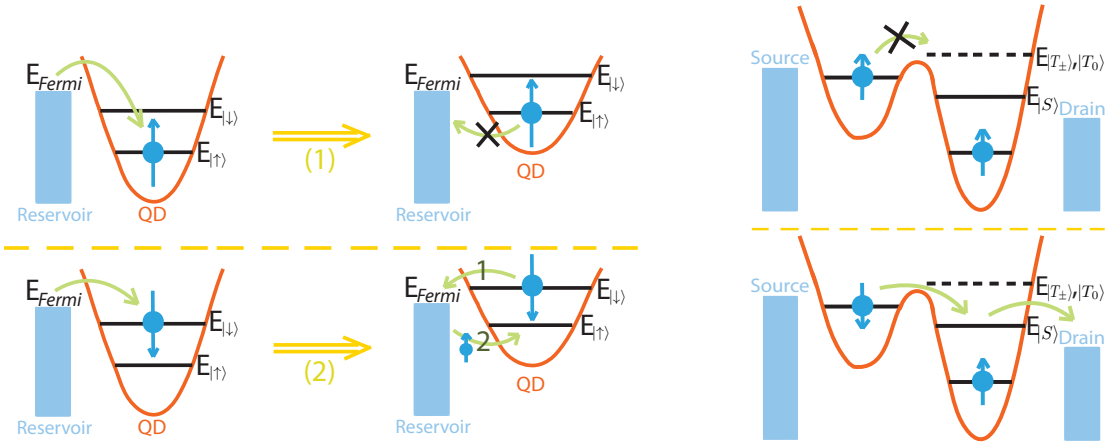


(a) $t = 0$ (b) $t \in (0, \tau_{\text{entangle}})$ (c) $t = \tau_{\text{entangle}}$

Figure 3.2: Simplified illustration for the spin exchange process in coupled QDs, with the barrier controlled by applied electric potentials. The two interacting electrons decay to the ground state (with symmetric spatial wavefunction in absence of any external magnetic field) at some time τ_{entangle}, when their spins are maximally entangled in the singlet state due to Pauli exclusion principle [173]. Note that exchange occurs *whenever* the spatial wavefunctions of the two electrons overlap, whose degree (controllable by adjusting the barrier) determines the coupling strengths [see Sec. 4.1.1]. Thus, virtual hopping processes are sufficient for the mechanism, though real electron tunnelling results in stronger coupling strengths. A similar process occurs for entangling the internal degree of freedom of two cold atoms in an optical lattice, controlled by applied laser fields [see Sec. 4.1.1] [153].

coupled QDs) [185]. Alternatively, with a magnetic field gradient integrated into the same system, an efficient one-step C_{Phase} gate has been realized, with an error probability below 10^{-4} [186].

Qubit measurement in such QDs can be achieved through *spin-to-charge conversion* [175], followed by sensitive charge detection with discrete conductance change in a one-dimensional quantum channel (called a quantum point contact or QPC [see Fig. 3.8(a)]) [187, 125]. The spin-to-charge conversion makes use of the *Coulomb blockade* effect in QDs [see Fig. 3.3] [188, 174, 175], and in this way single-shot measurement on the single-electron spin state in a QD (coupled to a reservoir with an external magnetic field) was experimentally demonstrated in 2004 [189]. Recently, a non-destructive measurement on the state of each single-electron spin in a double QD has also been carried out, under an inhomogeneous magnetic field [190]. Typical coherence (relaxation) time for a qubit of this kind is on the microsecond (millisecond [189]) scale, and the longest observed is $T_2 \simeq 200$ μs [191].



(a) Coulomb blockade effect ($B > 0$); (b) Spin blockade effect (B=0).

Figure 3.3: (a) In presence of an external magnetic field B, the energy levels for a single electron in the QD is spin dependent. The QD is emptied at both the beginning and the end, by controlling electric potentials such that $E_{Fermi} < E_{|\uparrow\rangle}$. Similarly, a spin of arbitrary state can be transferred from the reservoir to the QD when $E_{Fermi} > E_{|\downarrow\rangle}$. During the read-out with $E_{|\uparrow\rangle} < E_{Fermi} < E_{|\downarrow\rangle}$, the spin state $|\downarrow\rangle$ triggers a signal (with two contributions indicated) while the spin $|\uparrow\rangle$ is forbidden from any transfer process. The two spin states can thus be distinguished in this way [189]. (b) The similar spin blockade effect that occurs in the double QD arises due to the Pauli exclusion principle; the singlet energy level is lower than that of the triplets. The potentials are set such that the relevant energy levels have the indicated relations; the spin state of the single electron in the left QD can then be detected from the conductance measurement [185].

The other kind of QDs suitable for QIP are self-assembled nano-structures, which can be grown through the *Stranski-Krastanov* method [192, 193, 125, 172]. Such a QD is one of those isolated nanoscale regions (with a small band-gap) embedded in a large band-gap material (e.g, InAs/GaAs), and naturally provides three-dimensional confinement for electronic states in both the conduction (for spin-1/2 electrons) and valence (for spin-3/2 holes) bands [193, 125]. The system can thus be manipulated and measured optically [125, 194, 195]: Transitions between the hole and electron spin states can occur with the absorption or emission of circularly polarized photons, according to a set of selection rules conserving the total angular momentum [see Fig. 3.4] [193]. When an electron is optically excited from the valence band to the conduction band, an *exciton* (coupled electron-hole pair) arises in the QD, and

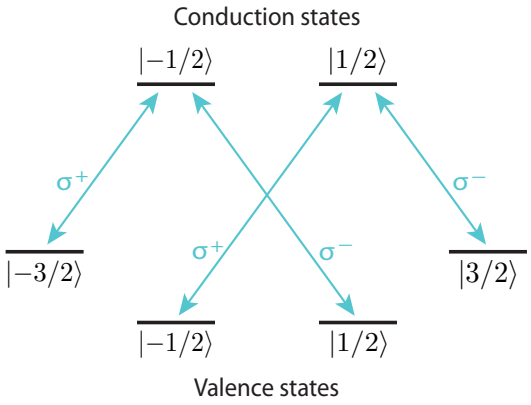


Figure 3.4: Allowed optical transitions between spin states in the valence and the lowest lying conduction bands of self-assembled QDs. The states $|m\rangle$ label the angular momentum projection with $J_z = m$. For each transition, the total angular momentum is conserved with the required photon polarization.

subsequently decays (with lifetime $\lesssim$ 1 ns at a few Kelvins [196, 197]) once the electron recombines with the hole emitting a photon [193]. Measurement can take place by applying probe pulses and observing the changes in the transmission [125, 198, 199].

The growth of these QDs is a random process, and thus it can be difficult to control their positions, sizes and shapes. Nevertheless, obtaining ordered QDs of this type is still possible [200], and it has been observed that with stacked multi-layers, these self-assembled QDs are more likely to line up *vertically* to minimize overall strain [201, 202]. Both the size and the shape of a QD affect the electric dipole moment between the ground and excited states, and hence can dramatically influence the energy levels and electronic properties of the QD [193, 171]. However, the fluctuations in the size and the shape ($\sim 10\%$ [203]) allow the non-resonant QDs to be individually addressed [195].

By doping or applying simple field effects, a single excess electron (hole) can be charged and confined in the conduction (valence) band of a self-assembled QD [204]; a qubit can then be encoded in the spin of this electron (hole). Again, circularly

polarized light can excite an electron from the valence band to create an exciton, which couples with the excess electron (hole) to form a *trion* [193, 125]. A trion typically relaxes with a similar lifetime to that of an exciton [196], but plays the key role in optical manipulations of the spin qubit [see Fig. 3.5] [88, 125, 193]. Utilizing

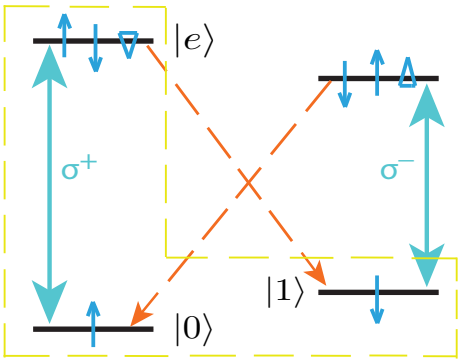


Figure 3.5: Simplified level structure for a self-assembled QD charged with a single excess electron in the conduction band, in presence of a small external magnetic field B_z in the growth direction (and hence the Zeeman splittings). Each spin state is coupled with the corresponding trion state (electron singlet plus hole) through appropriate optical transitions (green arrows). Weak spin-flip Raman processes (dashed arrows) are also allowed [205] such that the spin qubit can be optically initialized [206]. The story is similar for the hole spin qubit [207]. The yellow box outlines the elements for the distributed MBQC scheme proposed in Ref. [83] (with possible relabelling), and Ref. [88] analyses the prospect detailing the advantages and challenges ahead.

the weak spin-flip *Raman* transitions [see Fig. 3.5], optical spin polarization (in $|0\rangle$) was demonstrated with a high fidelity ($F = 99.8\%$) in 2006 [206]. This method, however, is rather slow ($\sim \mu$s [206]) constrained by the weak Raman processes. In the subsequent year, *Emary*, *Xu* and co-workers achieved much faster ($\sim$ ns) optical qubit initialization by applying a magnetic field B_x perpendicular to the QD growth direction and encoding the qubit (and the trion states) in the basis $\{|+\rangle, |-\rangle\}$ (*Voigt* geometry); linearly polarized light are used for the excitations [208, 209]. The same technique has been applied by *Dutt* and co-workers to generate electron spin coherence, with observed dephasing time $\sim$ 10 ns (at 4.8 K) [210, 211]. Coherence in the computation basis $\{|0\rangle, |1\rangle\}$ has also been demonstrated [212]. Recently,

observation of hole spin dephasing time exceeding 70 ns (below 500 mK) has been reported [213]. Theoretical studies suggest that for self-assembled QDs, the spin coherence time relevant for QC architectures can be much longer with $T_2 \sim 1 - 100$ μs [214]; the lower end ($\simeq 3$ μs at 2 K) has also been experimentally achieved using phase synchronization techniques in an ensemble [215]. Meanwhile, electron spin relaxation time of $T_1 \simeq 20$ ms (at 1 K) has been observed [216].

For such an electron spin, controlled ultrafast single qubit rotations around the optical axis (y) have been demonstrated (on the picosecond timescale) via precession about an effective magnetic field $B_{\rm Stark}$ [217], which arises from the optical *Stark* shift induced by intense tipping pulse [218]. Equivalently, higher gate fidelities ($F \gtrsim 90\%$) have been reported [219] with stimulated, two-pulse Raman (Λ) transitions under appropriate detuning [220, 221, 222]. Combined with *free* spin precession (around the z-axis[1]), the latter [219] has also illustrated that arbitrary single qubit rotations on the Bloch sphere may be achieved. In the Voigt geometry, *Greilich* and co-workers have performed similar tasks for the single spin qubits in an ensemble of self-assembled QDs, which exhibits stronger spin-photon coupling [194]. More recently, an optical geometric phase gate has been implemented [223], complementing those rotations around the optical axis so that universal single qubit operations can be readily realized [see Sec. 2.1.2] [7]. Alternatively, optical ESR experiments performed on such electron spins [224] also have the potential of complete control over single qubit rotations. Fast hole spin manipulation has been demonstrated in self-assembled QDs as well [195]. Furthermore, single-shot readout of the electron spin in single QDs is viable through spin-dependent resonance fluorescence [225, 226].

Although much has been done for the single qubit operations, experimental progress on entangling two or more qubits of this kind has been slow. Feasible

[1]This precession about the external magnetic field B_z occurs naturally, and is uncontrolled [28].

schemes put forward for entangling operations on these qubits mainly[2] utilize delocalized single exciton [227, 228, 229] or hole tunnelling [230] in two coupled, self-assembled QDs. Recently, *Kim* and co-workers have achieved the entanglement of two such qubits, based on electron tunnelling (on the picosecond timescale); both individual spins can be manipulated independently in the experiment [231].

The spin qubits in both types of QDs mentioned above (especially, in the gated QDs) could provide potential realization [see Chapter 4] for the spin-chain schemes to be introduced in Chapters 5 (entanglement distribution) and 6 (quantum memory). Note that both gated and self-assembled QDs also offer the possibility to encode charge qubits, such as the presence of a single electron spin in one of the two coupled, gated QDs [232] or the absence and presence of an exciton in a self-assembled QD [233]. However, these are not relevant to our research work, and hence beyond the scope of this thesis.

3.2.2 Impurities and defects

Dopant impurities in silicon [6] and diamond [234] offer alternative routes to confine single electronic and also nuclear spins, both of which can be employed as qubits. Popular candidate structures for QIP are arrays of phosphorus donors in silicon (Si:^{31}P) [235, 236] and nitrogen-vacancy defects (NV^- colour centres[3]) in diamond [16, 234]. The low natural abundance of nuclear spins (^{29}Si; ^{13}C, ^{14}N) and the small spin-orbit coupling exhibited in these host materials contribute to long electron spin coherence times [125, 238, 239, 240]. Indeed, the Si:P donor-bound electron spin has dephasing times on the millisecond timescale at a few Kelvins [238, 241], with the

[2]Here, we ignore alternative schemes using single photons as the mediator [193] or measurement assistance [83] for entanglement generation. With reliable single photon sources, entanglement can be generated between distant spin qubits (accounting for photon loss), which are suitable for the distributed architecture [83].
[3]The neutral state NV^0 could also be employed [237].

best measured[4] figure $T^{(e)}_{2(\mathrm{Si:P})} = 0.6$ s in an isotropically enriched ^{28}Si:P sample at 1.8 K [242]. Meanwhile, individual NV$^-$ centres in isotropically engineered, ultrapure diamond have witnessed the longest observed *room-temperature* electron spin coherence time $T^{(e)}_{2(\mathrm{NV})} = 1.8$ ms [240]. These numbers are unmatched by other quantum systems, and could be further increased [243, 244, 245] through *dynamical decoupling* from the surrounding nuclear spin-bath environment [246]. The relaxation times $T^{(e)}_{1(\mathrm{Si:P})}$ can reach hours for Si:P at low temperature [247], while $T^{(e)}_{1(\mathrm{NV})} \approx 7.5$ ms has been reported recently for NV$^-$ centres at room temperature [245]. This latter $T^{(e)}_{1(\mathrm{NV})}$ process has an exponential dependence on temperature, and can exceed seconds at liquid nitrogen temperatures[5] [248, 249].

In the original *Kane* proposal for a Si:P quantum computer, qubits are encoded in the ^{31}P nuclear spins; the phosphorus dopants should form large, ordered arrays at the atomic scale [235]. This fabrication challenge could be met using a scanning tunnelling microscope [250, 251]. The donor-bound electrons that can be manipulated by electric potentials [252] are required to mediate interactions between neighbouring nuclear spin qubits [235]. Alternatively, both the electronic and the nuclear spins from each ^{31}P impurity can be used as qubits [253], respectively for processing[6] [254] and storage [241]. Recent experiments show that quantum information storage in the ^{31}P nuclear spin has been achieved for as long as[7] $T^{(n)}_{2(\mathrm{Si:P})} = 192$ s (with $T^{(n)}_{1(\mathrm{Si:P})} \sim$ hrs) at 1.74 K [255]. The hyperfine coupled electron-nuclear spin

[4] By removing *instantaneous diffusion*, a dephasing time $\sim$ 1s is extracted in Ref. [242]; it is further extrapolated to $\sim$ 10 s in the presence of a magnetic field gradient which could suppress unwanted interactions [242].

[5] The relaxation mechanism was suggested to mainly originate from the two-phonon *Orbach* process [248], but more recent evidence indicated that there exist deviations from the model, possibly due to effects of the nuclear spins and spectral diffusion [249]. The $T^{(e)}_{2(\mathrm{NV})}$ time, however, remains at $\sim$ ms even at low temperature due to magnetic fluctuations from neighbouring spin flip-flops [240, 244, 245].

[6] The larger magnetic moment of electron spin, as compared to nuclear spin, means stronger interaction and hence faster manipulation (and also stronger decoherence). The electron spin also exhibits a multitude of couplings to other degrees of freedom, which can be harnessed [125].

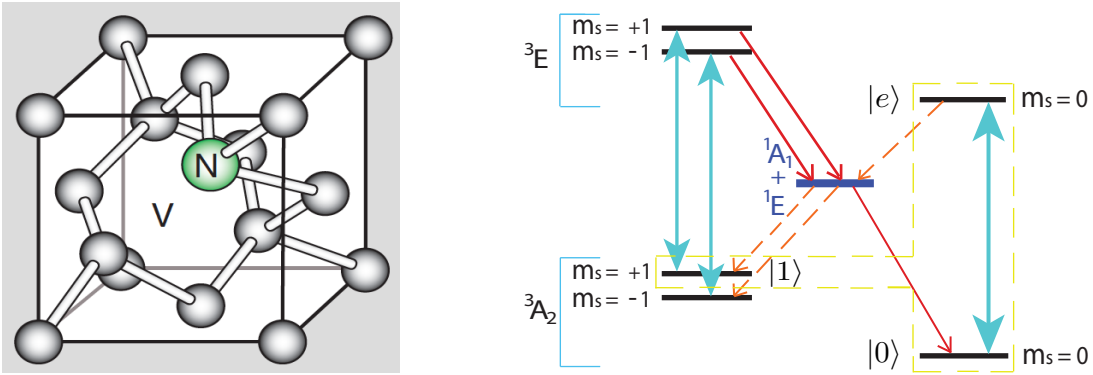
[7] This figure is obtained after dynamical decoupling sequences are applied; without decoupling, the dephasing time is 44 s at 1.74 K [255].

pair bound in each ^{31}P dopant exhibits four energy levels in the presence of an applied magnetic field, and can be manipulated by selective microwave (GHz, for electron spin) and radio-frequency (MHz, for nuclear spin) pulses [6, 241]. By choosing appropriate phase, power and duration for the resonant pulses, combined with suitable delays for free precession, qubit gates can be implemented on the electron-nuclear spin pair[8] [6, 125]; entanglement within the two-spin system has also been created in this way ($F = 98\%$), simultaneously for 10^{10} pairs in an Si:P ensemble[9] [259]. The electronic and the coupled nuclear spins can be measured by pulsed ESR [241] and electron-nuclear double resonance (ENDOR) [261], respectively. Spin-dependent recombination [262, 263] and tunnelling [264] offer further routes to read out the electron spin electrically. By using the latter with a single-electron transistor [265], *Morello* and co-workers have performed the first single-shot measurement on the *single* donor electron spin in Si:P (similar to the Coulomb blockade effect [see Fig. 3.3(a)]) [264]. Optical readout of the electronic and the nuclear spins can also be enabled by selective ionization [266] or optical excitation [267] of donors in specific spin states. Similar optical methods have been applied to polarize the spins significantly beyond expections at thermal equilibrium [268, 269], and this can be achieved for both the electronic and the nuclear spins within a second [269], providing a fast qubit initialization mechanism. Based on these tools and potential future improvement, a scheme of creating Si:P cluster states has been proposed in Ref. [89].

Over the past decade, NV^- centres in diamond have equally attracted huge attention for QIP implementation [234, 270]: Rich dynamics is enabled by the coupling

[8] It is suggested that microwave pulses alone could control the two-spin system, where qubit gates on the nuclear spin subsystem could be indirectly implemented through the coupled electron spin [256, 257]. The two spins can also be decoupled for longer coherence times [255], and to better play their separate roles [6, 258].

[9] Already in 2003, *Mehring* and co-workers demonstated the creation of pseudo-entanglement between the electron and nuclear spins, 'pseudo' because the initial states were highly mixed [260]. Nonetheless, they provided a neat way of performing density matrix tomography through varying phase gates [260].



(a) (b)

Figure 3.6: (a) Physical structure of NV^- centre in diamond (picture courtesy of Dr. Simon C. Benjamin [88] Copyright © 2009 WILEY-VCH Verlag GmbH & Co. kGaA, Weinherm); (b) Simplified electronic structure of the negatively charged NV^- defect and the qubit implementation, with the yellow box outlining elements for the distributed MBQC scheme [83, 88]. Linearly polarized optical pulses at 637 nm (green arrows) can cause spin-conserving transitions from the ground triplet $^3A_2$ to the excited ^3E states and vice versa for fluorescence relaxation, while spin-flippling transitions occur with zero probability at the first order [272, 273]. Two metastable singlet states $^1A_1$ and ^1E exist and act 'together' (thus labelled together for simplicity), providing a route for intersystem crossing relaxation (ISC, red arrows) from the excited triplet to the ground state: Thick red lines have associated ISC rates that are several orders of magnitude faster than the thinner red line, and dashed transitions can be considered to be negligible [274, 275, 276].

of the trapped electron spin to nuclear spins and photons, both of which can be harnessed at room temperature [16]. A nitrogen-vacancy defect consists of a substitutional nitrogen atom and an adjacent vacancy in diamond [see Fig. 3.6(a)]. In its negatively charged state, the NV^- centre traps an excess electron and possesses a paramagnetic ground state ($S = 1$) with extraordinarily long spin lifetime. For each NV^- centre, the spin-triplet ground state $^3A_2$ consists of the $m_s = 0$ and the degenerate (by C_{3v} symmetry) $m_s = \pm 1$ sublevels, which exhibits a zero-field splitting of 2.88 GHz (due to dipolar coupling of two unpaired electron spins) [248, 271]. An external magnetic field lifts the degeneracy between the $m_s = +1$ and the $m_s = -1$ sublevels. The 637 nm optical transitions between the ground and the excited (^3E) triplets are predominantly spin-conserving [272, 273]; an intersystem crossing (ISC) also occurs via two singlet states, $^1A_1$ and ^1E [see Fig. 3.6(b)] [274, 275, 276].

To use the electron spin of an NV^- centre as a qubit, one can, for example, encode the states $|0\rangle$ and $|1\rangle$ into the $m_s = 0$ and $m_s = +1$ sublevels of the ground triplet, respectively. Differences in the ISC transition rates enable optical pumping to polarize the qubit into the $|0\rangle$ state [see Fig. 3.6(b)] [274, 277]; strong polarization $\sim 90\%$ has been demonstrated for single NV^- centres at room temperature [278]. The qubit can also be read out optically through the NV^- centre fluorescence [279], which is visible only when the spin is in the $m_s = 0$ sublevel (owing to the different ISC rates [see Fig. 3.6(b)]) [274]. Resonant microwave pulses can be applied to perform single qubit operations, and in this way coherent superposition states have been observed [279]. All of these have also been realized for individual NV^- centres with nanoscale resolution under ambient conditions [280].

In addition, the long-lived, implanted ^{15}N nuclear spin ($I = 1/2$) associated with each $^{15}NV^-$ centre can act as a local, coherent memory, accessible via the hyperfine coupling [281]. The same role can be played by a neighbouring ^{13}C nuclear spin ($I = 1/2$) as well [282, 283, 284]: Recently, *Maurer* and co-workers have observed room-temperature $T_{2(NV)}^{(n)} \approx 8.2$ ms for the ^{13}C nuclear spin associated with an NV^- centre; by decoupling from the electron spin (and further from other nuclear spins), boosted dephasing time of 530 ms (and ~ 1 s) has been measured for that nuclear spin[10] [245]. Like Si:P, a universal set of quantum operations on the processing electronic and the memory nuclear spin qubits of each NV^- centre are available with selective microwave and radio-frequency pulses [16, 285, 286]. Single-shot readout on the single NV^- centre nuclear spin (in this case the native ^{14}N with $I = 1$) has been achieved through optical measurement on the correlated electron spin ($F = 92\%$) [287]. Moreover, by employing the ^{13}C nuclear spins in the vicinity, the electron spin qubit of a single NV^- centre can be repetitively measured: Full

[10]The nuclear spin relaxation time $T_{1(NV)}^{(n)}$ is at least seconds without decoupling at room temperature [245].

quantum control of up to three spins has been demonstrated [288, 289].

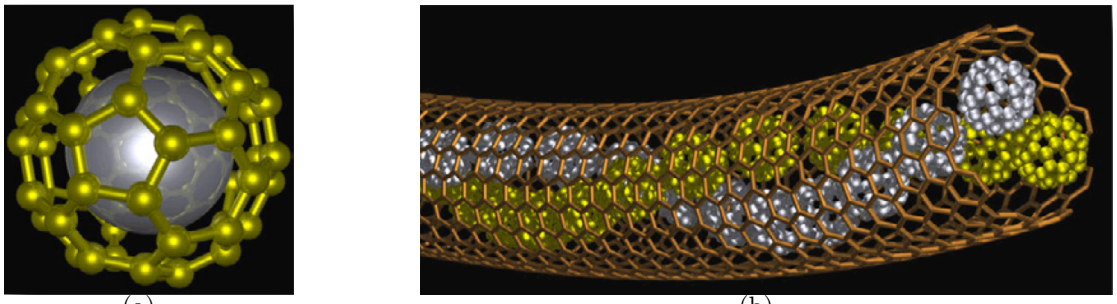
Two NV^- centres with only a small separation ($r \lesssim 10$ nm) may be entangled through direct electron spin dipole-dipole coupling ($\sim 1/r^3$ [see Sec. 4.1.2]) as long as a T_2 time on the order of milliseconds can be maintained [278]. Alternatively, an optical degree of freedom may be useful to mediate interactions between distant NV^- centres [290, 291]. Single NV^- centres can also couple to nearby single, dark nitrogen defects (each trapping a single excess electron with $S = 1/2$, to be read out by ESR) through direct electron spin dipole-dipole coupling [292, 293]. Note that nitrogen defects can also be created by ion implantation, and through subsequent high-temperature annealing a fraction of the defects form NV^- centres [294]. An increased yield of NV^- centres has been achieved with CN^- implantation, with ordered arrays formed through nanoapertures (precision of 80 nm demonstrated) [295]. The resolution could potentially be improved to below 10 nm [296].

Such a multitude of couplings exhibited by each NV^- centre makes it a promising candidate for implementing quantum registers with long coherence time at room temperature [88]. Chapter 7 will explore the practicality of a spin-chain quantum bus to connect distant NV^- centres. Moreover, an ensemble of NV^- centres can be utilized to collectively store photons [297], and perform full QIP when integrated with the measurement device suggested in Ref. [24] [also see Chapter 8].

3.2.3 Endohedral fullerenes

Another method of electron spin confinement for QIP is provided by embedding single atoms or ions in closely packed fullerene molecules such as C_{60} (or C_{82}, C_{70})[11] [298, 299]. Common examples are the $N@C_{60}$ (or $P@C_{60}$) and $Sc@C_{82}$ structures among various others [299]. Taking the widely studied $^{14}N@C_{60}$ molecule as

[11] Strictly speaking, these are molecular systems. However, unlike liquid-state NMR, these endohedral fullerene systems permit the controllability over single electron (and nuclear) spins [299].



(a) (b)

Figure 3.7: Carbon nanostructures fabricated here in Oxford (pictures courtesy of Dr. Simon C. Benjamin [299] Copyright © 2006 Institute of Physics): (a) Physical structure of the $N@C_{60}$ molecule: A nitrogen atom is caged inside the C_{60} fullerene molecule; (b) Nanotube 'peapod' structure: Fullerene molecules are packed inside a carbon nanotube.

an example [see Fig. 3.7(a)], it exhibits an electron spin $S = 3/2$, together with the hyperfine coupled ^{14}N nuclear spin, forming twelve energy levels [299]. One can encode the electronic and the nuclear spin qubits into, for example, the $m_s = \pm\frac{3}{2}$ and the $m_I = 0, 1$ sublevels, respectively [300]. Both spins are 'shielded' by the homogeneous carbon cage from the environment, and long electron spin dephasing time $T_2^{(e)}$ of 80 μs at room temperature and 250 μs at 170 K have been recorded for the highly symmetric $N@C_{60}$ molecules in CS_2 solution[12] [301]. Qubit control over the coupled electron-nuclear spin pair in $N@C_{60}$ molecules have been demonstrated through selective microwave and radio-frequency pulses [300, 303, 304]. High-fidelity storage ($F = 88\%$) of the $^{15}N@C_{60}$ electron spin qubit in its ^{15}N nuclear memory spin has shown $T_2^{(n)} \approx 140$ ms at 10 K for the endohedral fullerene [304]. Meanwhile, *pseudo*-entanglement between the electronic and the nuclear spins in $^{15}N@C_{60}$ molecules have been generated, due to the highly mixed nature of the initial ensemble state [305]. It is therefore desirable to perform operations on single fullerenes[13].

Novel carbon nanotube structures hold great promise for controlling single en-

[12] Metallofullerenes such as the $Sc@C_{82}$ structure can also possess long electron spin coherence times over 200 μs below 10 K [302]. The relaxation times T_1 are longer [301, 302].

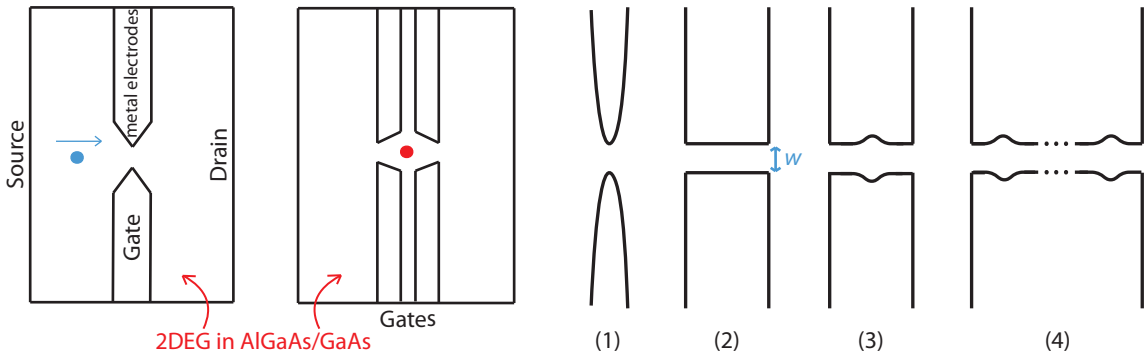
[13] Nevertheless, like NV^- centres, an ensemble of $N@C_{60}$ molecules can also be used to collectively store photons [19, 23] [see Sec. 4.4 and Chapter 8].

dohedral fullerenes to perform QIP tasks [299]. Both C_{60} fullerenes and carbon nanotubes can be produced through pulsed laser vaporization of graphite with appropriate metallic catalysts [306]. Moreover, endohedral fullerenes such as $N@C_{60}$ can be obtained from fullerene molecules through ion implantation [307]. Upon heating, the fullerenes spontaneously enter open nanotubes to form nanotube 'peapod' structures [e.g., see Fig. 3.7(b)] [306]. Ordered one-dimensional arrays of endohedral fullerene molecules can also form inside single-walled carbon nanotubes[14] (SWNTs) [306, 309, 310]: With the current record growth length of 18.5 cm [311], a SWNT could hold thousands or even millions of fullerene qubits in a row. Regularly spaced metal electrode side-gates can be fabricated onto carbon nanotubes [312] to address individual fullerene spins[15]. Again, neighbouring qubits can interact through the direct electron spin dipole-dipole coupling, whose strength depends on the spacings [see Sec. 4.1.2]. In addition, it has been suggested that for such ordered arrays of spin qubits, global control could be sufficient for QIP [299, 314, 315].

3.2.4 Free electrons

A spin qubit can also be encoded by a propagating electron, e.g., by using a turnstile to inject an electron into a 2DEG that is confined in a semiconductor heterostructure (AlGaAs/GaAs, say) [316], or into a semiconducting carbon nanotube[16] [317, 318]: Both permit ballistic transport in the quasi one-dimensional channels, and can act as electron waveguides with virtually no backscattering. The phase relaxation lengths L_φ for the charges in these materials are on the order of $0.1 - 1$ μm at liquid helium

[14] It is also possible to use multi-walled carbon nanotubes (MWNTs) to encapsulate fullerenes [308].
[15] Semiconducting carbon nanotubes can also define gated, individually controllable QDs [313].
[16] Two-dimensional graphene offers another venue for ballistic transport of electrons [319], with measured spin relaxation length around $1.5 - 2$ μm at room temperature [324] and spin dephasing lengths up to 8 μm at liquid helium temperature [325].



(a) Left: QPC; right: A similarly gated QD. (b) Simplified illustration of different QPCs.

Figure 3.8: Implementation of flying and static qubits with electron spins in gated semiconducting quantum wires. (a) *Left*: An electron spin (i.e., flying qubit) injected into a 2DEG confined in AlGaAs/GaAs semiconductor heterostructure is guided through the QPC with a source-to-drain potential; *right*: An electron spin (i.e., static qubit) is confined in a QD similarly gated by metal electrodes on top of the 2DEG. (b) Simplified shapes of different electrode gates: (1) resembles the QPC in (a) 'left' while (3) can be similar to (a) 'right' if the 'bulges' are deeper; (2)-(4) have larger channel lengths, whose adjustable width w determines its electron transport properties in the one-dimensional system. Here, for narrow enough channel width w, the propagating electron can have only one single transverse mode. On the other hand, as w increases, the channel can even become two dimensional. One can also accommodate a *single* electron (with weak confinement) in each of the QD regions ('bulges' in the diagrams) in (3) and (4).

temperature [320, 321, 322, 323, 317], while their spin relaxation[17] lengths L_s can generally be much larger with $\gtrsim 60$ μm already observed in a gated semiconductor heterostructure at 5 K [327]. These spins can serve as flying qubits to connect distant static spins[18] such as those in the gated QDs in these systems. Schemes on entanglement generation between these flying and static electron spins have been proposed [328, 329, 330].

For the relevant schemes [Chapters 5 – 6] in this thesis, we are concerned with the sequential injection of single electron spins[19], each of which then interacts with

[17] Simulation studies suggest that electron spin dephasing lengths $\gtrsim 20$ μm may be achieved in InP nanowires even at room temperature [326].

[18] Due to the restricted spin coherence lengths, the connection distance may be rather limited (to L_s) as compared to the link provided by photons (when possible). However, photons do suffer from loss in the connection medium.

[19] Electrons are injected into the quantum wire at the Fermi velocity, and may be controlled by

a specified number of single electron spins weakly bound in an array of gated QDs in a sequential manner. Based on the technology which allowed us to make QPC for a 2DEG, we can create fully confined QD structure [see Fig. 3.8(a)]; similarly, one can again use appropriately designed top gates to build an array of QDs [see Fig. 3.8(b)]. Outside the gated regions, the 2DEG behaves as a *Fermi* liquid with effectively negligible coupling to the propagating electron[20] [331]. The negatively charged metal electrodes repel the 2DEG beneath the surface further, and thus a single electron travelling through the one-dimensional channel can also be treated as effectively 'free'. Exceptions arise when the potential is randomly fluctuating (causing backscattering in such 'dirty' systems) or when the propagating electron moves into the vicinity of the static spins where they undergo spin-dependent interactions [see Sec. 4.1.1]. We shall, however, consider 'clean' systems with a 'flat' or at least slowly varying potential such that it is sufficient to only take into account of interactions between the flying and the static spins. We also regard the successive flying electrons as not interacting with each other, and further assume that the neighbouring static spins are not coupled, with suitable thresholds for the current density (bounded above) and the QD spacings (bounded below).

The experimental implementation of the flying-static spin system envisaged above may be challenging. The current electron spin injection efficiency is rather limited ($\lesssim 50\%$ [332, 333]), and injection of a single electron with a given spin into a quantum wire followed by manipulation of the spin and controlled interaction with a static spin has yet to be demonstrated. Nevertheless, this does not discourage us from discussing what may be achieved with such systems. The collective enhancement effects we shall explore in Chapters 5 and 6 provide an added incentive for carrying out the experiments to study these systems. We also note the more specula-

the source-to-drain potential. It may also slow down due to the presence of potential barriers.

[20]For our purposes, we regard the quasi-particle equivalent to the propagating electron, but with a modified effective mass m^* [171].

tive venue for implementing flying and static spin qubits through the semiconducting carbon nanotube 'peapod' structure [see Sec. 3.2.3], where each endohedral fullerene spin can encode a static qubit to interact with the injected electron spins.

An alternative approach to use free electron spins as qubits is to launch surface acoustic waves (SAWs) into the 2DEG through the use of a piezoelectric transducer in the semiconductor heterostructure. In this case, single electrons can be isolated at each of the SAW minima in the accurate and stable current source, travelling at the speed of sound [334]. Furthermore, single electrons floating on the surface of liquid helium under applied electric fields can also encode spin qubits, as they are weakly attracted and trapped by their image potential: Nanosecond scale qubit gate operations and long spin coherence time $T_2 = 0.1$ ms at 0.01 K could be feasible [335]. These can be useful for controlled interactions between the electrons in question.

3.2.5 Beyond spins

Beside spins, other degrees of freedom in solid-state systems can also be well harnessed to encode qubits for QIP. Examples include the flux-, phase-, and charge-states in superconducting circuits, fabricated with standard lithographic techniques[21] [336]. Charge-based superconducting qubits can each interact strongly to single microwave photons in an (one-dimensional) on-chip stripline cavity [338, 339], which offers the opportunity to couple with other electron spins (operating at similar frequencies). This is essential for the results in Chapter 8 of this thesis [also see Sec. 4.4], and we shall briefly describe the basic properties of superconducting charge qubits. Other forms of qubits are beyond the scope of this thesis.

Electrons in a superconductor can form *Cooper* pairs (to lower their energy), each of which consists of two electrons ($2e$) that are maximally entangled in the spin singlet state $|S\rangle$ [340]. This pairing is complete for all electrons in a superconductor

[21] The possibility of spin-based superconducting qubits are also being explored theoretically [337].

with a band-gap much larger than the one-electron Coulomb charging energy, at low enough temperatures (on the milliKelvin scale) [341]. Each Cooper pair can coherently tunnel through small-capacitance *Josephson* junctions between weakly coupled superconductors [342, 343, 344].

A specifically designed circuit can be used to confine Cooper pairs in a single superconducting 'island', called a Cooper pair box (CPB) [345, 346]. The CPB is weakly coupled to a superconducting electron reservoir via a small-capacitance Josephson junction; a voltage source is applied over the reservoir and the CPB with a gate capacitance so that tunnelling of single Cooper pairs through the junction can be controlled [345]. In the regime where the Josephson potential energy across the junction is much smaller than the two-electron Coulomb charging energy, fluctuations in the discrete number state $|n\rangle$ of Cooper pairs in the CPB are negligible, and one can encode a CPB qubit into two adjacent number states (e.g., $|0\rangle := |n\rangle$ and $|1\rangle := |n+1\rangle$) [345]. By applying small voltage pulses, coherent superposition states have been observed[22] for the CPB qubit [346]. Two CPB qubits can be coupled locally via a capacitor, and in this way an entangling C_{NOT} gate has been implemented [347]. Integrated with the stripline cavity, distant CPB qubits can also be connected through the virtual exchange of microwave photons in the cavity [348].

However, CPB qubits are very prone to low-frequency $(1/f)$ charge noise [336], which limits the coherence time of this aforementioned, original version of CPB qubits to $T_2 \sim 100$ ns [349]. Enhanced circuits have thus been proposed, including the 'quantronium' [350] and *transmon* CPB qubits [351], both aiming for operating the qubits at "optimal" conditions to eliminate the linear noise sensitivity. The latter (and more successful) approach has demonstrated an improvement of dephasing time by an order of magnitude to $2-3$ μs[23] [352, 353]. Although this can be potentially

[22] The detection can be achieved by measuring the tunnelling current through a probe junction [346], and the sensitivity level with a single-electron transistor would be required [336].
[23] The relaxation time has also been measured to be a couple of microseconds [352, 353].

improved further, the macroscopic nature of the qubits means that the task would be challenging [336].

This limitation of relatively short coherence time, together with the fact that CPB qubits operate at microwave frequencies, has inspired the novel idea of integrating an electron spin ensemble into the on-chip stripline cavity to collectively store multiple qubits from CPBs [22, 23]. The transfer process between each processing transmon CPB unit and the holographic quantum memory is mediated via single microwave photons in the cavity [22, 23]. Here, an ensemble is required to provide the $\sqrt{N}$-enhancement in the coupling of spins to single photons (with N being the number of spins), since a single electron spin only interacts with each photon very weakly [see Sec. 4.4] [23]. Strong coupling between the ensemble and the single photons have also been demonstrated [297, 354]. To further increase the qubit storage time in the memory, one may transfer the qubits from the electron spins into the nuclear degree of freedom of the ensemble (e.g., with an ensemble of $N@C_{60}$ molecules [23] or NV^- centres [297]).

Chapter 8 explores the feasibility of an ensemble-based quantum information processor, in absence of CPBs considering their rather short coherence time for gate operations. Nevertheless, a transmon CPB can be used to mediate a non-demolition read-out process for (microwave) photon number states in the cavity [24], which plays an essential role in the measurement-based ensemble processor [see Chapter 8].

3.3 Summary

With an overview of the physical systems relevant to our research work in later chapters, this concludes our background introduction to the QIP field. The focus has been on various solid-state spins, in particular electron spins, which are envisaged

to fit into our models to be introduced in the next chapter[24]. Those systems that also exhibit the nuclear spin degree of freedom are useful for the brokered MBQC approach [81], able to tolerate complete failures in the growth of graph states [see Sec. 2.2.2]. In addition, each hyperfine coupled electron-nuclear spin pair displays two degrees of freedom, suitable for processing and storing quantum information, respectively: The electron spin couples more strongly to other degrees of freedom (due to the larger magnetic moment) than the nuclear spin, but in the meantime endures faster decoherence processes for the same reason.

Next, we shall address the formalisms for spin chains and ensembles, as well as their implementation, to better understand the collective dynamics they may exhibit through the schemes we are proposing in the research chapters.

[24] We have therefore kept the descriptions in this chapter on the heuristic level.

Chapter 4

Spin chains and ensembles

In this chapter, we introduce the relevant interaction mechanisms and models for the realization of spin chains and spin ensembles. As the title suggests, the focus of this thesis is on solid-state spins, and in particular, electron spin qubits. We shall thus start with couplings between electron spins, emphasizing the kinds of interactions we would like to utilize for the related schemes in later chapters. Meanwhile, by exploiting an optical degree of freedom (when appropriate), certain effective Hamiltonians may also be implemented with electron spin-photon coupling. In Chapter 8, we work with electron spin-photon coupling only. Other interactions concerning the qubits are then treated as potential sources of decoherence, to be taken account of by more general error models [see Sec. 2.3.3] within the relevant coherence times or lengths. Examples of such couplings include the much weaker electron-nuclear spin-spin interactions (which may be decoupled [see Sec. 3.2]), and the weak spin-orbital couplings displayed in the host materials we choose; there is also the problem of photon loss when applicable. Whenever possible, we will also indicate other potential systems suitable for the spin-chain/ensemble schemes.

In all the ideal cases, the evolution of the state $|\Psi(t)\rangle$ for the qubits in question

is governed by the Schrödinger equation [12],

$$H\left|\Psi(t)\right\rangle = i\frac{\partial}{\partial t}\left|\Psi(t)\right\rangle . \tag{4.1}$$

We shall apply this equation for the understanding of the basic results behind the schemes, and then include error effects using the methods introduced in Sec. 2.3.3.

4.1 Electron spin-spin interactions

Electron spins can *directly* interact with each other through either *exchange* or *dipolar* couplings. The former arises from the overlap of their spatial wavefunctions and Coulombic interactions, and can together be determined by the Pauli exclusion principle [see Sec. 4.1.1]. Each electron spin also exhibits a magnetic dipole moment, which generates a magnetic field that affects nearby spins, and vice versa. This latter mechanism results in the direct dipole-dipole interaction ($\sim 1/r^3$ [see Sec. 4.1.2]) between electron spins that produce overlapping magnetic fields [28]. As we shall see in the following section, the exchange mechanism requires proximity for strong coupling strength, which decays exponentially with the overlap of the orbitals. Therefore, for sufficiently large separations, this short-range exchange interaction can be ignored. On the other hand, with small enough spacings, the exchange mechanism completely dominates over the dipolar coupling. The exchange coupling can also be suppressed by other means [see Sec. 4.1.1]. We shall now describe the electron spin-spin exchange interaction.

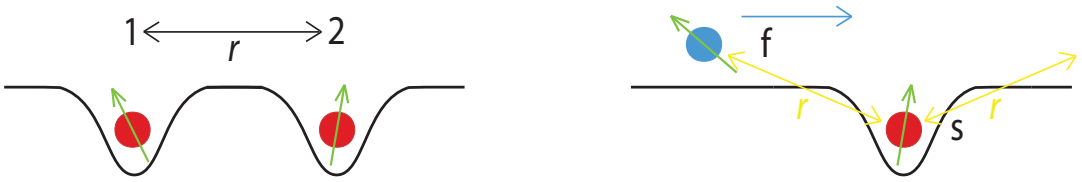
4.1.1 Exchange mechanism: Heisenberg and XY models

Let us first start with two separate, static electrons, e.g., with *weak* confinement in two neighbouring, identically gated QDs [see Fig. 4.1(a)]. This two-electron system

can be described by the *Hubbard* model [355] with the following Hamiltonian

$$H_{\text{Hubbard}} = -\,\mathtt{t}\sum_{\sigma}(a_{1\sigma}^{\dagger}a_{2\sigma} + a_{1\sigma}a_{2\sigma}^{\dagger}) + \mathrm{U}\sum_{i=1}^{2} n_{i\uparrow}n_{i\downarrow}, \tag{4.2}$$

where $\sigma = \uparrow$ or $\downarrow$, and $n_{i\sigma} = a_{i\sigma}^{\dagger}a_{i\sigma}$ with $a_{i\sigma}^{\dagger}$ ($a_{i\sigma}$) being the *fermionic* creation (annihilation) operator with spin σ at site i [356]. The hopping energy $\mathtt{t}$ corresponds to the transfer (or overlap) integral in the *tight binding* model [355] and decays exponentially with increasing separation r between the two bound electrons [see Fig. 4.1(a)] [357], while we assume the on-site Coulomb repulsion energy[1] $\mathrm{U} >> \mathtt{t}$. In this limit, Eq. 4.2 can be mapped onto the $\mathtt{t}-J$ model [358], which reduces to an effective *Heisenberg* spin-spin exchange Hamiltonian [Eq. 4.8] when each site only accommodates a single electron [359]. We shall follow Ref. [359] to outline the degenerate perturbation approach [12] for the derivation of the Heisenberg model.



(a) (b)

Figure 4.1: (a) Coupling between two single electrons, with each weakly confined in a gated QD (where double occupation is unlikely); (b) Interactions between a propagating electron and a weakly-bound electron in a gated quantum wire [see Sec. 3.2.4].

The unperturbed part in Eq. 4.2 is $H_0 := \mathrm{U}\sum_i n_{i\uparrow}n_{i\downarrow}$, and we have $H_0\,|n,l\rangle = E_n\,|n,l\rangle = n\mathrm{U}\,|n,l\rangle$ for the eigenstates $|n,l\rangle$ with spin degeneracy listing l, where $n = 0$ or 1 corresponding to the number of on-site electron pairs. Without the hopping term, the ground state $|0,l\rangle$ with $E_0 = 0$ has one electron per site, and exhibits a four-fold degeneracy $l \in \{\uparrow_1\uparrow_2, \uparrow_1\downarrow_1, \downarrow_1\uparrow_2, \downarrow_1\downarrow_2\}$. The perturbation $H_1 :=$

[1] U corresponds to the two-electron matrix element with the screened Coulomb potential, and can be treated roughly as a constant for sites in the same system. Moreover, Coulomb repulsion between electrons on different sites are neglected.

$-\,\mathsf{t}\sum_\sigma(a^\dagger_{1\sigma}a_{2\sigma}+\text{H.c.})$ then lifts this degeneracy [12], with the first-order corrections as the eigenvalues of the matrix $M^{(1)}$ with entries $M^{(1)}_{l'l} := \langle 0,l'|\,H_1\,|0,l\rangle = 0\ \forall$ l, l' (i.e., zero energy correction at this order). We thus proceed to the second-order perturbation with energy corrections as the eigenvalues of $M^{(2)}$ whose matrix elements are

$$M^{(2)}_{l'l} := \sum_{\{j\neq 0,k\}} \frac{\langle 0,l'|\,H_1\,|j,k\rangle\,\langle j,k|\,H_1\,|0,l\rangle}{E_0-E_j} = -\,\langle 0,l'|\,H_1^2\,|0,l\rangle\,/\mathrm{U}. \tag{4.3}$$

In the last step, we have applied the completeness relation $\sum_{j,k}|j,k\rangle\langle j,k| = \mathbb{1}$ [12] noting that the $\langle j,k|\,H_1\,|0,l\rangle$ is non-zero only when $j=1$. Therefore, up to the second order, the only non-zero energy values (or the eigenvalues) of the perturbed system H are the eigenvalues of $M^{(2)}_{l'l} = -\,\langle 0,l'|\,H_1^2\,|0,l\rangle\,/\mathrm{U}$ in Eq. 4.3, or equivalently those of $-H_1^2/\mathrm{U}$ restricted to the subspace with $n=0$. In another words, our two-electron system (with one per site) is governed by an effective Hamiltonian

$$H_{\text{eff}} = P_0\big(-H_1^2/\mathrm{U}\big)P_0 = P_0\bigg(-\frac{\mathsf{t}^2}{\mathrm{U}}\sum_{\sigma,\eta}(a^\dagger_{1\sigma}a_{2\sigma}+\text{H.c.})(a^\dagger_{1\eta}a_{2\eta}+\text{H.c.})\bigg)P_0, \tag{4.4}$$

where P_0 is the projection operator onto the $n=0$ subspace [359], rendering the on-site double creation (annihilation) terms zero. The remaining, non-zero contributions in Eq. 4.4 denote the second-order virtual hopping (v.h.) processes, with

$$\begin{aligned}
\text{v.h.} &= -\frac{\mathsf{t}^2}{\mathrm{U}}\sum_{\sigma,\eta}\big(a^\dagger_{1\sigma}a_{2\sigma}a_{1\eta}a^\dagger_{2\eta}+\text{H.c.}\big)\\
&= -\frac{\mathsf{t}^2}{\mathrm{U}}\sum_{\sigma,\eta}\big(a^\dagger_{1\sigma}a_{1\eta}(\delta_{\sigma\eta}-a^\dagger_{2\eta}a_{2\sigma})+\text{H.c.}\big)\ \ \text{anticommutation relations [356]}\\
&= -\frac{\mathsf{t}^2}{\mathrm{U}}\sum_{\sigma}\big(a^\dagger_{1\sigma}a_{1\sigma}(1-a^\dagger_{2\sigma}a_{2\sigma})-a^\dagger_{1\sigma}a_{1\bar\sigma}a^\dagger_{2\bar\sigma}a_{2\sigma}+\text{H.c.}\big)
\end{aligned} \tag{4.5}$$

for one electron per site. Identify the spin projection operator $S^i_z \equiv \frac{\sigma^i_z}{2} = \frac{1}{2}(n_{i\uparrow}-n_{i\downarrow})$,

and we have

$$\begin{aligned} S_z^1 S_z^2 &= \big(n_{1\uparrow}n_{2\uparrow} + n_{1\downarrow}n_{2\downarrow} - n_{1\uparrow}n_{2\downarrow} - n_{1\downarrow}n_{2\uparrow}\big)/4 \\ &= \frac{1}{4}\Big(n_{1\uparrow}n_{2\uparrow} + n_{1\downarrow}n_{2\downarrow} - n_{1\uparrow}(1-n_{2\uparrow}) - n_{1\downarrow}(1-n_{2\downarrow})\Big) \\ &= \frac{1}{4}\Big(\sum_\sigma 2n_{1\sigma}n_{2\sigma} - 1\Big), \end{aligned} \tag{4.6}$$

where we have applied the condition $\sum_\sigma n_{i\sigma} = 1$ for one electron per site in the last two steps. Together with the spin-flip operators $S_i^\pm \equiv \sigma_i^\pm := (\sigma_x^i \pm i\sigma_y^i)/2 = a_{i\uparrow(\downarrow)}^\dagger a_{i\downarrow(\uparrow)}$, Eq. 4.5 can be rewritten as

$$\begin{aligned} \text{v.h.} &= \frac{\mathsf{t}^2}{\mathrm{U}}\Big(\sum_\sigma \big(n_{1\sigma}(n_{2\sigma}-1) + (n_{1\sigma}-1)n_{2\sigma}\big) + 2\big(S_1^+S_2^- + S_1^-S_2^+\big)\Big) \\ &= \frac{4\mathsf{t}^2}{\mathrm{U}}\Big(S_z^1S_z^2 + \frac{1}{2}\big(S_1^+S_2^- + S_1^-S_2^+\big) - \frac{1}{4}\Big) \end{aligned} \tag{4.7}$$

by applying Eq. 4.6 and the condition $\sum_\sigma n_{i\sigma} = 1$.

Therefore, we have obtained the effective Hamiltonian [Eq. 4.7] for the interaction of the two single, static electron spins [see Fig. 4.1(a)]. This represents the isotropic Heisenberg spin-spin exchange model

$$H_{\text{Heisenberg}} := J\big(S_x^1S_x^2 + S_y^1S_y^2 + S_z^1S_z^2\big) = \frac{J}{2}\big(S_1^+S_2^- + S_1^-S_2^+ + 2S_z^1S_z^2\big), \tag{4.8}$$

by re-defining the zero-energy point (and ignoring the constant in Eq. 4.7). Here, the exchange coupling strength $J = 4\mathsf{t}^2/\mathrm{U}$, and the spin operators $S_\alpha^i = \frac{1}{2}\sigma_\alpha^i$. With appropriate summation over the sites starting from Eq. 4.2, it is also straightforward to extend the same mapping procedure to a linear array of single electron spins [359]. Alternatively, one can adopt the more systematic *canonical transformation* to derive the same results [358], namely, a Heisenberg antiferromagnetic spin chain.

The coupling[2] $J = 4\mathsf{t}^2/\mathrm{U}$ decays exponentially with t, with increasing inter-site spacing r. With gated GaAs QDs, one can achieve $J \sim 0.2$ meV, or equivalently $J \sim 2\pi \times 50$ GHz, for $r \simeq 20$ nm at zero field [360, 361]. This can also be completely suppressed by raising the potential barrier [173] or with an external magnetic field of suitable strength [361]. Note that this exchange mechanism is not limited to gated QDs, though the coupling strength does depend on the material system. For example, endohedral fullerenes in the nanotube 'peapod' structure [see Sec. 3.2.3] can be packed more closely, and with $\mathrm{Sc@C_{82}}$ spaced at $r \approx 0.33$ nm we could have $J \simeq 4$ meV or $J \simeq 2\pi \times 1$ THz [362, 363, 364].

More generally, magnetic semiconductors can display anisotropic exchange coupling $H_{\mathrm{ani}} = \sum_{\alpha=x,y,z} J_\alpha S^1_\alpha S^2_\alpha$ [365], which also arises in various condensed matter systems [366]. One extreme case is the XY model,

$$H_{\mathrm{XY}} := J\big(S^1_x S^2_x + S^1_y S^2_y\big) = \frac{J}{2}\big(S^+_1 S^-_2 + S^-_1 S^+_2\big). \tag{4.9}$$

This interesting and widely studied spin-spin interaction Hamiltonian [see Sec. 4.3.2] is the most relevant to the schemes in Chapters 5 – 7 of this thesis. Both the Heisenberg and the XY models could potentially also be implemented with an internal degree of freedom (effective spin) of cold atoms in an optical lattice with appropriate intensity, frequency, and polarization of the trapping lasers [158]. In that case, one can replace Eq. 4.2 with the following more general Hamiltonian to take into account of both fermionic and *bosonic* atoms in an optical lattice[3] [158],

$$H_{\mathrm{BH}} = -\sum_\sigma \mathsf{t}_\sigma(a^\dagger_{1\sigma}a_{2\sigma} + a_{1\sigma}a^\dagger_{2\sigma}) + \mathrm{U}_{\uparrow\downarrow}\sum_{i=1}^{2} n_{i\uparrow}n_{i\downarrow} + \frac{1}{2}\sum_{i,\sigma}\mathrm{U}_\sigma n_{i\sigma}(n_{i\sigma}-1). \tag{4.10}$$

[2] An inter-site Coulomb repulsion term $K_{12}n_1n_2$ (with $n_i = \sum_\sigma n_{i\sigma}$) can also be included in Eq. 4.2, and this shall correct the exchange coupling strength to $J' = 4\mathsf{t}^2/(\mathrm{U}-K)$ [358]. However, for our purposes, $K \ll \mathrm{U}$ and can thus be ignored.

[3] One can generalize this Hamiltonian to all three dimensions for a lattice of trapped atoms [158].

This time the on-site Coulomb repulsion include terms between parallel spins, but for fermionic atoms $\mathrm{U}_\sigma >> \mathrm{U}_{\uparrow\downarrow}$ [Pauli exclusion principle] and Eq. 4.10 reduces back to the Hubbard model [Eq. 4.2]. The tunnelling rate $\mathtt{t}_\sigma$ can also be tuned to be spin-dependent for the atoms by controlling the intensity of the trapping lasers [158]. Eq. 4.10 can be similarly mapped onto the anisotropic Heisenberg model $H_{\mathrm{ani}} = \sum_\alpha J_\alpha S_\alpha^1 S_\alpha^2$ for both fermionic and bosonic atoms, with $J_x = J_y = -\frac{4\mathtt{t}_\uparrow \mathtt{t}_\downarrow}{\mathrm{U}_{\uparrow\downarrow}}$ and $J_z = \frac{2(\mathtt{t}_\uparrow^2+\mathtt{t}_\downarrow^2)}{\mathrm{U}_{\uparrow\downarrow}} - \left[\frac{4\mathtt{t}_\uparrow^2}{\mathrm{U}_\uparrow} + \frac{4\mathtt{t}_\downarrow^2}{\mathrm{U}_\downarrow}\right]$ (e.g., by canonical transformtion) [158]. For fermionic atoms, the terms in the square brackets of J_z vanish since $\mathrm{U}_\sigma >> \mathrm{U}_{\uparrow\downarrow}$, and we recover the isotropic exchange coupling [Eq. 4.8] when the tunnelling rates are independent of spin ($\mathtt{t}_\uparrow = \mathtt{t}_\downarrow$); for spin-dependent tunneling $\mathtt{t}_\uparrow \neq \mathtt{t}_\downarrow$, we have $J_x = J_y < J_z$. On the other hand, an arbitrary ratio of J_z/J_x could be achieved for bosonic atoms: To implement the XY model, the condition can be $\mathrm{U}_{\uparrow\downarrow} = \mathrm{U}_\uparrow/2 = \mathrm{U}_\downarrow/2$ [158]. Thus, the Hamiltonian governing bosonic cold atoms in an optical lattice could be engineered to mimic condensed matter systems, and provide a useful substitute testbed for exchange models[4] that might be difficult to implement with solid-state spins.

The case with one electron propagating

Let us proceed to the interaction between a propagating electron and a weakly-bound electron in a gated quantum wire [see Fig. 4.1(b)]. In Chapters 5 and 6, we will encounter similar situations where multiple flying spins sequentially interact with a certain number of static spins. Below, we show that forward scattering is equivalent to Heisenberg spin-spin exchange interaction[5]. The full Hamiltonian for this one-dimensional flying-static electronic system can be written as

$$H_{fs} = -\frac{1}{2m^*}\left(\frac{\partial^2}{\partial x_1^2} + \frac{\partial^2}{\partial x_2^2}\right) + V(x_1) + V(x_2) + \frac{e^2}{4\pi\varepsilon_0\sqrt{(x_1-x_2)^2+\lambda^2}}, \qquad (4.11)$$

[4]For cold atoms: $\mathtt{t}$ can be tuned up to a few kHz while U $\sim$ kHz; typically, $J \sim 0.1$ kHz [157, 367].
[5]This derivation is attributed to Prof. J. H. Jefferson. Note that the exchange mechanism again originates from orbital overlap of the electrons and the Pauli principle.

where m^* is the electron's effective mass in the transport material, $V(x)$ is the effective one-electron potential of the QD, and λ is the effective distance between the two electrons when their spatial coordinates coincide $x_1 = x_2$ [329]; ε_0 is the vacuum permittivity. For negligible SO coupling, the total wavefunction Ψ of the two electrons can be uncoupled as

$$\Psi(x_1, \sigma_1, x_2, \sigma_2) = \Phi(x_1, x_2)\chi(\sigma_1, \sigma_2), \tag{4.12}$$

where Φ denotes the spatial wavefunction whose evolution is governed by Eq. 4.11, and the spin degree of freedom $\chi \in \{|S\rangle, |T_{0(\pm)}\rangle\}$, being appropriately symmetrised or anti-symmetrised to satisfy the overall antisymmetry of Ψ dictated by the Pauli principle[6] [328, 329]. As a direct consequence, the scattering process is spin-dependent: The *transmission* and *reflection* coefficients of the singlet state $|S\rangle$ are t_S and r_S, respectively, while similarly for the triplets $|T_{0(\pm)}\rangle$ we have t_T and r_T [328, 329]. Adopt the alternative notation $|s, m\rangle$ for χ with total spin s and magnetic quantum number $m = 0$ or ± 1, and identify $|S\rangle \equiv |0, 0\rangle$, $|T_0\rangle \equiv |1, 0\rangle$ and $\frac{1}{\sqrt{2}}(|T_+\rangle \pm |T_-\rangle) \equiv |1, \pm 1\rangle$. The spin-dependent scattering processes can therefore be expressed as

$$\begin{aligned} |0,0\rangle_i &\longmapsto r_S\,|0,0\rangle_r + t_S\,|0,0\rangle_t\,, \\ |1,m\rangle_i &\longmapsto r_T\,|1,m\rangle_r + t_T\,|1,m\rangle_t \end{aligned} \tag{4.13}$$

for the *incident* singlet and triplet states, respectively. The coefficients depend on the kinetic energy of the incident electron and other system parameters [329].

The next step is to apply Eq. 4.13 to find the two-spin evolution for the basis

[6] Due to the indistinguishability of electrons during scattering, we have labelled the electrons as 1 and 2, instead of f and s, for generality. The latter labelling scheme can be adopted beyond the scattering time interval.

states $\{|\uparrow_f\uparrow_s\rangle, |\uparrow_f\downarrow_s\rangle, |\downarrow_f\uparrow_s\rangle, |\downarrow_f\downarrow_s\rangle\}$. For anti-parallel configurations of the incident spin states, we have

$$\begin{aligned} |\uparrow_f\downarrow_s\rangle_i = \frac{|1,0\rangle_i + |0,0\rangle_i}{\sqrt{2}} &\longmapsto \frac{r_T\,|1,0\rangle_r + t_T\,|1,0\rangle_t + r_S\,|0,0\rangle_r + t_S\,|0,0\rangle_t}{\sqrt{2}} \\ &= r_{\text{nsf}}\,|\uparrow_f\downarrow_s\rangle_r + r_{\text{sf}}\,|\downarrow_f\uparrow_s\rangle_r + t_{\text{nsf}}\,|\uparrow_f\downarrow_s\rangle_t + t_{\text{sf}}\,|\downarrow_f\uparrow_s\rangle_t\,, \end{aligned} \tag{4.14}$$

where the non-spin-flip and spin-flip coefficients are expressed as $r_{\text{nsf}} = \frac{r_T+r_S}{2}$, $r_{\text{sf}} = \frac{r_T-r_S}{2}$, $t_{\text{nsf}} = \frac{t_T+t_S}{2}$ and $t_{\text{sf}} = \frac{t_T-t_S}{2}$, respectively [328]. Similarly,

$$\begin{aligned} |\downarrow_f\uparrow_s\rangle_i = \frac{|1,0\rangle_i - |0,0\rangle_i}{\sqrt{2}} &\longmapsto \frac{r_T\,|1,0\rangle_r + t_T\,|1,0\rangle_t - r_S\,|0,0\rangle_r - t_S\,|0,0\rangle_t}{\sqrt{2}} \\ &= r_{\text{nsf}}\,|\downarrow_f\uparrow_s\rangle_r + r_{\text{sf}}\,|\uparrow_f\downarrow_s\rangle_r + t_{\text{nsf}}\,|\downarrow_f\uparrow_s\rangle_t + t_{\text{sf}}\,|\uparrow_f\downarrow_s\rangle_t\,. \end{aligned} \tag{4.15}$$

In the parallel configurations, it is straightforward to see

$$\begin{aligned} |\uparrow_f\uparrow_s\rangle_i &\longmapsto r_T\,|\uparrow_f\uparrow_s\rangle_r + t_T\,|\uparrow_f\uparrow_s\rangle_t\,, \\ |\downarrow_f\downarrow_s\rangle_i &\longmapsto r_T\,|\downarrow_f\downarrow_s\rangle_r + t_T\,|\downarrow_f\downarrow_s\rangle_t\,. \end{aligned} \tag{4.16}$$

These four maps in Eqns. 4.14-4.16 completely determine the spin-spin interaction between the propagating and the weakly-confined electrons in Fig. 4.1(b). In the high energy limit for the incident electron, backscattering due to interaction with the static electron is negligible, i.e., $r_S, r_T \simeq 0$ and $|t_S|, |t_T| \simeq 1$. In general, we can write $t_S = e^{i\theta_S}$ and $t_T = e^{i\theta_T}$, where the appropriate phase shifts $\theta_{S(T)}$ are acquired during the approximately pure forward scattering. Therefore, in this limit the mapping in Eqns. 4.14-4.16 can be expressed as

$$\begin{aligned} |\uparrow_f\uparrow_s\rangle_i &\longmapsto e^{i(\bar{\theta}+\theta')}\,|\uparrow_f\uparrow_s\rangle_t\,, \\ |\downarrow_f\downarrow_s\rangle_i &\longmapsto e^{i(\bar{\theta}+\theta')}\,|\downarrow_f\downarrow_s\rangle_t\,, \end{aligned}$$

$$
\begin{aligned}
|\uparrow_f\downarrow_s\rangle_i &\longmapsto \frac{1}{2}\left(e^{i\theta_T}+e^{i\theta_S}\right)|\uparrow_f\downarrow_s\rangle_t + \frac{1}{2}\left(e^{i\theta_T}-e^{i\theta_S}\right)|\downarrow_f\uparrow_s\rangle_t \\
&= e^{i\bar{\theta}}\Big(\cos\theta'\,|\uparrow_f\downarrow_s\rangle_t + i\sin\theta'\,|\downarrow_f\uparrow_s\rangle_t\Big), \\
|\downarrow_f\uparrow_s\rangle_i &\longmapsto \frac{1}{2}\left(e^{i\theta_T}+e^{i\theta_S}\right)|\downarrow_f\uparrow_s\rangle_t + \frac{1}{2}\left(e^{i\theta_T}-e^{i\theta_S}\right)|\uparrow_f\downarrow_s\rangle_t \\
&= e^{i\bar{\theta}}\Big(\cos\theta'\,|\downarrow_f\uparrow_s\rangle_t + i\sin\theta'\,|\uparrow_f\downarrow_s\rangle_t\Big),
\end{aligned}
\tag{4.17}
$$

where $\bar{\theta} := \frac{\theta_T+\theta_S}{2}$ and $\theta' := \frac{\theta_T-\theta_S}{2}$. We claim that such a spin-spin interaction is equivalent to the Heisenberg exchange model [Eq. 4.8]: In this case, the effective coupling strength J depends on the separation between the flying and the static electron spins, and hence is time-dependent due to the propagating electron. By applying Eq. 4.1 (with $H_{\text{Heisenberg}}$) to the general two-electron spin state $|\chi(t)\rangle = U(t)\,|\chi(0)\rangle$, we find the time evolution operator $U_{\text{Hsb}}(t) = \exp[-i\theta(t)\big(\sigma_f^+\sigma_s^- + \sigma_f^-\sigma_s^+ + \frac{1}{2}\sigma_z^f\sigma_z^s\big)]$, where $\theta(t) = \int_0^t \frac{J(t')}{2}dt'$. In the computational basis $\{|\uparrow_f\uparrow_s\rangle, |\uparrow_f\downarrow_s\rangle, |\downarrow_f\uparrow_s\rangle, |\downarrow_f\downarrow_s\rangle\}$, we have

$$
U_{\text{Hsb}} = \begin{pmatrix}
1 & 0 & 0 & 0 \\
0 & e^{i\theta}\cos\theta & -ie^{i\theta}\sin\theta & 0 \\
0 & -ie^{i\theta}\sin\theta & e^{i\theta}\cos\theta & 0 \\
0 & 0 & 0 & 1
\end{pmatrix},
\tag{4.18}
$$

where we have treated $\theta(t)$ as a constant by choosing $[0,t]$ such that $J(0)$ and $J(t)$ are negligible as is $J(t')$ beyond this finite time interval. This is justified since we are only interested in the initial and final spin states, but not on the spin states during the scattering process in $[0,t]$. It can be readily see that the forward scattering process for the spins [Eq. 4.17] is equivalent to the evolution described by Eq. 4.18 up to an ignorable global phase factor $e^{i(\bar{\theta}+\theta')}$ [see Sec. 2.1.1], and we identify $\theta = -\theta' := \frac{\theta_S-\theta_T}{2}$. Both the phase shifts $\theta_{S(T)}$ and the time-integrated effective coupling θ depend on the kinetic energy of the incident electron, as well as the same set of system parameters (e.g., the size of the QD). Therefore, we

have formally established the equivalence of the spin-spin interaction for a forward-scattered electron incident on a bound electron with an effective Heisenberg model[7].

The assumption of forward scattering is important, and thus we require the kinetic energy of the incident electron to be high enough such that backscattering can be ignored[8], but not so high as to excite phonons and scatter during electron transport (resulting in momentum change) for schemes in Chapters 5 – 6. Simulations in Ref. [329] illustrated that in general backscattering can be regarded as negligible for the incident electron $\gtrsim 1$ eV with a narrow QD (~ 5 nm), and lower requirements $\gtrsim 0.4$ eV can be sufficient with a larger QD (~ 10 nm). The latter energy can give rise to to a phonon scattering rate $\sim 10^{12}$ Hz at room temperature [368], and at liquid nitrogen temperature $\sim 10^{10} - 10^{11}$ Hz should be attainable [369]. This means our electron transport is limited to $\sim 10 - 100$ ps for ignorable phonon scattering, or equivalently $\sim 1 - 10$ μm at a Fermi velocity $\sim 10^5$ m s^{-1}. We can thus assume the incident electron possesses almost constant momentum during this transport, whose range can also be within the spin coherence lengths [see Sec. 3.2.4]. For our purposes, we shall assume negligible spin decoherence for the incident electron.

We shall also give a simple and speculative estimate for the strength of the time-integrated effective coupling $\theta = \int_0^t \frac{J(t')}{2} dt'$. As mentioned earlier for GaAs QDs, $J \sim 2\pi \times 50$ GHz at a separation $r \simeq 20$ nm. Suppose that the propagating electron approaches the bound electron this close from the left at time t_1, and moves away from the right with the same separation at t_2 [see Fig. 4.1(b)]. We thus have $J(t') \gtrsim 2\pi \times 50$ GHz for $t' \in [t_1, t_2]$, during which J can be much larger due to its exponential dependence on the separation. Let us assume that the incident electron travels a few nanometres during this time interval $[t_1, t_2]$, and hence $t_2 - t_1 \sim 10 - 100$ fs

[7]Note that the singlet $|S\rangle$ and the triplet states $|T_{0(\pm)}\rangle$ are eigenstates of the Heisenberg Hamiltonian [Eq. 4.8], with eigenvalues $-\frac{3J}{4}$ and $\frac{J}{4}$, respectively (and hence their naming).

[8]At the price of allowing backscattering, the two electrons can be maximally entangled through resonant scattering [329]; this is, however, not what we want for the schemes in Chapters 5 and 6.

to cover this distance. Therefore, a lower bound for the estimated coupling lies $\sim 0.001 - 0.01$, by taking the lower limit of J throughout the interval $[t_1, t_2]$; we may take $\theta \sim 0.01$. This strength is far below the requirement for a SWAP ($\theta = \pi/2$). Fortunately, effective strong coupling ($\theta \sim \pi/2$) is possible for a much larger QD (~ 30 nm, say) [329]: In this case, the originally static electron experiences Coulomb repulsion from the incoming electron and gets 'pushed' out of the QD, while the incident electron then occupies the site. In a word, real 'exchange' between the flying and the static electrons takes place, but the spins are never close enough for strong exchange interactions in the large QD. Due to the indistinguishability of electrons, we can thus treat this mechanism as an effective SWAP[9], but only approximately (i.e., $\theta \sim \pi/2$) since weak spin-spin interactions can still occur [329]. To achieve a perfect SWAP, one needs to engineer the QD with system parameters such that the spin-spin interaction can be neglected. Note that this is *not* forward scattering, and hence the kinetic energy of the incident electron can be much lower (e.g., ~ 70 meV) [329]. Still, effective unit 'transmission' probability is required, and ideally for a wide range of kinetic energy values. The more speculative nanotube 'peapod' structure may offer large couplings between the flying electron and the embedded endohedral fullerene spin, due to the much smaller length scale (~ 1 nm).

This effective Heisenberg spin-spin exchange interaction between a flying and a static electron is closely related to the non-interacting spin chain to be introduced in Sec. 4.3.1, and hence the schemes in Chapters 5 and 6.

4.1.2 Magnetic dipole-dipole interaction

Each electron spin exhibits a magnetic dipole moment $\boldsymbol{\mu}_e = \gamma_e \mathbf{S}$ with the electron gyromagnetic ratio $\gamma_e = g_e \mu_B$, where g_e is the electron g-factor and $\mu_B = \frac{e}{2m_e}$ is the

[9]This interpretation for Fig. 12 in Ref. [329], which was not published in the original paper, is attributed to Prof. J. H. Jefferson. The QD size is large compared to the effective Bohr radius.

Bohr magneton [12]. This generates a vector potential $\boldsymbol{A}(\boldsymbol{r}) = \frac{\mu_0}{4\pi}\frac{\boldsymbol{\mu}\times\boldsymbol{r}}{r^3}$ with μ_0 being the vacuum magnetic permeability, and hence a magnetic field $\boldsymbol{B}(\boldsymbol{r}) = \nabla \times \boldsymbol{A}$ at position $\boldsymbol{r}$ relative to the spin ($r = |\boldsymbol{r}|$). If there is a second dipole $\boldsymbol{\mu}'$ at $\boldsymbol{r}$, the potential energy between the two dipoles is then $-\boldsymbol{\mu}' \cdot \boldsymbol{B}(\boldsymbol{r})$, translating to

$$H_{\text{dipole}} = -\frac{\mu_0 g_e^2 \mu_B^2}{4\pi r^3}\left(3\left(\mathbf{S}^1 \cdot \hat{\mathbf{r}}\right)\left(\mathbf{S}^2 \cdot \hat{\mathbf{r}}\right) - \mathbf{S}^1 \cdot \mathbf{S}^2\right) \tag{4.19}$$

for the direct dipole-dipole interaction between two electron spins, with $\hat{\mathbf{r}} = \boldsymbol{r}/r$ [28]. The prefactor in Eq. 4.19 denotes the dipolar coupling strength $\kappa_{\text{dipole}} := \frac{\mu_0 g_e^2 \mu_B^2}{4\pi r^3}$, which is about 52 kHz at $r = 10$ nm and scales as r^{-3}. This is much smaller than the exchange coupling for GaAs QDs at the same separation [360], and thus can be ignored in the case of flying-static spin-spin interactions [see Sec. 4.1.1]. We can nevertheless utilize this dipolar coupling between static spins by suppressing the exchange mechanism with a high potential barrier [173] or an external magnetic field [361]. When making comparison for endohedral fullerenes in a carbon nanotube, this dipolar interaction completely dominates over the exchange coupling at $r \gtrsim 10$ nm, but at the sub-nanometre length scale is orders of magnitude smaller than the exchange mechanism [see Sec. 4.1.1] [362]. We may assume a similar situation with our next focus on diamond impurities [see Sec. 3.2.2], for the purpose of analysis in Chapter 7. But in any case, with the large external magnetic field to be applied, we can regard the exchange mechanism as negligible between diamond defects separated by $r \geq 5$ nm.

It is interesting that through the longer-range dipolar coupling, an effective XY model could be achieved[10] between static electron spins, by applying *global* fields [16]. The XY model has been widely studied with readily available techniques to analyse quantum state transfer through an interacting spin chain [see Sec. 4.3.2] [15], which

[10]This is done at the price of reduced coupling strengths, which was *not* noticed in Ref. [16].

forms the basis of Chapter 7. We shall now follow Ref. [16] to demonstrate the equivalence of a driven dipolar interaction with the XY model, in the language of diamond defects (which possess long coherence times at room temperature [see Sec. 3.2.2]).

For our purposes, we only consider the interaction between two nitrogen defects (labelled as spin 1 and spin 2) or one nitrogen and one NV^- centre (the latter labelled as spin 0). We assume the presence of a constant magnetic field of strength B in the z-direction which is defined by the symmetry axis of the NV^- centre, i.e. the [111] crystal axis. The Hamiltonians for individual NV^- and N defects are given by [285, 292], respectively,

$$H_{\mathrm{NV}} = g_e \mu_B B S_z^{\mathrm{NV}} - g_n \mu_n B I_z^{\mathrm{NV}} + D(S_z^{\mathrm{NV}})^2 + \mathrm{A}_{\mathrm{NV}} \mathbf{I}^{\mathrm{NV}} \cdot \mathbf{S}^{\mathrm{NV}}, \tag{4.20}$$

$$H_{\mathrm{N}} = g_e \mu_B B S_z^{\mathrm{N}} - g_n \mu_n B I_z^{\mathrm{N}} + \mathbf{S}^{\mathrm{N}} \cdot \mathbf{A}_{\mathrm{N}} \cdot \mathbf{I}^{\mathrm{N}}, \tag{4.21}$$

where g_n is the nuclear g-factor, μ_n is the nuclear magneton, A_{NV} ($\mathbf{A}_{\mathrm{N}}$) denotes the hyperfine coupling constant (tensor), D is the zero-field splitting for the NV^- centre, and $\mathbf{I}$ is the full nuclear spin operator. Here, dipolar interactions involving nuclear spins are neglected due to their much smaller dipole moment.

For the NV^- centre, we encode the qubit basis states $|0\rangle$ and $|1\rangle$ in the $m_s = 0$ and $m_s = +1$ sublevels of the ground triplet [see Fig. 3.6(b)], respectively. Expressed in the computational basis of the qubit, we can approximate Eq. 4.20 as:

$$H_{\mathrm{NV}}^{\mathrm{qubit}} = \frac{\omega_0^{\mathrm{NV}}}{2} \sigma_z^0 + \frac{\mathrm{A}_{\mathrm{NV}}}{2} I_z^0 \sigma_z^0, \tag{4.22}$$

where the electronic Zeeman energy $\omega_0^{\mathrm{NV}} := D + g_e \mu_B B \approx 12.9$ GHz. The effective Hamiltonian above does not include the heavily suppressed hyperfine spin-flip terms, nor the negligible nuclear Zeeman term ($\mathrm{A}_{\mathrm{NV}}, g_n \mu_n B \sim \mathrm{MHz} \ll \omega_0^{\mathrm{NV}}$) [285]. For the

i^{th} nitrogen defect with $S = 1/2$, Eq. 4.21 can be similarly approximated as

$$H_{\text{N}}^{i} = \frac{\omega_0^{\text{N}}}{2}\sigma_z^i + \frac{\text{A}_{\text{N}\parallel}^{i}}{2} I_z^i \sigma_z^i, \tag{4.23}$$

where $\omega_0^{\text{N}} := g_e \mu_B B \approx 10$ GHz, and the hyperfine couplings $\text{A}_{\text{N}\parallel}^{i}$ depend on the *Jahn-Teller* orientation of each nitrogen defect [16, 370, 371]. The two possible values of $\text{A}_{\text{N}\parallel}^{i}$ were calculated as -118.9 MHz and -159.7 MHz [16].

With the defects arranged in the z-direction[11] [see Fig. 7.1], the dipolar coupling [see Eq. 4.19] between two electron spins i and j is

$$\begin{aligned} H_{\text{dip}}^{ij} &= \frac{\mu_0 g_e^2 \mu_B^2}{4\pi r_{ij}^3}\left(\mathbf{S}^i \cdot \mathbf{S}^j - 3(\mathbf{S}^i \cdot \hat{\mathbf{r}})(\mathbf{S}^j \cdot \hat{\mathbf{r}})\right) = \kappa_{\text{dipole}}(r_{ij})\left(S_x^i S_x^j + S_y^i S_y^j - 2S_z^i S_z^j\right) \\ &\simeq -2\kappa_{\text{dipole}}(r_{ij})\; S_z^i S_z^j \end{aligned} \tag{4.24}$$

where in the last step we have neglected the spin-flip terms as before, since $\kappa_{\text{dipole}} \ll \text{A}_{\text{NV}}, \text{A}_{\text{N}\parallel}^{i}$ for spacings $r \geq 5$ nm [16, 285]. We therefore [372] write the Hamiltonians for a pair of spins as

$$H_{\text{N,N}} = \kappa\; \sigma_z^1 \sigma_z^2 + \sum_{i=1,2} \frac{(\omega_0^{\text{N}} + \delta_i)}{2}\; \sigma_z^i, \tag{4.25}$$

$$H_{\text{N,NV}} = g\; \sigma_z^0 \sigma_z^1 + \frac{(\omega_0^{\text{NV}} + \delta)}{2}\; \sigma_z^0 + \frac{(\omega_0^{\text{N}} + \delta_1)}{2}\; \sigma_z^1, \tag{4.26}$$

where the hyperfine terms $\delta := \pm\text{A}_{\text{NV}}/2$ and $\delta_i := \pm\text{A}_{\text{N}\parallel}^{i}/2$, and the couplings $\kappa := -\frac{1}{2}\kappa_{\text{dipole}}(r_{\text{N,N}})$ and $g := -\frac{1}{2}\kappa_{\text{dipole}}(r_{\text{N,NV}})$.

We assume that the spins are driven by the following resonant global fields

$$H_{\text{drive}} = \sum_i \Omega_i\; \sigma_x^i \cos\omega_i t, \tag{4.27}$$

[11] We deliberately choose a different orientation as compared to Ref. [16], to maximize the effective XY coupling strength. However, to support the register architecture with the desired two- or three-dimensional lattices, connections perpendicular to the applied field will also be required.

where $\omega_0 := \omega_0^{\rm NV} + \delta$, and $\omega_i := \omega_0^{\rm N} + \delta_i$ $(i \neq 0)$ with all four possible frequencies [see Eqns 4.23 and 4.26] applied to address the nitrogen impurities [16]. The field intensities Ω_i are chosen to fit in the hierarchy $g, \kappa \ll \Omega_i \ll \omega_i$. Making rotating wave approximations (RWAs) in the usual rotating frame and adopting the rotated basis $(x, y, z) \longmapsto (z, -y, x)$ [16] then yields an effective XY model (if $\Omega_i = \Omega \; \forall \; i$) between the electron spins of two nitrogen defects or one nitrogen and one NV^- centre. Below we outline the procedures for the RWAs, taking two nitrogen spins as an example.

Under the additional driving field of Eq. 4.27, the total Hamiltonian for two nitrogen electronic spin qubits reads

$$H_{\rm N,N}^{\rm tot} = \kappa \; \sigma_z^1 \sigma_z^2 + \sum_{i=1,2} \frac{\omega_i}{2} \sigma_z^i + \sum_{i=1,2} \Omega_i \; \sigma_x^i \cos \omega_i t \tag{4.28}$$

$$= \begin{pmatrix} \kappa + \frac{\omega_1+\omega_2}{2} & \Omega_2 \cos\omega_2 t & \Omega_1 \cos\omega_1 t & 0 \\ \Omega_2 \cos\omega_2 t & -\kappa + \frac{\omega_1-\omega_2}{2} & 0 & \Omega_1 \cos\omega_1 t \\ \Omega_1 \cos\omega_1 t & 0 & -\kappa + \frac{\omega_2-\omega_1}{2} & \Omega_2 \cos\omega_2 t \\ 0 & \Omega_1 \cos\omega_1 t & \Omega_2 \cos\omega_2 t & \kappa - \frac{\omega_1+\omega_2}{2} \end{pmatrix}.$$

The unitary transformation for moving into the rotating frame, which encompasses the same dynamics, is given by

$$U = \begin{pmatrix} e^{i\theta_1 t} & 0 & 0 & 0 \\ 0 & e^{i\theta_2 t} & 0 & 0 \\ 0 & 0 & e^{i\theta_3 t} & 0 \\ 0 & 0 & 0 & e^{i\theta_4 t} \end{pmatrix}, \tag{4.29}$$

where $\theta_{1(4)} = (-)\frac{\omega_1+\omega_2}{2}$ and $\theta_{2(3)} = (-)\frac{\omega_1-\omega_2}{2}$. Applying the transformation $H_{\rm RF} = i\dot{U}U^\dagger + UHU^\dagger$ and making the usual rotating wave approximation[12] (RWA) [126,

[12]The fast oscillating terms $e^{\pm 2i\omega_i t}$ are neglected, for the integrated effect, in the RWA.

128, 137], justified since $\Omega_i, \kappa \ll \omega_i$, yields:

$$H_{\text{RWA}} = \begin{pmatrix} \kappa & \frac{\Omega_2}{2} & \frac{\Omega_1}{2} & 0 \\ \frac{\Omega_2}{2} & -\kappa & 0 & \frac{\Omega_1}{2} \\ \frac{\Omega_1}{2} & 0 & -\kappa & \frac{\Omega_2}{2} \\ 0 & \frac{\Omega_1}{2} & \frac{\Omega_2}{2} & \kappa \end{pmatrix} = \kappa\ \sigma_z^1\sigma_z^2 + \sum_{i=1,2} \frac{\Omega_i}{2}\sigma_x^i. \tag{4.30}$$

In the rotated basis with $(x, y, z) \longmapsto (z, -y, x)$ [i.e., $|0(1)\rangle \mapsto |+(-)\rangle$], the Hamiltonian in Eq. 4.30 then becomes

$$\begin{aligned} H_{\text{RF}} &= \kappa\ \sigma_x^1\sigma_x^2 + \sum_{i=1,2} \frac{\Omega_i}{2}\sigma_z^i = \kappa\ (\sigma_1^+ + \sigma_1^-)(\sigma_2^+ + \sigma_2^-) + \sum_{i=1,2} \frac{\Omega_i}{2}\sigma_z^i \\ &\simeq \kappa\ (\sigma_1^+\sigma_2^- + \sigma_1^-\sigma_2^+) + \sum_{i=1,2} \frac{\Omega_i}{2}\sigma_z^i. \end{aligned} \tag{4.31}$$

Here, a second RWA was made in the last line by neglecting the non-spin-conserving terms [126], which is valid when $\kappa \ll \Omega_i$. The sum in Eq. 4.31 simply denote the effective Zeeman splittings, and have no overall effect when $\Omega_i = \Omega\ \forall\ i$. In that case, Eq. 4.31 is then equivalent to the XY model [Eq. 4.9]. □

The same procedure can be straightforwardly generalized to a linear chain of nitrogen spins, and with an NV^- centre at each end. Moreover, controlling the magnitude Ω_0 can also effectively tune the coupling g [see Eq. 4.26] between the NV^- and the nitrogen defect spins through the ground state structure of the NV^- centre [16], though we shall not be concerned with this aspect. Meanwhile, we stress two important points about this implementation of the XY model for static electron spins through the direct dipole-dipole interaction. *Firstly*, with the basis rotation, physical T_1 (T_2) processes for the spins now translate to phase-flip[13] (spin-flip) errors

[13]Note that the physical relaxation (or decay) does not correspond exactly to spin dephasing in the computational basis. Nevertheless, for our purposes we shall consider the phase-flip errors in the rotated basis being characterized by the T_1 times [see Chapter 7].

in the computational basis. This has to be considered since T_2 times are usually much shorter than the T_1 times for each electron spin [see Chapter 3]. *Secondly*, the couplings κ, g are at best only 1/2 of the usual dipolar interaction strength κ_{dipole} at the same separation r, and thus there is also a sacrifice of reducing the effective coupling in the realisation of the XY model. For example, while $\kappa_{\text{dipole}} \approx 52$ kHz at $r = 10$ nm, κ is only 26 kHz at that separation.

4.2 Electron spin-photon coupling

Beside electron spin-spin interactions, coupling of the spins to photons is also a useful aspect in studying the collective dynamics in this thesis. For example, with the cavity quantum electrodynamics (QED) system suggested in Refs. [373, 374], one could effectively implement a Heisenberg-type exchange model between photon polarization and the pseudo-spin ($S = 1/2$) exhibited by an embedded QD. Here,

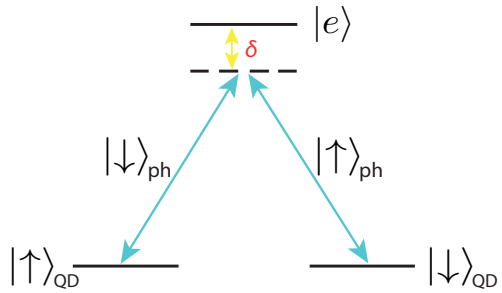


Figure 4.2: Simplified illustration of the exchange coupling between photon polarization and the effective pseudo-spin of a self-assembled QD embedded in the semiconductor photonic waveguide. Once virtually excited, the QD may 'decay' back to the original level or to the opposite spin state (i.e., a spin-flip), emitting a photon of the appropriate polarization. This corresponds to an effective Heisenberg-type exchange model [373, 374].

a one-dimensional semiconductor photonic waveguide is used to reliably transport single photons, each of which displays two frequency-degenerate, orthogonally polarized modes $\left(\text{denoted as } \{|\uparrow\rangle_{\text{ph}}, |\downarrow\rangle_{\text{ph}}\}\right)$ [373, 374]. Furthermore, the system could

embed self-assembled, multi-level QDs [see Sec. 3.2.1], with each accommodating an effective pseudo-spin in the degenerate doublet ground state [219, 220]. With a sufficiently large detuning δ, an exchange model may be achieved between the two degrees of freedom, through the two-photon Raman (Λ) processes involving virtual population of an excited level [see Fig. 4.2] [373, 374]. Since this is simply another potential realisation of the Heisenberg exchange coupling between a flying and a static qubit, we shall not go into the details. Instead, we note that when applicable, photons could connect distant static qubits of much larger separations than that provided by propagating electrons, since photons are largely decoherence free[14] [see Sec. 3.1.1].

Jaynes-Cummings Hamiltonian

The main focus on electron spin-photon coupling in this thesis shall be the *Jaynes-Cummings* model[15] $H_{\rm JC}$ [127, 128] for Chapter 8. The full system Hamiltonian governing a single electron spin coupled with a single-mode quantized radiation field in a cavity, in presence of a bias field B, can be expressed as [126, 127, 128]

$$\begin{aligned} H_{\rm full} &= \omega_c\big(c^\dagger c+\frac{1}{2}\big)+\frac{\omega_s}{2}\sigma_z+g_{sc}(c^\dagger+c)(\sigma^++\sigma^-) \\ &\simeq \omega_c\big(c^\dagger c+\frac{1}{2}\big)+\frac{\omega_s}{2}\sigma_z+g_{sc}(c^\dagger\sigma^-+c\sigma^+) =: H_{\rm JC}, \end{aligned} \tag{4.32}$$

where $c^\dagger$ (c) denotes the cavity photon creation (annihilation) operator, and ω_c, ω_s are the cavity photon and electron Zeeman energy, respectively; the spin-cavity coupling strength $g_{sc} \sim 0.1$ kHz [23] is very weak, considering the typical spin coherence times [see Chapter 3]. Again, the non-spin-conserving terms are ignored

[14] Photons do, however, experience loss due to absorption by the transport medium; one would want the waveguide to exhibit a low photon loss rate.

[15] This model was originally derived to consider the interaction between single photons and a two-level atom, which is effectively a spin-1/2 system. We shall not be concerned with the detailed, yet standard quantization procedures, which can be found in textbooks such as Refs. [126, 127, 128].

in the second step by a RWA[16]. Moreover, the constant can also be dropped by re-defining the zero-energy point. Thus, Eq. 4.32 can be re-written as

$$H_{sc} = \omega_s\big(\frac{\sigma_z}{2} + c^\dagger c\big) + g_{sc}(c^\dagger\sigma^- + c\sigma^+) - \Delta_{sc}c^\dagger c, \tag{4.33}$$

where we have the spin-cavity detuning $\Delta_{sc} := \omega_s - \omega_c$. This shall form the basis for the analysis of an ensemble of N electron spins coupled to an on-chip stripline cavity, where the collective coupling $\bar{g}$ displays a $\sqrt{N}-$enhancement over g_{sc} [see Sec. 4.4]. Note that only the radial mode is permitted in the stripline cavity, and therefore the polarization degree of freedom is not relevant in this set-up.

4.3 Spin chains and their implementations

Thus far, we have seen that the interactions are typically rather weak between a flying and a static spin or for two static spins with separations larger than a few tens of nanometres. This has motivated researchers to consider using spin chains and ensembles to connect or store qubits. In order to study the collective dynamics, we now briefly go through the spin-chain concept, followed by a concise review of spin ensembles.

4.3.1 Non-interacting spin chain with external coupling

A spin chain is a one-dimensional, ordered array of spins of the same type, with intra-chain spacings r that are taken to be the same in the *ideal* case. The coupling strength between neighbouring spins depend on their separation r, and can be ignored for sufficiently large r according to the appropriate timescale. In any case, the exchange mechanism between static electron spins in gated QDs can be highly

[16]More explicitly, one moves to the interaction picture, and neglects the fast oscillating terms involving $e^{\pm i(\omega_c+\omega_s)t}$, valid since $|\omega_c - \omega_s| << \omega_c + \omega_s$.

suppressed by raising the potential barrier whenever necessary [173]. The dipolar coupling $\kappa_{\text{dipole}} \approx 6.5$ kHz at $r = 20$ nm, and this can be safely neglected for processes within a microsecond. Therefore, an array of single electrons in gated QDs with high barriers and separated by $r \geq 20$ nm can be regarded as a non-interacting spin chain within 1 μs. Of course, this is of little use without any external coupling. Nevertheless, interaction between a propagating electron and the static spins in a *sequential* manner may be utilized to collectively store the flying qubit in the chain [see Chapter 6]. The sequential nature of the interaction can be justified for $r \gtrsim 40$ nm since the exchange mechanism between the flying and the static spins has an exponential dependence on their distance, and moreover, the wavelength for the propagating electron is about 6 nm $<< r$ at ~ 0.4 eV. Within spin coherence length and also for negligible phonon scattering, we assume the flying spin can be transported through a few microns and in less than a nanosecond [see Sec. 4.1.1], for which there may be as many as a few hundred QDs ($N \sim 300$, say) in the non-interacting (and sequential) regime. A similar, yet more speculative implementation may be envisaged with an electron propagating through a semiconducting carbon nanotube embedding a chain of endoheral fullerene spins [see Sec. 3.2.3]: The exchange mechanism for this system is negligible at 10 nm [362] and thus the intra-chain spacing r can be shorter, permitting more static spins. Furthermore, the much smaller dimension of the nanotube could also allow stronger couplings. The SAW approach [334] offers a further alternative, and could provide larger exchange coupling due to the much slower transport speed (of sound).

Other external coupling includes the photon polarization modes in a semiconductor photonic waveguide, embedding a chain of self-assembled QDs [see Fig. 4.2]. However, since the optical photons are of much larger wavelengths $\sim 0.1 - 1$ μm, sequential interaction between the flying qubit and the static spins is only justified for intra-chain separations $r > 1$ μm. Within the single-photon lifetime ~ 1 ps

at a wavelength of 400 nm [373], the photon can be transported through 300 μm, corresponding to a chain of $N \lesssim 300$ QDs for sequential interactions.

It may be rather challenging to implement an XY model between a flying and a static spin for the solid-state systems we have mentioned. Nonetheless, one could consider testing any related schemes with bosonic cold atoms in an optical lattice [see Eq. 4.10], and then devising suitable control mechanism to realize the desired interaction model with solid-state spins. Single trapped atoms in the *Mott*-insulator regime [367, 375] can be regarded as effective static spins, while coherent transport of atoms could be achieved by controlled tunnelling [376] which have also been reported [156, 377, 378, 379]. One possibility for implementing the flying-static XY model is to use a spatial light modulator[17] (SLM) [380, 381, 382] to generate the required potential by imaging correct pattern onto the atoms in two dimensions and having a light sheet in the other dimensions to confine the atoms to a single plane.

Finally, we can think of a current of flying spins as a moving chain, and interacting with a static spin sequentially. This can be useful for transfering the identical state of the flying spin-singlets to two static spins in an accumulative fashion [see Chapter 5]. In this set-up, the sequential nature can be satisfied for low current densities, e.g., $I \lesssim 100$ nA for each propagating electron interacting with the static spin at less than 1 ps [see Sec. 4.1.1]. In this regime, we can also assume the flying spins are not interacting with each other.

4.3.2 Interacting spin chain

Moving on to the interacting spin chain, we restrict ourselves to an array of static electron spins, which can be used to coherently transfer quantum state between distant end qubits [383, 384, 385]. For example, in the language of diamond defects, a chain of N dark nitrogen impurities could connect two distant NV^- colour centres

[17] One may dynamically reconfigure the potential rapidly for ballistic transport a controlled fashion.

(labelled as 0 and $N+1$) [see Fig. 7.1] [16]. We assume an effective nearest-neighbour XY model for the spin-spin interactions in the chain, which could be implemented with global fields [see Sec. 4.1.2]. By extending the argument in Sec. 4.1.2 to an $N+2$ chain, the effective system Hamiltonian in Eq. 4.31 can be generalized to

$$H_{\rm eff}^{\rm XY} = \sum_{i=1}^{N-1} \kappa \, (\sigma_i^+ \sigma_{i+1}^- + \sigma_{i+1}^- \sigma_i^+) + \sum_{j=0,N} g \, (\sigma_j^+ \sigma_{j+1}^- + \sigma_{j+1}^- \sigma_j^+), \tag{4.34}$$

in the rotated basis with $(x, y, z) \longmapsto (z, -y, x)$.

The standard procedure for analysing the chain starts from the *Jordan-Wigner* transformation [386] applied to Eq. 4.34, yielding

$$H_{\rm eff} = \sum_{i=1}^{N-1} \kappa \, (a_i^\dagger a_{i+1} + a_i a_{i+1}^\dagger) + \sum_{j=0,N} g \, (a_j^\dagger a_{j+1} + a_j a_{j+1}^\dagger), \tag{4.35}$$

with the fermion creation and annihilation operators,

$$\begin{aligned} a_j^\dagger &:= \sigma_j^+ \exp\Big[-i\pi \sum_{l=0}^{j-1} \sigma_l^+ \sigma_l^- \Big] = \sigma_j^+ \prod_{l=0}^{j-1} \exp\big[-i\pi \, \sigma_l^+ \sigma_l^- \big], \\ a_j &:= \exp\Big[i\pi \sum_{l=0}^{j-1} \sigma_l^+ \sigma_l^- \Big] \, \sigma_j^- = \prod_{l=0}^{j-1} \exp\big[i\pi \, \sigma_l^+ \sigma_l^- \big] \, \sigma_j^-, \end{aligned} \tag{4.36}$$

where the second equalities follow since the $\sigma_l^+ \sigma_l^-$s commute [12]. One can verify that $\exp\big[-i\pi \, \sigma_l^+ \sigma_l^- \big] = 1 - 2\sigma_l^+ \sigma_l^-$ by acting on $\{|\uparrow\rangle, |\downarrow\rangle\}$, and hence observe the anticommutator relations $\{a_i^\dagger, a_j\} = \delta_{ij}$ and $\{a_i, a_j\} = 0 = \{a_i^\dagger, a_j^\dagger\}$, as well as that $\sigma_i^+ \sigma_{i+1}^- = a_i^\dagger a_{i+1}$ [386]. The reason for this step is that the Pauli operators do not preserve correct anti-commutation relations, with $\{\sigma_i^+, \sigma_i^-\} = 1$ but $[\sigma_i^+, \sigma_j^-] = 0$ for $j \neq i$. To solve this, we have transformed the spin degree of freedom into the presence or absence of a fermion at the relevant system site. This allows further canonical transformation to diagonalize the Hamiltonian in Eq. 4.35, and to analyse the spectrum of the system [386]. In Chapter 7, we shall start with the perturbation

approach illustrated in Ref. [16] to outline the quantum state transfer processes in the ideal case. We then extend to numerical studies for error effects, and investigate the practicality of the spin-chain connection. We restrict to intra-chain spacings $r \in (5\text{ nm}, 20\text{ nm})$ to utilize the dipolar interaction for the effective XY coupling.

4.4 Spin ensemble coupled to stripline cavity

Let us now consider the interaction between a spin ensemble and cavity photons. As early as in 2000, the concept of mapping single photon states onto an atomic ensemble was proposed [387], and this was followed by experimental demonstrations with trapped cold atoms [388, 389, 390, 391]. Later in 2006, it was observed that due to the extremely small mode volumes in stripline cavities, strong coupling to polar molecules should be possible [20, 21, 392]. *Wesenberg* and co-workers then suggested, in 2009, that this also holds for electron spin ensembles via the magnetic dipoles with a collective field [23]. Inspired by earlier holographic schemes with atomic ensembles [22, 393, 394], they further proposed that the various spin waves in the ensemble could be used as independent quantum registers [23], for which a proof-of-principle experiment was later carried out showing the storage and readout of multiple classical excitations [19]. The strong coupling has also been demonstrated recently by independent experimental groups [297, 354], which distinguishes the electron spin ensemble with a stripline cavity from the earlier atomic approach.

We shall follow Ref. [23] to briefly illustrate the collective storage of multiple photon states in an ensemble of N@C_{60} or NV^- centre [297] electron spins, coupled to an on-chip stripline cavity [see Fig. 8.1]. One can generalize Eq. 4.33 to account for N electron spins (labelled by q), with the following system *interaction* Hamiltonian,

$$H_{sc}^{\text{int}} = \sum_{q=1}^{N} g_q (c^\dagger \sigma_{(q)}^- + c\sigma_{(q)}^+) - \Delta_{sc} c^\dagger c = \sqrt{N}\bar{g}\ (c^\dagger b + c b^\dagger) - \Delta_{sc} c^\dagger c, \tag{4.37}$$

where the collective spin raising and lowering operators are $b^\dagger := \frac{1}{\sqrt{N}} \sum_q \sigma^+_{(q)} g_q/\bar{g}$ and $b := \frac{1}{\sqrt{N}} \sum_q \sigma^-_{(q)} g_q/\bar{g}$, respectively. Although the average coupling strength $\bar{g} := \sqrt{\sum_q |g_q|^2/N} \approx 2\pi \times 20$ Hz is small, the ensemble exhibits a strong collective coupling $J_{\text{col}} := \sqrt{N}\bar{g} \approx 2\pi \times 6$ MHz for $N \sim 10^{11}$ spins[18] [23].

Suppose the ensemble is in its ground state $|\mathbf{0}\rangle = |0...0\rangle$ and that the cavity contains a single microwave photon. If the bias field B is such that the spins' Zeeman splitting is resonant with the microwave photon (i.e., $\Delta_{sc} = 0$), then the ensemble will collectively absorb that photon on a timescale that is proportional to $1/J_{\text{col}} \sim 1/\sqrt{N}$ [apply Eq. 4.37]. The ensemble state after the photon absorption is then given by

$$|\psi_1(0)\rangle = \frac{1}{\sqrt{N}} \sum_q \frac{g_q}{\bar{g}} |0_1...1_q...0_N\rangle \,. \tag{4.38}$$

The above state and state $|\mathbf{0}\rangle$ together form an effectively closed two-level system, i.e., a mode qubit. More formally, we can verify that $[b, b^\dagger] = 1$, and thus the excitation is like that of a simple harmonic oscillator [23].

Now if no parameters are changed then the quantum of energy will "flip-flop" back and forth between the cavity and the collective state [see Eq. 4.37]. However, if we wish to stop the flip-flopping, i.e., decouple the cavity from this memory mode, then we will temporarily apply a linear gradient in the magnetic field such that each spin will acquire phase at a different rate. If the gradient pulse causes the field to vary in the z direction, and writing the coordinate of the q^{th} spin as z_q, then the collective state becomes [23]

$$|\psi_1(k)\rangle = \frac{1}{\sqrt{N}} \sum_q \frac{g_q}{\bar{g}} e^{ik(\xi)z_q} |0_1...1_q...0_N\rangle \,. \tag{4.39}$$

Here, parameter k depends on the strength of the gradient and its duration ξ, and

[18] This large number of spins could be accommodated within a dimension of 25 mm $\times$ 10 μm [23]. Therefore, the microwave cavity photon ($\lambda = 25$ mm) interacts with all the spins simultaneously. We ignore the much weaker spin-spin interactions.

consequently the various terms in Eq. 4.39 have developed relative phases with one another. This prevents the $\sqrt{N}$-enhanced mode-cavity coupling, and a single excitation is thus stored in the spin ensemble. Indeed, if we were to introduce a new photon into the cavity at this stage then that photon will resonantly transfer to the ensemble almost independently of the presence of the former excitation [23]. After the application of the second gradient pulse, this procedure can be repeated yet again. As long as the number of the excitations $n \ll N$ with an upper limit of $n_{max} \leq \sqrt{N}$ (since the coupling enhancement of $\sqrt{N-n} \sim \sqrt{N}$ is still very large for small n), single excitations can be *independently* stored into and read out of the different collective modes i by appropriately applying $\pm k_i$-pulses with $k_i = k(\xi_i)$ [see Chapter 8 for more details] [23]. One can verify this formally by defining the k_i-mode creation and annihilation operators $b^\dagger(k_i) := \frac{1}{\sqrt{N}} \sum_q \sigma^+_{(q)} e^{ik_i z_q} g_q/\bar{g}$ and $b(k_i) := \frac{1}{\sqrt{N}} \sum_q \sigma^-_{(q)} e^{-ik_i z_q} g_q/\bar{g}$, and observing $[b(k_i), b^\dagger(k_j)] = \sum_q e^{i(k_j - k_i)z_q} |g_q|^2/N\bar{g}^2 = \delta_{ij}$ for $\{k_i\} = \{0, 3, 4, 7, 8, ...\}(2\pi/L)$, where L is the dimension of the ensemble in the z direction (and equals the photon wavelength λ for simultaneous spin-cavity couplings) [23].

Note that in order not to affect the superconducting transmission line cavity, the magnetic field and hence the gradient are applied strictly parallel to the plane of the thin film superconductor. The bias field is $B = 180$ mT for resonance with the cavity $\omega_c = 2\pi \times 10^5$ GHz; for a reasonable gradient of 13 mT m^{-1}, it takes about 100 ns to implement a k_i-pulse [23].

4.5 Summary

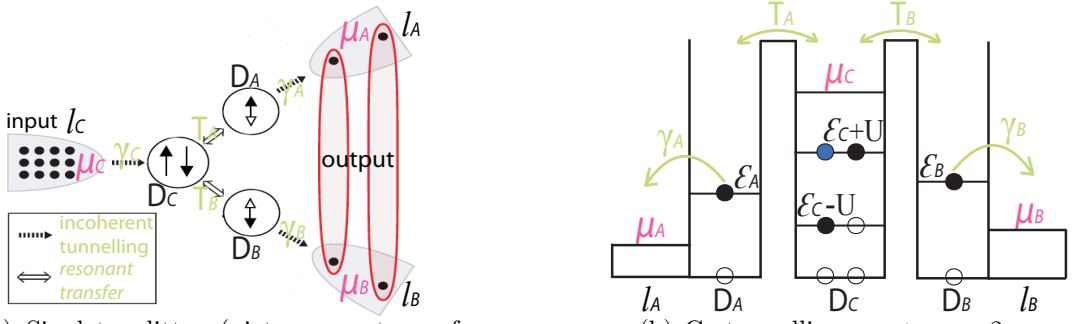
We are now equipped with the tools to study the collective dynamics in spin chains and ensembles, and shall move on to the various schemes from the next chapter onwards.

Chapter 5

Passive generator for distributed spin-entanglement

5.1 Motivation

In Sec. 2.2, we have seen that entanglement is the essential resource for QIP. To entangle two distant solid-state qubits, one may utilize a mediator such as single photons [193], or even combine this with the assistance of measurement [83, 94, 95]. Alternatively, when the optical degrees of freedom are not available, separating locally entangled qubits could also produce distributed entanglement: An example is illustrated in Fig. 5.1, where a series of three gated QDs are employed to split electron spin singlet states [395, 396, 397]. Here, the dot coupled to the input lead can be populated with a singlet state each time. The other two QDs are there to split the singlet through the *co-tunnelling* regime, and each then transfers the electron (half of the singlet) to the corresponding output lead for further distribution. Repeatedly, large spin-entangled currents can form in the two separate leads, and this could be accomplished in a completely *passive* manner requiring no active quantum control [397]. Furthermore, one can also use a superconducting lead to replace the



(a) Singlet splitter (picture courtesy of Dr. Simon C. Benjamin)

(b) Co-tunnelling: $\varepsilon_A + \varepsilon_B \approx 2\varepsilon_C$.

Figure 5.1: Illustration of the entanglement distribution device with three QDs, each being coupled to its own lead. The potentials are set such that (a) Electrons incoherently tunnel from the input lead l_C onto dot D_C, populating a singlet state, which can coherently co-tunnel and split to the two separate dots D_A and D_B. Each spin from the separated pair then incoherently tunnels to the corresponding output lead, and is transported further apart. In such a fashion, large spin-entangled currents are formed in the two separate, output leads l_A and l_B [397] Copyright © 2009 Institute of Physics; (b) The co-tunnelling condition is that $\varepsilon_A + \varepsilon_B \approx 2\varepsilon_C$, for the lowest single-particle energy ε_i in D_i. Moreover, for the splitter to work, the requirement for the potentials are that dots D_A and D_B only confines a single electron, while dot D_C can confine two; the input lead potential μ_c is above the singlet ground state energy, but below that of the triplet in dot D_C [395].

role of the dot for singlet population, and act as the input lead [398, 399, 400]. In this latter case, Cooper pairs (electron spin singlets [see Sec. 3.2.5]) can split to the two QDs through the crossed *Andreev* reflection process [398, 399, 400]. This has been demonstrated more recently with InAs [13] and carbon nanotube QDs [14], to generate spin-entangled currents in the two separate output leads.

However, it is not clear how such an entangled resource could be used for QIP applications, since the control and measurement of a single flying solid-state qubit has yet to be demonstrated experimentally. Furthermore, the macroscopic nature of the currents [13, 14] makes this even more difficult, since the electrons are indistinguishable. In order to access such an entangled current resource, we therefore consider the possibility of converting such mobile entanglement to a static form in this chapter. We shall show that it is possible to achieve this in a completely passive way, and

this distinguishes this work from other distributed entanglement generation schemes which control the mediators and the systems in an active way [83, 94, 95, 193].

5.2 Set-up, model and basic results

At the centre of our proposed device is the spin-entangled current generator that passively outputs entangled pairs of spins f_i in the singlet state $|S\rangle_f$ down two different channels i [397]. Each spin encounters a further, static spin s_i downstream of the generator in each channel, and interacts with it [see Fig. 5.2]. We think

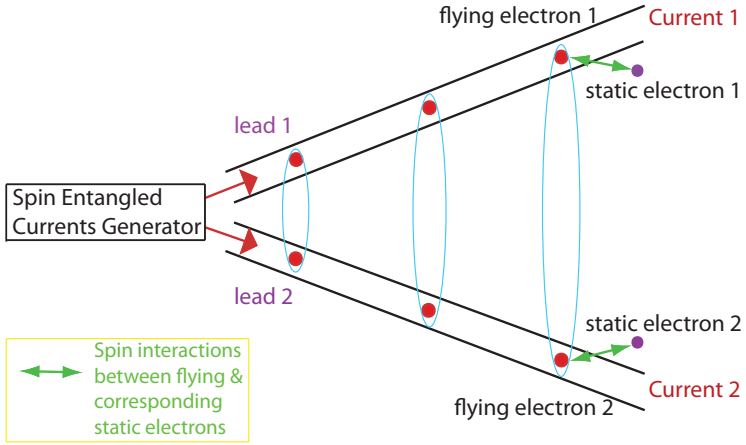


Figure 5.2: Illustration of our passive entanglement generation device between two distant, static electron spins. Two currents, composed of successive electron pairs that are maximally spin-entangled, emerge from a generator and pass down two channels. A static electron is situated downstream of the generator in each channel, and the static pair is spatially well separated. The mobile spins in each lead interact with corresponding static spins as they pass. Note that the two flying spins of the same Bell pair are not required to, and will normally not, arrive at the sites of interaction with their corresponding static spins at the same time.

of each static spin as confined in a gated QD [see Sec. 3.2.1], though alternatives include endohedral fullerene spins in a semiconducting carbon nanotube 'peapod' [see Sec. 3.2.3] and the SAW structure [334]. We assume that in each channel the

flying spins *sequentially* interact with the static spin for currents $I \lesssim 100$ nA [see Sec. 4.3.1]. For the convenience of illustrations, we shall start with the XY model [Eq. 4.9] as an effective Hamiltonian coupling each flying-static spin pair, and then extend to the justified Heisenberg case later. Similar to Eq. 4.18, in the XY model the time evolution operator U_i describing an interaction event between the flying-static pair i is

$$U_i = \begin{pmatrix} 1 & 0 & 0 & 0 \\ 0 & \cos\theta_i & -i\sin\theta_i & 0 \\ 0 & -i\sin\theta_i & \cos\theta_i & 0 \\ 0 & 0 & 0 & 1 \end{pmatrix} \tag{5.1}$$

in the computational basis $\{|\uparrow_{s_i}\uparrow_{f_i}\rangle,\ |\uparrow_{s_i}\downarrow_{f_i}\rangle,\ |\downarrow_{s_i}\uparrow_{f_i}\rangle,\ |\downarrow_{s_i}\downarrow_{f_i}\rangle\}$. Here, the time-integrated coupling (or the forward scattering phase) θ_i depends on the kinetic energy of the incident qubits, as well as a set of system parameters [see Sec. 4.1.1].

5.2.1 Attractor

We first consider the case where $\theta_1 = \theta_2 = \theta$ and initially the static spins are in the state $|\uparrow_{s_1}\uparrow_{s_2}\rangle$. The starting state of the two static and the first pair of flying spins is then $\frac{1}{\sqrt{2}}(|\uparrow_{s_1}\uparrow_{f_1}\rangle|\uparrow_{s_2}\downarrow_{f_2}\rangle - |\uparrow_{s_1}\downarrow_{f_1}\rangle|\uparrow_{s_2}\uparrow_{f_2}\rangle)$. Using the product of two unitary operators of the form of Eq. 5.1, we find that after interaction the state becomes, in a modified but obvious notation, $\cos\theta\,|\uparrow\uparrow\rangle_s|S\rangle_f - i\sin\theta\,|S\rangle_s|\uparrow\uparrow\rangle_f$. Since this first flying pair will no longer interact with the static spins nor with the following flying pairs, we can trace out this first flying pair to find the density matrix describing the static pair after the interaction: $\cos^2\theta\,|\uparrow\uparrow\rangle_s\langle\uparrow\uparrow| + \sin^2\theta\,|S\rangle_s\langle S|$.

In order to find the behaviour of our system for multiple passages of flying qubits,

we require the following four maps which describe a single interaction event, U_1, U_2:

$$\begin{aligned}
|\uparrow\uparrow\rangle_s \langle\uparrow\uparrow| &\mapsto \cos^2\theta \ |\uparrow\uparrow\rangle_s \langle\uparrow\uparrow| + \sin^2\theta \ |S\rangle_s \langle S| \,; \\
|\downarrow\downarrow\rangle_s \langle\downarrow\downarrow| &\mapsto \cos^2\theta \ |\downarrow\downarrow\rangle_s \langle\downarrow\downarrow| + \sin^2\theta \ |S\rangle_s \langle S| \,; \\
|S\rangle_s \langle S| &\mapsto \frac{1}{4}\sin^2 2\theta \big(|\uparrow\uparrow\rangle_s \langle\uparrow\uparrow| + |\downarrow\downarrow\rangle_s \langle\downarrow\downarrow| \big) + \sin^4\theta \ |T_0\rangle_s \langle T_0| + \cos^4\theta \ |S\rangle_s \langle S| \,; \\
|T_0\rangle_s \langle T_0| &\mapsto |T_0\rangle_s \langle T_0| \,. \qquad (5.2)
\end{aligned}$$

These maps imply that the triplet state $|T_0\rangle_s$ is an attractor for this process, and by tracking the states of the static spins through multiple passages of the flying spins it is clear that the system will converge towards this maximally entangled attractor; we need not consider any further maps since other static spin states are never accessed. This fixed point is also consistent with spin-invariant scattering of the flying singlets from a static $|T_0\rangle$ triplet, as can be verified directly from the Schrödinger equation.

5.2.2 Convergence

We now calculate the probabilities of obtaining the $|T_0\rangle_s$ state after a number of flying spin passages. The reduced density operator for the static spins after n iterations is, by definition, $\rho_s^{(n)} = \mathbf{P}_n \cdot \mathscr{P}$, where the vector of projection operators for the base states is $\mathscr{P} := \big(|\uparrow\uparrow\rangle_s \langle\uparrow\uparrow|, |\downarrow\downarrow\rangle_s \langle\downarrow\downarrow|, |S\rangle_s \langle S|, |T_0\rangle_s \langle T_0| \big)^T$ and the corresponding vector of probabilities is $\mathbf{P}_n := \big(P_{\uparrow\uparrow}(n),\, P_{\downarrow\downarrow}(n),\, P_S(n),\, P_{T_0}(n)\big)^T$. Under the map, Eq. 5.2, $\mathscr{P} \mapsto L\mathscr{P}$ and hence $\rho_s^{(n)} \mapsto \rho_s^{(n+1)} = \mathbf{P}_n \cdot (L\mathscr{P}) = (L^T\mathbf{P}_n) \cdot \mathscr{P}$. Equivalently, $\mathbf{P}_n \mapsto \mathbf{P}_{n+1} = \mathbf{M_0}\mathbf{P}_n$, where, by direct substitution,

$$\mathbf{M_0} \equiv L^T = \begin{pmatrix} \cos^2\theta & 0 & \frac{1}{4}\sin^2 2\theta & 0 \\ 0 & \cos^2\theta & \frac{1}{4}\sin^2 2\theta & 0 \\ \sin^2\theta & \sin^2\theta & \cos^4\theta & 0 \\ 0 & 0 & \sin^4\theta & 1 \end{pmatrix} . \qquad (5.3)$$

Note that the map, Eq. 5.3, preserves total probability, as it should. Since the matrix $\mathbf{M_0}$ describes the evolution of the state probabilities, its eigenvalues λ_i must satisfy $|\lambda_i| \leqslant 1$. Except when θ is a multiple of π, there is always one (and only one) eigenvalue equal to unity, and the corresponding eigenvector is then our attractor state $|T_0\rangle\langle T_0|$. Using *Mathematica* and Eq. 5.3, we have derived closed analytic expressions for $\mathbf{M_0}^n$ and $P_{T_0}(n)$. For the initial conditions $\mathbf{P}_0 = (1,0,0,0)^T$, we have

$$1 - P_{T_0}(n) = 2^{-4n-1}[(B^n + C^n) - \frac{5+\cos 2\theta}{A}(B^n - C^n)], \tag{5.4}$$

where

$$\begin{aligned} A &= \sqrt{2\cos^2\theta(17+\cos 2\theta)} \\ B &= 7 + 8\cos 2\theta + \cos 4\theta - 4A\sin^2\theta \\ C &= 7 + 8\cos 2\theta + \cos 4\theta + 4A\sin^2\theta. \end{aligned}$$

For large n, when $(4A\sin^2\theta)/(7+8\cos 2\theta+\cos 4\theta) \in (0,2)$, i.e., when $\theta \lesssim 0.89$, C^n dominates over B^n and we have

$$\ln\big(1 - P_{T_0}(n)\big) \simeq \alpha(\theta)\ n + \beta(\theta), \tag{5.5}$$

where $\alpha(\theta) = \ln(C/16) \leqslant 0$ and $\beta(\theta) = \ln[(A+5+\cos 2\theta)/(2A)]$. For $\theta \ll 1$, $(5+\cos 2\theta)/A \to 1$, and $\beta(\theta) \to 0$. We plot the probability of obtaining the $|T_0\rangle_s\langle T_0|$ state against θ, for different values of n in Fig. 5.3(a).

As the number of rounds increases, the range of θ values for which there is a high probability of obtaining the static $|T_0\rangle$ state becomes wider; we plot the probability $P_{T_0}(n)$ against the number of rounds, n, for some weak coupling strengths in Fig. 5.3(b)-(d). For the tunnelling rates Γ in [14], the time interval t_0 between successive flying qubits are on the order of $1/\Gamma \approx 67$ ps (and hence $I \approx 2.4$ nA),

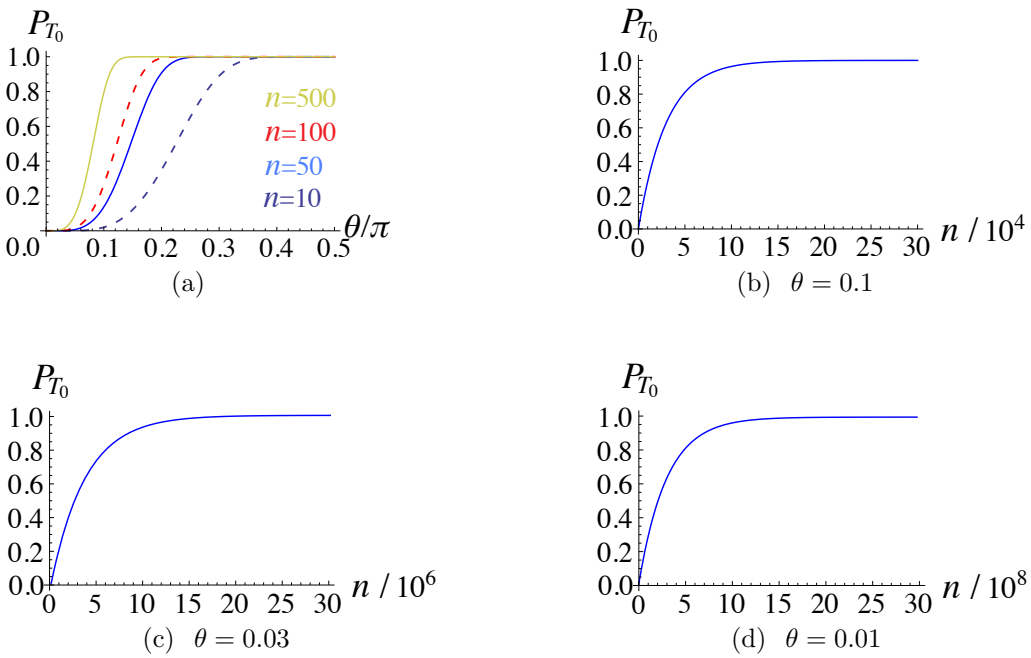


Figure 5.3: Plots of the probabilites of obtaining the $|T_0\rangle_s \langle T_0|$ state (a) against $\frac{\theta}{\pi}$, after $10, 50, 100, 500$ rounds of interactions, respectively; (b) - (d) against the number of rounds of interactions, n, for $\theta = 0.1$, 0.03 and 0.01, respectively.

and thus the time it takes for the static spins to converge to the state $|T_0\rangle$ would be 20 μs, 2 ms and 0.2 s for $\theta = 0.1$, 0.03 and 0.01, respectively. These time intervals t_0 are at least one order less in [13], and have the potential of being shortened further. Therefore, within the electron spin coherence times [see Sec. 3.2.1] the convergence may take place for θ as small as 0.03 at the tunnelling rate achieved in [13]. This is on the same order as estimated for what may be achieved [see Sec. 4.1.1]. Note that the nanotube 'peapod' system has the potential for phase shifts $\theta \gtrsim 1$ due to larger exchange interactions arising from nanometre length scales [see Sec. 4.1.1] [362].

5.3 Generalizations

Let us now generalize our analysis, to include arbitrary coupling strengths ($\theta_1 \neq \theta_2$), and arbitrary starting states for the static qubits. With the time evolution operators

U_i defined as in Eq. 5.1, we can find a completely positive map $\mathcal{L}_s$ which represents the effect on the static spin density operator ρ_s of a passing flying qubit pair:

$$\rho_s^{(k+1)} = \mathcal{L}_s[\rho_s^{(k)}] = \mathrm{Tr}_f[(U_1 \bigotimes U_2)(\rho_s^{(k)} \bigotimes \rho_f^{(k)})(U_1 \bigotimes U_2)^\dagger], \tag{5.6}$$

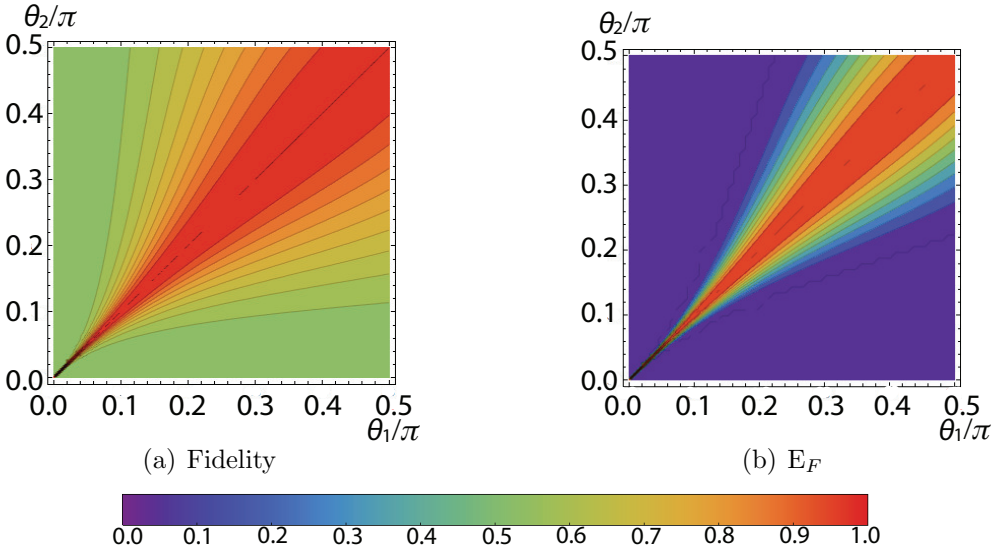
where $\rho_f = |S\rangle_f \langle S|$. Eq. 5.6 corresponds to a set of 16 recurrence relations for the elements of $\rho_s^{(k)}$. When $\theta_1 = \theta_2$, four of these relations decouple from all the others, as we found in our argument earlier. The superoperator $\mathcal{L}_s$ is not a linear map, and we thus vectorize the density operator states by listing the entries in the following order as a column vector, $(\rho_{11}\rho_{12}...\rho_{14}\rho_{21}...\rho_{24}\rho_{31}.....\rho_{44})^T =: \tilde{\rho}$. The map corresponding to the action of the superoperator $\mathcal{L}_s$, $\tilde{\mathcal{L}}_s : \tilde{\rho}_s^{(k)} \longmapsto \tilde{\rho}_s^{(k+1)}$ is then linear and can be written as a simple 16×16 matrix $\mathbf{M}$, whose entries can be easily calculated using Eq. 5.6. We find that $\mathbf{M}$ always has an eigenvalue $\lambda = 1$, independent of the values of the coupling strengths. The multiplicity of this eigenstate is one, unless θ_1 and θ_2 are multiples of π. The corresponding eigenvector $\tilde{\rho}_1$ is then a single attractor state that is independent of the initial configuration of the static spins, which when transformed back to its density matrix form is

$$\rho_1 = \frac{1}{2(a+b)} \begin{pmatrix} a & 0 & 0 & 0 \\ 0 & b & \frac{1}{\sqrt{2}} & 0 \\ 0 & \frac{1}{\sqrt{2}} & b & 0 \\ 0 & 0 & 0 & a \end{pmatrix}, \tag{5.7}$$

where

$$\begin{aligned} a &= \frac{(\cos\theta_1 - \cos\theta_2)^2(1 + \cos\theta_1\cos\theta_2)\csc^3\theta_1 \csc^3\theta_2}{2\sqrt{2}} \geq 0, \\ b &= \frac{\csc\theta_1 \csc\theta_2(\csc^2\theta_1 + \csc^2\theta_2) - \cot\theta_1\cot\theta_2(2 + \csc^2\theta_1 + \csc^2\theta_2)}{2\sqrt{2}} \geq \frac{1}{\sqrt{2}}. \end{aligned}$$

When $\theta_1 = \theta_2$, we have $a = 0$ and $b = \frac{1}{\sqrt{2}}$, and ρ_1 reduces the $|T_0\rangle\langle T_0|$ state as in the simple case. When $\theta_1, \theta_2 \in (0, \pi/2]$, all the other eigenvalues are numerically in the range $(-1, 1)$, and their corresponding eigenvectors, when back in matrix form, all have trace zero and hence do not correspond to physical density operators. This has to be the case, as can be seen from the following argument. We can express any density state as $\rho = \sum_{i=1}^{16} a_i \rho_i$, since the set of eigenvectors $\tilde{\rho}_i$ (vectorized ρ_i) form a basis for $\mathbf{M}$. The coefficients a_i can take any values, so long as $\mathrm{Tr}(\rho) = 1$ and ρ is positive semi-definite and Hermitian. Hence, $\mathcal{L}_s[\rho] = \sum_{i=1}^{16} a_i \lambda_i \rho_i$, or more generally $\mathcal{L}_s^n[\rho] = \sum_{i=1}^{16} a_i \lambda_i^n \rho_i$, which also has trace 1 as a density matrix. As $n \to \infty$, $\lambda_i^n \to 0$ $\forall |\lambda_i| < 1$ which is when $i = 2, 3, ..., 16$, and thus $\mathcal{L}_s^n[\rho] \to a_1 \rho_1$. So, $\mathrm{Tr}(\mathcal{L}_s^n[\rho]) \to a_1$ since we defined $\mathrm{Tr}(\rho_1) = 1$, and this requires $a_1 = 1$. We thus obtain $\rho = \rho_1 + \Sigma_{i=2}^{16} a_i \rho_i$, and the trace requirement results in $\Sigma_{i=2}^{16} a_i \mathrm{Tr}(\rho_i) = 0$, which holds for various combinations of a_i's. This can only be true when $\mathrm{Tr}(\rho_i) = 0$ $\forall i = 2, 3, ..., 16$. □.



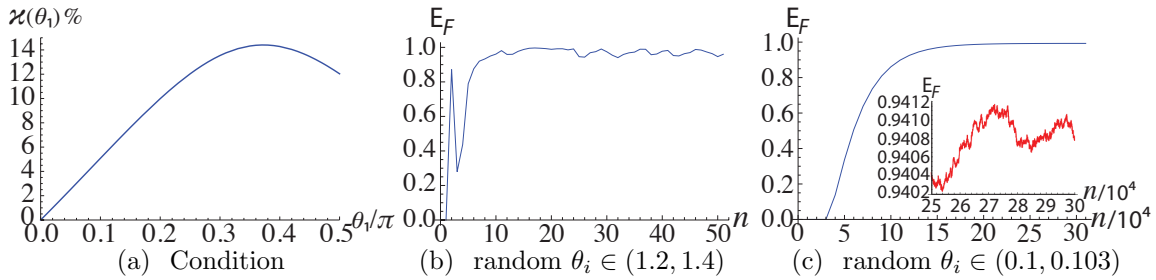
(a) Fidelity (b) E_F

Figure 5.4: Contour plots of (a) the fidelity between the attractor ρ_1 and the $|T_0\rangle\langle T_0|$ state; and (b) the entanglement of formation E_F of ρ_1; each are plotted as a function of θ_1 and $\theta_2 \in (0, \pi/2]$.

Now, we can find how close ρ_1 is to the state $|T_0\rangle\langle T_0|$, for various values of θ_1 and θ_2, by calculating the fidelity F [Eq. 2.14]. In our case, we have

$$F(\rho_1, |T_0\rangle\langle T_0|) = \mathrm{Tr}\left(\sqrt{\sqrt{\rho_1}\,|T_0\rangle\langle T_0|\,\sqrt{\rho_1}}\,\right) = \sqrt{\frac{b+\frac{1}{\sqrt{2}}}{2(a+b)}} \tag{5.8}$$

which takes a value of unity when $\theta_1 = \theta_2$, as expected. Its contour plot in Fig. 5.4(a) illustrates that even when θ_1 and θ_2 are different, ρ_1 is still very close to $|T_0\rangle\langle T_0|$ for any (θ_1, θ_2) in the central region. The fidelity values also indicate the levels of degradation in our entangled resource through unequal coupling, the degree of which can be further established by calculating the entanglement of formation E_F that the bipartite state ρ_1 has (by numerically applying the straightforward formula in Ref. [401]). We construct the contour plot for E_F in Fig. 5.4(b) showing that the degree of entanglement ρ_1 possesses is very large, higher than 0.9, for any (θ_1, θ_2) in the central red region.



(a) Condition (b) random $\theta_i \in (1.2, 1.4)$ (c) random $\theta_i \in (0.1, 0.103)$

Figure 5.5: (a) Plot of the maximum allowed percentage difference $\kappa(\theta_1)$ against θ_1/π for obtaining final $E_F(\rho_s) \geq 0.9$; (b) & (c) Example plots of the evolutions of E_F for the static spins as a function of the number of flying pairs n, for strong and weak random couplings, respectively. The inset in (c) zooms in on the corresponding fluctuations.

The attractor state ρ_1 remains similar for (θ_1, θ_2) values in the same colour region in Fig. 5.4, and close to $|T_0\rangle\langle T_0|$ for the central red region. As a result, a high degree of entanglement with $E_F \geq 0.9$ is achieved for the static spins even when $\theta_i(k)$ varies with the iteration k, as long as in each round $\Delta\theta := |\theta_1 - \theta_2|$ satisfy the condition set

in Fig. 5.4(b) such that (θ_1, θ_2) lies in the central red region. The maximum possible percentage difference in coupling strengths needed to maintain a highly entangled state may be defined as $\kappa(\theta_1) := \max_{E_F \geq 0.9}(\Delta\theta/\theta_1)$, and this quantity depends on θ_i itself [see Fig. 5.5(a)]. The maximum value for $\kappa(\theta_1)$ occurs at a θ_1 value away from $\pi/2$ because the maximum allowed $\Delta\theta$ values for final $E_F(\rho_s) \geq 0.9$ do not vary much for θ_i close to $\pi/2$. For θ_i as weak as 0.1, the maximum allowed percentage difference $\kappa(0.1) \simeq 1.6\%$. We show two example plots for the evolutions of E_F for the static spins vs n for θ_i values that can vary within some range from round to round, in Fig. 5.5(b)-(c). From these results we see that the convergence times are of the same order as for the case when $\theta_1 = \theta_2$ [see Fig. 5.3] for both strong and weak couplings. We can also see that the condition on $\kappa(\theta_1)$ in each round as specified in Fig. 5.5(a) only needs to be satisfied by the majority of the interaction rounds.

5.4 Decoherence

Decoherence of the static and flying spins caused by the environment will degrade our final entangled resource to some extent, and we shall consider such effects in this section.

5.4.1 Static spins

We first take into account the decoherence of the static spin pair, which in general is coupled to the surrounding environment. The process can be modelled by the Lindblad master equation [Eq. 2.12] with decoherence channels k and corresponding decay rates γ_k:

$$\frac{d}{dt}\rho_s(t) = \sum_{k=1}^{15} \gamma_k (A_k \rho_s A_k^\dagger - \frac{1}{2} A_k^\dagger A_k \rho_s - \frac{1}{2} \rho_s A_k^\dagger A_k), \tag{5.9}$$

where we have ignored the unitary term $-i[H, \rho_s]$ on the assumption that the duration of the spin-spin interaction is much shorter than time interval t_0 between successive flying qubits. This assumption about the much shorter timescale also means that we do not need to consider decoherence during interactions events. Therefore, the evolution of $\rho_s(t)$ can be tracked through application of the map $\tilde{L}_s$ to describe interaction events and using the solution of the master equation between events. The resulting behaviour is a function of the products $\gamma_k t_0$, and we assume t_0 to be constant for simplicity.

For certain decoherence models, analytical results can be found. For example, if we assume that there are two independent dephasing channels $\sigma_z^{s_1} \bigotimes I^{s_2}$ and $I^{s_1} \bigotimes \sigma_z^{s_2}$ with rates γ_1 and γ_2 respectively, then for $\theta_1 = \theta_2$ the final fidelity of the state of the static spins with respect to $|T_0\rangle \langle T_0|$ is, immediately prior to an interaction events:

$$\sqrt{\frac{2 + 2e^{2(\gamma_1+\gamma_2)t_0} \csc^4\theta - \cot^2\theta(2 + 2\csc^2\theta)}{4e^{2(\gamma_1+\gamma_2)t_0} \csc^2\theta(2\csc^2\theta - 1) - 4\cot^2\theta(1 + 2\csc^2\theta)}} \tag{5.10}$$

We know that for the device to generate a large degree of static entanglement, we need θ_1 and θ_2 to be in the central red region of Fig. 5.4. For example, working with random $\theta_i \in [1.3, 1.4]$, calculations show that robustness to decoherence requires that $\gamma_k t_0$ are at most on the order of 10^{-2}. For $\gamma_1 = \gamma_2 = 1$ MHz (i.e., a coherence time of 1 μs), Fig. 5.6(a) illustrates the behaviour of the fidelity against current of flying pairs e/t_0, with e the electronic charge. When the current is large enough, more than 10 pA (i.e., $t_0 \lesssim 10$ ns) in this case, the fidelity only fluctuates slightly. Fig. 5.6(b) then shows that the final state of the static spin pair possesses a large degree of entanglement and does not depend on the initial set up. A similar effect is observed for the bit-flip errors, with slightly reduced final fidelity. This 10 pA

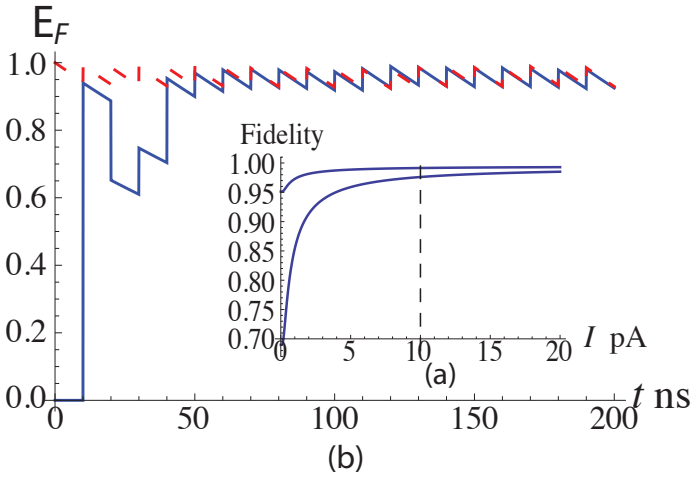


Figure 5.6: Plots of the state of the static spin pair in the presence of pure dephasing errors at random $\theta_i \in [1.3, 1.4]$ and $\gamma_1 = \gamma_2 = 1$ MHz: (a) Fidelity of final states at equilibrium against current with the higher and lower lines representing the states right after and before XY couplings, respectively; (b) E_F against time for a spin-entangled current of 10 pA, with the dashed and solid lines representing the initial static spins being in the $|T_0\rangle$ and the pure $|\uparrow\uparrow\rangle$ states, respectively. For the latter case, the initial rise and the subsequent fall in E_F is due to the presence of the singlet state.

is much smaller than the $\sim$ nA scales observed in [13, 14], i.e. the strong coupling regime is robust to decoherence of the static spins. For weak couplings, a higher current is required for the same decoherence rates, e.g., at $\sim$ 100 nA ($t_0 \sim 1$ ps) is needed for $\theta_i \simeq 0.03$ (or at $\sim$ 1 nA with spin coherence times in Ref. [191]). We see that decoherence will reduce the fidelity and hence the degree of entanglement of the steady state for the static spins, and thus in Fig. 5.4 the regions for high fidelity and high degree of entanglement will be narrower in the presence of decoherence.

5.4.2 Flying spins

Next, let us consider the decoherence of the flying singlets before they interact with the static spins. The whole analysis in Sec. 5.3 [still starting from Eq. 5.6] applies when we refine our model by allowing random error deviations $\epsilon^{(k)}$ of $\rho_f^{(k)}$ from the

singlet state in each round such that [see Eq. 2.9]

$$\rho_f^{(k)} = (1-\epsilon^{(k)})\,|S\rangle_f\,\langle S| + \sum_{j=1}^{3} \epsilon_j^{(k)} \sigma_j^{f_1}\,|S\rangle_f\,\langle S|\,\sigma_j^{f_1}, \tag{5.11}$$

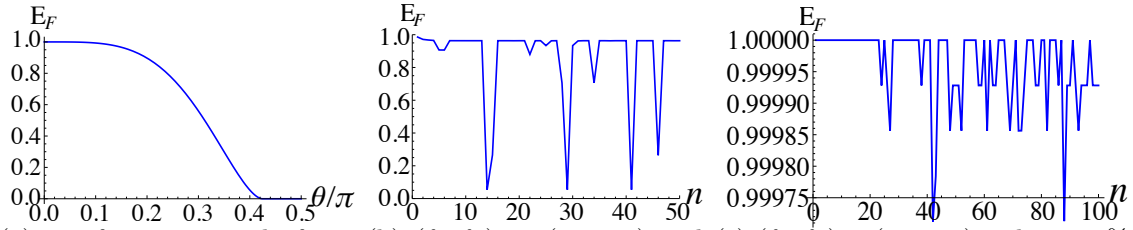
where the errors $\epsilon^{(k)} = \sum_{j=1}^{3} \epsilon_j^{(k)}$ for each k are due to spin-orbit coupling and interactions with the environment as the flying qubit propagates. We find that the single attractor state now has small error-dependent terms c for the corner entries on the minor diagonal of ρ_1 in Eq. 5.7, and both a and b now also depend on $\epsilon_j^{(k)}$. As a result, the final $\mathrm{E}_F(\rho_1)$ is reduced, and the larger the errors the smaller it will be. We also find that the strong coupling regime can tolerate larger errors compared with weak coupling. This is because the static entanglement built up per round of interaction is much smaller for weak couplings and the errors $\epsilon_j^{(k)}$ can drastically reduce the accumulated entanglement. In either case, the average of $\epsilon^{(k)}$ mainly determines the final E_F for the static spins for fixed θ_i. For strong couplings, the error tolerance on $\epsilon^{(k)}$ is of order 0.01, which corresponds to flying pairs with an average E_F of $\sim 0.8-0.9$. This error tolerance is much smaller for weak couplings, but this could also be feasibile experimentally since couplings become weaker at high carrier speed, which also means a smaller interaction of the flying qubits with the environment before they arrive at the static qubit sites.

5.5 Splitting efficiency

We now consider the efficiency of successful splittings of the Cooper pairs via the double dots in the generator [13, 14] in Fig. 5.2. When unsuccessful, a singlet pair enters the same lead and this has the effect of reducing the static entanglement [see Fig. 5.7(a)]. For a success rate $\eta = 50\%$[1] in Ref. [14], the static spins converge to

[1]The reported success rate as the first attempt discussed in Ref. [13] was only 2%. The authors managed to increase this to 50% in 2011, and by fabricating the QDs of the right size this could be

a completely mixed state regardless of the coupling strengths. We therefore classify the usefulness of the entangled current resource depending on the success rates in terms of final static entanglement we could achieve for the steady state of the static spins. For large coupling strengths, $\mathrm{E}_F(\rho_s)$ switches between close to 0 and almost 1 from round to round depending on the success of splitting. Thus in this case, a threshold criterion for η would be that the state of the static pair spends a certain fraction of its time in states with E_F close to 1 [see Fig. 5.7(b)]. In that case, the average $\mathrm{E}_F \approx 0.88$ for $\eta = 95\%$. In the weak coupling regime, the steady state E_F of the static spins is large and fluctuates slightly for sufficiently high success rates [Fig. 5.7(c)]. The condition is that the amount of reduction in static entanglement by a single unsuccessful event should be smaller than the accumulated entanglement built up from a certain number N of consecutive successful splittings. In this case then $\eta = \frac{N}{N+1}$, and we find for example, when $\theta \simeq 0.1$, for $\eta \simeq 99.9\%$, then very high entanglement can be maintained [see Fig. 5.7(c)].



(a) ρ_s after one round of unsuccessful splitting

(b) $(\theta_1, \theta_2) = (1.2, 1.3)$ and $\eta = 95\%$

(c) $(\theta_1, \theta_2) = (0.1, 0.1)$ and $\eta = 99\%$ at steady state

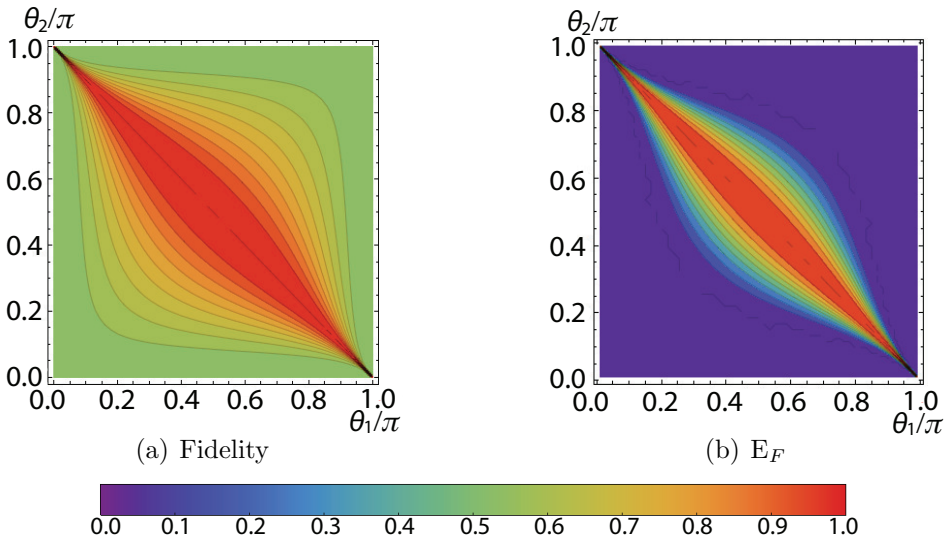
Figure 5.7: Plots for the evolutions of E_F for the static spins: (a) of the attractor state ρ_1 after one round of interactions with the flying singlet pair entering the same lead, against various $\theta \in [0, \frac{\pi}{2}]$; (b)-(c) examples of the corresponding steady states against number of rounds n when no other errors are present. Once the steady state is achieved, the success rates required can be lowered for weak couplings, as shown in (c); otherwise, $\eta = 99.9\%$ is required for $\theta_i = 0.1$ starting from an arbitrary state.

In either case, for the current resource to be useful in terms of our scheme, the success rates for splittings should improve from those in [13, 14] to at least 90%.

boosted further without any fundamental (theoretical) limit [*Workshop on Quantum Spintronics II*, Sardinia, Italy (October 2011)].

5.6 Other models

We now adapt the analysis so far to the Heisenberg case by replacing the time evolution operator in Eq. 5.1 with Eq. 4.18. As shown in Sec. 4.1.1, this model can effectively describe the spin evolutions of single forward scattering electrons incident on a static electron.



(a) Fidelity (b) E_F

Figure 5.8: Contour plots for the single attractor state of the static spins in the Heisenberg exchange model: (a) Fidelity with respect to the singlet state as a function of $\theta_i \in [0, \pi]$; (b) E_F as a function of $\theta_i \in [0, \pi]$.

We found that the singlet state is now the only attractor for Eq. 5.6 with the Heisenberg exchange model, and the required condition is that $\theta_1(k) + \theta_2(k) \simeq \pi$ in each round of interaction [see Fig. 5.8]. Results on decoherence effects as well as the splitting efficiency are similar.

5.7 Conclusion

We have shown that distributed and static spin entanglement can be generated from a source of entangled currents and Coulomb interactions in a completely passive way.

By using currents rather than just a single spin pair, the scheme works with weak interaction strengths for the XY model, as a result of the collective enhancement. This could be achieved with cold atoms in an optical lattice [see Sec. 4.3.1 and Eq. 4.10] [158], though the splitting of singlets may require a similar co-tunnelling regime [402] as for the electrons [395, 396, 397]. With the electron spins (Heisenberg model [see Sec. 4.1.1]), couplings of around $\pi/2$ would be required in practice, which may nevertheless be implemented effectively [see Sec. 4.1.1] [329]. In this latter case, using the currents can tolerate deviations from the effective SWAP gate ($\theta = \pi/2$) [see Sec. 5.6].

The entanglement generated is robust to errors from various sources, e.g., small variations in the kinetic energy of the flying spins, and hence changes in the couplings $\theta_i^{(k)}$ do not affect the validity of the scheme [see Sec. 5.3]. With the typical spin coherence lengths and also for negligible phonon scattering, the electron transport length $\sim 1 - 10$ μm [see Sec. 4.1.1] means that the static pair of entangled electron spins can have a separation at least comparable to more conventional protocols for entanglement generation, for which the separation (~ 1 μm) is limited by quantum tunnelling or similar local interactions [398, 399, 400]. Our scheme also has the potential of achieving an order of magnitude improvement in the degree of separation (~ 10 μm versus ~ 1 μm). Moreover, the high degree of entanglement can be maintained by the current resource against decoherence of the static spins, where compatible current density has been demonstrated [13, 14] for typical spin coherence times [see Sec. 5.4]. Moderately stronger currents could also make the scheme more robust to the decoherence.

Splitting inefficiency seems to be the most damaging effect, especially when the coupling is weak; this will, however, be further improved from the first experimental demonstrations in Ref. [13, 14] [see Sec. 5.5].

We anticipate that spin-entangled currents could be utilized in the way we have

proposed in a range of experimental systems [see Sec. 4.3.1], thus opening up the possibility of quantum information processors based on entangled currents.

Chapter 6

Coherent and passive spin-chain quantum memory

6.1 Set-up, model and basic results

Having investigated how certain currents of spins could transfer their identical state to static spins, we now consider a similar, yet different scenario: We show that the state of a flying qubit may be transferred to a chain of N identical, ferromagnetically aligned, but non-interacting, static spins [see Sec. 4.3.1] in a *passive* way. During this process the flying qubit is coherently polarized, emerging in the direction of the majority static spins. We shall show that this process is reversible for at least two flying qubits injected sequentially and thus has the potential to be exploited as a passive quantum memory [see Fig. 6.1] to encode the flying qubits *without* the necessity of resetting between successive encoding operations. The quantum information may be spread over many static spins in the memory chain, making the mechanism resistent to spin decoherence and other imperfections.

Let us start by considering the first flying qubit in some arbitrary state $|\psi_1\rangle_{f_1} = \alpha_1 |\uparrow\rangle + \beta_1 |\downarrow\rangle$ and its associated quantum state transfer process with the static

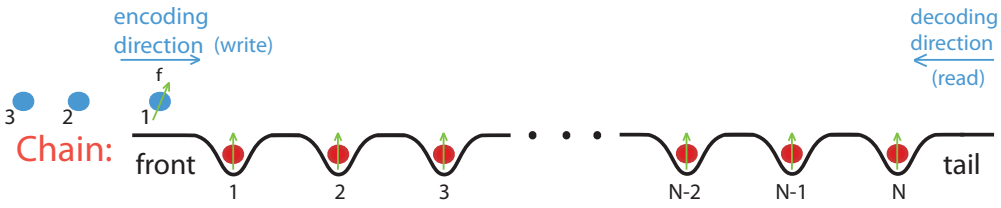


Figure 6.1: Illustration of the passive memory system (not to scale) with the associated quantum state transfer scheme. The coherent quantum memory consists of a sufficiently long, ferromagnetically aligned chain $|F\rangle$ of non-interacting, static spins (red). Each flying qubit (blue) enters the front end of the chain, interacts with the static spins sequentially and eventually emerges as polarised $|\uparrow\rangle_f$ at the tail end. The chain can then encode subsequent flying qubits sequentially in the same fashion. To read out from the memory, one simply injects a polarised qubit $|\uparrow\rangle_f$ back from the tail end, and the state of the last encoded flying qubit is then recovered automatically out from the flying spin emerging from the front. More states can be recovered sequentially in the same way by further injecting back polarised qubits $|\uparrow\rangle_f$ from the tail. There is no need to reset between successive encoding (decoding) rounds. Any multi-partite entanglement between injected qubits is also recovered in the read operations.

spins in the fully polarized chain $|F\rangle_c = |\uparrow_{s_1} ... \uparrow_{s_N}\rangle$. As shown in Fig. 6.1, during encoding (or the 'write' operation) $|\psi_1\rangle_{f_1}$ enters from the front into the chain and interacts with the static spins s_1 to s_N sequentially. Again, we first consider the XY spin-spin exchange interaction [Eq. 5.1] between the flying and each static spin s_k, with $\theta_k = \theta \in (0, \pi/2]\ \forall\ k$.

Starting from the total state $|\psi_1, F\rangle = |\psi_1\rangle_{f_1} |F\rangle_c$, we apply U_k of the form of Eq. 5.1 to the flying qubit and the k^{th} static spin sequentially for s_1 through to s_N. The state $|\uparrow, F\rangle$ with amplitude α_1 remains the same during this write operation, while $|\downarrow, F\rangle$, with amplitude β_1, evolves as follows:

$$
\begin{aligned}
|\downarrow, F\rangle \quad &\Rightarrow_1 \quad \cos\theta\ \underline{|\downarrow, F\rangle} - i \sin\theta\ \widehat{S}_1^- |\uparrow, F\rangle \\
&\Rightarrow_2 \quad \cos\theta \big(\cos\theta\ \underline{|\downarrow, F\rangle} - i \sin\theta\ \widehat{S}_2^- |\uparrow, F\rangle \big) - i \sin\theta\ \widehat{S}_1^- |\uparrow, F\rangle \\
&\Rightarrow_k \quad ...\ \forall\ k = 3, ..., N-1 \\
&\Rightarrow_N \quad -i \sin\theta \sum_{k=1}^{N} \cos^{k-1}\theta\ \widehat{S}_k^- |\uparrow, F\rangle + \cancelto{0\ as\ N \to \infty}{\cos^N \theta}\, |\downarrow, F\rangle\,,
\end{aligned}
\tag{6.1}
$$

where $\Rightarrow_k$ corresponds to the occurrence of an interaction event for the flying qubit with the static spin s_k, and $\widehat{S}_k^-$ denotes a spin down-flip in the k^{th} position of the chain. Note that the only component which evolves further in each superposition is underlined in Eq. 6.1. Combining both parts, we see that the flying qubit emerges as polarized $|\uparrow\rangle_{f_1}$ with probability $1-\cos^{2N}\theta \to 1$ for $N \to \infty$. In this limit, the initial quantum information which $|\psi_1\rangle_{f_1}$ held before encoding has now been transferred to the chain, and the decoupled total state of the flying qubit and the chain is

$$\left(\alpha_1 - i\beta_1 \sin\theta \sum_{k=1}^{N\to\infty} \cos^{k-1}\theta \ \widehat{S}_k^-\right) |\uparrow, F\rangle \,. \tag{6.2}$$

This is model independent by conservation of total spin, and so the argument is equally valid for the Heisenberg model (up to factors of $e^{ik\theta}$). Note that the probability of a single down-flip at site k is $|\beta_1|^2 \sin^2\theta \cos^{2(k-1)}\theta$, a quantity that decays exponentially along the chain. Summing over all these probabilities gives $|\beta_1|^2$, as expected by conservation of total probability.

To read out the state $|\psi_1\rangle$ of the original flying qubit from the memory at a later stage, we inject a polarized flying qubit $|\uparrow\rangle_f$ from the tail end back along the chain, i.e., in the opposite direction as for the encoding operation [see Fig. 6.1]. This is the simplest decoding method for the memory system, especially when the level of quantum control is limited. The flying qubit sequentially interacts with the static spins through s_N to s_1, and we first assume that it has the same kinetic energy (and hence θ) as the emitted qubit f_1. The state $|\uparrow, F\rangle$ with amplitude α_1 again remains the same during decoding, while each state $\widehat{S}_k^- |\uparrow, F\rangle$, with amplitude $-i\beta_1 \sin\theta \cos^{k-1}\theta$, evolves as follows, as the flying spin passes each member of the

chain:

$$
\begin{aligned}
\widehat{S}_k^- \left|\uparrow, F\right\rangle \Longrightarrow_{N(\to\infty)} \ldots \Longrightarrow_{k+1} \widehat{S}_k^- \left|\uparrow, F\right\rangle & \\
\Longrightarrow_k \quad & \cos\theta\ \widehat{S}_k^- \left|\uparrow, F\right\rangle - i\sin\theta\ \underline{\left|\downarrow, F\right\rangle} \\
\Longrightarrow_{k-1} & \cos\theta\ \widehat{S}_k^- \left|\uparrow, F\right\rangle - i\sin\theta\ \left(\cos\theta\ \underline{\left|\downarrow, F\right\rangle} - i\sin\theta\ \widehat{S}_{k-1}^- \left|\uparrow, F\right\rangle\right) \\
\Longrightarrow_{k'} \quad & \ldots \forall\ k' = k-2, \ldots, 2 \\
\Longrightarrow_1 \quad & \cos\theta\ \widehat{S}_k^- \left|\uparrow, F\right\rangle - i\sin\theta\cos^{k-1}\theta \left|\downarrow, F\right\rangle \\
& \quad - \sin^2\theta \sum_{j=1}^{k-1} \cos^{j-1}\theta\ \widehat{S}_{k-j}^- \left|\uparrow, F\right\rangle \quad \text{if } k \geq 2, \\
\text{or} \quad & \cos\theta\ \widehat{S}_1^- \left|\uparrow, F\right\rangle - i\sin\theta \left|\downarrow, F\right\rangle \quad \text{if } k = 1.
\end{aligned} \tag{6.3}
$$

Thus, by linearity, the total state after decoding becomes

$$
\begin{aligned}
& \alpha_1 \left|\uparrow, F\right\rangle - i\beta_1 \sin\theta\ \left(\cos\theta\ \widehat{S}_1^- \left|\uparrow, F\right\rangle - i\sin\theta \left|\downarrow, F\right\rangle\right) \\
& \quad - i\beta_1 \sin\theta \sum_{k=2}^{\infty} \cos^{k-1}\theta \left(\cos\theta\ \widehat{S}_k^- \left|\uparrow, F\right\rangle - i\sin\theta\cos^{k-1}\theta \left|\downarrow, F\right\rangle\right) \\
& \quad + i\beta_1 \sin\theta \sum_{n=2}^{\infty} \cos^{n-1}\theta \left(\sin^2\theta \sum_{j=1}^{n-1} \cos^{j-1}\theta\ \widehat{S}_{n-j}^- \left|\uparrow, F\right\rangle\right),
\end{aligned} \tag{6.4}
$$

where in the last line we have replaced the dummy variable k by n. By absorbing the bracketed terms in the first line into the summation of the second line, Eq. 6.4 is equivalent to

$$
\begin{aligned}
& \left(\alpha_1 \left|\uparrow, F\right\rangle - \beta_1 \underbrace{\sin^2\theta \sum_{k=1}^{\infty} \cos^{2(k-1)}\theta}_{1} \left|\downarrow, F\right\rangle\right) - i\beta_1 \sin\theta\ \times \\
& \qquad \left(\sum_{k=1}^{\infty} \cos^k\theta\ \widehat{S}_k^- - \sin^2\theta \sum_{n=2}^{\infty} \sum_{j=1}^{n-1} \cos^{n+j-2}\theta\ \widehat{S}_{n-j}^-\right) \left|\uparrow, F\right\rangle, \qquad \to 0
\end{aligned} \tag{6.5}
$$

where the first sum is simply a geometric series. For the double summation we want to focus on the coefficients for $\widehat{S}_k^-$, and hence the sum over j can be replaced by a sum over k with $k = n - j \geq 1$, i.e.,

$$\sum_{n=2}^{\infty}\sum_{j=1}^{n-1}\cos^{n+j-2}\theta\ \widehat{S}_{n-j}^- = \sum_{k=1}^{\infty}\sum_{n=k+1}^{\infty}\cos^{2(n-1)-k}\theta\ \widehat{S}_k^- = \sum_{k=1}^{\infty}\underbrace{\frac{\cos^k\theta}{1-\cos^2\theta}}_{\sin^2\theta}\ \widehat{S}_k^-, \quad (6.6)$$

where we have swapped the double summations as the sum over n runs to infinity. Therefore, the second line in Eq. 6.5 becomes zero due to complete cancellations for each $k = 1, 2, ... \infty$, and the total state after decoding is then simply

$$\left(\alpha_1 |\uparrow\rangle - \beta_1 |\downarrow\rangle\right)_f \bigotimes |F\rangle_c . \quad (6.7)$$

The complete cancellations only require that $N \to \infty$, which is the same condition as for the encoding procedure. Thus in this limit, the state of the flying qubit with matching kinetic energy can be transferred to and back from the memory in the way we have proposed. Thus, after the read operation the chain returns to the original fully polarized state and is disentangled from the flying qubit, whose state emerges from the front as $\sigma_z^f |\psi_1\rangle_{f_1}$. In other words we have recovered the original state of this flying qubit, up to a phase flip which can be corrected by a simple σ_z^f gate. This will always be the case for the XY model, and importantly distinguishes the decoding process from a time reversal operation. However, if we employ the Heisenberg model, the state of the flying qubit can still be encoded into the chain; but once read back, the total state of the system becomes (by tracking the extra phases $e^{ik'\theta}$ in the derivation above),

$$\left(\alpha_1 |\uparrow\rangle + \beta_1' |\downarrow\rangle\right)_f \bigotimes |F\rangle_c + \sum_{k=1}^{\infty}\gamma_k |\uparrow\rangle_f \bigotimes\ \widehat{S}_k^- |F\rangle_c , \quad (6.8)$$

where

$$\beta_1' = -\beta_1 \sin^2\theta \sum_{k=1}^{\infty} e^{2ik\theta} \cos^{2(k-1)}\theta = \frac{-\beta_1 e^{2i\theta}\sin^2\theta}{1-e^{2i\theta}\cos^2\theta}$$

$$\gamma_k = -i\beta_1 e^{i\theta}\sin\theta \left(e^{ik\theta}\cos^k\theta \; - \sin^2\theta \sum_{n=k+1}^{\infty} e^{i(2n-k)\theta}\cos^{2(n-1)-k}\theta \right)$$

$$= -i\beta_1 \sin\theta \cos^k\theta \; e^{i(k+1)\theta}\left(\frac{1-e^{2i\theta}}{1-e^{2i\theta}\cos^2\theta}\right)$$

for all $k \in \mathbb{Z}^+$. The decoding procedure no longer works due to the extra phases, except when $\theta = \frac{\pi}{2}$. Here, Eq. 6.8 is consistent with the XY model once we identify each extra phase $e^{i\theta}$ with 1 accordingly. Therefore, at arbitrary θ values, we currently envisage implementing the memory with bosonic cold atoms, controlled by a SLM [see Sec. 4.3.1] to achieve the desired XY model between the flying-static spins.

6.1.1 Memory size scales with coupling strength

To see how the size N of the memory chain required to store one qubit scales with the coupling strength θ, we note that the only condition is $\cos^{2N}\theta \to 0$ for sufficiently large N. Given any error tolerance $\epsilon > 0$ such that $\cos^{2N}\theta < \epsilon$, we require

$$2N(\theta) > \frac{\ln\epsilon}{\ln\cos\theta} \approx -\frac{2\ln\epsilon}{\theta^2} \quad (\text{for} \quad \theta \ll 1). \tag{6.9}$$

Thus we see that the required memory size increases significantly with decreasing coupling strength θ for fixed ϵ. For example, with $\epsilon \sim 10^{-4}$ and $\theta = 1$, $N_{\min} \simeq 8$ rising to ~ 920 for $\theta = 0.1$. However, in the weak coupling regime, the qubit state stored in the chain is delocalised; each static spin only shares a fraction of the total information, and thus has the potential to store more. On the other hand, for strong couplings a relatively short chain can already store a number of flying qubits. In the special case where $\theta = \frac{\pi}{2}$, one polarized static spin in the chain is sufficient

to store a flying qubit, since now U_k in Eq. 5.1 is simply a SWAP_k gate (up to a phase of '$-i$'). Encoding of subsequent flying qubits is thus also obvious, as are their readout procedures (since $\mathrm{SWAP}_k^2 = \mathrm{I}$ up to a phase of '-1'). These qubits are stored locally in the memory: By induction and linearity, one finds that n ordered flying qubits $|\psi_n\rangle_{f_n} \ldots |\psi_1\rangle_{f_1}$ are encoded sequentially into the memory and the chain state becomes $|\tilde{\psi}_n\rangle_{s_1} \ldots |\tilde{\psi}_1\rangle_{s_n} |\uparrow \ldots \uparrow\rangle_s$ after the whole write operation. Once read back, we obtain $|\tilde{\psi}_n\rangle_{f_n} \ldots |\tilde{\psi}_1\rangle_{f_1}$, where $\tilde{}$ denote the appropriate phase changes for the XY model. For this special case the argument also holds for the Heisenberg exchange model, though the extra phase flips will not be present. Indeed in the Heisenberg case the decoding process is nothing but a time reversal of the encoding operation. In fact, realisation of time reversal ($\theta \to -\theta$) for arbitrary θ would make the memory system viable even for the Heisenberg case in general. However, this would require tuning from ferromagnetic coupling g_k (write) to anti-ferromagnetic $-g_k$ (read), which is impractical.

6.1.2 Coupling mismatch between encoding and decoding

When the kinetic energy of the flying qubit during the read operation differs from

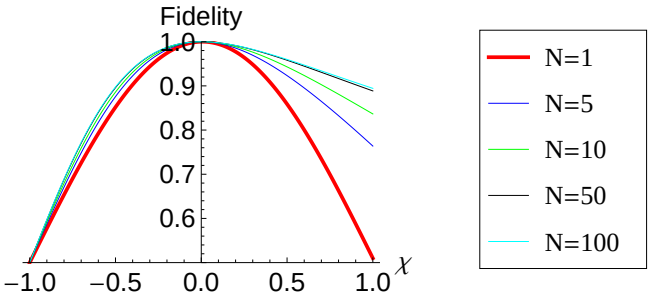


Figure 6.2: Plots of the fidelity of the retrieved qubit, relative to the input $|+\rangle_{f_1}$, against the fractional difference χ between the coupling strengths during encoding (θ_{enc}) and decoding (θ_{dec}), for various chain lengths. For each N, the whole chain collectively stores the qubit, i.e., $N_s = N$.

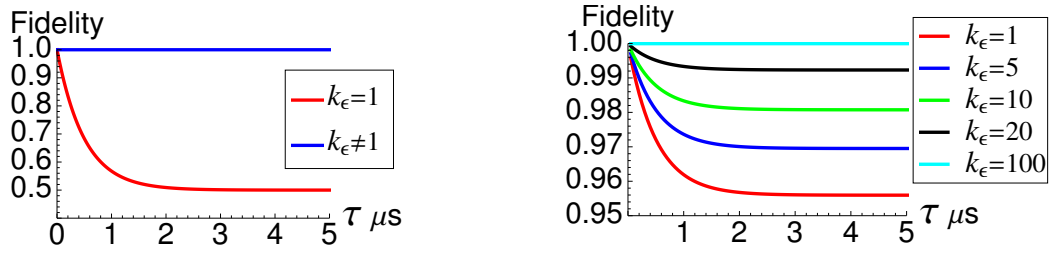
that of the input for encoding (i.e., $\theta_{\text{dec}} \neq \theta_{\text{enc}}$), we numerically simulate how the error effects on the memory for various chain lengths N in Fig. 6.2, where $\chi = (\theta_{\text{dec}} - \theta_{\text{enc}})/\theta_{\text{enc}}$. Here, θ_{enc} is adjusted so that each chain with length N is just enough to collectively store the qubit (it is defined by setting $\cos^N \theta_{\text{enc}} = 0.01$).

From Fig. 6.2, we see that after the decoding round, the retrieved qubit is of a high fidelity ($\geq 99\%$) with respect to the original input, for small mismatches ($\sim 10\%$) in the encoding and decoding θ values. Moreover, as the number N of static spins increases, the memory's tolerance to such errors improves.

6.2 Decoherence of static spins

We now consider the effect of decoherence on a chain in which one qubit state $|+\rangle_{f_1} = \big(|\uparrow\rangle_{f_1} + |\downarrow\rangle_{f_1}\big)/\sqrt{2}$ is stored. Both the write and the read operations are assumed to be fast; the principal effect of decoherence is on the static spins for the time (τ) during which the qubit is stored in the chain. We model this using the Lindblad master equation [Eq. 2.12], and by restricting to the subspace consisting of only zero or one excitations among the static spins. We simulated the behaviour for the memory chain of a fixed length $N = 100$ under dephasing errors. We also vary θ such that the qubit is stored in the first N_s ($\leq N$) number of static spins with $\epsilon \sim 10^{-2}$ [see Eq. 6.9], to monitor the effects of spreading the quantum information stored in the memory. For homogeneous dephasing, in which each spin is subject to the same, independent decoherence process, the total decoherence for the memory is essentially the same for all θ values. In our simulations we take a dephasing rate $\Gamma = 1$ MHz for each static spin and each resulting curve coincides exactly with the red curve in Fig. 6.3(a), regardless of the chosen $N_s \leq N$. In other words, the decoherence rate does not depend on how local or distributed the information is in the quantum memory, since the relevant qubits which contain the quantum

information each decohere at the same rate Γ. It also follows that the fidelity must eventually saturate to $\frac{1}{2}$ when all the memory qubits lose their quantum information.



(a) $N_s = 1$ (b) $N_s = 100$

Figure 6.3: Plots for the fidelity of the retrieved qubit, relative to the input $|+\rangle_{f_1}$, against the storage time τ under inhomogeneous dephasing with rate $\Gamma = 1$ MHz (coherence time 1 μs) for the k_ϵ^{th} static spin and *zero* for all others ($N = 100$). We vary θ such that the qubit is stored in the first N_s number of static spins with $\epsilon \sim 10^{-2}$ [see Eq. 6.9]: (a) The qubit is stored entirely in the first qubit ($\theta = \pi/2$); (b) The whole chain of 100 spins store the qubit collectively ($\theta \simeq 0.30$). Note that the homogeneous case (independent dephasing in each spin with equal rate) is not shown here, but each curve coincides with the red curve in (a), regardless of the chosen value $N_s \leq N$ (and hence independent of θ).

On the other hand, for inhomogeneous decoherence processes in which the spins decohere at different rates, distributing the quantum information does reduce the variance of the total memory decoherence rate compared with locally stored information, and this difference can be very large. We illustrate this in Fig. 6.3 for the case when just one static spin is subject to decoherence. When the quantum information is stored locally (in the first qubit with $\theta = \frac{\pi}{2}$ in Fig. 6.3(a)) then the fidelity F saturates to $\frac{1}{2}$ when the decohering spin is the first, whereas $F = 1$ if the decohering spin is any of the other $N-1$ spins. However, when the quantum information is spread over all N spins ($\theta \simeq 0.30$ in Fig. 6.3(b)), the saturated fidelity becomes $\gtrsim 1 - \frac{1}{2N}$, independent of which spin is subject to the decoherence. This result may easily be extended to cases when more than one spin decoheres, or the spins decohere at different rates. Spreading the information over many qubits will again *smooth* the statistical fluctuations in information loss.

6.3 Generalizations to multiple flying qubits

The general result for encoding and decoding an arbitrary number of input flying qubits with arbitrary multi-particle superpositions remains presently a conjecture, but we have strong evidence that it is true. In particular, we have extended the proof from one to two flying qubits, including entangled states, as well as for the case where there is only one $|\downarrow\rangle_f$ among any number of flying $|\uparrow\rangle_f$ qubits.

6.3.1 Collective 1-spin down-flip distributions

For the second of the two proofs just mentioned, we first define a 0^{th} collective 1-spin down-flip operator on the chain $|F\rangle_c$ arising from Eq. 6.1,

$$\widehat{D}_0^{(1)} = \sum_{k=1}^{\infty} a_0^{(1)}(k)\ \widehat{S}_k^- := \sum_{k=1}^{\infty} (-i \sin\theta \cos^{k-1}\theta)\ \widehat{S}_k^-, \tag{6.10}$$

where $|a_0^{(1)}(k)|^2$ corresponds to the probability of the k^{th} static spin being $|\downarrow\rangle_{s_k}$. We find $\sum_k |a_0^{(1)}(k)|^2 = 1$, as expected for unit total probability. The mean position $\mu_0^{(1)}$ of the down-flip and the associated standard deviation $\sigma_0^{(1)}$ are

$$\mu_0^{(1)} = \sum_{k=1}^{\infty} k\ |a_0^{(1)}(k)|^2 = \csc^2\theta, \qquad \sigma_0^{(1)} = \sqrt{\sum_{k=1}^{\infty} k^2 |a_0^{(1)}(k)|^2 - (\mu_0^{(1)})^2} = \cos\theta \csc^2\theta. \tag{6.11}$$

Here, evalutions of the following series are required:

$$\begin{aligned}
\sum_{k=1}^{\infty} k y^{k-1} &\equiv \frac{d}{dy}\Big(\sum_{k=1}^{\infty} y^k\Big) = \frac{d}{dy}\left(\frac{y}{1-y}\right) = \frac{1}{(1-y)^2}, \\
\sum_{k=1}^{\infty} k^2 y^{k-1} &\equiv \sum_{k=1}^{\infty} (k+1) k y^{k-1} - \sum_{k=1}^{\infty} k y^{k-1} \equiv \frac{d^2}{dy^2}\Big(\sum_{k=1}^{\infty} y^{k+1}\Big) - \frac{1}{(1-y)^2} \\
&\equiv \frac{d^2}{dy^2}\left(\frac{y^2}{1-y}\right) - \frac{1}{(1-y)^2} = \frac{2}{(1-y)^3} - \frac{1}{(1-y)^2} = \frac{1+y}{(1-y)^3},
\end{aligned} \tag{6.12}$$

followed by seting $y = \cos^2\theta$ to substitute into Eq. 6.11 for the second equalities.

Our next goal is to find the l^{th} collective 1-spin down-flip distribution $\big(\widehat{D}_l^{(1)} = \sum_k a_l^{(1)}(k)\widehat{S}_k^-\big)$ in the memory which results from further encoding l subsequent flying $|\uparrow\rangle_f$ qubits. We find that after encoding one flying $|\uparrow\rangle_f$ qubit into a chain with state $\widehat{S}_k^- \, |F\rangle_c$ $\forall$ finite $k \ll N$, the total state becomes

$$|\uparrow\rangle_f \bigotimes \big(\cos\theta \ \widehat{S}_k^- - \sin^2\theta \sum_{n=k+1}^{\infty} \cos^{n-k-1}\theta \ \widehat{S}_n^-\big) \, |F\rangle_c \, , \tag{6.13}$$

which is derived step-by-step as before. Thus, by linearity [apply Eq. 6.13], encoding one flying $|\uparrow\rangle_f$ qubit into the chain with distribution $\widehat{D}_0^{(1)} = \sum_k a_0^{(1)}(k)\widehat{S}_k^-$ gives rise to the following 1-spin down-flip distribution

$$\widehat{D}_1^{(1)} = \sum_{k=1}^{\infty} a_0^{(1)}(k)\big(\cos\theta \ \widehat{S}_k^- - \sin^2\theta \sum_{n=k+1}^{\infty} \cos^{n-k-1}\theta \ \widehat{S}_n^-\big). \tag{6.14}$$

Again, we want to focus on the coefficients of $\widehat{S}_k^-$ terms. Note that $a_0^{(1)}(k)/\cos^{k-1}\theta = -i\sin\theta$, independent of k. Thus, the double sum [Eq. 6.14] is

$$\begin{aligned} &-\sin^2\theta \sum_{k=1}^{\infty}\sum_{n=k+1}^{\infty} a_0^{(1)}(k)\cos^{n-k-1}\theta \ \widehat{S}_n^- = -\tan^2\theta \sum_{k=1}^{\infty}\sum_{n=k+1}^{\infty} (-i\sin\theta)\cos^n\theta \ \widehat{S}_n^- \\ &= -\tan^2\theta(-i\sin\theta)\sum_{n=1}^{\infty}\sum_{k=n+1}^{\infty}\cos^k\theta \ \widehat{S}_k^- = -\tan^2\theta(-i\sin\theta)\sum_{k=1}^{\infty}(k-1)\cos^k\theta \ \widehat{S}_k^- \\ &= -\tan^2\theta\sum_{k=1}^{\infty}(k-1) \ a_0^{(1)}(k)\cos\theta \ \widehat{S}_k^- \end{aligned} \tag{6.15}$$

where we have interchanged the labelling of dummy variables n and k in the third line, and evaluated the sum of geometric series in the fourth. Substituting back into Eq. 6.14 and comparing with the more general definition of $\widehat{D}_l^{(1)}$, we have

$$a_1^{(1)}(k) = a_0^{(1)}(k)\cos\theta \ \big(1 - (k-1)\tan^2\theta\big). \tag{6.16}$$

We can then apply the same procedure [with Eq. 6.13] to encoding one flying $|\uparrow\rangle_f$ qubit into $\widehat{D}_1^{(1)} = \sum_k a_1^{(1)}(k)\widehat{S}_k^-$ to find, again by linearity, amplitudes for the second 1-spin down-flip distribution

$$a_2^{(1)}(k) = a_0^{(1)}(k)\cos^2\theta\,\Big(1 - 2(k-1)\tan^2\theta + \frac{(k-1)(k-2)}{2}\tan^4\theta\Big), \tag{6.17}$$

where [as also illustrated in Eq. 6.15] we have evaluated the following weighted sums of geometric series (by first relabelling the dummy variables to focus on $\widehat{S}_k^-$),

$$\begin{aligned}&\sum_{k=1}^{\infty}\sum_{n=k+1}^{\infty}(k-1)\cos^n\theta\;\widehat{S}_n^- = \sum_{n=1}^{\infty}\sum_{k=n+1}^{\infty}(n-1)\cos^k\theta\;\widehat{S}_k^-\\ =&\sum_{k=2}^{\infty}\left(\sum_{n=1}^{k-1}(n-1)\right)\cos^k\theta\;\widehat{S}_k^- = \sum_{k=3}^{\infty}\frac{(k-1)(k-2)}{2}\cos^k\theta\;\widehat{S}_k^-.\end{aligned} \tag{6.18}$$

Note that the general term of the bracketed series are obtained from evaluation of the weighted geometric series in the previous step (evaluating the lower order distribution).

Now, with the key inductive steps to relabel the dummy variables (to focus on $\widehat{S}_k^-$), and evaluating the following series [as done above and in Eq. 6.15],

$$\sum_{n=l'+1}^{k-1}(-1)^{l'}\frac{1}{l'!}\prod_{m=0}^{l'-1}(l'-m)\frac{1}{l'!}\prod_{j=1}^{l'}(n-j) \equiv \frac{(-1)^{l'+1}}{(l'+1)!}\prod_{j=1}^{l'+1}(k-j), \tag{6.19}$$

we can inductively derive the amplitudes

$$\begin{aligned}a_l^{(1)}(k) &= a_0^{(1)}(k)\cos^l\theta\sum_{r=0}^{\min\{l,k-1\}}(-1)^r\left(\frac{1}{r!}\prod_{m=0}^{r-1}(l-m)\right)\frac{1}{r!}\prod_{j=1}^{r}(k-j)\tan^{2r}\theta\\ &= a_0^{(1)}(k)\cos^l\theta\sum_{r=0}^{\min\{l,k-1\}}(-1)^r\binom{k-1}{r}\binom{l}{r}\tan^{2r}\theta\\ &= a_0^{(1)}(k)\cos^l\theta\;{}_2F_1(1-k,-l;1;-\tan^2\theta)\end{aligned} \tag{6.20}$$

for the general l^{th} collective 1-spin down-flip operator $\widehat{D}_l^{(1)} = \sum_k a_l^{(1)}(k)\widehat{S}_k^-$. In the more compact form of Eq. 6.20, ${}_2F_1(a, b; c; z)$ denotes the *Gauss* hypergeometric function [403], and $a_0^{(1)}(k)\cos^l\theta$ renders possible divergence of $\tan^{2r}\theta$ convergent in Eq. 6.20 (analytic continuation is assumed implicitly here). Note that Eq. 6.13 has two terms, the first (and lower order) of which inductively adds to the lower order terms (in $\tan^2\theta$) in Eq. 6.20, to give rise to the bracketed product coefficient concerning l.

This expression for the l^{th} collective 1-spin down-flip distribution can also be obtained through a combinatorial argument, as follows. For any fixed down-flip position k, and assuming $k > (l+1)$, the amplitude is a sum of $l+1$ terms , each of which corresponds to a different origin for the $\widehat{S}_k^-$. In general a spin-up qubit passing along the chain can either cause no spin flips at all, or can move a spin down from a site nearer the front of the chain to one further along it. The 0^{th} term results from the situation in which the down spin is initially localized on spin state k and where all l subsequent $|\uparrow\rangle_f$ qubits move along the chain without executing further flips. Each has contributed a factor of $\cos\theta$ due to the exchange interaction and thus an overall factor of $\cos^l\theta$ is present in addition to $a_0^{(1)}(k)$. In general, the r^{th} term $(r > 0)$ occurs when r movements of the initial spin down position occur before that spin down reaches its final position k. There are $\binom{l}{r}$ ways of choosing the r qubits which cause the flips from the l total, and $\binom{k-1}{r}$ ways of choosing which r of the $(k-1)$ static spins which precede the k^{th} will hold the spin down at some point before the spin down finally occurs at site k. The other terms in the summation come from the fact that each double spin flip (or movement of the spin down location) gives rises to a factor of $(-i\sin\theta)^2$, while losing a factor of $\cos\theta$; in addition, the other $(l-r)$ $|\uparrow\rangle_f$ qubits passed the down-flipped spin without exchanging, and each contributed a factor of $\cos\theta$. Combining these coefficients gives rise to Eq. 6.20.

Decoding this more general memory state can be achieved by injecting successive

$|\uparrow\rangle_f$ spins in the decoding direction. After the first such spin passes, the new memory state down-spin amplitude for the k^{th} site, $a_{l-1}^{\prime(1)}(k)$, results from two possible scenarios: Either this $|\uparrow\rangle_f$ passed the k^{th} site which was already in the down state, without exchange, or it transported the $(k+s)^{\text{th}}$ down spin to the k^{th} position. Taking into account of the factors contributed, we have

$$a_{l-1}^{\prime(1)}(k) = a_l^{(1)}(k)\cos\theta + (-i\sin\theta)^2 \sum_{s=1}^{\infty} a_l^{(1)}(k+s)\cos^{s-1}\theta \equiv a_{l-1}^{(1)}(k). \tag{6.21}$$

To establish this last equivalence, we multiply both sides of the following identity

$$\frac{{}_2F_1(a,b;1;z)}{1-z} + \frac{z}{1-z}\sum_{s=1}^{\infty}\frac{{}_2F_1(a-s,b;1;z)}{(1-z)^s} \equiv {}_2F_1(a,b+1;1;z) \tag{6.22}$$

by $a_0^{(1)}(k)\cos^{l-1}\theta$, and substitute for $a = 1-k, b = -l$, and $z = -\tan^2\theta$; we then obtain $a_{l-1}^{\prime(1)}(k) \equiv a_{l-1}^{(1)}(k)$ from Eq. 6.21. Here, $l \in \mathbb{N}$ can be arbitrary. This means that the 1-spin down-flip distributions can be manipulated in both directions, essential for the chain to act as a memory. The proof of Eq. 6.22 follows below: We work with the *Euler*'s integral representation for the hypergeometric function

$${}_2F_1(a,b;1;z) = \frac{1}{B(b,1-b)}\int_0^1 \frac{t^{b-1}(1-t)^{-b}}{(1-zt)^a}dt \tag{6.23}$$

for $|z| \leq 1$, and apply analytic continuation to other values of z. Here, $B(p,q) = \Gamma(p)\Gamma(q)/\Gamma(p+q)$ is the *beta* function, where $\Gamma(p+1) = p\Gamma(p)$ is the *gamma* function [403]. We see that

$$B(b,1-b) = \frac{\Gamma(b)\Gamma(1-b)}{\Gamma(1)} = \frac{\frac{1}{b}\Gamma(b+1)(-b)\Gamma(-b)}{\Gamma(1)} = -B(b+1,-b) \tag{6.24}$$

Thus, by substituting both Eqns. 6.23 and 6.24 back into Eq. 6.22 [and multiplying

both sides by $(1-z)B(b,1-b)]$, our task reduces to proving that

$$\int_0^1 \frac{t^{b-1}(1-t)^{-b}}{(1-zt)^a}dt + \sum_{s=1}^{\infty} \frac{z}{(1-z)^s} \int_0^1 \frac{t^{b-1}(1-t)^{-b}}{(1-zt)^{a-s}}dt \equiv -(1-z)\int_0^1 \frac{t^b(1-t)^{-b-1}}{(1-zt)^a}dt, \tag{6.25}$$

where the extra minus sign on the right hand side comes from Eq. 6.24. Evaluating the summation in Eq. 6.25, we have

$$\begin{aligned}\sum_{s=1}^{\infty} \frac{z}{(1-z)^s} \int_0^1 \frac{t^{b-1}(1-t)^{-b}}{(1-zt)^{a-s}}dt &= \int_0^1 z\left[\sum_{s=1}^{\infty}\left(\frac{1-zt}{1-z}\right)^s\right]\frac{t^{b-1}(1-t)^{-b}}{(1-zt)^a}dt \\ &= \int_0^1 \not{z}\left(\frac{1-zt}{\not{z}(t-1)}\right)\frac{t^{b-1}(1-t)^{-b}}{(1-zt)^a}dt. \end{aligned} \tag{6.26}$$

Hence, the left hand side of Eq. 6.25 is equivalent to

$$\int_0^1 \left(1-\frac{1-zt}{1-t}\right)\frac{t^{b-1}(1-t)^{-b}}{(1-zt)^a}dt = -(1-z)\int_0^1 \frac{t}{1-t}\frac{t^{b-1}(1-t)^{-b}}{(1-zt)^a}dt, \tag{6.27}$$

which is exactly the right hand side of Eq. 6.25. □

Having established this important feature [Eq. 6.21], we now show that each distribution corresponds to a unique storage mode and the modes are independent, i.e., expressed as the following (discrete) orthonormal condition

$$\sum_{k=1}^{\infty} a_{l'}^{(1)*}(k)\; a_l^{(1)}(k) = \delta_{l'l}. \tag{6.28}$$

This ensures the unit total probability for each distribution. To establish this discrete orthonormal condition Eq. 6.28, we first introduce the normalized *Meixner* polynomials [403] (with j, x integers),

$$M_j'(x;\mu,\nu) := \nu^{\frac{j}{2}}\; {}_2F_1\left(-j,-x;\mu;1-\frac{1}{\nu}\right) \equiv \nu^{\frac{j}{2}}\; {}_2F_1\left(-x,-j;\mu;1-\frac{1}{\nu}\right), \tag{6.29}$$

where the equivalence comes from the symmetry of the hypergeometric function in

its first two arguments. Note that the different normalization is present since we are only summing over $x \in \mathbb{N}$ (instead of $\mathbb{Z}$). The orthonormality condition for the Meixner polynomials states that

$$\sum_{x=0}^{\infty} M'_j(x;\mu,\nu) M'_{j'}(x;\mu,\nu)\omega(x;\mu,\nu) = \delta_{jj'}, \tag{6.30}$$

where the discrete weight[1] $\omega(x;\mu,\nu) = (1-\nu)^{\mu}\frac{(\mu)_x}{x!}\nu^x$ [403]. Setting $x = k-1$, $j = l, \mu = 1, \nu = \cos^2\theta$, and substituting Eq. 6.29 into Eq. 6.30, we have

$$\sum_{k=1}^{\infty} {}_2F_1(1-k,-l;1;-\tan^2\theta)\ {}_2F_1(1-k,-l';1;-\tan^2\theta) \times \sin^2\theta\cos^{2(k+l-1)}\theta = \delta_{ll'} \tag{6.31}$$

which is exactly the desired condition Eq. 6.28. □

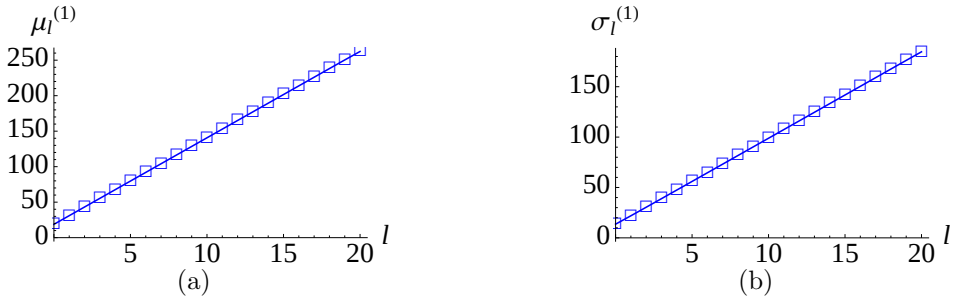


Figure 6.4: Plots with a non-special coupling strength $\theta = 0.4$ for (a) the mean positions $\mu_l^{(1)}$ of the down-flip against the number l of subsequent flying $|\uparrow\rangle_f$ qubits encoded into the memory; (b) the corresponding standard deviations $\sigma_l^{(1)}$ against l. The linear relationships are also observed for other θ values [see Eq. 6.11].

The independence of these unique storage modes are best illustrated by considering their mean positions $\mu_l^{(1)}$ of the down-flip and the corresponding standard deviations $\sigma_l^{(1)}$, which can be calculated in a similar way to how we found Eq. 6.11. We find that for any given coupling strength θ, both $\mu_l^{(1)}$ and $\sigma_l^{(1)}$ increase *linearly* with l; an example is demonstrated in Fig. 6.4, with a non-special value $\theta = 0.4$.

[1]Here, $(\mu)_x \equiv \frac{\Gamma(\mu+x)}{\Gamma(\mu)}$ denotes the Pochhammer symbol [403].

Finally, we numerically simulate the 1-spin down-flip distributions, by encoding a flying $|\downarrow\rangle_f$ qubit followed by l subsequent $|\uparrow\rangle_f$ into the initially polarized chain. In order to numerically simulate the evolution for the state of the whole system $|\psi_f, \Phi_c\rangle$, we apply the write and read operators,

$$U_{\text{write}} = U_{fN}...U_{f2}U_{f1}, \qquad U_{\text{read}} = U_{f1}U_{f2}...U_{fN}, \tag{6.32}$$

where each $2^{N+1} \times 2^{N+1}$ time evolution matrix U_{fi} describes the interaction between the flying qubit and the i^{th} static spin under the standard basis $\{f, s_1, s_2, ..., s_N\}$):

$$U_{fk} = \left(\begin{array}{cc|cc} \mathbb{1}_{2^{N-k}} & \mathbb{0}_{2^{N-k}} & & \\ & \ddots & & \ddots \\ \mathbb{0}_{2^{N-k}} & \mathbb{C}_{2^{N-k}} & & \mathbb{S}_{2^{N-k}} \\ \hline & \mathbb{S}_{2^{N-k}} & \mathbb{C}_{2^{N-k}} & \mathbb{0}_{2^{N-k}} \\ & \ddots & & \ddots \\ & \mathbb{S}_{2^{N-k}} & & \mathbb{C}_{2^{N-k}} \\ & & \mathbb{0}_{2^{N-k}} & \mathbb{1}_{2^{N-k}} \end{array}\right), \tag{6.33}$$

where $\mathbb{1}_m$ is the $m \times m$ identity matrix, $\mathbb{C}_m = \cos\theta_k \; \mathbb{1}_m$ while $\mathbb{S}_m = -i \sin\theta_k \; \mathbb{1}_m$; both $\mathbb{0}_m$ and blank fields correspond to blocks of 0s. The dots represent the *alternating* repetitive patterns (along the diagonal in the upper left and lower right blocks these are $\mathbb{1}_m$, $\mathbb{C}_m$, $\mathbb{1}_m$, $\mathbb{C}_m$ ...; along the diagonals in the lower left and upper right blocks these are $\mathbb{S}_m$, $\mathbb{0}_m$, $\mathbb{S}_m$, $\mathbb{0}_m$ ...), and there are an equal number of blocks of $\mathbb{1}_m$'s, $\mathbb{C}_m$'s and $\mathbb{S}_m$'s. This is readily obtained by considering the exchange processes between the flying qubit and the k^{th} static spin, regardless of the state of other spins; the alternating repetitive pattern is due to spins s_1 to s_{k-1} and the size of each block is due to s_{k+1} to s_N. Note that each U_{fk} is symmetric, and

centrosymmetric (symmetric about the centre point and a property that is closed under matrix multiplications) [404]. When the whole system is restricted to at

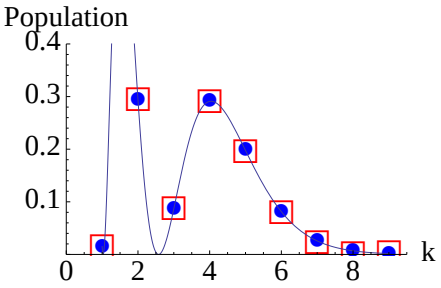


Figure 6.5: Plots of the down-flip distribution $|a_2^{(1)}(k)|^2$ in a chain with $N = 9$, and $\theta = 1.2$: The discrete plots are from our simulations ("blue circle" for $|a_2^{(1)}(k)|^2$ and "red square" for $|a_2'^{(1)}(k)|^2$ [see Eq. 6.21]), while the curve corresponds to the analytical solution [Eq. 6.20] (only values for integer k are relevant).

most one excitation, the state space consisting of more than one excitations is never accessed and can thus be ignored for the purpose of simulation. In this way, the dimension $(N+2)\times(N+2)$ of the density matrix (with only zero or one excitation) grows linearly with the number N of chain spins; simulations of very long chains can then be done conveniently [as shown in Fig. 6.3]. An example is illustrated in Fig. 6.5, and shows agreement with our analytical solutions for $|a_l^{(1)}(k)|^2$.

6.3.2 $(0,\ 0)^{\text{th}}$ 2-spin down-flip distribution

To generalize the results from above, we need to show that the chain can store a spin state that includes an arbitrary number n of down-spins

$$\widehat{D}^{(n)}_{(l_1,\ldots,l_n)} = \sum_{k_1<\ldots<k_n} a^{(n)}_{(l_1,\ldots,l_n)}(k_1,\ldots,k_n)\ \widehat{S}^{-}_{(k_1,\ldots,k_n)}, \tag{6.34}$$

where the k_is denote the spin-flip positions and l_i denotes the number of $|\uparrow\rangle_f$ encoded between the i^{th} and $(i+1)^{\text{th}}$ flying $|\downarrow\rangle_f$ qubits. This would mean that the chain can

store the information from a number of flying qubits, each of which was originally either $|\uparrow\rangle_f$ or $|\downarrow\rangle_f$ and can be further retrieved by the aforementioned decoding mechanism. Arbitrary multi-particle superpositions and entanglement then follows by linearity. Unfortunately, this procedure becomes impractical for more than two down-spins due to the difficulty of keeping track of all the indices (with large numbers of parameters l_is and k_js), and a rigorous proof for an arbitrary number of up-spin and down-spin qubits remains an open challenge.

Nevertheless, we have proved that encoding and decoding two $|\downarrow\rangle_f$ qubits in the chain $|F\rangle_c$ can be done in a similar fashion as before, with the $(0,0)^{\text{th}}$ collective 2-spin down-flip distribution being

$$\widehat{D}^{(2)}_{(0,0)} = \sum_{k_1<k_2} a^{(2)}_{(0,0)}(k_1,k_2)\ \widehat{S}^-_{(k_1,k_2)} \tag{6.35}$$

after having encoded only two $|\downarrow\rangle_f$ in the chain. Going through step-by-step we find that the total state of the system, after encoding one flying $|\downarrow\rangle_f$ qubit into a chain with state $\widehat{S}^-_k\,|F\rangle_c$, becomes

$$|\uparrow\rangle_f \bigotimes (-i\sin\theta)\sum_{k'=2}^{\infty}\cos^{k'-2}\theta\ \widehat{S}^-_k\widehat{S}^-_{k'}\,|F\rangle_c \quad \text{if } k=1, \tag{6.36a}$$

or, for finite $2\le k\ll N$,

$$\begin{aligned}|\uparrow\rangle_f \bigotimes (-i\sin\theta)\Bigg[&\sum_{k'=k+1}^{\infty}\cos^{k'-2}\theta\ \widehat{S}^-_k\widehat{S}^-_{k'} + \sum_{k'=1}^{k-1}\cos^{k'}\theta\ \widehat{S}^-_k\widehat{S}^-_{k'}\\ &-\tan^2\theta\sum_{k'=1}^{k-1}\sum_{k''=k+1}^{\infty}\cos^{k'+k''-k}\theta\ \widehat{S}^-_{k'}\widehat{S}^-_{k''}\Bigg]|F\rangle_c\,.\end{aligned} \tag{6.36b}$$

Note that by applying a combinatorial argument as illustrated before, one can obtain the same results. Thus by linearity, after encoding the $|\downarrow\rangle_f$ into $\widehat{D}^{(1)}_0\,|F\rangle_c$, we

have

$$\widehat{D}^{(2)}_{(0,0)} = (-i\sin\theta)^2\Bigg[\sum_{k=1}^{\infty}\sum_{k'=k+1}^{\infty}\cos^{k+k'-3}\theta\ \widehat{S}^-_k\widehat{S}^-_{k'} + \sum_{k=2}^{\infty}\Bigg(\sum_{k'=1}^{k-1}\cos^{k+k'-1}\theta\ \widehat{S}^-_k\widehat{S}^-_{k'} - \tan^2\theta\sum_{k'=1}^{k-1}\sum_{k''=k+1}^{\infty}\cos^{k'+k''-1}\theta\ \widehat{S}^-_{k'}\widehat{S}^-_{k''}\Bigg)\Bigg]. \tag{6.37}$$

By manipulating the double and triple summations as before, we find that

$$\widehat{D}^{(2)}_{(0,0)} = (-i\sin\theta)^2\sum_{k_1=1}^{\infty}\sum_{k_2=k_1+1}^{\infty}\Big(\cos^{k_1+k_2-3}\theta + \cos^{k_1+k_2-1}\theta - (k_2-k_1-1)\tan^2\theta\cos^{k_1+k_2-1}\theta\Big)\widehat{S}^-_{k_1}\widehat{S}^-_{k_2}. \tag{6.38}$$

Therefore, the $(0,0)^{\text{th}}$ collective 2-spin amplitude $\big($after encoding only $|{\downarrow_{f_2}}{\downarrow_{f_1}}\rangle\big)$ is

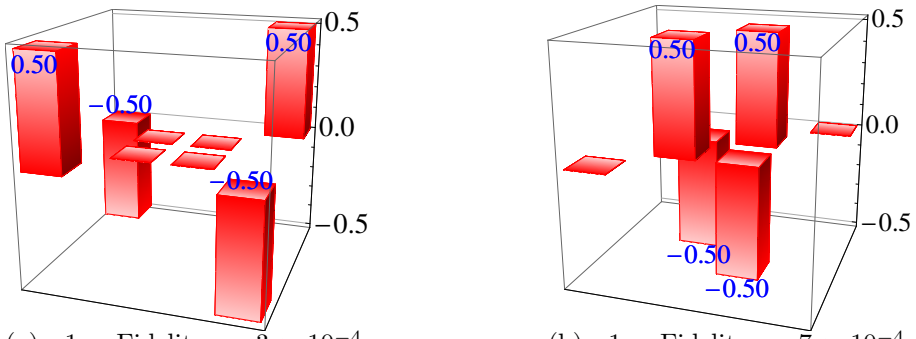
$$a^{(2)}_{(0,0)}(k_1,k_2) = (-i\sin\theta)^2\cos^{k_1+k_2-1}\theta\ \big(2-(k_2-k_1-2)\tan^2\theta\big). \tag{6.39}$$

We find the total probability $\sum_{k_1<k_2}|a^{(2)}_{(0,0)}(k_1,k_2)|^2 = 1$, as expected. The qubits can also be recovered sequentially, as can be shown by going through step-by-step or using a combinatorial argument.

We have thus shown that the memory can encode and decode $|{\uparrow_{f_2}}{\uparrow_{f_1}}\rangle$ [trivial], $|{\uparrow_{f_2}}{\downarrow_{f_1}}\rangle$ [Sec. 6.3.1], $|{\downarrow_{f_2}}{\uparrow_{f_1}}\rangle$ [Sec. 6.1], and $|{\downarrow_{f_2}}{\downarrow_{f_1}}\rangle$ [Sec. 6.3.2]. By linearity, the memory can store two qubits of arbitrary state, *entangled* or not (and hence qubits of mixed states). We conjecture that the memory chain can store multiple flying qubits of arbitrary states using the described mechanism[2]. A numerical check for $N = 8$ static spins and two fully entangled flying qubits is shown in Fig. 6.6, demonstrating that this state can be retrieved with high fidelity and errors within the expected

[2]Note that an implication of this result is that we can relax the condition of the initial memory being perfectly polarized to possessing a sufficiently long, ferromagnetically aligned tail. The most damaging error would be that the tail end of the chain was initially not completely polarized.

limits.



(a) $1 - \text{Fidelity} = 3 \times 10^{-4}$, $|\Phi^-\rangle_{f_{12}} = (|\uparrow\uparrow\rangle - |\downarrow\downarrow\rangle)/\sqrt{2}$;

(b) $1 - \text{Fidelity} = 7 \times 10^{-4}$, $|\Psi^-\rangle_{f_{12}} = (|\uparrow\downarrow\rangle - |\downarrow\uparrow\rangle)/\sqrt{2}$.

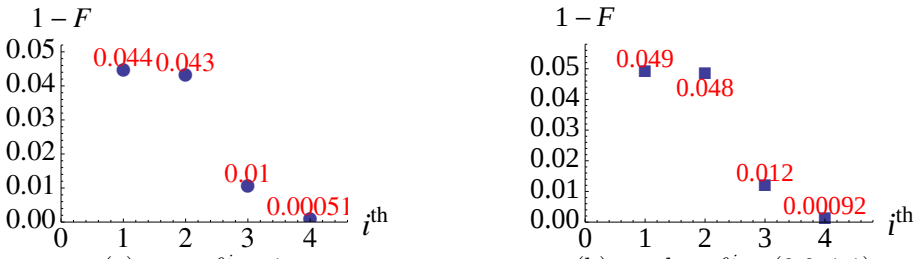
Figure 6.6: Density state tomograms constructed for the corresponding, retrieved (two-qubit) quantum state from a memory chain $|F\rangle_c$ consisting of $N = 8$ static spins without decoherence. (a) and (b) represent two separate cases of memory storage and retrieval of quantum information. The inputs, both entangled, are indicated in each case, together with the corresponding infidelity of the retrieved state. We chose a non-special value $\theta = 1.1$; for a tolerance $\epsilon \sim 10^{-4}$, this requires $N \geq 6$ to reliably store one qubit, as predicted by Eq. 6.9.

Further support for the conjecture is provided by numerical simulations as shown in Fig. 6.7(a) for short chains with a few flying qubits of randomly generated states, and θ chosen to give a high probability for a ferromagnetically aligned tail after encoding. Analysis of the fidelity after decoding gives results which are consistent with the conjecture within the expected error bounds.

6.4 Variations in coupling strengths

The example numerical simulation in Fig. 6.7(a) involves the memory storage and retrieval of four randomly-generated, pure qubits, with the same coupling strength ($\theta^i = \theta \; \forall \; i$). We now extend to consider the effects of the different kinetic energy that each qubit may possess, and the memory's tolerance to the resulting coupling strength variations.

To separate the effects of finite chain length, we employ the same qubits $\{\rho_i\}_4$

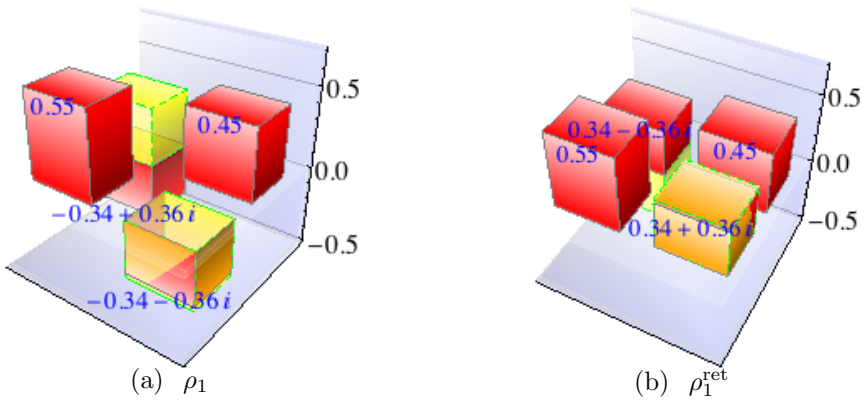


(a) same $\theta^i = 1$ (b) random $\theta^i \in (0.9, 1.1)$

Figure 6.7: Plots for the infidelity $1 - F$ of the retrieved qubit (with phase corrected), relative to the corresponding input ρ_i, against the ordinal number i of the inputs. Here, four randomly-generated pure qubits $\{\rho_i\}_4$ are sequentially encoded into the memory chain $|F\rangle_c$ ($N = 9$), and then retrieved one by one in the reverse order without decoherence. θ^i denotes the coupling strength between the i^{th} qubit ρ_i and each static spin during both encoding and decoding rounds; site-to-site variations are ignored here, and considered later. (a) $\theta^i = 1$, and hence for $\epsilon \sim 10^{-4}$ (or 10^{-2}) it requires $N \geq 7$ (or 4) to reliably store one qubit. The finite chain length restricts the number of qubits the memory can hold; within its capacity the last encoded (or the first retrieved) qubit always has the highest fidelity, since part of the quantum information stored for the earliest qubits may have been 'pushed out' of the memory by the later ones during encoding. (b) Random θ^i and hence ten independent runs of simulations are performed, and for each qubit the average is taken for the phase-corrected fidelity.

generated in Fig. 6.7(a) and simulate their storage and retrieval from the memory $|F\rangle_c$ with the same length $N = 9$, but with random $\theta^i \in (0.9, 1.1)$ for each i. Each θ^i matches for the corresponding decoding and encoding operations of ρ_i [effects of such mismatch were considered in Fig. 6.2]; site-to-site variations are also ignored, but considered below. Fig. 6.7(b) thus illustrates the effects of small round-to-round variations ($\sim \pm 10\%$) in the coupling strengths, and shows that the memory is robust towards such imperfections as long as the memory has sufficient capacity to store each qubit reliably (i.e., has a large enough N).

To consider site-to-site variations in θ_k, we encode and decode only ρ_1 into the chain $|F\rangle_c$ with $N = 9$, with variable coupling strengths $\theta_k \in (0.9, 1.1)$ between the qubit and k^{th} static spin. Note that again θ_k matches for the decoding and encoding operations for the same position k. In this case, we found the infidelity (averaged over ten independent runs) between $\tilde{\rho}_1^{\text{ret}}$ and ρ_1 to be $\sim 10^{-5}$ [see Fig. 6.8], similar



(a) ρ_1 (b) ρ_1^{ret}

Figure 6.8: Density state tomograms ("red" for real components and "yellow" for imaginary) constructed for (a) the input ρ_1 generated in Fig. 6.7; (b) the retrieved qubit ρ_1^{ret}, by encoding *only* ρ_1 into the the memory chain $|F\rangle_c$ (with $N = 9$) and then read back (without correcting the phase). We have random $\theta_k \in (0.9, 1.1)$ between the qubit and the k^{th} static spin. The infidelity $1 - F$ of the retrieved qubit, if phase corrected, is 7.4×10^{-6}, which is again averaged over the results from ten independent runs of simulations. For comparison, the corresponding infidelity for $\theta_k = 1\ \forall k$ is 6.1×10^{-6}.

to that in the case of $\theta_k = 1\ \forall k$. Thus, the memory can also tolerate small site-to-site variations ($\sim \pm 10\%$) in the coupling strengths θ_k.

6.5 Conclusion

We have illustrated how a polarized, non-interacting spin chain may be utilized to collectively store multiple flying qubits in a passive way. Weak couplings between the flying-static spins are permitted, and moreover, spreading the information over many qubits (small θ) will 'smooth' the statistical fluctuations in local information loss. The memory is also resilient to other error effects, such as coupling disorders.

Unlike for the scheme presented in Chapter 5, the XY model is the key here to allowing the encoding and decoding of qubits within the memory for arbitrary couplings. We would therefore propose to first implement this scheme with bosonic cold atoms, to be controlled by a SLM [see Sec. 4.3.1] [381, 382].

Chapter 7

Spin-chain quantum to classical channel transition in diamond

7.1 Background

We now turn to *coupled* spin chains, which are promising candidates [383, 384, 385] for interconnecting distant sub-registers of parallel parts in a scalable, solid-state quantum computer [314]. The nearest-neighbour XY model has been studied extensively for this purpose [15]. In Sec. 4.1.2, we have illustrated how such a model could be implemented with a chain of N implanted, 'dark' nitrogen impurities 'wiring up' two distant, end NV^- centres [see Fig. 7.1], by applying suitable *global* fields only. This connection can work at room temperature [15], and is valuable since individual addressability of the NV^- centre qubits demands large separations, when the direct dipolar coupling becomes too weak [see Sec. 4.1.2].

An important question is how well the quantum state transfer processes perform in the presence of realistic errors and imperfections. Since this is based on free Hamiltonian time evolution, one would expect that timing precision and low levels of coupling disorder (due to defect implantation imprecision) are crucial ingredients

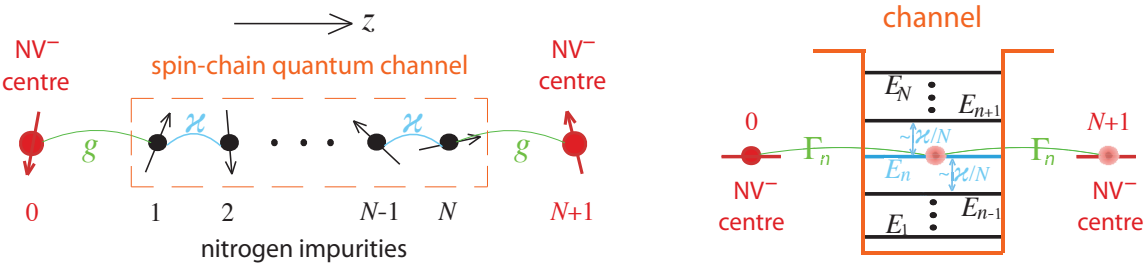


Figure 7.1: (a) Two distant NV$^-$ centres are coupled through a spin chain consisting of N nitrogen impurities; all spins are assumed to interact through nearest-neighbour dipole-dipole couplings. The intra-chain and qubit-chain coupling strengths κ and g, respectively, are determined by the geometrical arrangement of the defects, and the latter can be tuned through the NV$^-$ centre ground state structure to enable high fidelity state transfer for $g \ll \kappa/\sqrt{N}$ [15]. (b) Illustration of the equivalent fermionic tunnelling picture: The channel possesses N energy levels with spacings $|E_n - E_{n\pm1}| \sim \kappa/N$. When tuned into resonance with a channel level E_n, an NV$^-$ spin excitation tunnels through the channel and emerges on the opposite NV$^-$ centre after a time $\tau_n = \pi/(\sqrt{2}\Gamma_n)$, where Γ_n is the effective tunnelling rate. Off-resonant coupling to other levels is negligible provided that $\Gamma_n \ll |E_n - E_{n\pm1}|$ which is equivalent to $g \ll \kappa/\sqrt{N}$ (see text).

for achieving a high fidelity [405]. However, for the regime $g \ll \kappa/\sqrt{N}$ [see Eq. 4.34], the quantum state transfer between the NV$^-$ centre spin qubits through the spin-chain channel has been found to be surprisingly robust against disorder in the inter-chain coupling κ [17]. From our own calculations, we found this is also the case in the strong coupling regime $g \approx \kappa$ [see Fig. 7.8]. The simulations in this chapter also suggest that timing imprecision is not a practical issue, since we will show the distribution of high fidelity quantum state transfer is broadly peaked in time.

The dominant error then arises due to the inevitable environmental decoherence of the spins in the channel. As shown in Sec. 4.1.2, the couplings κ, g are reduced from the usual dipolar interaction strength by 1/2 at the same spacing to implement the XY model, and moreover, a T_2 (T_1) process acting on the physical spin corresponds to a spin-flip (phase-flip) error in the computation basis [for Eq. 4.34 due to the rotation $(x, y, z) \to (z, -y, x)$]. Both have critical implications for the decoherence of the spin-chain channel. Focusing on such quantum noise, we shall argue

that this is indeed the limiting factor, and that current diamond-based architectures will fall far short of the fidelities required to meet quantum error-correction thresholds [see Sec. 2.3.2]. Fortunately, the spin-chain channel is still able to function in the more modest role as a mediator of noisy entanglement supporting distributed QIP, provided that we use subsequent purification. Furthermore, we show that re-purposing the chain this way can remove the restriction to nearest-neighbour interactions, so eliminating the need for complicated dynamical decoupling sequences.

7.2 Practicality for fault tolerance

Let us first follow Ref. [15] to analyse the ideal case with $g \ll \kappa$, starting from the transformed effective system Hamiltonian [Eq. 4.35] $H_{\text{eff}} = H_0 + H'$, where

$$H_0 = \sum_{i=1}^{N-1} \kappa \; a_i^\dagger a_{i+1} + \text{H.c.}, \qquad H' = \sum_{j=0,N} g \; a_j^\dagger a_{j+1} + \text{H.c.}, \tag{7.1}$$

with $a_i^\dagger$ (a_i) being the fermionic creation (annihilation) operators acting on site i. This can be treated perturbatively [15], and by applying [386, 406, 407]

$$f_n^\dagger = \frac{1}{\sqrt{(N+1)/2}} \sum_{j=1}^{N} \sin \frac{jn\pi}{N+1} \; a_j^\dagger, \qquad f_n = \frac{1}{\sqrt{(N+1)/2}} \sum_{j=1}^{N} \sin \frac{jn\pi}{N+1} \; a_j, \tag{7.2}$$

we can diagonalize the unperturbed part in Eq. 7.1 to yield

$$\tilde{H}_0 = \sum_{n=1}^{N} 2\kappa \cos \frac{n\pi}{N+1} \; f_n^\dagger f_n. \tag{7.3}$$

Similarly, Eq. 7.2 transforms the perturbation in Eq. 7.1 to

$$\tilde{H}' = \sum_{n=1}^{N} \Gamma_n \left(a_0^\dagger f_n + (-1)^{n-1} a_{N+1}^\dagger f_n + \text{H.c.} \right), \tag{7.4}$$

where $\Gamma_n = g \sin \frac{n\pi}{N+1} / \sqrt{(N+1)/2}$. The channel can thus be described by $\tilde{H}_0$, possessing N modes with energies $E_n = 2\kappa \cos \frac{n\pi}{N+1}$. One can tune the energy of both NV^- centres to E_n by means of applying an appropriate detuning to $S_z^{0,N+1}$ in the rotated basis. This couples the NV^- centres resonantly to the channel mode n with a tunnelling rate Γ_n [see Fig. 7.1(b)].

Based on pure Hamiltonian evolution, the first full swap of the *two* end fermions occurs after a time

$$t_n = \frac{\pi}{\sqrt{2}\Gamma_n} = \frac{\pi\sqrt{N+1}}{2g \sin \frac{n\pi}{N+1}} \quad (\sim N \quad \text{for} \quad g \ll \kappa/\sqrt{N}). \tag{7.5}$$

The final 'swapped' state acquires a controlled phase $[i^{N+1}(-1)^{\#\text{fermions}-1}]$ depending on the chain length N and the total number of fermions in the system [15, 408]. Since for $g \ll \kappa/\sqrt{N}$ off-resonant coupling to other channel modes is negligible, the phase arises from the single mode and, while generally unknown at finite temperature, is well-defined; it can then be corrected by employing a two-round protocol [15, 16, 409]. Based on this protocol, quantum state transfer with single-mode coupling is *independent* of the initial chain state. Eq. 7.5 implies that the transfer time scales *linearly* with the separation between the end qubits, which provides a cubic speed-up as compared to the direct dipole-dipole coupling ($\sim r^{-3}$ [see Sec. 4.1.2]). Below, we describe the necessity and the implementation of this two-round scheme.

7.2.1 Two-round protocol

With the standard one-spin encoding, the acquired phase for the transferred state depends on the initial chain state, e.g., when $N = 3$,

$$\begin{aligned} |+\rangle_a |000\rangle |0\rangle_b &\longmapsto_\tau |0\rangle_a |000\rangle |+\rangle_b , \\ |+\rangle_a |010\rangle |0\rangle_b &\longmapsto_\tau |0\rangle_a |010\rangle |-\rangle_b , \end{aligned} \tag{7.6}$$

where the transfer completes after time τ for the end qubits a and b. If we start from the initial state $|+\rangle_a \left(|0\rangle |+\rangle |0\rangle \right) |0\rangle_b$, the spin b after the transfer will be entangled with the chain spins, and we obtain the reduced density matrices $|0\rangle_a \langle 0|$ and $\left(|0\rangle_b \langle 0| + |1\rangle_b \langle 1| \right)/2$ at τ for the spins a and b, respectively [combine both parts of Eq. 7.6]. The coherences are *lost* in this case. More generally, at room temperature the thermal state of the nitrogen impurities is mixed, and in a similar fashion the coherences are not preserved during the quantum state transfer processes.

This problem can, however, be overcome by utilizing two spins to encode each end qubit and using the channel twice. There are two quantum state transfer rounds, with the first between a and b and the other between a' and b'. We thus have

$$\begin{aligned}
&|\uparrow\uparrow\rangle_{aa'} |\uparrow\uparrow\uparrow\rangle |\uparrow\uparrow\rangle_{bb'} \longrightarrow_{2\tau} |\uparrow\uparrow\rangle_{aa'} |\uparrow\uparrow\uparrow\rangle |\uparrow\uparrow\rangle_{bb'} \\
&|\downarrow\downarrow\rangle_{aa'} |\uparrow\uparrow\uparrow\rangle |\uparrow\uparrow\rangle_{bb'} \longrightarrow_{2\tau} |\uparrow\uparrow\rangle_{aa'} |\uparrow\uparrow\uparrow\rangle |\downarrow\downarrow\rangle_{bb'} \\
&|\uparrow\uparrow\rangle_{aa'} |\uparrow\downarrow\uparrow\rangle |\uparrow\uparrow\rangle_{bb'} \longrightarrow_{2\tau} |\uparrow\uparrow\rangle_{aa'} |\uparrow\downarrow\uparrow\rangle |\uparrow\uparrow\rangle_{bb'} \\
&|\downarrow\downarrow\rangle_{aa'} |\uparrow\downarrow\uparrow\rangle |\uparrow\uparrow\rangle_{bb'} \longrightarrow_{\tau} -|\uparrow\downarrow\rangle_{aa'} |\uparrow\downarrow\uparrow\rangle |\downarrow\uparrow\rangle_{bb'} \longrightarrow_{\tau} (-1)^2 |\uparrow\uparrow\rangle_{aa'} |\uparrow\uparrow\uparrow\rangle |\downarrow\downarrow\rangle_{bb'},
\end{aligned} \tag{7.7}$$

and hence the coherences are preserved, e.g.,

$$\left(\frac{|\uparrow\uparrow\rangle + |\downarrow\downarrow\rangle}{\sqrt{2}} \right)_{aa'} \left(|\uparrow\rangle |+\rangle |\uparrow\rangle \right) |\uparrow\uparrow\rangle_{bb'} \longrightarrow_{2\tau} |\uparrow\uparrow\rangle_{aa'} \left(|\uparrow\rangle |+\rangle |\uparrow\rangle \right) \left(\frac{|\uparrow\uparrow\rangle + |\downarrow\downarrow\rangle}{\sqrt{2}} \right)_{bb'}. \tag{7.8}$$

To implement this protocol in practice, we utilize both the electronic spin qubit and the nuclear spin for each NV^- centre. The nuclear memory spin in NV^- centre a stores the state $|\phi_a\rangle = \alpha_a |0\rangle_{a'} + \beta_a |1\rangle_{a'}$, and similarly for centre b. (i) For each NV^- centre, we first initialize the processing electronic spin qubit to $|0\rangle_{a(b)}$, and then apply a C_{NOT} gate through the hyperfine coupling [16, 285, 286] to obtain state $|\Phi_a\rangle = \alpha_a |0\rangle_a |0\rangle_{a'} + \beta_a |1\rangle_a |1\rangle_{a'}$ for centre a, and similarly for centre b. (ii) The next step is to apply the standard channel twice, with the first between a and b

and then between a' and b' [see below]. In this way, the final acquired phase of the system after the transfer time 2τ will be consistent for all initial chain states, with coherences preserved at arbitrary temperature [see Eq. 7.8]. (iii) Finally, another C_{NOT} gate is applied to the electron-nuclear spin pair of each NV^- centre such that the nuclear spin in centre a now stores state $|\phi_b\rangle$ and vice versa [16]. Note that in implementing the second step (ii) in practice, we first allow the evolution in the system Hamiltonian [Eq. 4.35] between the electronic spin qubits a and b. Then, a SWAP gate is applied to the electron-nuclear spin pair of each NV^- centre, after which the quantum state transfer process occurs again through the channel between the two electronic spin qubits (which is now effectively between a' and b').

7.2.2 Meeting the fault-tolerance thresholds

We next consider how well the channel behaves in the presence of decoherence. It is readily seen that the tunnelling rate Γ_n reaches its maximal value for odd N and $n = (N+1)/2$ with $E_n = 0$ [see Eq. 7.4]. In this case, no detuning is required, and the end NV^- qubits resonantly couple to the zero-energy mode of the channel. We adopt this case of odd N as the ideal implementation of the protocol. Since our calculations are not restricted to the single excitation subspace used in Ref. [17], we specifically consider the two cases of $N = 3$ and $N = 5$ resulting in simulations involving 6 and 8 spins (chain plus two registers and one ancilla) as explained further on. We simulate the full system dynamics by numerically integrating the Lindblad master equation [Eq. 2.12] using the Hamiltonian in Eq. 4.34. Unless stated otherwise, we take the inter-spin spacing in the chain to be $r_{\mathrm{N,N}} = 10$ nm ($\kappa = 26$ kHz [see Sec. 4.1.2]) while g remains fully tuneable.

We first simulate the quantum state transfer in the weak coupling regime, $g = \kappa/(10\sqrt{N})$. For simplicity, we consider the chain to be initially polarized, and

assume only one application of the channel. After the complete transfer (at time τ) the acquired phase ± 1 of the target state is corrected to enable a direct comparison with the initial state[1]. To evaluate the fidelity of the transfer process, we use the measure $F^2(\rho,\sigma) = \mathrm{Tr}\left(\sqrt{\sqrt{\rho}\sigma\sqrt{\rho}}\right)^2$, which is directly linked to the fault-tolerance error thresholds [see Sec. 2.3.3].

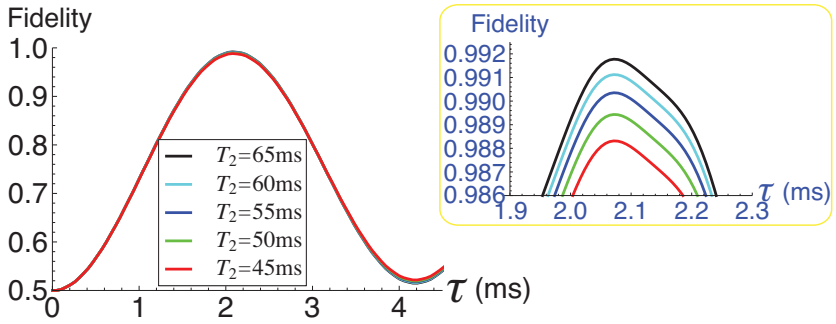


Figure 7.2: Fidelity F^2 of the transferred state ρ with respect to the input $\sigma = |+\rangle\langle+|$, through the $N = 3$ chain as a function of the transfer time τ. The initial state is $|+\rangle_0 |000\rangle |0\rangle_{N+1}$, and we operate in the weak coupling regime $g = \kappa/(10\sqrt{N})$ for $\kappa = 26$ kHz. The nitrogen spins experience independent dephasing at a rate $\gamma = 1/T_2$. Whilst the curves seem to coincide in the main plot, the inset shows a zoomed-in view near the maximum on the scale relevant for fault tolerance.

The nitrogen defect spins are each subject to independent physical T_2 processes, realized as *spin flips* in the computational basis; this is a choice corresponding to the case where the source of the noise is predominantly local to each spin, and reflects the spatial extent of the spin chain where each channel spin will interact with its own environment, e.g. the nuclear spin bath, nearby defect sites and local phonons due to lattice distortion. Fig. 7.2 shows that meeting the benchmark target[2] $F^2 \geq 99\%$ [see Sec. 2.3.2] requires unrealistically long coherence times of the defect spins. More specifically, the shortest non-trivial $N = 3$ chain achieves a sufficiently high fidelity

[1]The fidelity under the two-round protocol (which automatically corrects the acquired phase) will be further reduced from what we have shown in Fig. 7.2, since it will take at least double the one-round transfer time τ [see Sec. 7.2.1] and hence shall be more susceptible to decoherence.
[2]Note that for qubits embedded in diamond and linked by spin chains, the most relevant thresholds are those for architectures where qubits are arranged on a lattice-like structure with each qubit being 'wired' to *only* a few others.

only for $T_2 \geq 54$ ms, whereas this number increases to $T_2 \geq 88$ ms for $N = 5$.

As shown earlier, in the weak coupling regime NV^- centre excitations tunnel through the (single) zero-energy mode of the chain, and off-resonant coupling to other modes is negligible. This enables high-fidelity quantum state transfer for long enough coherence times. However, because transfer time $\tau \sim 1/g$ [see Eq. 7.5] is longer for weaker g, the state transfer is more susceptible to decoherence, and it may thus be advantageous overall to use stronger g at the cost of coupling to several modes and sacrificing some theoretical fidelity. In the following table we list the T_2 times in milliseconds required for achieving an error rate below 1% for different g/κ ratios with $\kappa = 26$ kHz:

g/κ	$0.1/\sqrt{N}$	0.1	0.2	0.3	0.4	0.5	0.6	0.7	0.8	0.9	1
$N = 3$	54	31	77	–	19	–	–	31	6.8	10	–
$N = 5$	88	43	30	25	–	–	–	28	16	–	–

where '–' denotes that the desired fidelity is never achieved for the initial state $|+\rangle_0 |000\rangle |0\rangle_{N+1}$ or $|+\rangle_0 |00000\rangle |0\rangle_{N+1}$. The fluctuating behavior seen in this table is consistent with the results reported in Ref. [15]. Thus for the studied chains, fault-tolerant QC demands coherence times of several milliseconds for the $N = 3$ chain and a few tens of milliseconds for the more interesting $N = 5$ chain, even when dropping the weak coupling constraint and in the absence of any other imperfections[3]. The requirement under the optimal g/κ ratio is 16 ms for $N = 5$. By contrast, the longest measured T_2 time of the NV^- centre is an order of magnitude[4] below this number at 1.8 ms [240]. Reported coherence times of the nitrogen impurity are much shorter, e.g. 5.5 μs at room temperature and 80 μs at 2.5 K [249]. While this should

[3]Interestingly, the required T_1 time, causing phase flips in the computational basis, may be much shorter (see Ref. [17]).

[4]Thus, our conclusion is not limited to the specific target of 1%, which is a conservative estimate for the error rate threshold (with the current best up to $1.1-1.4\%$ [98]) as a requirement for real-world QIP [see Sec. 2.3.2]. Note that this target is for one round, and in practice a two-round protocol (which is more susceptible to decoherence) is required at room temperature [see Sec. 7.2.1].

be improvable, the nitrogen impurity is unlikely to substantially surpass the NV^- centre, since the coherence time of both types of spin is ultimately limited by the same physical processes: additional electronic defect spins, the nuclear spin bath, and the coupling to local phonons arising from a lattice distortion around the impurity sites [88]. Experimental evidence for the NV^- and N spin T_2 being limited by the same spin bath has been reported in Ref. [249]. Optimal control strategies can mitigate the loss of coherence due to a small set of interacting quantum systems, e.g. small environments of up to 6 additional spins were addressed by Ref. [410]. However, as the complexity and size of the environment increase, these techniques become more difficult to implement and the coherence time will necessarily begin to decrease [410]. Optimal control can thus help to combat one source of decoherence but will not be able to overcome other unavoidable (Markovian) decoherence channels supported by the relatively large diamond crystal required for the envisaged architecture. In reality, chains longer than $N = 5$ will be desirable to properly separate the NV^- centres. We therefore conclude that using quantum state transfer as a fault-tolerant two-qubit operation may well be an infeasible target for foreseeable diamond technology.

7.3 Quantum to classical channel transition

Nonetheless, the suggested spin-chain quantum bus may still be able to support the distribution of entanglement, opening the possibility of employing distillation protocols to create high-fidelity entanglement over several runs [70, 71, 77]. Recent studies show that highly imperfect inter-site links can be tolerated given that one has three or four qubits at each local site [411, 412]. The key enabling property of the channel is then simply that it should be 'quantum' in contrast to a 'classical' channel, i.e. a channel that is capable of transmitting a finite amount of entanglement with

each run. Identifying the transition from quantum to classical channel with respect to realistic decoherence processes is then our next goal. To address this question we attempt to transfer one half of a Bell state through the channel. More specifically, the *near* ($i = 0$) NV^- centre starts off in a maximally entangled singlet state with an additional ancilla spin, $|\Psi^-\rangle = (|0\rangle_a |1\rangle_0 - |1\rangle_a |0\rangle_0)/\sqrt{2}$, and our observable is the entanglement of formation E_F [see Sec. 2.2] between this ancilla and the *remote* NV^- centre at position $N + 1$ after the transfer[5].

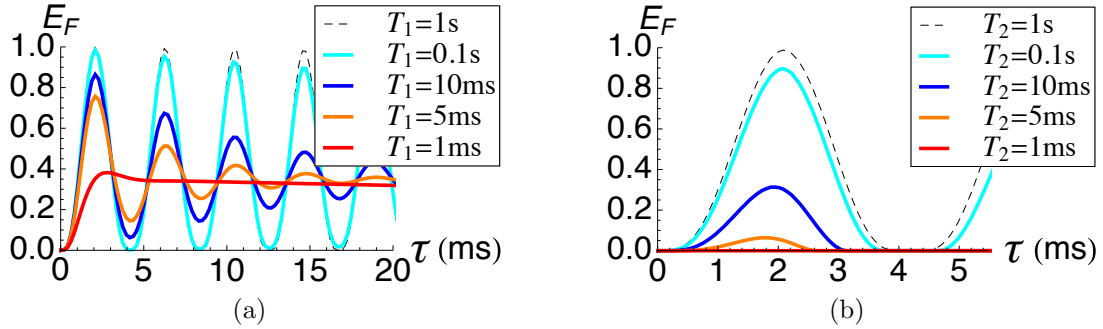
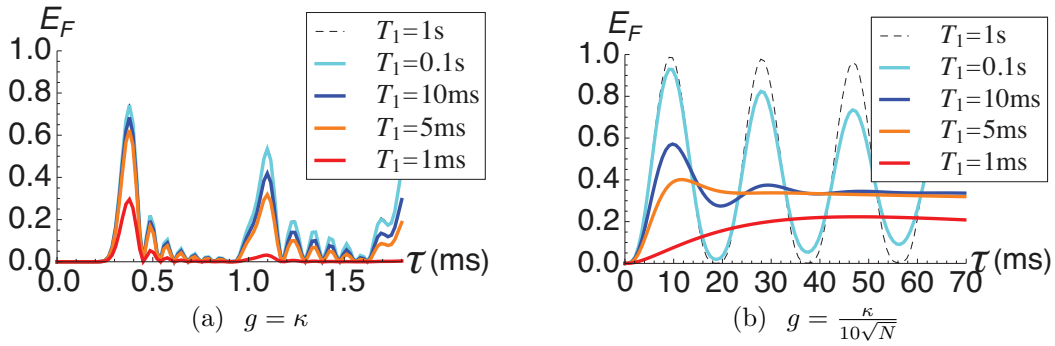


Figure 7.3: Entanglement of formation E_F between the ancilla and the remote NV^- centre qubit as a function of the transfer time τ under an independent (a) spin-flip and (b) phase-flip error model for the nitrogen spins ($N = 3$). The errors are applied as Lindblad operators [Eq. 2.12] on each chain spin: (a) $A_i = \sigma_z^i$ with rate $\gamma = 1/T_1$; (b) $A_i = \sigma_x^i$ with rate $\gamma = 1/T_2$. The initial state is $|\Psi^-\rangle_{a0} |000\rangle |0\rangle_{N+1}$, and $g = \kappa/(10\sqrt{N})$ with $\kappa = 26$ kHz.

Let us start with $N = 3$ as the shortest nontrivial odd chain[6]. Fig. 7.3(a) shows that this channel is robust against physical spin-flip (i.e. T_1-type[7]) errors, which act as phase-flip errors in the basis of the system Hamiltonian [Eq. 4.34]. A high degree of transferred entanglement is achievable for $T_1 > 5$ ms, and a finite amount of entanglement survives in the presence of much larger error rates. We have also

[5]The phase acquired during the swap maps the singlet to a Bell equivalent state without degrading the quality of entanglement.
[6]All channels with $N > 1$ possess more than one mode, so perfect quantum state transfer for all values of g is limited to $N = 1$ [384].
[7]We here take the inverse spin-flip error rate as the T_1 time; this is not strictly the same as a T_1 time from energy relaxation.

confirmed that this behaviour is independent of the initial chain state, and that our results are in agreement with Ref. [17]. Considering only T_1 processes and restricting ourselves to the zero and single excitation (computational) subspace[8] significantly reduces the numerical complexity, allowing us study longer chains. Fig. 7.4 illustrates that a sizeable amount entanglement can be transmitted through a $N = 15$ chain for T_1 times as short as a millisecond, both for strong and weak coupling of the NV^- centres to the chain. When the bit-flip rate gets small, $T_1 \gtrsim 0.1$ s, the weak coupling approach possesses a much higher entangling power, despite taking substantially longer. For $T_1 \sim 10$ ms [245], however, both approaches are comparable. Taking into account the increased robustness of the strong coupling case against T_2 processes [see Fig. 7.6 and below] suggests that overall $g \approx \kappa$ is likely the better choice for tackling decoherence.



(a) $g = \kappa$ (b) $g = \frac{\kappa}{10\sqrt{N}}$

Figure 7.4: Entanglement of formation E_F between the ancilla spin and the remote NV^- qubit as a function of the transfer time τ under an independent, physical bit-flip model for nitrogen spins with rate $\gamma = 1/T_1$. The chain length is $N = 15$, and all chain spins are initially in the state $|0\rangle$. Only nearest-neighbour interactions are included.

Fig. 7.5 considers different chain lengths with $g = \kappa$ coupling, showing the optimal transfer duration τ and maximally achievable E_F for each case under an independent bit-flip model with $T_1 = 10$ ms. Unsurprisingly, the performance of the chain is more affected for longer chains, although the reduction is much less drastic

[8] i.e. no more than one spin may be found to be in the $|1\rangle$ while all others are in the $|0\rangle$ state if a measurement were performed.

than for T_2 noise [see below], and a finite amount of entanglement can be transferred even for long chains.

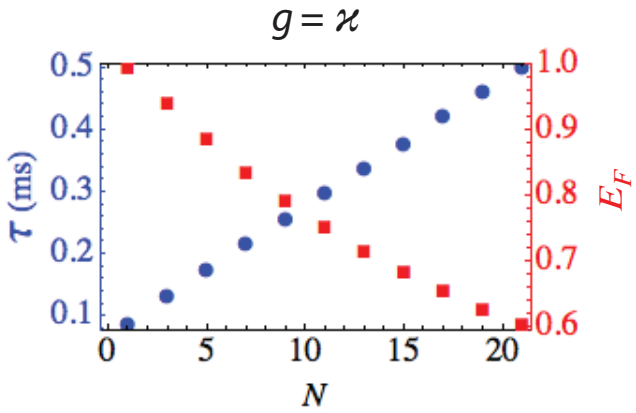


Figure 7.5: Plot of the transfer time τ (the first peaks in plots like Fig. 7.4) and the resulted E_F values between the distant spin and the $(N+1)^{\mathrm{th}}$ NV^- qubit as a function of the channel length N, with fixed intra-chain spacing $r_{\mathrm{N,N}} = 10$ nm ($g = \kappa = 26$ kHz), under an independent phase-flip model (in the rotated basis $x \leftrightarrow z$) on each nitrogen spin with practically relevant rate $\gamma = 1/T_1 = 100$ Hz ($\mathrm{T}_1 = 10$ ms). The channel spins are initially all in the state $|0\rangle$, and interact with their nearest neighbours only.

T_2 processes

On the other hand, dephasing of the physical spins, characterized by their T_2 time, induces spin-flip errors in the computational basis, with a much more damaging effect on the entangling power of the channel [see Fig. 7.3(b)]. For weak coupling between the NV^- centres and the channel, the state transfer becomes classical, i.e. E_F vanishes completely, for $T_2 \leq 3.2$ ms. Applying the same model to the $N = 5$ chain, the transition between a classical and a quantum channel occurs at $T_2 = 7.6$ ms. This *threshold* increases further for larger N due to the transfer time becoming longer [see Eq. 7.5], as effectively more spins are exposed to the noise for longer. Unlike the high fidelity transfer of a particular quantum state, entanglement distribution does not benefit from coupling to only a single channel mode, allowing

us to explore stronger coupling by varying g. Fig. 7.6(a) shows the T_2 threshold which separates the quantum from a classical data bus for chains with $N = 3$ and $N = 5$, and we see that the highest tolerable dephasing rate occurs in the interval $g \in (0.8\kappa, \kappa)$. Expressed as a T_2 time threshold, this gives 0.25 ms (0.55 ms) for

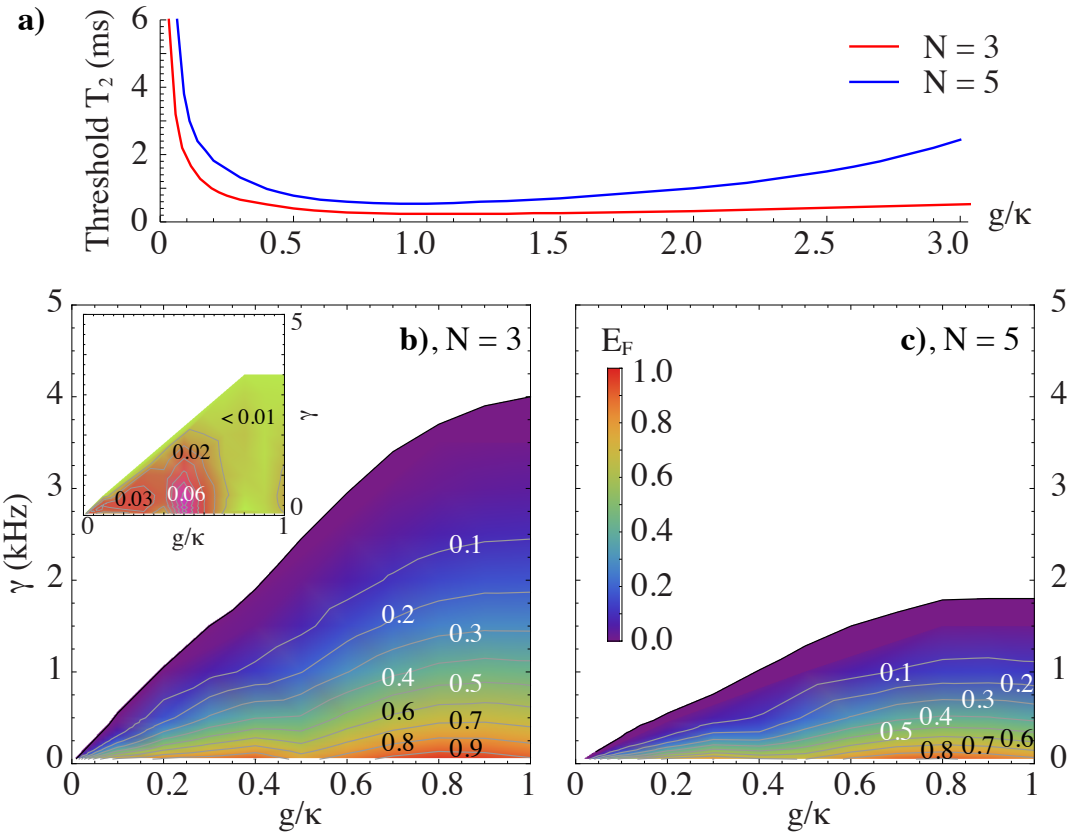


Figure 7.6: (a) T_2 threshold separating classical ($E_F = 0$) and quantum ($E_F > 0$) state transfer. The initial chain states are $|\Psi^-\rangle_{a0}|000\rangle|0\rangle_{N+1}$ and $|\Psi^-\rangle_{a0}|00000\rangle|0\rangle_{N+1}$, respectively, but the threshold for other initial states is similar. (b) and (c) Maximally achievable entanglement of formation E_F between the ancilla spin and the remote NV^- centre spin as a function of g/κ and independent channel spin-flip rate $\gamma = 1/T_2$ for $N = 3$ and $N = 5$. The channel is entirely classical in the white regions. The inset in (b) shows the variation in E_F occurring for the eight different initial states of the channel spins in the $N = 3$ case; in all cases the range of values of E_F is small and always less than 0.07. Random checks for the $N = 5$ case suggest a similar behaviour for longer chains.

the $N = 3$ ($N = 5$) chain with $r_{N,N} = 10$ nm. In Fig. 7.6(b) and 7.6(c), we show the entangling capacity of the $N = 3$ and $N = 5$ channels as a function of g

and the dephasing rate $\gamma = 1/T_2$. We note that high channel entangling power is only realised for a small decoherence rate of the nitrogen spins, even for larger g. Unsurprisingly, the channel is highly inefficient close to the classical threshold.

To 'connect' two NV^- centres separated by a fixed distance of 40 nm, we consider a chain comprising three and five nitrogen spins. In both cases the register spins are assumed to be 10 nm away from the ends of the chain, so that the chain's inter-spin distances are $r_{N,N} = 10$ nm and $r_{N,N} = 5$ nm, respectively. The first case then corresponds to the $N = 3$ chain we have studied so far, but for the $N = 5$ case we obtain a minimal $T_2 \simeq 70$ μs for quantum communication (for $g \approx \kappa$) which is significantly shorter than 0.25 ms for the $N = 3$ chain. The benefit of stronger coupling therefore outweighs the drawback of a longer chain for a fixed separation between the register spins by speeding up the transfer process. However, how many impurity spins can be deployed will crucially depend on the achievable implantation precision, since even sub-nanometre imperfections entail significant coupling disorder for closely spaced chains.

Interestingly, the Lindblad master equation [Eq. 2.12] governing the whole system only involves the three parameters g, κ, and γ; and the dynamics of the systems is invariant under a suitable rescaling of the coupling strength, unit of time and noise rate. Therefore, coherence time thresholds can be easily obtained for coupling strengths different from the ones presented in this paper: For example, if one is interested in g and κ that are only half as large, the noise rate simply needs to be halved and the corresponding coherence time doubled. This rescaling then gives rise to the same entangling capacity E_F of the channel, and also correctly captures the quantum to classical transition.

7.4 Beyond nearest-neighbour couplings

So far, we have assumed nearest-neighbour couplings [see Eq. 4.34], which could be realized through dynamical decoupling [16]. In practice, one needs a coupling strength 'high pass filter', which would typically reduce effective coupling strengths and add further complexity to experimental implementations. We now relax this assumption and include all pairwise couplings with a dipole-dipole interaction $1/r^3$ distance dependence, including register to chain spin couplings.

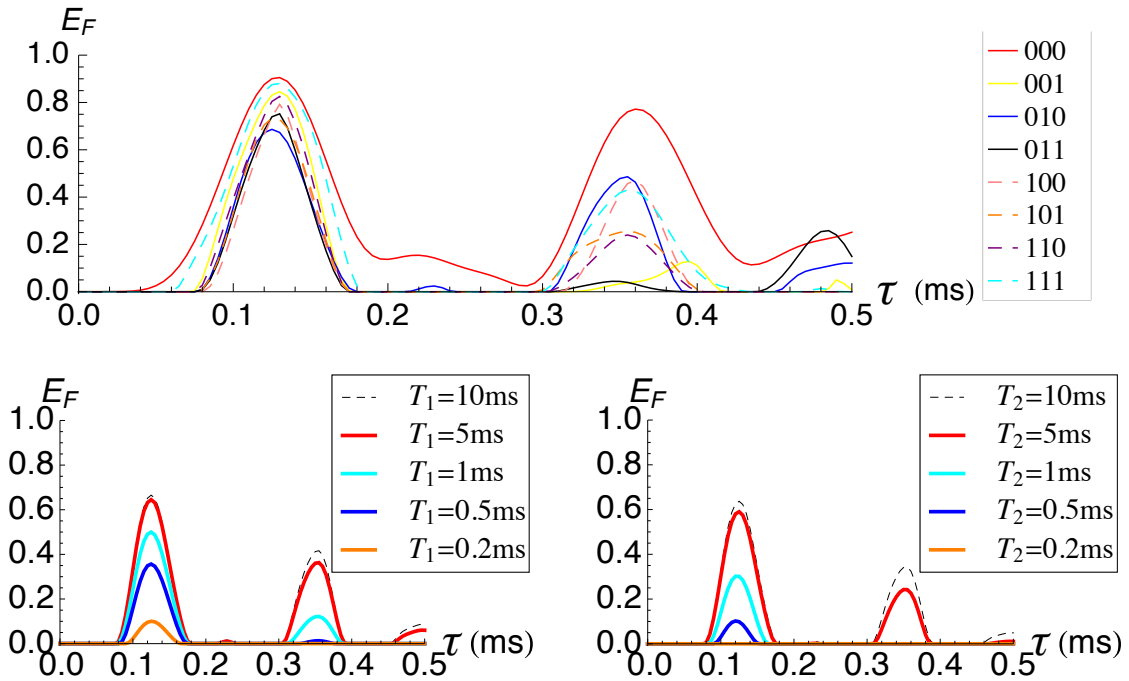


Figure 7.7: Top: E_F between the ancilla spin and the remote NV^- centre as a function of the transfer time τ for all eight initial chain states of the $N = 3$ non-nearest neighbour chain. All spins are assumed equally spaced, with the coupling strength for nearest neighbours being 26 kHz. Bottom: E_F for the initial state $|\Psi^-\rangle_{a0}\,|010\rangle\,|0\rangle_{N+1}$ with decoherence processes of independent phase-flip noise (left) and spin-flip noise (right) in the basis of Hamiltonian in Eq. 4.34 corresponding to physical T_1 and T_2 processes, respectively.

Fig. 7.7 demonstrates that the entanglement transfer for a uniformly spaced spin chain now depends on the initial chain state. However, the first maximum of all initial states coincides and gives rise to a reasonable degree of transferred en-

tanglement. Thus we pick the initial chain state $|\Psi^-\rangle_{a0}|010\rangle|0\rangle_{N+1}$ as an example that is indicative of the performance to be expected. Interestingly, T_1 and T_2 type processes degrade the E_F with much more similar severity compared to the nearest-neighbour only coupling case[9]. Nevertheless, there still exists a threshold in the T_2 coherence time, and to ensure quantum communication for an arbitrary initial state, we require $T_2 \geq 0.28$ ms, which is only slightly longer than for the nearest-neighbour chain. For the case of the $N = 5$ chain (not shown), we have determined the transition threshold to be $T_2 \geq 0.67$ ms, which again only represents a modest increase. Taking into account the complexity and expected reduction in effective coupling strengths from dynamical decoupling sequences, it may thus be more practical to drop the restriction of only nearest-neighbour interactions. As we show below, the state transfer still remains similarly robust to small coupling-strength disorder.

7.5 Coupling disorder

In this section, we simulate disorder in the intra-chain coupling strength κ, as would arise from imprecisions when implanting the nitrogen impurities. For numerical convenience, we once more restrict our calculations to the single excitation subspace. We assume the spacings between the neighbouring spins obey a Gaussian distribution around the mean value $r_{\mathrm{N,N}} = 10$ nm ($\kappa = 26$ kHz). Our results are averages over a hundred independent runs for each data point.

Fig. 7.8 shows that even a sizeable 15% spread in the κ distribution does not have a catastrophic impact on the entangling capacity of the chains. In fact, the reduction of achievable E_F is rather similar to that obtained from a T_1 time of around 10 ms. While the difference is not huge, the nearest-neighbour coupled chain proves to be consistently more robust.

[9]Restoring nearest-neighbour coupling only for the register spins largely reintroduces the asymmetric behaviour with respect to the two different types of noise.

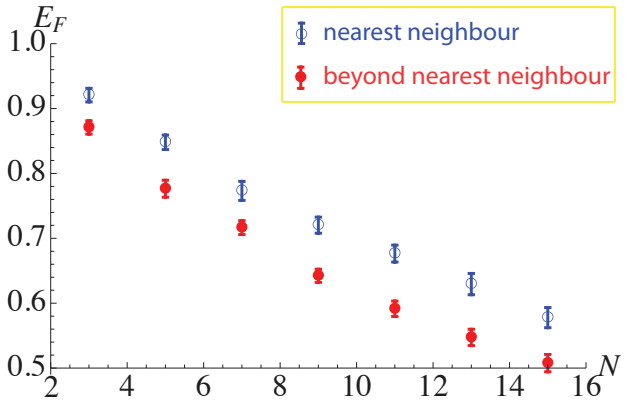


Figure 7.8: Maximally achievable E_F between the ancilla and the remote NV^- qubit for different chain lengths N. The intra-chain spacings are assumed to follow a Gaussian distribution with mean $r_{N,N} = 10$ nm with a standard deviation corresponding to 5% disorder ($\sim$ 15% disorder in the intra-chain coupling strength κ). The channel spins are initialized in the state $|0\rangle$, and each data point is the result of an average of 100 independent runs. The error bars indicate a 95% confidence interval. The 'nearest-neighour' case uses the more practically relevant strong coupling regime $g = \kappa_{mean}$. For 'beyond nearest-neighbour coupling', all pairwise spin couplings are included in accordance with the dipolar $1/r^3$ distance dependence.

However, for the short chains we have considered, a small amount of disorder in κ is unlikely to be the limiting factor preventing entanglement distribution. Ultimately, we expect the major challenge for this protocol is attaining sufficiently long T_2 times to overcome the limitations discussed in Sec. 7.3.

7.6 Conclusion

In conclusion, by employing numerical simulations we have studied the impact of inevitable decoherence processes on the entanglement capacity of a spin-chain bus that is realized by dipole-dipole coupling of crystal defects. Limiting our discussion to chains of length $N = 3$ and $N = 5$ as likely candidates for a first experimental demonstration (and also for numerical tractability) has allowed us to obtain insight into important characteristics of such a protocol in the presence of realistic noise. Our conclusions will be equally relevant for longer chains, which are known to be even

more susceptible to decoherence [413, 414, 415, 416]. We have shown that directly meeting quantum error correction thresholds remains unfeasible even if all spins possessed the exceptional coherence time of NV^- centres. In contrast, the distribution of a finite amount of entanglement appears realistic with current systems, offering the possibility of applying distillation protocols to boost the transmitted entanglement with additional local operations and classical communication [70, 71, 77, 417].

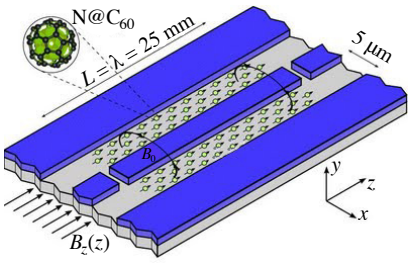
Though the enhancement (cubic speed-up) provided by the spin-chain quantum bus is not sufficient for the purpose of fault-tolerant QC, recent studies suggest that an ensemble of nitrogen impurities may further improve the quantum state transfer processes [18]. Having studied the different types of spin chains in the last three chapters, next we shall proceed to consider a spin-ensemble quantum processor.

Chapter 8

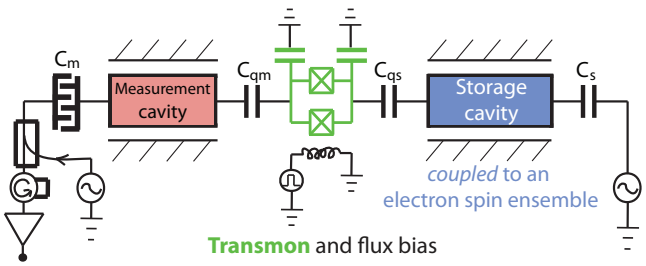
Measurement-based spin-ensemble quantum information processor

8.1 Motivation, set-up and model

In Sec. 4.4, we have shown that an ensemble of electron spins, coupled to an on-chip stripline cavity [see Fig. 8.1(a)], is capable of storing multiple excitations from sin-



(a) Spin ensemble memory.



(b) Illustration of integrated device for ensemble QIP.

Figure 8.1: (a) Physical setup of an electron spin ensemble (memory), doped on substrate, coupled to an on-chip stripline (storage) cavity (picture courtesy of Dr. Janus H. Wesenberg [23] Copyright © American Physical Society). A bias field is applied to bring the spin *Larmor* precession in resonance with the cavity, and a switchable linear magnetic gradient for appropriate time lengths (gradient pulses) is required to access the different collective modes of the ensemble. (b) Circuit diagram of the integrated device as an ensemble quantum informtion processor (see details of physical implementation on a chip in Ref. [24]). The number of photons in storage cavity affects the transmon state, which is indicated from microwave probing the measurement cavity.

gle cavity photons by applying appropriate bias field and magnetic gradient pulses. However, promoting the memory system to a full QIP device is non-trivial because the allowed operations in such a system are analogous to those in linear optics, and thus the provision of entangling gates requires non-linearity supplied by other components. One suggestion involves integrating a transmon CPB onto the microwave stripline cavity; moving a memory qubit to the CPB would facilitate universal qubit operations, as well as the read-out procedures [22, 23, 418].

However, CPBs are not ideal for representing qubits due to their short coherence times [see Sec. 3.2.5]. Here, we propose a composite system [see Fig. 8.1] where such devices are only used for measurement, but in such a fashion that in addition to simple readout, entangling projections can also be implemented. We envisage the use of a system that is both number resolving [419] and also non-destructive; recent experimental demonstrations of such systems have been accomplished [24, 420]. The realization consists of two cavities coupled via a transmon CPB; measurement of the number of single photons in the storage cavity is achieved via a read-out procedure involving the second cavity [24]. In effect this allows one to ask the question, *are there exactly n photons in the storage cavity*? If we wish to subsequently ask about a different n, we would employ a flux bias to tune the transmon frequency (a nanosecond timescale process). In the ideal case when no errors are present, if the result is NO then any coherent superposition of photon number states other than $|n\rangle$ is preserved in the storage cavity [24], which is coupled to the electron spin ensemble [23]. In contrast to previous proposals, here the CPB no longer performs the role of gate operations on the mode qubits nor to store the qubits. We shall show that, by using *dual-rail* encoding, a universal set of quantum gates can be implemented for the logical qubits. Any single qubit rotation can be achieved by applying appropriate magnetic gradient pulses and adjusting the bias field when necessary. Importantly, the two-qubit parity projection that we shall presently discuss can enable general

QIP through, for example, the creation of graph states [see Sec. 2.2.2].

As shown in Sec. 4.4, the superradiant state $|\psi_1(0)\rangle$ [Eq. 4.39] corresponds to the $k = 0$ mode of the spin ensemble, and each time a k_i-pulse is applied it maps the $k = 0$ mode to the i^{th} mode. Therefore, to access a particular mode i a $-k_i$-pulse is applied to map it to the $k = 0$ mode, which then interacts with the cavity strongly upon resonance. A k_i-pulse is then applied to map the mode back. To stop the the mode-cavity coupling, one can simply tune the bias field such that the cavity is out of resonance with the ensemble spins [23]. Therefore, the Hamiltonian coupling a particular mode i with the cavity for a single excitation with energy ϵ is

$$H_i^{(1)} = \epsilon\ (m_i^\dagger m_i + c^\dagger c) + J(m_i^\dagger c + m_i c^\dagger) = \begin{pmatrix} \epsilon & J \\ J & \epsilon \end{pmatrix} \tag{8.1}$$

in the basis of $|1_{\text{M}}0_{\text{C}}\rangle$, $|0_{\text{M}}1_{\text{C}}\rangle$. Here, $m_i^\dagger$ ($c^\dagger$) and m_i (c) are the corresponding mode excitation (cavity photon) creation and annihilation operators, and $J = \sqrt{N}\bar{g}$ is the effective coupling strength [see Sec. 4.4]. This effective coupling J is orders of magnitude larger than the decay rates of collective spin excitations and the cavity decay rate [23]. The corresponding time evolution operator for a single excitation is then

$$S^{(1)}(t) = e^{-i\epsilon t} \begin{pmatrix} \cos Jt & -i\sin Jt \\ -i\sin Jt & \cos Jt \end{pmatrix}. \tag{8.2}$$

After a time $t = \tau := \frac{\pi}{2J} \simeq 40$ ns, a full SWAP of one single excitation has occurred between the cavity and mode i, whereas for $t \leq \tau$ only a partial SWAP operation has taken place.

When two or more excitations n exist between a particular mode i interacting with the cavity, the coupling strength and thus the time required for an exchange are adjusted by a factor of $\sqrt{n}$. The cavity-mode Hamiltonian for two excitations is

then

$$H_i^{(2)} = \begin{pmatrix} 2\epsilon & \sqrt{2}J & 0 \\ \sqrt{2}J & 2\epsilon & \sqrt{2}J \\ 0 & \sqrt{2}J & 2\epsilon \end{pmatrix} \tag{8.3}$$

in the basis of $|2_{\mathrm{M}}0_{\mathrm{C}}\rangle$, $|1_{\mathrm{M}}1_{\mathrm{C}}\rangle$, $|0_{\mathrm{M}}2_{\mathrm{C}}\rangle$, with the corresponding time evolution operator

$$S^{(2)}(t) = e^{-2i\epsilon t} \begin{pmatrix} \cos^2 Jt & -\frac{i}{\sqrt{2}}\sin 2Jt & -\sin^2 Jt \\ -\frac{i}{\sqrt{2}}\sin 2Jt & \cos 2Jt & -\frac{i}{\sqrt{2}}\sin 2Jt \\ -\sin^2 Jt & -\frac{i}{\sqrt{2}}\sin 2Jt & \cos^2 Jt \end{pmatrix}. \tag{8.4}$$

Note that a full SWAP of two excitations still occurs after the same time $t = \tau$ as for the single excitation case. For simplicity, from this point on whenever we say a particular mode i is interacting with the cavity for some time t, a $-(+)k_i$-pulse is by default applied right before (after) the interaction which has a duration of t with the bias field necessary for resonance. Note that the time for the necessary gradient pulses could be shortened by increasing the gradient strength [23].

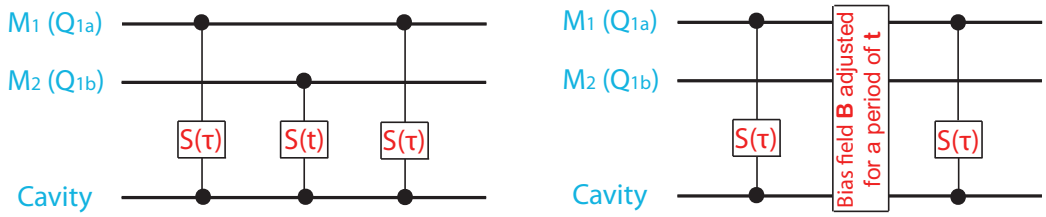
8.2 Single qubit operations in dual-rail encoding

We encode the qubits in the dual-rail representation, where each logical qubit occupies two collective modes of the spin ensemble [see Fig. 8.2]. A logical qubit $|Q_1\rangle_{\mathrm{L}} = \alpha\,|0\rangle_{\mathrm{L}} + \beta\,|1\rangle_{\mathrm{L}}$ corresponds to the physical state of modes $|\mathrm{M}_1\mathrm{M}_2\rangle_{\mathrm{M}} = \alpha\,|10\rangle_{\mathrm{M}} + \beta\,|01\rangle_{\mathrm{M}}$, where the ket notation denotes the number of excitations in the relevant mode for the physical qubits. Adopting a dual-rail encoding of course doubles the resource cost. However, the capacity of the ensemble quantum memory is of the order of $\sqrt{N}$; assuming $N = 10^{11}$, this is therefore not a practical constraint.

An experiment would begin with cooling the spins so that there are a negligible number of excitations in the ensemble, which is then approximately in the ground

state $|\mathbf{0}\rangle$. For each logical qubit we then load the cavity with a single photon, and perform a SWAP gate between the cavity and the appropriate memory mode to represent $|0\rangle_{\mathrm{L}}$. A logical qubit $|Q\rangle_{\mathrm{L}}$ of arbitrary state can then be prepared through an appropriate single qubit rotation on the Bloch sphere.

Any single qubit rotation can be formed from a combination of rotations about two different axes [see Sec. 2.1.2]. In Fig. 8.2 we show how rotations about the x-axis, and the z-axis can be performed in the dual-rail enconding. Both these rotations involve SWAP operations between the memory modes and an initially empty cavity.



(a) X-type rotations: σ_x gate when $t = \tau$ (b) Z rotations: phase gates

Figure 8.2: Single qubit rotations in two independent directions, whose combinations constitute any single qubit operations for the dual-rail encoded qubits. Note that the cavity is assumed to be empty initially.

8.2.1 X rotations

Suppose that our logical qubit is initially in the general state $|Q_1\rangle = \cos\frac{\theta}{2}|0\rangle_{\mathrm{L}} + e^{i\phi}\sin\frac{\theta}{2}|1\rangle_{\mathrm{L}}$. We thus start with the initial state $\left(\cos\frac{\theta}{2}|10\rangle_{\mathrm{M}} + e^{i\phi}\sin\frac{\theta}{2}|01\rangle_{\mathrm{M}}\right)|0\rangle_{\mathrm{C}}$, where C denotes the cavity state. After the first full SWAP, the physical state becomes

$$\cos\frac{\theta}{2}|00\rangle_{\mathrm{M}}|1\rangle_{\mathrm{C}} + e^{i\phi}\sin\frac{\theta}{2}|01\rangle_{\mathrm{M}}|0\rangle_{\mathrm{C}}\,. \tag{8.5}$$

To implement a rotation around the x-axis on the Bloch sphere, a partial SWAP is now performed between the cavity and mode 2, resulting in the following state:

$$\begin{aligned} & \cos\frac{\theta}{2}\left(\cos\theta'|00\rangle_{\mathrm{M}}|1\rangle_{\mathrm{C}} - i\sin\theta'|01\rangle_{\mathrm{M}}|0\rangle_{\mathrm{C}}\right) \\ + \quad & e^{i\phi}\sin\frac{\theta}{2}\left(\cos\theta'|01\rangle_{\mathrm{M}}|0\rangle_{\mathrm{C}} - i\sin\theta'|00\rangle_{\mathrm{M}}|1\rangle_{\mathrm{C}}\right) \end{aligned} \tag{8.6}$$

or equivalently,

$$a\,|00\rangle_{\rm M}\,|1\rangle_{\rm C} + b\,|01\rangle_{\rm M}\,|0\rangle_{\rm C} \tag{8.7}$$

where

$$a = \cos\frac{\theta}{2}\cos\theta' - ie^{i\phi}\sin\frac{\theta}{2}\sin\theta', \qquad b = -i\cos\frac{\theta}{2}\sin\theta' + e^{i\phi}\sin\frac{\theta}{2}\cos\theta',$$

and $\theta' = Jt$. When the second full SWAP has completed, the empty cavity decouples from the qubit $|Q_1\rangle = a\,|0\rangle_{\rm L} + b\,|1\rangle_{\rm L}$, ignoring a non-detectable global phase. An σ_x gate is implemented in this way [see Fig. 8.2(a)] when $t = \tau$, i.e., when $\theta' = \frac{\pi}{2}$.

8.2.2 Z rotations

To obtain a phase gate [see Fig. 8.2(b)], we begin in the same fashion and obtain the state in Eq. 8.5. However, we now exploit the fact that applying a different magnetic bias field does not affect the phase evolution of the component $\cos\frac{\theta}{2}\,|00\rangle_{\rm M}\,|1\rangle_{\rm C}$ (which still acquires phase at the same rate ϵ), since the cavity photon energy is not affected by the magnetic field. On the other hand, a change δB in the bias field shifts the spin ensemble mode energy to $\epsilon+\delta(\delta B)$, which results in a phase evolution of $e^{-i(\epsilon+\delta)t}$ for the part $e^{i\phi}\sin\frac{\theta}{2}\,|01\rangle_{\rm M}\,|0\rangle_{\rm C}$ during the time t. Ignoring the undetectable global phase $e^{-i\epsilon t}$, after the second full SWAP the empty cavity again decouples from the qubit $|Q_1\rangle = \cos\frac{\theta}{2}\,|0\rangle_{\rm L} + e^{i(\phi-\delta t)}\sin\frac{\theta}{2}\,|1\rangle_{\rm L}$. The relative phase accumulated $e^{-i\delta t}$ manifests itself as a phase gate for the logical qubit, where the phase can be controlled by the time t and the bias shift δB.

8.3 Measurement-assisted entanglement

Having established how to perform single qubit operations, we now require an entangling operation in order to produce a universal set of qubit gates [7]. In this section,

we show how certain types of measurement can facilitate such an entangling scheme [see Fig. 8.3]. In essence, we perform a measurement on the *parity* of two chosen

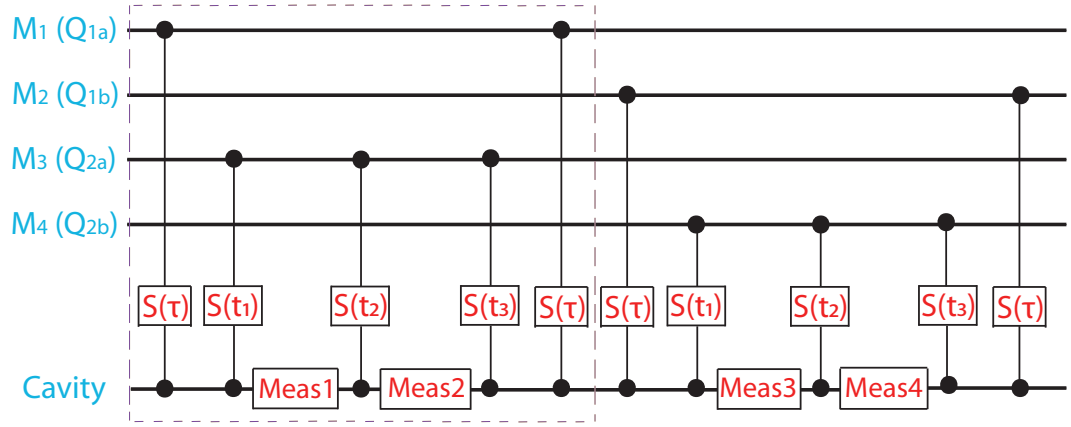


Figure 8.3: The entangling operation for the dual-rail encoded qubits, implemented by a parity projection. A 'building block' consists of all the operations inside the dashed box, and the parity projection requires two of such blocks. Each building block rules out the possibility of two excitations in the relevant two modes while preserving coherence between states with different occupation numbers. This requires two NO results for each block to the question whether there are 2 photons in the cavity or not. The initial cavity state is assumed to be empty, and the interaction times are chosen as follows: $t_1 = \frac{\pi}{4J} \simeq 20$ ns, $t_2 = \frac{\pi}{2J} \simeq 40$ ns and $t_3 = 2\tau - t_1 - t_2 = \frac{\pi}{4J} \simeq 20$ ns.

logical qubits. If the parity is found to be odd $\left(|01\rangle_{\mathrm{L}} \text{ or } |10\rangle_{\mathrm{L}}\right)$, then we proceed with the protocol. Conversely, if the parity is found to be even $\left(|00\rangle_{\mathrm{L}} \text{ or } |11\rangle_{\mathrm{L}}\right)$, then we reject the state. This is therefore a probabilistic entangling operation, however, it is well established that such operations suffice for efficient universal quantum computing [88]. Our approach can be thought of as a filtering process; we detect the state $|00\rangle_{\mathrm{L}}$ and reject it, and then similarly we detect and reject the state $|11\rangle_{\mathrm{L}}$. Any state that passes through this process without rejection must be in the odd parity subspace $\{|01\rangle_{\mathrm{L}}, |10\rangle_{\mathrm{L}}\}$. Our protocol therefore consists of two basic blocks of operations, each ruling out the possibility of having two excitations in the relevant two modes while not destroying the quantum coherence between contributions to the state with different occupation numbers. As before, the cavity is emptied before

the entangling gate operation, and it is tuned out of resonance with the ensemble modes during each measurement procedure.

Let us now consider the first block of operations, concerning modes M_1 and M_3 with the cavity. For each correctly encoded logical qubit, the two dual-rail modes together only contain a single excitation. However, for the M_3 mode-cavity interaction there is still the possibility of exchange of two excitations, originally from different qubits. This two-excitation exchange is governed by the Hamiltonian $H^{(2)}$ in Eq. 8.3, which has three distinct eigenvalues 2ϵ, $2(\epsilon - J)$ and $2(\epsilon + J)$, with corresponding eigenvectors

$$\begin{aligned} |v_0\rangle_{\rm MC} &= \frac{1}{\sqrt{2}}\big(\,|20\rangle - |02\rangle\,\big) \\ |v_-\rangle_{\rm MC} &= \frac{1}{2}\big(\,|20\rangle - \sqrt{2}\,|11\rangle + |02\rangle\,\big) \\ |v_+\rangle_{\rm MC} &= \frac{1}{2}\big(\,|20\rangle + \sqrt{2}\,|11\rangle + |02\rangle\,\big), \end{aligned} \tag{8.8}$$

respectively. Therefore, if the M_3 mode-cavity state after the first full SWAP is $|11\rangle = \frac{1}{\sqrt{2}}(|v_+\rangle - |v_-\rangle)$, it evolves to $\frac{1}{\sqrt{2}}(|v_+\rangle + |v_-\rangle) = \frac{1}{\sqrt{2}}(|20\rangle + |02\rangle)$ for an interaction time $t_1 = \frac{\pi}{4J} \simeq 20$ ns. Performing a measurement designed to detect whether there are 2 photons in the cavity [24] then removes the $|02\rangle$ component if the measurement result is a NO outcome. After a further exchange of $t_2 = \frac{\pi}{2J} \simeq 40$ ns, the part $|20\rangle$ evolves to $|02\rangle$ which can be ruled out by a second measurement if the outcome is NO again. Thus, up to now when successful, we are assured that there will be at most one excitation between the modes M_1 and M_3, after it has been swapped back from the cavity. So far, we have only considered the two-excitation exchange, while there is also the exchange of one excitation. In order for the block to perform an identity operation, i.e., two SWAPs, on the one-excitation exchange subspace, a further interaction between the mode M_3 and cavity is required for a time of $t_3 = 2\tau - t_1 - t_2 = \frac{\pi}{4J} \simeq 20$ ns, followed by a full SWAP between the mode

M_1 and cavity.

Due to symmetry, the second block of operations has the same effect on modes M_2 and M_4, ensuring that there is also at most one excitation in between, if successful. Hence, starting with two correctly encoded qubits $|Q_1Q_2\rangle_L = (\alpha_1 |0\rangle_L + \beta_1 |1\rangle_L) \bigotimes (\alpha_2 |0\rangle_L + \beta_2 |1\rangle_L)$ or physically $|M_1M_2M_3M_4\rangle = \alpha_1\alpha_2 |1010\rangle + \alpha_1\beta_2 |1001\rangle + \beta_1\alpha_2 |0110\rangle + \beta_1\beta_2 |0101\rangle$, successful implementation of the entangling gate leaves us with the mode state $\mathcal{N}(\alpha_1\beta_2 |1001\rangle + \beta_1\alpha_2 |0110\rangle)$ or $\mathcal{N}(\alpha_1\beta_2 |0_{Q_1}1_{Q_2}\rangle_L + \beta_1\alpha_2 |1_{Q_1}0_{Q_2}\rangle_L)$ in the logical basis, where $\mathcal{N}$ is a normalisation constant. This is an odd-parity projection operation, which generates a maximally entangled Bell state when we start with $|+\rangle_{Q_1} |+\rangle_{Q_2}$ as the initial state of the logical qubits. Notably, such parity projections together with single qubit operations are adequate for universal QIP [88].

8.4 Major errors

With the above set of universal quantum gates, our integrated device is capable of performing probabilistic QIP within the electron spin ensemble, in the ideal case when no errors are present. We shall now consider the various error sources, namely, collective excitation decay, imprecise timing in cavity-mode swap, cavity photon leakage, and measurement errors.

As mentioned before, the decay rates of the collective spin excitations and that of cavity photon leakage are orders of magnitude smaller than the collective coupling J [23]. Moreover, errors resulted from imperfect pulse timings are all linear, and timing precision with a nanosecond resolution is feasible [23]. Therefore, these errors shall be treated negligible as compared to measurement errors [24], which shall be evaluated for the entangling gate in this section. We start with the logical qubit

state

$$|+\rangle_{Q_1}|+\rangle_{Q_2} = \frac{1}{2}\big(|1010\rangle + |1001\rangle + |0110\rangle + |0101\rangle\big)_{\mathrm{M_1M_2M_3M_4}} \tag{8.9}$$

with the cavity being $|\mathrm{C}\rangle = |0\rangle$. There are two types of measurement errors to consider, corresponding to different incorrect outcomes to the question whether there are two photons in the cavity or not [24].

8.4.1 Type I measurement error

This type of error occurs when the measurement outcome gives a NO while the cavity is populated with two photons, and this occurs with an independent probability of η_1 for each measurement. It has an effect on the overall fidelity F [Eq. 2.14] of this entangling gate, reducing the degree of entanglement generated in the final state. With the cavity state $|0\rangle_{\mathrm{C}}$ decoupled from the modes at the end of the protocol, the final density state for the modes $|\mathrm{M_1M_2M_3M_4}\rangle$ in this case is

$$\rho = \frac{1}{1+\eta_1}\left(|\Psi^+\rangle\langle\Psi^+| + \frac{\eta_1}{2}(\sigma_1+\sigma_2)\right) \tag{8.10}$$

where

$$\begin{aligned}
|\Psi^+\rangle &= \frac{1}{\sqrt{2}}\Big(|1001\rangle + |0110\rangle\Big) \longrightarrow \frac{1}{\sqrt{2}}(|01\rangle + |10\rangle)_{Q_1Q_2},\\
\sigma_1 &= \frac{1}{2}\left(\frac{(|0020\rangle - |2000\rangle)(\langle 0020| - \langle 2000|)}{2} + |1010\rangle\langle 1010|\right),\\
\sigma_2 &= \frac{1}{2}\left(\frac{(|0002\rangle - |0200\rangle)(\langle 0002| - \langle 0200|)}{2} + |0101\rangle\langle 0101|\right).
\end{aligned} \tag{8.11}$$

Below we outline the evolution of the total mode-cavity state under the entangling operation with type I measurement error η_1, to derive the final state ρ [Eqns. 8.10-8.11]. Since there are two excitations in the whole system, the phase evolution $e^{-2i\epsilon t}$ is global and ignored at all times. The initial total state $|\mathrm{M_1M_2M_3M_4C}\rangle$

of the modes [Eq. 8.9] and the cavity evolves to

$$\frac{1}{2}\Big(-\frac{|00200\rangle+|00002\rangle}{\sqrt{2}}-i\frac{|00011\rangle-i\,|00110\rangle}{\sqrt{2}}+\frac{|01100\rangle-i\,|01001\rangle}{\sqrt{2}}+|01010\rangle\Big) \tag{8.12}$$

after the first full M_1C SWAP followed by the M_3C coupling $S(t_1)$. When the first measurement gives an outcome of NO, we are left with the density state

$$\rho_1=\frac{8}{7+\eta_1}\Big(\frac{7}{8}\,|A_1\rangle\langle A_1|+\frac{1}{8}\eta_1\,|00002\rangle\langle 00002|\Big), \tag{8.13}$$

where

$$|A_1\rangle=\sqrt{\frac{2}{7}}\Big(\frac{-1}{\sqrt{2}}\,|00200\rangle+\frac{-i\,|00011\rangle-|00110\rangle}{\sqrt{2}}+\frac{|01100\rangle-i\,|01001\rangle}{\sqrt{2}}+|01010\rangle\Big),$$

both normalized. Note that here with the set-up in Ref. [24], we have assumed that the measurement apparatus interacts with the cavity-ensemble system regardless of its ability in reporting correct answers. In so doing, even when $\eta_1=1$ where no information is to be learned from the measurement result, the state has still changed, namely, dephased according to Eq. 8.13. The M_3C coupling $S(t_2)$ is a full SWAP for both the exchange of one and two excitations. Conditional on the second measurement giving an answer NO as well, the density state becomes

$$\rho_2=\frac{1}{2(3+\eta_1)}\Big(6\,|A_2\rangle\langle A_2|+\eta_1\,|00002\rangle\langle 00002|+\eta_1\,|00200\rangle\langle 00200|\Big), \tag{8.14}$$

where

$$|A_2\rangle=\frac{1}{\sqrt{6}}\Big((-\,|00110\rangle+i\,|00011\rangle)+(-i\,|01001\rangle-|01100\rangle)+\sqrt{2}\,|01010\rangle\Big),$$

both normalized. The remaining operations in the first block results in the density

state

$$\frac{1}{3+\eta_1}\Big(3\,|A_{f_1}\rangle\,\langle A_{f_1}| + \eta_1\rho_0\Big), \tag{8.15}$$

where

$$|A_{f_1}\rangle = \frac{1}{\sqrt{3}}\Big(\,|10010\rangle - |01100\rangle + |01010\rangle\,\Big),$$

and

$$\rho_0 = \frac{1}{2}\Big(\frac{(|00200\rangle - |20000\rangle)(\langle 00200| - \langle 20000|)}{2} + |10100\rangle\,\langle 10100|\,\Big)$$

which does not evolve further during the rest of this entangling gate operation since the second block of operations never access the modes M_1 and M_3. At this point, the cavity is empty and decoupled from the modes. Similarly due to symmetry, upon the completion of the second block of operations on the modes M_2 and M_4, the cavity state $|0\rangle_{\mathrm{C}}$ is again decoupled from the modes and we have for the modes $\mathrm{M}_1\mathrm{M}_2\mathrm{M}_3\mathrm{M}_4$ the density state as given in Eqns. 8.10-8.11. □

In the ideal case where $\eta_1 = 0$, the resulting state after the entangling operation is the maximally entangled state $|\Psi^+\rangle$ [Eq. 8.11], as expected. For finite η_1 errors, the final mixed state ρ describes that for bipartite *quinits* Q_1 and Q_2, where each quinit is a five-level system. Mapping the different physical states of the dual-rail modes $|10\rangle$, $|01\rangle$, $|20\rangle$, $|02\rangle$ and $|00\rangle$ to the logical quinit levels $|0\rangle$, $|1\rangle$, $|2\rangle$, $|3\rangle$ and $|4\rangle$, respectively for each Q_i, Eq. 8.11 becomes

$$\begin{aligned}
\sigma_1 \;&\longrightarrow\; \frac{1}{2}\Big(\frac{(|42\rangle - |24\rangle)(\langle 42| - \langle 24|)}{2} + |00\rangle\,\langle 00|\,\Big)_{Q_1Q_2}, \\
\sigma_2 \;&\longrightarrow\; \frac{1}{2}\Big(\frac{(|43\rangle - |34\rangle)(\langle 43| - \langle 34|)}{2} + |11\rangle\,\langle 11|\,\Big)_{Q_1Q_2}.
\end{aligned} \tag{8.16}$$

Although also being entangled in the levels $|2\rangle$, $|3\rangle$ and $|4\rangle$, we shall only be interested in the entanglement between the two levels $|0\rangle$ and $|1\rangle$, which span the computational

basis space for conventional QIP tasks. Fig. 8.4(a) plots the fidelity F [Eq. 2.14] of the resulting state ρ [Eq. 8.10] with the ideal state $|\Psi^+\rangle\langle\Psi^+|$ against the error η_1,

$$F(\rho, |\Psi^+\rangle\langle\Psi^+|) = \mathrm{Tr}\left(\sqrt{\sqrt{\rho}\,|\Psi^+\rangle\langle\Psi^+|\,\sqrt{\rho}}\right) = \sqrt{\frac{1}{1+\eta_1}}, \tag{8.17}$$

where $|\Psi^+\rangle$ is embedded in the five-level system by filling the levels that lie outside the computational basis with zero population.

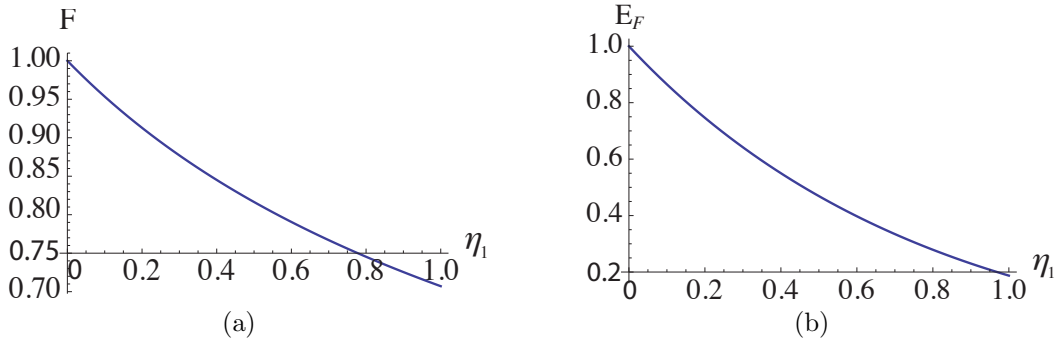


Figure 8.4: Plots for the final state ρ after the entangling operation, against the type I error η_1 for each measurement, showing (a) the fidelity F with respect to $|\Psi^+\rangle\langle\Psi^+|$; (b) the entanglement of formation E_F when the population outside the computational subspace are simply ignored and projected out.

We see from Fig. 8.4(a) that a high fidelity is possible as long as the error η_1 remains small, however, this does not automatically guarantee the presence of entanglement for the bipartite quinits. We therefore apply an entanglement measure to see how the degree of entanglement changes as η_1 increases. The simplest (but questionable) way of doing so is to apply *Wootter*'s entanglement of formation E_F [69] to the state ρ projected onto the computational subspace, while ignoring the population in the other levels [see Fig. 8.4(b)]. The reason we consider this metric incorrect is that artificial entanglement is created by this projection process. Moreover, even small amounts of population in levels outside the computational subspace may result in a significant reduction in the degree of entanglement for the larger system in

certain scenarios, as has recently been explored by Ref. [421]. Thus instead of the entanglement of formation, a more useful measure involving the whole five levels of the bipartite quinits is needed.

We apply the generalized m-concurrence C_m^2 measure in d dimensions as defined in [422] and derived in [423], where m denotes the number of parties involved and equals 2 in this case. In d dimensions, C_2^2 ranges from zero for separable states to $\frac{2(d-1)}{d}$ for the maximally entangled generalized Bell states, such as $\frac{1}{\sqrt{d}}\sum_{i=0}^{d-1}|ii\rangle$. Moreover, it reduces to the Wootter's concurrence squared C^2 [69] when $d = 2$. Fig. 8.5(a) illustrates the 2-concurrence (*dashed green*) of the final state ρ [Eq. 8.10] with $d = 5$ against the error η_1. This is marginally lower than the projectively im-

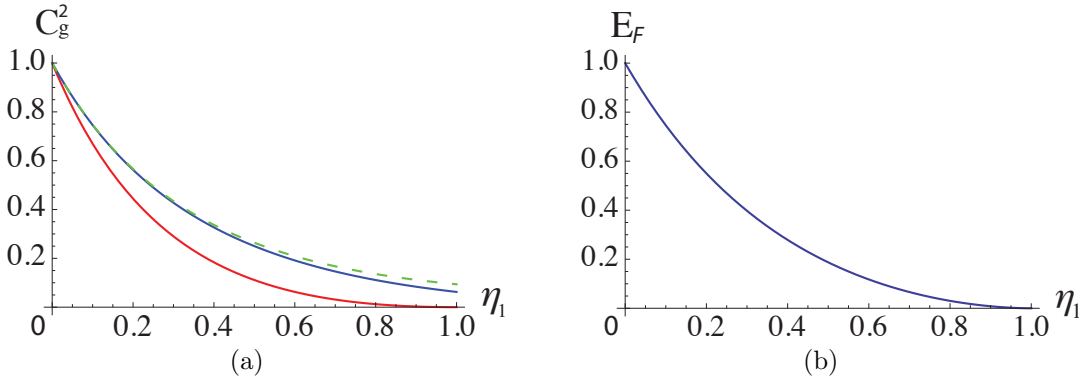


Figure 8.5: (a) Plots of the generalized 2-concurrence C_2^2 in 5 dimensions against the η_1 error, for ρ (*dashed green*), ρ with dephased population outside the computational subspace (*solid blue*), and ρ with all population discounted into the computational subspace (*solid red*); (b) Entanglement of formation E_F plot for the discounted final state ρ_d [Eq. 8.18] (red in (a)) against η_1.

plemented Wootter's concurrence squared (not shown here), for each finite $\eta_1 \neq 0$. The difference is insignificant, partly due to the fact that the state ρ [Eq. 8.10] is also entangled outside the computational space through the error components σ_1 and σ_2 [Eq. 8.16]. Interestingly, even when $\eta_1 = 1$, the 2-concurrence is still greater than zero, although no information is learnt at any of the four measurements. This can be understood as follows: we have assumed that the phase between the measured

state and the rest of the superposition is lost through the interaction between the system and the measurement apparatus [24]. This corruption of phase information affects the subsequent evolution of the state and effectively causes a leakage of population from the components $|00\rangle_{Q_1Q_2}$ ($|11\rangle_{Q_1Q_2}$) in the computational subspace to $|42(3)\rangle_{Q_1Q_2}$ and $|2(3)4\rangle_{Q_1Q_2}$. Entanglement then appears to exist – and is registered by the 2-concurrence – both within and outside the computational subspace. However, we stress that this apparent entanglement is useless for our purpose due to a complete lack of information about heralded failures, which prevents the required post-selection of successful runs of the protocol.

Therefore, our final state generally contains both useful and also 'spurious' entanglement. We thus require a new metric for filtering out the latter kind to obtain a lower bound on the degree of useful entanglement. We shall achieve this by identifying a suitable theoretical operation that can be applied to the final state. It turns out to be insufficient to replace all population outside the computational basis with a completely mixed state in these levels, since the resulting curve [*solid blue* in Fig. 8.5(a)] still does not hit zero as $\eta_1 \to 1$. In this case only the entanglement outside the computational subspace has been removed, but the entanglement inside of it is still present. Since no information has been learnt in the measurement, this entanglement is of the 'spurious' kind which we want to discount. A better approach therefore proceeds as follows: we add any population that has leaked from the levels $|00\rangle_{Q_1Q_2}$ or $|11\rangle_{Q_1Q_2}$ back into computational subspace in a way that mixes the resulting state to the largest possible extent:

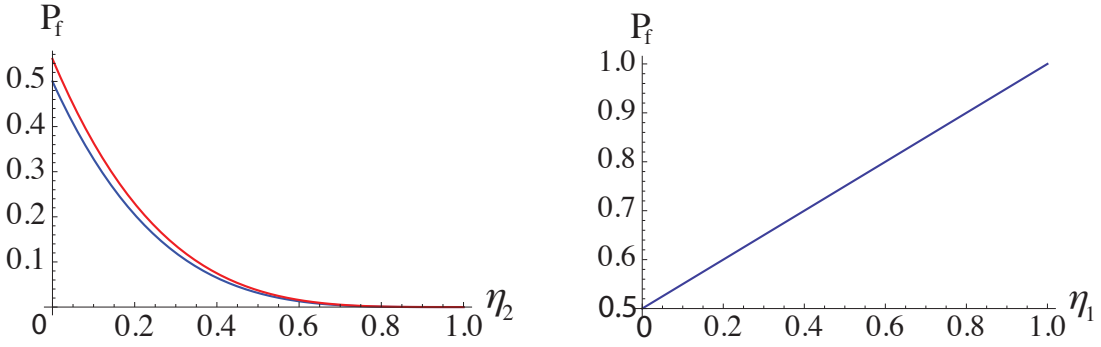
$$\rho_d = \frac{1}{1+\eta_1}\left(|\Psi^+\rangle\langle\Psi^+| + \frac{\eta_1}{2}\big(|00\rangle\langle 00| + |11\rangle\langle 11| \big) \right)_{Q_1Q_2} \tag{8.18}$$

The C_2^2 curve in 5 dimensions for this state then coincides with the square of Wootter's concurrence C^2 for two 2-dimensional systems, hitting zero as $\eta_1 \to 1$ [*solid*

red in Fig. 8.5(a)]. Indeed, this is what we would reasonably expect for maximal error η_1 when the measurement fails to report any useful information. Since only two levels are involved for ρ_d, we can also plot its entanglement of formation against η_1 in Fig. 8.5(b), which is lower than that shown in Fig. 8.4(b) as expected. We see that in order to achieve a high degree of useful entanglement as the result of the parity projection operation, η_1 has to be small. For example, $\mathrm{E}_F(\rho_d) \approx 0.75$ when $\eta_1 = 10\%$ which is achievable with the current technology [24].

8.4.2 Type II measurement error

This type of error occurs when a measurement outcome reports a YES while there are not two photons in the cavity, and this happens with an independent probability of η_2 for each measurement. For this kind of error, the entangling procedure is



(a) $\eta_1 = 0$ (blue) and 0.1 (red); (b) $\eta_2 = 0$.

Figure 8.6: The probability P_f (a) for a type II error η_2 with $\eta_1 = 0$ (blue) and $\eta_1 = 0.1$ (red), respectively; (b) for a type I error η_1 with $\eta_2 = 0$. In the latter case, note that in spite of the increase in the probability P_f the final state is still degraded as η_1 becomes larger.

STOPPED and we have to start all over since a YES is reported. Consequently, this only affects the overall probability that we reach the end of the protocol without a heralded failure. We found this by considering the overall probability of passing

all four measurement tests, and thus obtain

$$P_{\rm f} = \frac{7(1-\eta_2)+\eta_1}{8} \times \frac{(6+\eta_1)(1-\eta_2)+\eta_1}{7+\eta_1} \times \frac{(5+2\eta_1)(1-\eta_2)+\eta_1}{6+2\eta_1} \times \frac{(4+3\eta_1)(1-\eta_2)+\eta_1}{5+3\eta_1}, \tag{8.19}$$

for the entire entangling operation [see Fig. 8.6].

In the absence of any error, the probability $P_{\rm f}$ of reaching the end of the protocol is 50%. $P_{\rm f}$ decreases with η_2 for fixed η_1, and increases with η_1 for fixed η_2, although the quality of entanglement is of course reduced in this case. For the 10% error in η_1 which gives rise to an 80% concurrence, a type II error of $\eta_2 = 10\%$ [24] results in a probability $P_{\rm f} \simeq 36.4\%$, i.e., roughly a third of the times.

8.4.3 Cavity photon leakage

Measurement errors are only important during the entangling scheme, while all other errors also affect the single qubit gate fidelities. Cavity photon loss is likely the next dominant error source, whereas timing errors and collective excitation decay can be considered negligible in comparison.

For this reason, we shall now briefly discuss an adaptation of our proposed circuit which can achieve a reduction of the cavity leakage effect. For each measurement procedure a $C_{\rm NOT}$ gate is first implemented on the transmon, which takes about 50 ns. The $C_{\rm NOT}$ gate is controlled by the number of photons in the cavity, so in this case the $C_{\rm NOT}$ gate is triggered whenever there are two photons in the cavity. The measurement cavity is then read out using a microwave probe, taking a time of about 400 ns [24]. As the probe measurement thus takes a much longer time than the $C_{\rm NOT}$ gates and the SWAP operations, we can adapt our earlier circuit to reduce the number of read-out steps required in each block of the entangling operation [see

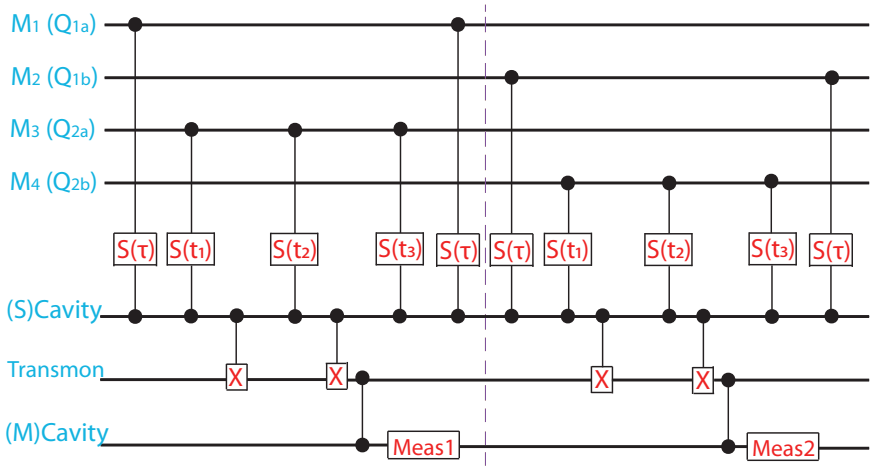


Figure 8.7: The modified circuit for the whole integrated device during the entangling operation, where the number of measurements is halved. Nonetheless, the circuit still consists the same blocks of basic operations.

Fig. 8.7]. This modified block achieves the same effect as our previous circuit, i.e. it removes all components of the wavefunction with double excitations in the relevant two modes while not disturbing the remaining components of the state. For a cavity with photon decay time of $\frac{20}{2\pi} \simeq 3.2\mu$s [24] we expect a photon leakage of about 15.6% during a 0.5 μs operation, but this source of error can be further suppressed by increasing the Q-factor of the storage cavity in the integrated device.

8.5 Read-out scheme

Full quantum state tomography can be carried out on the logical qubits to determine the dual-rail mode states. This is achieved through a sequence of SWAP operations followed by measurements on the storage cavity. This can also be extended to consider the entangled bipartite quinits as in Eq. 8.10, by measuring the number of photons in the cavity swapped from each mode: Three measurements are then needed for each mode to determine whether there are zero, one, or two photons in the cavity.

While the above-described full state tomography is straightforward to implement in principle, the number of measurements required for each run of the circuit might be challenging in a first experimental demonstration. Therefore, we propose the following alternative as a simpler verification of the entangling protocol: The aim is to use appropriate measurement statistics on the final state to reconstruct a density matrix that is consistent with the one given by Eq. 8.18. To achieve this, we start with repeated runs of the solid circuit in Fig. 8.8(a), with each measurement only

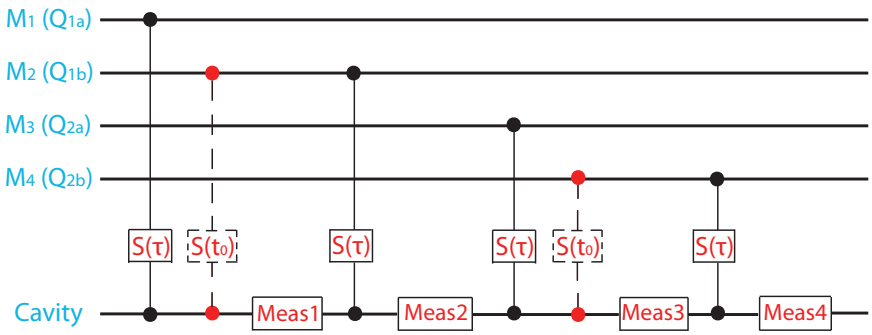


Figure 8.8: Qubit measurement in two independent bases: (a) with only the solid ciruit, corresponding to measurement in the logical basis of $\{|0\rangle_{Q_i}, |1\rangle_{Q_i}\}$; (b) with the full circuit including the dashed gates, corresponding to measurement in the logical basis of $\{|+\rangle_{Q_i}, |-\rangle_{Q_i}\}$ for $t_0 = \frac{\tau}{2}$.

checking whether there is a single photon in the cavity or not. An answer of NO means that there must have been either zero or two photons in the relevant mode M_i. Our default assumption in this case will be that the mode was in the state $|0\rangle_{\mathrm{M}_i}$. Only when we obtain the total combination $|0000\rangle_{\mathrm{M}_1\mathrm{M}_2\mathrm{M}_3\mathrm{M}_4}$, do we assume that there must have existed two excitations in one of the four modes. However, such states only occur due to errors in the protocol; they lie outside the computational basis and do not contribute towards the final entangled resource state. As discussed in Sec. 8.3, we account for these errors by adding their population to the computational subspace in a way that ensures that the quality of the desired resource is not artificially boosted. Performing many runs of this circuit then allows us to fill the diagonal entries of the

density matrix (in the $\{|0\rangle_{Q_i}, |1\rangle_{Q_i}\}$ basis), and to compare them with Eq. 8.18.

However, the above procedure alone is not sufficient to distinguish quantum entanglement from classical correlations. We therefore also carry out repeated runs of the complete circuit including the dashed gates in Fig. 8.8(b), corresponding to measurement in the logical basis of $\{|+\rangle_{Q_i}, |-\rangle_{Q_i}\}$ for $t_0 = \frac{\tau}{2}$. This enables us to obtain the coherences of the density matrix, which can then once more be compared with Eq. 8.18. Note that in measuring the coherences, population outside the computational basis is no longer relevant, and can be directly discarded. Combining the two similar procedures described above, one can verify whether the entangled resource at the end of the protocol is consistent with the discounted qubit state ρ_d [Eq. 8.18] for a known fixed η_1 error, up to a certain confidence level.

8.6 Conclusion

An electron spin ensemble can collectively couple to an on-chip stripline cavity, providing enhanced interaction strength and acting as a coherent quantum memory [see Sec. 4.4]. In this chapter, we have devised measurement-based entanglement protocol for dual-rail encoded qubits in the collective excitations of the memory ensemble, with the cavity linked to a measurement apparatus, and hence promote to a full quantum information processor. An detailed analysis of the predominant error sources of the integrated device indicates that probabilistic QIP with the spin ensemble should be feasible with the current technology.

Chapter 9

Summary and outlook

In this thesis, we have explored the dynamics of quantum systems involving different spin chains [Chapters 5 − 7] and spin ensemble [Chapters 8] for the purpose of creating distributed entanglement [Chapters 5, 7 and 8] or storing qubits [Chapters 6 and 8], which are two major aspects of QIP. We have found that the spin collectives can provide enhancement for weak couplings that are normally encountered in manipulating a single spin. By exploiting the 'natural' or inherent physical behaviour of the spins, we sought ways to reduce the level of active quantum control .

We have analysed the primary error effects in the physical implementation of each scheme presented. The spin collectives are remarkably robust against most noise effects, though there are specific error types (such as the splitting inefficiency in Chapter 5 and the phase noise in diamond defects in Chapter 7) that can significantly degrade performance. In these cases, we may need to concede that the spin chains can be insufficient for *direct* fault-tolerant QC due to the extremely high fidelities required; the ensembles (with more spins) may do better [18]. The latter have mainly been studied for collective storage of excitations [see Sec. 4.4], and thus more investigations are needed to analyse their performance in other roles, such as to mediate quantum state transfer between distant qubits [18] or to carry out quantum metrology to achieve better precision [55].

Nevertheless, provided the subsequent application of distillation protocols [70, 71, 77], both spin chains and ensembles can be used to perform QIP tasks with improved coherence properties. From this perspective, they can usually outperform single spins with effectively 'enhanced' couplings:

- Chapter 5 proposes a scheme to utilize the spin-entangled current resource [13, 14] that may otherwise be difficult to access. Moreover, the distributed, static entanglement generated can have higher separations than more conventional protocols that only exploit quantum tunnelling effects.
- Chapter 6 introduces a spin-chain quantum memory that may be used to collectively store multiple flying qubits, such as the internal states of bosonic cold atoms. The fluctuations of local information loss in the memory could be 'smoothed' when the information is spread. This is also fundamentally different from the ensemble-based quantum memory [see Sec. 4.4].
- Chapter 7 analyses the practicality of spin-chain 'wiring' for diamond defects, and shows that lifting the assumption of 'nearest-neighbour only' for the couplings (and hence avoiding complicated dynamical decoupling sequences) does not result in any significant penalty on the performance of the channel.
- Chapter 8 promotes an electron spin-ensemble quantum memory, which is coupled to an on-chip stripline cavity, to a full quantum information processor. This removes the unstable CPB qubit that was otherwise needed to provide the non-linearity to entangle the collective modes of the memory.

These schemes either illustrate alternative, new ideas or re-purpose earlier studies to allow realistic noise effects, making further steps towards closing the gap between theory and experiment. [*word count*[1]: 37,300]

[1]This is accurate to the nearest hundred words, and is in compliance with the rules set out in the form GSO.21, i.e., it excludes references, diagrams (figures), tables, *etc.* There are 252 *lines* of equations, with each approximated by 10 words on average and included in this total word count. All footnotes are excluded, but they account for about 1,600 words.

Bibliography

[1] *The world's most innovative companies* http://www.forbes.com/special-features/innovative-companies.html (Forbes, 2012).

[2] N. D. Evans, *Business innovation and disruptive technology* (Pearson, 2003).

[3] P. Gupta, *Business innovation in the 21st century* (Accelper Consulting, 2007).

[4] S. Hartmann, *The world as a process: Simulations in the natural and social sciences* Phil. Sci. Archive 2412 http://philsci-archive.pitt.edu/2412/ (2005).

[5] E. H. Shortliffe and M. S. Blois, *Biomedical informatics: Computer applications in health care and biomedicine, 3rd edition* (Springer, 2006).

[6] J. J. L. Morton, D. R. McCamey, M. A. Eriksson, and S. A. Lyon, *Embracing the quantum limit in silicon computing* Nature **479**, 345 (2011).

[7] M. A. Nielsen and I. L. Chuang, *Quantum computation and quantum information, 10th anniversary edition* (Cambridge, 2010).

[8] R. P. Feynman, *Simulating physics with computers* Int. J. Theor. Phys. **21**, 467 (1982).

[9] D. Deutsch, *Quantum theory, the Church-Turing principle and the universal quantum computer* Proc. Roy. Soc. (London) A **400**, 97 (1985).

[10] A. M. Turing, *Systems of logic based on ordinals (Ph. D. thesis)* (Princeton, 1939).

[11] H.-S. Goan and Y.-N. Chen, *Solid-state quantum computing* AIP Conf. Proc. **1074**, 132 (Springer, 2009).

[12] C. Cohen-Tannoudji, B. Diu, and F. Laloe, *Quantum Mechanics* (Wiley, 1978).

[13] L. Hofstetter, S. Csonka, J. Nygard, and C. Schoenenberger, *Cooper pair splitter realized in a two-quantum-dot Y-junction* Nature **461**, 960 (2009).

[14] L. G. Herrmann, F. Portier, P. Roche, A. Levy Yeyati, T. Kontos and C. Strunk, *Carbon nanotubes as cooper-pair beam splitters* Phys. Rev. Lett. **104**, 026801 (2010).

[15] N. Y. Yao, L. Jiang, A. V. Gorshkov, Z.-X. Gong, A. Zhai, L.-M. Duan, and M. D. Lukin, *Robust Quantum State Transfer in Random Unpolarized Spin Chains* Phys. Rev. Lett. **106**, 040505 (2011).

[16] N. Y. Yao, L. Jiang, A. V. Gorshkov, P. C. Maurer, G. Giedke, J. I. Cirac, and M.D. Lukin, *Scalable architecture for a room temperature solid-state quantum information processor* Nature Comms. **3**, 800 (2012).

[17] N. Y. Yao, Z.-X. Gong, C. R. Laumann, S. D. Bennett, L.-M. Duan, M. D. Lukin, L. Jiang, and A. V. Gorshkov, *Quantum logic between remote quantum registers* Phys. Rev. A **87**, 022306 (2013).

[18] H. Weimer, N. Y. Yao, and M. D. Lukin, *Collectively enhanced interactions in solid-state spin qubits* Phys. Rev. Lett. **110**, 067601 (2013).

[19] H. Wu, R. E. George, J. H. Wesenberg, K. Mølmer, D. I. Schuster, R. J. Schoelkoef, K. M. Itoh, A. Ardavan, J. J. L. Morton, and G. A. D. Briggs, *Storage of Multiple Coherent Microwave Excitations in an Electron Spin Ensemble* Phys. Rev. Lett. **105**, 140503 (2010).

[20] P. Rabl, D. Demille, J. .M. Doyle, M. .D. Lukin, R. J. Schoelkopf, and P. Zoller, *Hybrid quantum processors: Molecular ensembles as quantum memory for solid state circuits* Phys. Rev. Lett. **97**, 033003 (2006).

[21] A. André, D. Demille, J. M. Doyle, M. D. Lukin, S. E. Maxwell, P. Rabl, R. J. Schoelkopf, and P. Zoller, *A coherent all-electrical interface between polar molecules and mesoscopic superconducting resonators* Nature Physics **2**, 636 (2006).

[22] K. Tordrup, A. Negretti, and K. Mølmer, *Holographic Quantum Computing* Phys. Rev. Lett. **101**, 040501 (2008).

[23] J. H. Wesenberg, A. Ardavan, G. A. D. Briggs, J. J. L. Morton, R. J. Schoelkopf, D. I. Schuster, and K. Mølmer, *Quantum computing with an electron spin ensemble* Phys. Rev. Lett. **103**, 070502 (2009).

[24] B. R. Johnson, M. D. Reed, A. A. Houck, D. I. Schuster, Lev S. Bishop, E. Ginossar, J. M. Gambetta, L. DiCarlo, L. Frunzio, S. M. Girvin, and R. J. Schoelkopf, *Quantum non-demolition detection of single microwave photons in a circuit* Nature Physics **6**, 663 (2010).

[25] C. W. Curtis, *Linear algebra: An introductory approach* (Springer, 2000).

[26] G. C. Knee, S. Simmons, E. M. Gauger, J. J. L. Morton, H. Riemann, N. V. Abrosimov, P. Becker, H.-J. Pohl, K. M. Itoh, M. L. W. Thewalt, G. A. D. Briggs, and S. C. Benjamin, *Violation of a Leggett-Garg inequality with ideal non-invasive measurements* Nature Comms. **3**, 606 (2012).

[27] A. J. Leggett and A. Garg, *Quantum mechanics versus macroscopic realism: Is the flux there when nobody looks?* Phys. Rev. Lett. **54**, 857 (1985).

[28] M. H. Levitt, *Spin dynamics: Basics of nuclear magnetic resonance* (Wiley, 2001).

[29] A. Barenco, C. H. Bennett, R. Cleve, D. P. DiVincenzo, N. Margolus, P. Shor, T. Sleator, J. A. Smolin and H. Weinfurter, *Elementary gates for quantum computation* Phys. Rev. A **52**, 5 (1995).

[30] A. S. Kholevo, *Some estimates for information quantity transmitted by quantum communication channel* Probl. Inform. Transm. **9**, 3 (1973).

[31] W. K. Wootters and W. H. Zurek, *A single quantum cannot be cloned* Nature **299**, 802 (1982).

[32] D. Deutsch and R. Jozsa *Rapid solutions of problems by quantum computation* Proc. Roy. Soc. (London) A 439 (1992).

[33] P. W. Shor, *Polynomial-time algorithms for prime factorization and discrete logarithms on a quantum computer* SIAM J. Sci. Stats. Comp. **26**, 1484 (1997).

[34] L. K. Grover, *A fast quantum mechanical algorithm for database search* Proc. 28^{th} Annu. ACM Symp. Theor. Comp. 212 (ACM Press, New York, 1996).

[35] M. Mosca, *Quantum algorithms* arXiv:0808.0369 Encyclopedia of Complexity and Systems Science (Springer, 2009).

[36] A. M. Childs and W. van Dam, *Quantum algorithms for algebraic problems* Rev. Mod. Phys. **82**, 1 (2010).

[37] R. Rivest, A. Shamir and L. Adleman, *A method for obtaining digital signatures and public-key cryptosystems* Comm. ACM **21**, 120 (1978).

[38] C. H. Bennett and G. Brassard, *Quantum cryptography: Public-key distribution and coin tossing* IEEE Proc. Int. Conf. Computers, Systems and Signal Processing, Bangalore, India 175 (1984).

[39] H. -K. Lo and H. F. Chau, *Unconditional security of quantum key distribution over arbitrarily long distances* Science **283**, 2050 (1999).

[40] P. W. Shor and J. Preskill, *Simple proof of security of the BB84 quantum key distribution protocol* Phys. Rev. Lett. **85**, 441 (2000).

[41] A. Leverrier, R. Garcí-Patrón, R. Renner, and N. J. Cerf, *Security of continuous-variable quantum key distribution against general attacks* Phys. Rev. Lett. **110**, 030502 (2013).

[42] H.-K. Lo, M. Curty, and B. Qi, *Measurement-device-independent quantum key distribution* Phys. Rev. Lett. **108**, 130503 (2012).

[43] R. Ursin, et al., F. Tiefenbacher, T. Schmitt-Manderbach, H. Weier, T. Scheidl, M. Lindenthal, B. Blauensteiner, T. Jennewein, J. Perdigues, P. Trojek, B. Ömer, M. Fürst, M. Meyenburg, J. Rarity, Z. Sodnik, C. Barbieri, H. Weinfurter, and A. Zeilinger, *Entanglement-based quantum communication over 144 km* Nature Physics **3**, 481 (2007).

[44] T. Scheidl, R. Ursin, A. Fedrizzi, S. Ramelow, X.-S. Ma, T. Herbst, R. Prevedel, L. Ratschbacher, J. Kofler, T. Jennewein, and A. Zeilinger, *Feasibility of 300km quantum key distribution with entangled states* New J. Phys. **11**, 085002 (2009).

[45] A. R. Dixon, Z. L. Yuan, J. F. Dynes, A. W. Sharpe and A. J. Shields, *Gigahertz decoy quantum key distribution with 1 Mbit/s secure key rate* Optics Express **16**, 18790 (2008).

[46] A. R. Dixon, Z. L. Yuan, J. F. Dynes, A. W. Sharpe, and A. J. Shields, *Continuous operation of high bit rate quantum key distribution* Appl. Phys. Lett. **96**, 161102 (2010).

[47] V. Scarani, H. Bechmann-Pasquinucci, N. J. Cerf, M. Dusek, N. Lutkenhaus and M. Peev, *The security of practical quantum key distribution* Rev. Mod. Phys. **81**, 1301 (2009).

[48] M. Sasaki *et al.*, *Field test of quantum key distribution in the Tokyo QKD Network* Optics Express **19**, 010387 (2011).

[49] I. Choi, K. A. Patel, J. F. Dynes, A. W. Sharpe, A. R. Dixon, Z. L. Yuan, R. V. Penty, and A. J. Shields, *High speed quantum key distribution for smart city distances with data multiplexing* 2nd Annu. Conf. QCrypt., Singapore (2012).

[50] R. Alléaume, J. Bouda, C. Branciard, T. Debuisschert, M. Dianati, N. Gisin, M. Godfrey, P. Grangier, T. Länger, A. Leverrier, N. Lütkenhaus, P. Painchault, M. Peev, A. Poppe, T. Pornin, J. Rarity, R. Renner, G. Ribordy, M. Riguidel, L. Salvail, A. Shields, H. Weinfurter, and A. Zeilinger, *SECOQC white paper on quantum key distribution and cryptography* arXiv:quant-ph/0701168 (2007).

[51] P. Kok, S. L. Braunstein, and J. P. Dowling, *Quantum lithography, entanglement and Heisenberg-limited parameter estimation* J. Opt. B: Quantum Semiclass. Opt. **6**, S811 (2004).

[52] V. Giovannetti, S. Lloyd and L. Maccone, *Quantum-enhanced measurements: Beating the standard quantum limit* Science **306**, 1330 (2004).

[53] V. Giovannetti, S. Lloyd and L. Maccone, *Quantum metrology* Phys. Rev. Lett. **96**, 010401 (2006).

[54] T. Nagata, R. Okamoto, J. L. O'Brien, K. Sasaki, and S. Takeuchi, *Beating the standard quantum limit with four-entangled photons* Science **316**, 726 (2007).

[55] M. Schaffry, E. M. Gauger, J. J. L. Morton, J. Fitzsimons, S. C. Benjamin, and B. W. Lovett, *Quantum metrology with molecular ensembles* Phys. Rev. A **82**, 042114 (2010).

[56] G. Balasubramanian, I. Y. Chan, R. Kolesov, M. Al-Hmoud, J. Tisler, C. Shin, C.-D. Kim, A. Wojcik, P. R. Hemmer, A. Krueger, T. Hanke, A. Leitenstorfer, R. Bratschitsch, F. Jelezko, and J. Wrachtrup, *Nanoscale imaging magnetometry with diamond spins under ambient conditions* Nature **455**, 648 (2008).

[57] C. Zalka, *Simulating quantum systems on a quantum computer* Proc. Roy. Soc. (London) A **454**, 313 (1998).

[58] D. S. Abrams and S. Lloyd, *Simulation of many-body Fermi systems on a universal quantum computer* Phys. Rev. Lett. **79**, 2586 (1997).

[59] A. Einstein, B. Podolsky and N. Rosen, *Can quantum-mechanical description of physical reality be considered complete?* Phys. Rev. **47**, 777 (1935).

[60] A. Afriat and F. Selleri, *The Einstein, Podolsky, and Rosen paradox: in atomic, nuclear, and particle physics* (Plenum, 1999).

[61] J. S. Bell, *On the Einstein Podolsky Rosen paradox* Physics **1**, 195 (1964).

[62] J. F. Clauser, M. A. Horne, A. Shimony and R. A. Holt, *Proposed experiment to test local hidden-variable theories* Phys. Rev. Lett. **23**, 880 (1969).

[63] A. Aspect, J. Dalibard and G. Roger, *Experimental test of Bell's inequalities using time- varying analyzers* Phys. Rev. Lett. **49**, 1804 (1982).

[64] B. S. Cirel'son, *Quantum generalizations of Bell's inequality* Lett. Math. Phys. **4**, 93 (1980).

[65] R. Horodecki, P. Horodecki, M. Horodecki and K. Horodecki, *Quantum entanglement* Rev. Mod. Phys. **81**, 865 (2009).

[66] C. H. Bennett, G. Brassard, C. Crpeau, R. Jozsa, A. Peres and W. K. Wootters, *Teleporting an unknown quantum state via dual classical and Einstein-Podolsky-Rosen channels* Phys. Rev. Lett. **70**, 1895 (1993).

[67] X.-M. Jin, J.-G. Ren, B. Yang, Z.-H. Yi, F. Zhou, X.-F. Xu, S.-K. Wang, D. Yang, Y.-F. Hu, S. Jiang, T. Yang, H. Yin, K. Chen, C.-Z. Peng, and J.-W. Pan, *Experimental free-space quantum teleportation* Nature Photonics **4**, 376 (2010).

[68] S. Hill and W. K. Wootters, *Entanglement of a pair of quantum bits* Phys. Rev. Lett. **78**, 5022 (1997).

[69] W. K. Wootters, *Entanglement of formation of an arbitrary state of two qubits* Phys. Rev. Lett. **80**, 2245 (2000).

[70] C. H. Bennett, H. J. Bernstein, S. Popescu and B. Schumacher, *Concentrating partial entanglement by local operations* Phys. Rev. A **53**, 2046 (1996).

[71] C. H. Bennett, G. Brassard, S. Popescu, B. Schumacher, J. A. Smolin and W. K. Wooters, *Purification of noisy entanglement and faithful teleportation via noisy channels* Phys. Rev. Lett. **76**, 722 (1996).

[72] J.-W. Pan, C. Simon, Č. Brunker, and A. Zeilinger, *Entanglement purification for quantum communication* Nature **410**, 1067 (2001).

[73] J.-W. Pan, S. Gasparoni, R. Ursin, G. Weihs, and A. Zeilinger, *Experimental entanglement purification of arbitrary unknown states* Nature **423**, 417 (2003).

[74] R.-F. Dong, M. Lassen, J. Heersink, C. Marquardt, R. Fili, G. Leuchs, and U. L. Andersen, *Experimental entanglement distillation of mesoscopic quantum states* Nature Physics **4**, 919 (2008).

[75] B. Hage, A. Samblowski, J.. DiGuglielmo, J. Fiurášek, and R. Schnabel, *Iterative entanglement distillation: Approaching the elimination of decoherence* Phys. Rev. Lett. **105**, 230502 (2010).

[76] P. Horodecki and M. Demianowicz, *Fidelity thresholds in single copy entanglement distillation* Phys. Lett. A **354**, 40 (2006).

[77] C. H. Bennett, D. P. DiVincenzo, J, A. Smolin and W. K. Wooters, *Mixed state entanglement and quantum error correction* Phys. Rev. A **54**, 3824 (1996).

[78] V. Coffman, J. Kundu and W. K. Wootters, *Distributed entanglement* Phys. Rev. A **61**, 052306 (2000).

[79] R. Raussendorf and H. J. Briegel, *A one-way quantum computer* Phys. Rev. Lett. **86**, 5188 (2001).

[80] H. J. Briegel, D. E. Browne, W. Dür, R. Raussendorf, and M. Van den Nest, *Measurement-based quantum computation* Nature Physics **5**, 19 (2009).

[81] S. C. Benjamin, D. E. Browne, J. Fitzsimons and J. J. L. Morton, *Brokered graph state quantum computing* New J. Phys. **8**, 141 (2006).

[82] P. Walther, K. J. Resch, T. Rudolph, E. Schenck, H. Weinfurter, V. Vedral, M. Aspelmeyer and A. Zeilinger, *Experimental one-way quantum computing* Nature **434**, 169 (2005).

[83] S. D. Barrett and P. Kok, *Efficient high-fidelity quantum computation using matter qubits and linear optics* Phys. Rev. A **71**, 060310(R) (2005).

[84] Y. L. Lim, A. C. Beige and L. C. Kwek, *Repeat-until-success linear optics distributed quantum computing* Phys. Rev. Lett. **95**, 030505 (2005).

[85] E. T. Campbell, J. Fitzsimons, S. C. Benjamin, and P. Kok, *Efficient growth of complex graph states via imperfect path erasure* New J. Phys. **9**, 196 (2007).

[86] E. T. Campbell, *Distributed quantum-information processing with minimal local resources* Phys. Rev. A **76**, 040302(R) (2007).

[87] Y. Matsuzaki, S. C. Benjamin and J. Fitzsimons, *Probabilistic growth of large entangled states with low error accumulation* Phys. Rev. Lett. **104**, 050501 (2010).

[88] S. C. Benjamin, B. W. Lovett, and J. M. Smith, *Prospects for measurement-based quantum computing with solid state spins* Laser Phontonics Rev. **3**, 556 (2009).

[89] J. J. L. Morton, *A silicon-based cluster state quantum computer* arXiv:0905.4008 (2009).

[90] N. H. Lindner and T. Rudolph, *A photonic cluster state machine gun* Phys. Rev. Lett. **103**, 113602 (2009).

[91] S. E. Economou, N. H. Lindner and T. Rudolph, *Optically generated 2-dimensional photonic cluster state from coupled quantum dots* Phys. Rev. Lett. **105**, 093601 (2010).

[92] M. Ohliger and J. Eisert, *Efficient measurement-based quantum computing with continuous-variable systems* Phys. Rev. A **85**, 062318 (2012).

[93] W.-B. Gao, X.-C. Yao, J.-M. Cai, H. Lu, P. Xu, T. Yang, C.-Y. Lu, Y.-A. Chen, Z.-B. Chen, and J.-W. Pan, *Experimental measurement-based quantum computing beyond the cluster-state model* Nature Photonics **5**, 117 (2011).

[94] S. Bose, P. L. Knight, M. B. Plenio, and V. Vedral, *Proposal for teleportation of an atomic state via cavity decay* Phys. Rev. Lett. **83**, 5158 (1999).

[95] C. Cabrillo, J. I. Cirac, P. García-Fernández, and P. Zoller, *Creation of entangled states of distant atoms by interference* Phys. Rev. A **59**, 1025 (1999).

[96] P. W. Shor, *Fault-tolerant quantum computation* IEEE Proc. 37$^{\text{th}}$ Annu. Symp. Fund. Comp. Sci., Los Alamitos, CA 56 (1996).

[97] A. W. Cross, D. P. DiVincenzo, and B. M. Terhal, *A comparative code study for quantum fault-tolerance* Quant. Inf. Comp. **9**, 0541 (2009).

[98] D. S. Wang, A. G. Fowler, and L. C. L. Hollenberg, *Surface code quantum computing with error rates over 1%* Phys. Rev. A **83**, 020302(R) (2011).

[99] D. G. Cory, M. D. Price, W. Maas, E. Knill, R. Laflamme, W. H. Zurek, T. F. Havel, and S. S. Somaroo, *Experimental quantum error correction* Phys. Rev. Lett. **81**, 2152 (1998).

[100] P. W. Shor, *Scheme for reducing decoherence in quantum computer memory* Phys. Rev. A **52**, R2493 (1995).

[101] A. M. Steane, *Error correcting codes in quantum theory* Phys. Rev. Lett. **77**, 793 (1996).

[102] R. Laflamme, C. Miquel, J. P. Paz and W. H. Zurek, *Perfect quantum error correcting code* Phys. Rev. Lett. **77**, 198 (1996).

[103] A. R. Calderbank and P. W. Shor, *Good quantum error-correcting codes exist* Phys. Rev. A **54**, 1098 (1996).

[104] A. Steane, *Multiple-particle interference and quantum error correction* Proc. Roy. Soc. (London) A **452**, 2551 (1996).

[105] D. Gottesman, *Class of quantum error-correcting codes saturating the quantum Hamming bound* Phys. Rev. A **54**, 1862 (1996).

[106] A. Yu. Kitaev, *Fault-tolerant quantum computation by anyons* Annals Phys. **303**, 2 (2003).

[107] T. Brun, I. Devetak and M.-H. Hsieh, *Correcting quantum errors with entanglement* Science **314**, 436 (2006).

[108] D. Gottesman, *An Introduction to Quantum Error Correction and Fault-Tolerant Quantum Computation* arXiv:0904.2557 (2009).

[109] J. Chiaverini, D. Leibfried, T. Schaetz, M. D. Barrett, R. B. Blakestad, J. Britton, W. M. Itano, J. D. Jost, E. Knill, C. Langer, R. Ozeri, and D. J. Wineland, *Realization of quantum error correction* Nature **432**, 602 (2004).

[110] T. B. Pittman, B. C. Jacobs, and J. D. Franson, *Demonstration of quantum error correction using linear optics* Phys. Rev. A **71**, 052332 (2005).

[111] M. D. Reed, L. DiCarlo, S. E. Nigg, L. Sun, L. Frunzio, S. M. Girvin, and R. J. Schoelkopf, *Realization of three-qubit quantum error correction with superconducting circuits* Nature **482**, 382 (2012).

[112] M. Lassen, M. Sabuncu, A. Huck, J. Niset, G. Leuchs, N. J. Cerf, and U. L. Andersen, *Quantum optical coherence can survive photon losses using a continuous-variable quantum erasure-correcting code* Nature Photonics **4**, 700 (2010).

[113] X.-C. Yao, T.-X. Wang, H.-Z. Chen, W.-B. Gao, A. G. Fowler, R. Raussendorf, Z.-B. Chen N.-L. Liu, C.-Y. Lu, Y.-J. Deng, Y.-A. Chen, and J.-W. Pan, *Experimental demonstration of topological error correction* Nature **482**, 489 (2012).

[114] J.-F. Zhang, D. Gangloff, O. Moussa, and R. Laflamme, *Experimental quantum error correction with high fidelity* Phys. Rev. A **84**, 034303 (2011).

[115] P. Schindler, J. T. Barreiro, T. Monz, V. Nebendahl, D. Nigg, M. Chwalla, M. Hennrich, and R. Blatt, *Experimental repetitive quantum error correction* Science **332**, 1059 (2011).

[116] A. G. Fowler, M. Mariantoni, J. M. Martinis, and A. N. Cleland, *Surface codes: Towards practical large-scale quantum computation* Phys. Rev. A **86**, 032324 (2012).

[117] J. R. Wootton and D. Loss *High threshold error correction for the surface code* Phys. Rev. Lett. **109**, 160503 (2012).

[118] E. Knill, *Quantum computing with realistically noisy devices* Nature **434**, 39, (2005).

[119] J. Fern, *An upper bound on quantum fault tolerant thresholds* arXiv:0801.2608 (2008).

[120] R. Raussendorf and J. Harrington, *Fault-tolerant quantum computation with high threshold in two dimensions* Phys. Rev. Lett. **98**, 190504 (2007).

[121] R. Raussendorf, J. Harrington, and K. Goyal, *Topological fault-tolerance in cluster state quantum computation* New J. Phys. **9**, 199 (2007).

[122] H. -P. Breuer and F. Petruccione, *The theory of open quantum systems* (Oxford, 2002).

[123] D. D'Alessandro, *Introduction to quantum control and dynamics* (Chapman and Hall/CRC, 2008).

[124] R. Jozsa, *Fidelity for mixed quantum states* J. Mod. Opt. **41**, 2315 (1994).

[125] J. J. L. Morton and B. W. Lovett, *Hybrid solid state qubits: the powerful role of electron spins* Annu. Rev. Cond. Mat. Phys. **2**, 189 (2011).

[126] M. O. Scully and M. S. Zubairy, *Quantum optics* (Cambridge, 1997).

[127] D. F. Walls and G. J. Milburn, *Quantum optics, 2nd edition* (Springer, 2008).

[128] P. Kok and B. W. Lovett, *Introduction to optical quantum information processing* (Cambridge, 2010).

[129] R. C. Jones, *A new calculus for the treatment of optical systems* J. Opt. Soc. America **31**, 488 (1941).

[130] J. L. O'Brien, *Optical quantum computing* Science **318**, 1567 (2007).

[131] E. Knill, R. Laflamme, and G. J. Milburn, *A scheme for efficient quantum computation with linear optics* Nature **409**, 46 (2001).

[132] M. A. Nielsen, *Optical quantum computation using cluster states* Phys. Rev. Lett. **93**, 040503 (2004).

[133] D. E. Browne and T. Rudolph, *Resource-efficient linear optical quantum computation* Phys. Rev. Lett. **95**, 010501 (2005).

[134] R. Prevedel, P. Walther, F. Tiefenbacher, P. Böhi, R. Kaltenbaek, T. Jennewein, and A. Zeilinger, *High-speed linear optics quantum computing using active feed-forward* Nature **445**, 65 (2007).

[135] C.-Y. Lu, X.-Q. Zhou, O. Gühne, W. B. Gao, J. Zhang, Z.-S. Yuan, A. Goebel, T. Yang, and J.-W. Pan, *Experimental entanglement of six photons in graph states* Nature Physics **3**, 91 (2007).

[136] C. M. Dawson, H. L. Haselgrove, and M. A. Nielsen, *Noise thresholds for optical cluster-state quantum computation* Phys. Rev. A **73**, 052306 (2006).

[137] C. J. Foot, *Atomic physics* (Oxford, 2005).

[138] J. I. Cirac and P. Zoller, *Quantum computations with cold trapped ions* Phys. Rev. Lett. **74**, 4091 (1995).

[139] K. R. Brown, A. C. Wilson, Y. Colombe, C. Ospelkaus, A. M. Meier, E. Knill, D. Leibfried, and D. J. Wineland, *Single-qubit-gate error below 10^{-4} in a trapped ion* Phys. Rev. A **84**, 030303(R) (2011).

[140] H. C. Nägerl, D. Leibfried, H. Rohde, G. Thalhammer, J. Eschner, F. Schmidt-Kaler, and R. Blatt, *Laser addressing of individual ions in a linear ion trap* Phys. Rev. A **60**, 145 (1999).

[141] F. Schmidt-Kaler, H. Häffner, M. Riebe, S. Gulde, G. P. T. Lancaster, T. Deuschle, C. Becher, C. F. Roos, J. Eschner, and R. Blatt, *Realization of the Cirac-Zoller controlled-NOT quantum gate* Nature **422**, 408 (2003).

[142] D. Leibfried, B. DeMarco, V. Meyer, D. Lucas, M. Barrett, J. Britton, W. M. Itano, B. Jelenkovic, C. Langer, T. Rosenband, and D. J. Wineland, *Experimental demonstration of a robust, high-fidelity geometric two ion-qubit phase gate* Nature **422**, 412 (2003).

[143] H. Häffner, C. F. Roos, and R. Blatt, *Quantum computing with trapped ions* Phys. Rep. **469**, 155 (2008).

[144] J. J. Bollinger, D. J. Heinzen, W. M. Itano, S. L. Gilbert, and D. J. Wineland, *A 303-MHz frequency standard based on trapped Be^+ ions* IEEE Trans. Instr. Meas. **40**, 126 (1991).

[145] H. Häffner, F. Schmidt-kaler, W. Hänsel, C. F. Roos, T. Körber, M. Chawalla, M. Riebe, J. Benhelm, U. D. Rapol, C. Becher, R. Blatt, *Robust entanglement* Appl. Phys. B **81**, 151 (2005).

[146] D. J. Wineland, *Quantum information processing and quantum control with trapped atomic ions* Phys. Scr. **T137**, 014007 (2009).

[147] T. Monz, P. Schindler, J. T. Barreiro, M. Chwalla, D. Nigg, W. A. Coish, M. Harlander, W. Hänsel, M. Hennrich, and R. Blatt, *14-qubit entanglement: Creation and coherence* Phys. Rev. Lett. **106**, 130506 (2011).

[148] J. M. Amini, J. Britton, D. Leibfried, and D. J. Wineland, *Atom chips: Microfabricated chip traps for ions* arXiv:0812.3907 (Wiley, 2011).

[149] P. Grangier, G. Reymond, and N. Schlosser, *Implementations of quantum computing using cavity quantum electrodynamics schemes* Fortschr. Phys. **48**, 859 (2000).

[150] L.-M. Duan, A. Kuzmich, and H. J. Kimble, *Cavity QED and quantum-information processing with hot trapped atoms* Phys. Rev. A **67**, 032305 (2003).

[151] C.-H. Su, A. D. Greentree, W. J. Munro, K. Nemoto, and L. C. Hollenberg, *High-speed quantum gates with cavity quantum electrodynamics* Phys. Rev. A **78**, 062336 (2008).

[152] I. H. Deutsch, G. K. Brennen, and P. S. Jessen, *Quantum Computing with Neutral Atoms in an Optical Lattice* Forsch. der Phys. **48**, 925 (2000).

[153] D. Jaksch, *Optical lattices, ultracold atoms and quantum information processing* Contemporary Phys. **45**, 367 (2007).

[154] P. Treutlein, T. Steinmetz, Y. Colombe, B. Lev, P. Hommelhoff, J. Reichel, M. Greiner, O. Mandel, A. Widera, T. Rom, I. Bloch, and T. W. Hänsch, *Quantum information processing in optical lattices and magnetic microtraps* Fortschr. Phys. **54**, 702 (2006).

[155] M. Lewenstein, A. Sanpera, and V. Ahufinger, *Ultracold atoms in optical lattices: Simulating quantum many-body systems* (Oxford, 2012).

[156] M. Anderlini, P. J. Lee, B. L. Brown, J. Sebby-Strabley, W. D. Phillips, and J. V. Porto, *Controlled exchange interaction between pairs of neutral atoms in an optical lattice* Nature **448**, 452 (2007).

[157] S. Trotzky, P. Cheinet, S. Fölling, M. Feld, U. Schnorrberger, A. M. Rey, A. Polkovnikov, E. A. Demler, M. D. Lukin, and I. Bloch, *Time-resolved oberva-tion and control of superexchange interactions with ultracold atoms in optical lattices* Science **319**, 295 (2008).

[158] L.-M. Duan, E. Demler, and M. D. Lukin, *Controlling spin exchange interactions of ultracold atoms in optical lattices* Phys. Rev. Lett. **91**, 090402 (2003).

[159] D. Schrader, I. Dotsenko, M. Khudaverdyan, Y. Miroshnychenko, A. Rauschenbeutel, and D. Meschede, *Neutral atom quantum register* Phys. Rev. Lett. **93**, 150501 (2004).

[160] T. F. Havel, S. S. Somaroo, C.-H. Tseng and D. G. Cory, *Principles and demonstrations of quantum information processing by NMR spectroscopy* AAECC **10**, 339 (2000).

[161] J. A. Jones, *Quantum computing with NMR* Prog. NMR Spectrosc. **59**, 91 (2011).

[162] M. D. Price, S. S. Somaroo, C. H. Tseng, J. C. Gore, A. F. Fahmy, T. F. Havel and D. G. Cory, *Construction and implementation of NMR quantum logic gates for two spin systems* J. Magn. Reson. **140**, 371 (1999).

[163] I. L. Chuang, L. M. K. Vandersypen, X.-L. Zhou, D. W. Leung, and S. Lloyd, *Experimental realization of a quantum algorithm* Nature **393**, 143 (1998).

[164] L. M. K. Vandersypen, M. Steffen, G. Breyta, C. S. Yannoni, M. H. Sherwood and I. L. Chuang, *Experimental realization of Shor's quantum factoring algorithm using nuclear magnetic resonance* Nature **414**, 883 (2001).

[165] N. Boulant, M. A. Pravia, E. M. Fortunato, T. F. Havel and D. G. Cory, *Experimental concatenation of quantum error correction with decoupling* Quantum Info. Process. **1**, 135 (2002).

[166] E. Knill, R. Laflamme, R. Martinez and C. Negreverne, *Benchmarking quantum computers: The five-qubit error correcting code* Phys. Rev. Lett. **86**, 5811 (2001).

[167] W. S. Warren, *The usefulness of NMR quantum computing* Science **277**, 1688 (1997).

[168] S. L. Braunstein, C. M. Caves, R. Jozsa, N. Linden, S. Popescu and R. Schack, *Separability of very noisy mixed states and implications for NMR quantum computing* Phys. Rev. Lett. **83**, 1054 (1999).

[169] E. Abe, K. M. Itoh, T. D. Ladd, J. R. Goldman, F. Yamaguchi and Y. Yamamoto, *Solid-state silicon NMR quantum computer* J. Supercond. **16**, 175 (2003).

[170] U. Hohenester, *Optical properties of semiconductor nanostructures: Decoherence versus quantum control* arXiv:cond-mat/0406346 (2004).

[171] P. Harrison, *Quantum wells, wires and dots: Theoretical and computational physics of semiconductor nanostructures, 3rd edition* (Wiley, 2009)

[172] R. Hanson and D. D. Awschalom, *Coherent manipulation of single spins in semiconductors* Nature **453**, 1043 (2008).

[173] D. Loss and D. P. DiVincenzo, *Quantum computation with quantum dots* Phys. Rev. A **57**, 120 (1998).

[174] E. A. Laird, *Electrical control of quantum dot spin qubits (Ph.D. thesis)* (Harvard, 2009).

[175] R. Hanson, L. P. Kouwenhoven, J. R. Petta, S. Tarucha, and L. M. K. Vandersypen, *Spins in few-electron quantum dots* Rev. Mod. Phys. **79**, 1217 (2007).

[176] A. Kumar, S. E. Laux, and F. Stern, *Electron states in a GaAs quantum dot in a magnetic field* Phys. Rev. B **42**, 5166 (1990).

[177] L. P. Kouwenhoven, D. G. Austing, and S. Tarucha, *Few-electron quantum dots* Rep. Prog. Phys. **64**, 701 (2001).

[178] J. A. Weil and J. R. Bolton, *Electron paramagnetic resonance: Elementary theory and practical applications, 2nd edition* (Wiley, 2007).

[179] F. H. L. Koppens, C. Buizert, K. J. Tielrooij, I. T. Vink, K. C. Nowack, T. Meunier, L. P. Kouwenhoven, and L. M. K. Vandersypen, *Driven coherent oscillations of a single electron spin in a quantum dot* Nature **442**, 766 (2006).

[180] M. Pioro-Ladrière, T. Obata, Y. Tokura, Y.-S. Shin, T. Kubo, K. Yoshida, T. Taniyama, and S. Tarucha, *Electrically driven single-electron spin resonance in a slanting Zeeman field* Nature Physics **4**, 776 (2008).

[181] T. Obata, M. Pioro-Ladrière, Y. Tokura, Y.-S. Shin, T. Kubo, K. Yoshida, T. Taniyama, and S. Tarucha, *Coherent manipulation of individual electron spin in a double quantum dot integrated with a micromagnet* Phys. Rev. B **81**, 085317 (2010).

[182] S. Bellucci and P. Onorato, *Spintronic single-qubit gate based on a* Π*-shaped lateral quantum dot with spin-orbit interaction* Phys. Rev. B **79**, 045314 (2009).

[183] S. Nadj-Perge, S. M. Frolov, E. P. A. M. Bakkers, and L. P. Kouwenhoven, *Spin-orbit qubit in a semiconductor nanowire* Nature **468**, 1084 (2010).

[184] J. R. Petta, A. C. Johnson, J. M. Taylor, E. A. Laird, A. Yacoby, M. D. Lukin, C. M. Marcus, M. P. Hanson, and A. C. Gossard, *Coherent manipulation of coupled electron spins in semiconductor quantum dots* Science **309**, 2180 (2005).

[185] R. Brunner, Y.-S. Shin, T. Obata, M. Pioro-Ladrière, T. Kubo, K. Yoshida, T. Taniyama, Y. Tokura, and S. Tarucha, *Two-qubit gate of combined single-spin rotation and interdot spin exchange in a double quantum dot* Phys. Rev. Lett. **107**, 146801 (2011).

[186] T. Meunier, V. E. Calado, and L. M. K. Vandersypen, *Efficient controlled-phase gate for single-spin qubits in quantum dots* Phys. Rev. B **83**, 121403(R) (2011).

[187] A. C. Johnson, *Charge sensing and spin dynamics in GaAs quantum dots (Ph.D. thesis)* (Harvard, 2005).

[188] M. Ciorga, A. S. Sachrajda, P. Hawrylak, C. Gould, P. Zawadzki, S. Jullian, Y. Feng, and Z. Wasilewski, *Addition spectrum of a lateral dot from Coulomb and spin-blockade spectroscopy* Phys. Rev. B **61**, R16315 (2000).

[189] J. M. Elzerman, R. Hanson, L. H. W. van Beveren, B. Witkamp, L. M. K. Vandersypen, and L. P. Kouwenhoven, *Single-shot read-out of an individual electron spin in a quantum dot* Nature **430**, 431 (2004).

[190] Y.-S. Shin, T. Obata, Y. Tokura, M. Pioro-Ladrière, R. Brunner, T. Kubo, K. Yoshida, and S. Tarucha, *Single-Spin Readout in a Double Quantum Dot Including a Micromagnet* Phys. Rev. Lett. **104**, 046802 (2010).

[191] H. Bluhm, S. Foletti, I. Neder, M. Rudner, D. Mahalu, V. Umansky, and A. Yacoby, *Dephasing time of GaAs electron-spin qubits coupled to a nuclear bath exceeding 200μs* Nature Physics **7**, 109 (2011).

[192] P. M. Petroff, A. Lorke, and A. Imamoglu, *Epitaxially self-assembled quantum dots* Physics Today **54**, 46 (2001).

[193] E. M. Gauger, *Applications of quantum coherence in condensed matter nanostructures (Ph.D. Thesis)* (Oxford, 2009).

[194] A. Greilich, S. E. Economou, S. Spatzek, D. R. Yakovlev, D. Reuter, A. D. Wieck, T. L. Reinecke and M. Bayer, *Ultrafast optical rotations of electron spins in quantum dots* Nature Physics **5**, 262 (2009).

[195] A. J. Ramsay, S. J. Boyle, R. S. Kolodka, J. B. B. Oliveira, J. Skiba-Szymanska, H. Y. Liu, M. Hopkinson, A. M. Fox and M. S. Skolnick, *Fast optical preparation, control, and readout of a single quantum dot spin* Phys. Rev. Lett. **100**, 197401 (2008).

[196] P. Borri, W. Langbein, S. Schneider, and U. Woggon, *Ultralong dephasing time in InGaAs quantum dots* Phys. Rev. Lett. **87**, 157401 (2001).

[197] C. Bardot, M. Schwab, M. Bayer, S. Fafard, Z. Wasilewski, and P. Hawrylak, *Exciton lifetime in InAs/GaAs quantum dot molecules* Phys. Rev. B **72**, 035314 (2005).

[198] J. Berezovsky, M. H. Mikkelsen, O. Gywat, N. G. Stoltz, L. A. Coldren and D. D. Awschalom, *Nondestructive optical measurements of a single electron spin in a quantum dot* Science **314**, 1916 (2006).

[199] M. H. Mikkelsen, J. Berezovsky, N. G. Stoltz, L. A. Coldren and D. D. Awschalom, *Optically detected coherent spin dynamics of a single electron in a quantum dot* Nature Physics **3**, 770 (2007).

[200] G. Springholza, M. Pinczolitsa, V. Holyb, S. Zerlautha, I. Vavrac, and G. Bauer, *Vertical and lateral ordering in self-organized quantum dot superlattices* Physica E **9**, 149 (2001).

[201] Q. Xie, A. Madhukar, P. Chen, and N. P. Kobayashi, *Vertically self-organized InAs quantum box islands on GaAs(100)* Phys. Rev. Lett. **75**, 2542 (1995).

[202] G. S. Solomon, J. A. Trezza, A. F. Marshall, and J. S. Harris, Jr, *Vertically aligned and electronically coupled growth induced InAs islands in GaAs* Phys. Rev. Lett. **76**, 952 (1996).

[203] D. Leonard, M. Krishnamurthy, C. M. Reaves, S. P. Denbaars, and P. M. Petroff, *Direct formation of quantumsized dots from uniform coherent islands of InGaAs on GaAs surfaces* Appl. Phys. Lett. **63**, 3203 (1993).

[204] R. J. Warburton, C. Schäflein, D. Haft, F. Bickel, A. Lorke, K. Karrai, J. M. Garcia, W. Schoenfeld, and P. M. Petroff, *Optical emission from a charge-tunable quantum ring* Nature **405**, 926 (2000).

[205] P. Machnikowski, A. Grodecka, C. Weber, and A. Knorr, *Optical control and decoherence of spin qubits in quantum dots* Materials Science (Poland) **26**, 851 (2008).

[206] M Atatüre, J. Dreiser, A. Badolato, A. Högele, K. Karrai and A. Imamoglu, *Quantum-dot spin-state preparation with near-unity fidelity* Science **312**, 551 (2006).

[207] B. Eble, P. Desfonds, F. Fras, F. Bernardot, C. Testelin and M. Chamarro, *Hole and trion spin dynamics in quantum dots under excitation by a train of circularly polarized pulses* Phys. Rev. B **81**, 045322 (2010).

[208] C. Emary, X.-D. Xu, D. G. Steel, S. Saikin, and L. J. Sham, *Fast initialization of the spin state of an electron in a quantum dot in the Voigt configuration* Phys. Rev. Lett. **98**, 047401 (2007).

[209] X.-D. Xu, Y.-W. Wu, B. Sun, Q. Huang, J. Cheng, D. G. Steel, A. S. Bracker, D. Gammon, C. Emary, and L. J. Sham, *Fast spin state initialization in a singly charged InAs-GaAs quantum dot by optical cooling* Phys. Rev. Lett. **99**, 0907401 (2007).

[210] M. V. G. Dutt, J. Cheng, B. Li, X.-D. Xu, X.-Q. Li, P. R. Berman, D. G. Steel, A. S. Bracker, D. Gammon, S. E. Economou, R.-B. Liu, and L. J. Sham, *Stimulated and spontaneous optical generation of electron spin coherence in charged GaAs quantum dots* Phys. Rev. Lett. **94**, 227403 (2005).

[211] M. V. G. Dutt, J. Cheng, Y.-W. Wu, X.-D. Xu, D. G. Steel, A. S. Bracker, D. Gammon, S. E. Economou, R.-B. Liu, and L. J. Sham, *Ultrafast optical control of electron spin coherence in charged GaAs quantum dots* Phys. Rev. B **74**, 125306 (2006).

[212] A. Greilich, R. Oulton, E. A. Zhukov, I. A. Yugova, D. R. Yakovlev, M. Bayer, A. Shabaev, Al. L. Efros, I. A. Merkulov, V. Stavarache, D. Reuter, and A. Wieck, *Optical control of spin coherence in singly charged (In, Ga)As/GaAs quantum dots* Phys. Rev. Lett. **96**, 227401 (2006).

[213] T. Korn, M. Kugler, M. Griesbeck, R. Schulz, A. Wagner, M. Hirmer, C. Gerl, D. Schuh, W. Wegscheider, and C Schüller, *Engineering ultralong spin coherence in two-dimensional hole systems at low temperatures* New J. Phys. **12**, 043003 (2010).

[214] R. de Sousa and S. Das Sarma, *Electron spin coherence in semiconductors: Considerations for a spin-based solid-state quantum computer architecture* Phys. Rev. B **67**, 033301 (2003).

[215] A. Greilich, D. R. Yakovlev, A. Shabaev, Al. L. Efros, I. A. Yugova, R. Oulton, V. Stavarache, D. Reuter, A. Wieck, and M. Bayer, *Mode locking of electron spin coherences in singly charged quantum dots* Science **313**, 341 (2006).

[216] M. Kroutvar, Y. Ducommun, D. Heiss, M. Bichler, D. Schuh, G. Abstreiter, and J. J. Finley, *Optically programmable electron spin memory using semiconductor quantum dots* Nature **432**, 81 (2004).

[217] J. Berezovsky, M. H. Mikkelsen, N. G. Stoltz, L. A. Coldren and D. D. Awschalom, *Picosecond coherent optical manipulation of a single electron spin in a quantum dot* Science **320**, 349 (2008).

[218] J. A. Gupta, R. Knobel, N. Samarth, and D. D. Awschalom, *Ultrafast manipulation of electron spin coherence* Science **292**, 2458 (2001).

[219] D. Press, T. D. Ladd, B.-Y. Zhang, and Y. Yamamoto, *Complete quantum control of a single quantum dot spin using ultrafast optical pulses* Nature **456**, 218 (2008); also see references therein, for theoretical and experimental development of this technique.

[220] A. Imamoḡlu, D. D. Awschalom, G. Burkard, D. P. DiVincenzo, D. Loss, M. Sherwin, and A. Small, *Quantum information processing using quantum dot spins and cavity QED* Phys. Rev. Lett. **83**, 4204 (1999).

[221] P.-C. Chen, C. Piermarocchi, L. J. Sham, D. Gammon, and D. G. Steel, *Theory of quantum optical control of a single spin in a quantum dot* Phys. Rev. B **69**, 075320 (2004).

[222] Y.-W. Wu, E. D. Kim, X.-D. Xu, J. Cheng, D. G. Steel, A. S. Bracker, D. Gammon, S. E. Economou, and L. J. Sham, *Selective optical control of electron spin coherence in singly charged GaAs-$Al_{0.3}Ga_{0.7}As$ quantum dots* Phys. Rev. Lett. **99**, 097402 (2007).

[223] E. D. Kim, K. Truex, X.-D. Xu, B. Sun, D. G. Steel, A. S. Bracker, D. Gammon, and L. J. Sham, *Fast spin rotations by optically controlled geometric phases in a charge-tunable InAs quantum dot* Phys. Rev. Lett. **104**, 167401 (2010).

[224] M. Kroner, K. M. Weiss, B. Biedermann, S. Seidl, S. Manus, A. W. Holleitner, A. Badolato, P. M. Petroff, B. D. Gerardot, R. J. Warburton, and K. Karrai, *Optical detection of single-electron spin resonance in a quantum dot* Phys. Rev. Lett. **100**, 156803 (2008).

[225] A. N. Vamivakas, Y. Zhao, C.-Y. Lu, and M. Atatüre, *Spin-resolved quantum-dot resonance fluorescence* Nature Physics **5**, 198 (2009).

[226] A. N. Vamivakas, C.-Y. Lu, C. Matthiesen, Y. Zhao, S. Fält, A. Badolato, and M. Atatüre, *Observation of spin-dependent quantum jumps via quantum dot resonance fluorescence* Nature **467**, 297 (2010).

[227] A. Nazir, B. W. Lovett, S. D. Barrett, T. P. Spiller and G. A. D. Briggs, *Selective spin coupling through a single exciton* Phys. Rev. Lett. **93**, 150502 (2004).

[228] E. M. Gauger, A. Nazir, S. C. Benjamin, T. M Stace and B. W. Lovett, *Robust adiabatic approach to optical spin entangling in coupled quantum dots* New J. Phys. **10**, 073016 (2009).

[229] C. Emary and L. J. Sham, *Optically controlled logic gates for two spin qubits in vertically coupled quantum dots* Phys. Rev. B **75**, 125317 (2007).

[230] L.-B. Chen, L. J. Sham, and E. Waks, *Optically controlled phase gate for two spin qubits in coupled quantum dots* Phys. Rev. B **85**, 115319 (2012).

[231] D. Kim, S. G. Carter, A. Greilich, A. S. Bracker, and D. Gammon, *Ultrafast optical control of entanglement between two quantum-dot spins* Nature Physics **7**, 223 (2011).

[232] T. Hayashi, T. Fujisawa, H. D. Cheong, Y. H. Jeong, and Y. Hirayama, *Coherent manipulation of electronic states in a double quantum dot* Phys. Rev. Lett. **91**, 226804 (2003).

[233] S. M. de Vasconcellos, S. Gordon, M. Bichler, T. Meier, and A. Zrenner, *Coherent control of a single exciton qubit by optoelectronic manipulation* Nature Photonics **4**, 545 (2010); also see references therein.

[234] J. Wrachtrup and F. Jelezko, *Processing quantum information in diamond* J. Phys.: Condens. Matter **18**, S807 (2006).

[235] B. E. Kane, *A silicon-based nuclear spin quantum computer* Nature **393**, 133 (1998).

[236] R. Vrijen, E. Yablonovitch, K. Wang, H. W. Jiang, A. Balandin, V. Roychowdhury, T. Mor, and D. DiVincenzo, *Electron-spin-resonance transistors for quantum computing in silicon-germanium heterostructures* Phys. Rev. A **62**, 012306 (2000).

[237] G. Waldherr, J. Beck, M. Steiner, P. Neumann, A. Gali, Th. Frauenheim, F. Jelezko, and J. Wrachtrup, *Dark states of single nitrogen-vacancy centers in diamond unraveled by single shot NMR* Phys. Rev. Lett. **106**, 157601 (2011).

[238] A. M. Tyryshkin, S. A. Lyon, A. V. Astashkin, and A. M. Raitsimring, *Electron spin relaxation times of phosphorus donors in silicon* Phys. Rev. B **68**, 193207 (2003).

[239] E. Abe, A. M. Tyryshkin, S. Tojo, J. J. L. Morton, W. M. Witzel, A. Fujimoto, J. W. Ager, E. E. Haller, J. Isoya, S. A. Lyon, M. L. W. Thewalt, and K. M. Itoh, *Electron spin coherence of phosphorus donors in silicon: Effect of environmental nuclei* Phys. Rev. B **82**, 121201(R) (2010).

[240] G. Balasubramanian, P. Neumann, D. Twitchen, M. Markham, R. Kolesov, N. Mizuochi, J. Isoya, J. Achard, J. Beck, J. Tissler, V. Jacques, P. R. Hemmer, F. Jelezko, and J. Wrachtrup, *Ultralong spin coherence time in isotopically engineered diamond* Nature Materials **8**, 383 (2009).

[241] J. J. L. Morton, A. M. Tyryshkin, R. M. Brown, S. Shankar, B. W. Lovett, A. Ardavan, T. Schenkel, E. E. Haller, J. W. Ager, and S. A. Lyon, *Solid-state quantum memory using the* ^{31}P *nuclear spin* Nature **455**, 1085 (2008).

[242] A. M. Tyryshkin, S. Tojo, J. J. L. Morton, H. Riemann, N. V. Abrosimov, P. Becker, H.-J. Phol, T. Schenkel, M. L. W. Thewalt, K. M. Itoh, and S. A. Lyon, *Electron spin coherence exceeding seconds in high-purity silicon* Nature Materials **11**, 143 (2012).

[243] A. M. Tyryshkin, Z.-H. Wang, W.-X. Zhang, E. E. Haller, J. W. Ager, V. V. Dobrovitski, and S. A. Lyon, *Dynamical decoupling in the presence of realistic pulse errors* arXiv:1011.1903 (2010).

[244] N. Bar-Gill, L. M. Pham, C. Belthangady, D. Le Sage, P. Cappellaro, J. R. Maze, M. D. Lukin, A. Yacoby, and R. Walsworth, *Suppression of spin-bath dynamics for improved coherence of multi-spin-qubit systems* Nature Comms. **3**, 858 (2012).

[245] P. C. Maurer, G. Kucsko, C. Latta, L. Jiang, N. Y. Yao, S. D. Bennett, F. Pastawski, D. Hunger, N.Chisholm, M. Markham, D. J. Twitchen, J. I. Cirac, and M. D. Lukin, *Room-temperature quantum bit memory exceeding one second* Science **336**, 1283 (2012).

[246] G. de Lange, Z. H. Wang, D. Ristè, V. V. Dobrovitski, and R. Hanson, *Universal dynamical decoupling of a single solid-state spin from a spin bath* Science **330**, 60 (2010).

[247] G. Feher, *Electron spin resonance experiements on donors in silicon: II. Electron spin relaxation effects* Phys. Rev. **114**, 1245 (1959).

[248] D. A. Redman, S. Brown, R. H. Sands, and S. C. Rand, *Spin dynamics and electronic states of N-V centers in diamond by EPR and four-wave-mixing spectroscopy* Phys. Rev. Lett. **67**, 3420 (1991).

[249] S. Takahashi, R. Hanson, J. van Tol, M. S. Sherwin, and D. D. Awscholm, *Quenching spin decoherence in diamond through spin bath polarization* Phys. Rev. Lett. **101**, 047601 (2008).

[250] J. L. O'Brien, S. R. Schofield, M. Y. Simmons, R. G. Clark, A. S. Dzurak, N. J. Curson, B. E. Kane, N. S. McAlpine, M. E. Hawley, and G. W. Brown, *Towards the fabrication of phosphorus qubits for a silicon quantum computer* Phys. Rev. B **64**, 161401(R) (2001).

[251] F. J. Ruess, L. Oberbeck, M. Y. Simmons, K. E. J. Goh, A. R. Hamilton, T. Hallam, S. R. Schofield, N. J. Curson, and R. G. Clark, *Toward atomic-scale device fabrication in silicon using scanning probe microscopy* Nano Lett. **4**, 1969 (2004).

[252] G. P. Lansbergen, R. Rahman, C. J. Wellard, I. Woo, J. Caro, N. Collaert, S. Biesemans, G. Klimeck, L. C. L. Hollenberg, and S. Rogge, *Gate-induced quantum-confinement transition of a single dopant atom in a silicon FinFET* Nature Physics **4**, 656 (2008).

[253] A. J. Skinner, M. E. Davenport and B. E. Kane, *Hydrogenic spin quantum computing in silicon: A digital approach* Phys. Rev. Lett. **90**, 087901 (2003).

[254] J. J. Pla, K. Y. Tan, J. P. Dehollain, W. H. Lim. J. J. L. Morton, D. N. Jamieson, A. S. Dzurak, and A. Morello *A single-atom electron spin qubit in silicon* Nature **489**, 541 (2012).

[255] M. Steger, K. Saeedi, M. L. W. Thewalt, J. J. L. Morton, H. Riemann, N. V. Abrosimov, P. Becker, and H.-J. Phol, *Quantum information storage for over 180s using donor spins in a ^{28}Si "semiconductor vacuum"* Science **336**, 1280 (2012).

[256] N. Khaneja, *Switched control of electron nuclear spin systems* Phys. Rev. A **76**, 032326 (2007).

[257] J. S. Hodges, J. C. Yang, C. Ramanathan, and D. G. Cory, *Universal control of nuclear spins via anisotropic hyperfine interactions* Phys. Rev. A **78**, 010303(R) (2008).

[258] D. R. McCamey, J. van Tol, G. W. Morley, and C. Boehme, *Electronic spin storage in an electrically readable nuclear spin memory with a lifetime > 100 seconds* Science **330**, 1652 (2010).

[259] S. Simmons, R. M. Brown, H. Riemann, N. V. Abrosimov, P. Becker, H.-J. Pohl, M. L. W. Thewalt, K. M. Itoh, and J. J. L. Morton, *Entanglement in a solid-state spin ensemble* Nature **470**, 69 (2011).

[260] M. Mehring, J. Mende, and W. Scherer, *Entanglement between an electron and a nuclear spin 1/2* Phys. Rev. Lett. **90**, 153001 (2003).

[261] A. M. Tyryshkin, J. J. L. Morton, A. Ardavan, and S. A. Lyon, *Davies electron-nuclear double resonance revisited: Enhanced sensitivity and nuclear spin relaxation* J. Chem. Phys. **124**, 234508 (2006).

[262] A. R. Stegner, C. Boehme, H. Huebl, M. Stutzmann, K. Lips, and M. S. Brandt, *Electrical detection of coherent ^{31}P spin quantum states* Nature Physics **2**, 835 (2006).

[263] H. Morishita, L. S. Vlasenko, H. Tanaka, K. Semba, K. Sawano, Y. Shiraki, M. Eto, and K. M. Itoh, *Electrical detection and magnetic-field control of spin states in phosphorus-doped silicon* Phys. Rev. B **80**, 205206 (2009).

[264] A. Morello, J. J. Pla, F. A. Zwanenburg, K. W. Chan, K. Y. Tan, H. Huebl, M. Möttönen, C. D. Nugroho, C.-Y. Yang, J. A. van Donkelaar, A. D. C. Alves, D. N. Jamieson, C. C. Escott, L. C. L. Hollenberg, R. G. Clark,and A. S. Dzurak *Single-shot readout of an electron spin in silicon* Nature **467**, 687 (2010).

[265] M. H. Devoret and R. Schoelkopf, *Amplifying quantum signals with the single-electron transistor* Nature **406**, 1039 (2000).

[266] A. Yang, M. Steger, D. Karaiskaj, M. L. W. Thewalt, M. Cardona, K. M. Itoh, H. Riemann, N. V. Abrosimov, M. F. Churbanov, A. V. Gusev, A. D. Bulanov, A. K. Kaliteevskii, O. N. Godisov, P. Becker, H.-J. Pohl, J. W. Ager III, and E. E. Haller, *Optical detection and ionization of donors in specific electronic and nuclear spin states* Phys. Rev. Lett. **97**, 227401 (2006).

[267] M. Steger, T. Sekiguchi, A. Yang, K. Saeedi, M. E. Hayden, M. L. W. Thewalt, K. M. Itoh, H. Riemann, N. V. Abrosimov, P. Becker, and H.-J. Pohl, *Optically-detected NMR of optically-hyperpolarized ^{31}P neutral donors in ^{28}Si* J. Appl. Phys. **109**, 102411 (2011).

[268] D. R. McCamey, J. van Tol, G. W. Morley, and C. Boehme, *Fast nuclear spin hyperpolarization of phosphorus in silicon* Phys. Rev. Lett. **102**, 027601 (2009).

[269] A. Yang, M. Steger, T. Sekiguchi, M. L. W. Thewalt, T. D. Ladd, K. M. Itoh, H. Riemann, N. V. Abrosimov, P. Becker, and H.-J. Pohl, *Simultaneous subsecond hyperpolarization of the nuclear and electron spins of phosphorus in silicon by optical pumping of exciton transitions* Phys. Rev. Lett. **102**, 257401 (2009).

[270] A. M. Stoneham, A. H. Harker, and G. W. Morley, *Could one make a diamond-based quantum computer* J. Phys.: Condens. Matter **21**, 364222 (2009).

[271] E. van Oort, N. B. Manson, and M. Glasbeek, *Optically detected spin coherence of the diamond N-V centre in its triplet ground state* J. Phys. C: Solid State Phys. **21**, 4385 (1988).

[272] G. Davies and M. F. Hamer, *Optical studies of the 1.945 eV vibronic band in diamond* Proc. Roy. Soc. (London) A **348**, 285 (1976).

[273] Ph. Tamarat, N. B. Manson, J. P. Harrison, R. L. McMurtrie, A. Nizovtsev, C. Santori, R. G. Beausoleil, P. Neumann, T. Gaebel, F. Jelezko, P. Hemmer, and J. Wrachtrup, *Spin-flip and spin-conserving optical transitions of the nitrogen-vacancy centre in diamond* New J. Phys. **10**, 045004 (2008).

[274] N. B. Manson, J. P. Harrison, and M. J. Sellars, *Nitrogen-vacancy center in diamond: Model of the electronic structure and associated dynamics* Phys. Rev. B **74**, 104303 (2006).

[275] L. J. Rogers, S. Armstrong, M. J. Sellars, and N. B. Manson, *New infrared emission of the NV centre in diamond: Zeeman and uniaxial stress studies* New J. Phys. **10**, 103024 (2008).

[276] M. W. Doherty, N. B. Manson, P. Delaney, and L. C. L. Hollenberg, *The negatively charged nitrogen-vacancy centre in diamond: the electronic solution* New J. Phys. **13**, 025019 (2011).

[277] J. Harrison, M. J. Sellars, N. B. Manson, *Measurement of the optically induced spin polarization of N-V centres in diamond* Diam. Relat. Mater. **15**, 586 (2006).

[278] P. Neumann, R. Kolesov, B. Naydenov, J. Beck, F. Rempp, M. Steiner, V. Jacques, G. Balasubramanian, M. L. Markham, D. J. Twitchen, S. Pezzagna, J. Meijer, J. Twamley, F. Jelezko, and J.Wrachtrup, *Quantum register based on coupled electron spins in a room-temperature solid* Nature Physics **6**, 249 (2010).

[279] F. Jelezko, T. Gaebel, I. Popa, A. Gruber, and J.Wrachtrup, *Observation of coherent oscillations in a single electron spin* Phys. Rev. Lett. **92**, 076401 (2004).

[280] P. C. Maurer, J. R. Maze, P. L. Stanwix, L. Jiang, A. V. Gorshkov, A. A. Zibrov, B. Harke, J. S. Hodges, A. S. Zibrov, A. Yacob1, D. Twitchen, S.W. Hell, R. L.Walsworth, and M. D. Lukin *Far-field optical imaging and manipulation of individual spins with nanoscale resolution* Nature Physics **6**, 912 (2010).

[281] G. D. Fuchs, G. Burkard, P. V. Klimov, and D. D. Awschalom, *A quantum memory intrinsic to single nitrogenvacancy centres in diamond* Nature Physics **7**, 789 (2011).

[282] F. Jelezko, T. Gaebel, I. Popa, M. Domhan, A. Gruber, and J. Wrachtrup, *Observation of coherent oscillation of a single nuclear spin and realization of a two-qubit conditional quantum gate* Phys. Rev. Lett. **93**, 130501 (2004).

[283] M. V. G. Dutt, L. Childress, L. Jiang, E. Togan, J. Maze, F. Jelezko, A. S. Zibrov, P. R. Hemmer, and M. D. Lukin, *Quantum register based on individual electronic and nuclear spin qubits in diamond* Science **316**, 1312 (2007).

[284] L. Jiang, M. V. G. Dutt, E. Togan, L. Childress, P. Cappellaro, J. M. Taylor, and M. D. Lukin, *Coherence of an optically illuminated single nuclear spin qubit* Phys. Rev. Lett. **100**, 073001 (2008).

[285] L. Childress, M. V. G. Dutt, J. M. Taylor, A. S. Zibrov, F. Jelezko, J. Wrachtrup, P. R. Hemmer, and M. D. Lukin, *Coherent dynamics of coupled electron and nuclear spin qubits in diamond* Science **314**, 281 (2006).

[286] P. Cappellaro, L. Jiang, J. S. Hodges, and M. D. Lukin, *Coherence and control of quantum registers based on electronic spin in a nuclear spin bath* Phys. Rev. Lett. **102**, 210502 (2009).

[287] P. Neumann, J. Beck, M. Steiner, F. Rempp, H. Fedder, P. R. Hemmer, J. Wrachtrup, F. Jelezko, *Single-shot readout of a single nuclear spin* Science **329**, 542 (2010).

[288] L. Jiang, J. S. Hodges, J. R. Maze, P. Maurer, J. M. Taylor, D. G. Cory, P. R. Hemmer, R. L. Walsworth, A. Yacoby, A. S. Zibrov, and M. D. Lukin, *Repetitive readout of a single electronic spin via quantum logic with nuclear spin ancillae* Science **326**, 267 (2009).

[289] L. Robledo, L. Childress, H. Bernien, B. Hensen, P. F. A. Alkemade, and R. Hanson, *High-fidelity projective read-out of a solid-state spin quantum register* Nature **477**, 574 (2011).

[290] H. Bernien, L. Childress, L. Robledo, M. Markham, D. Twitchen, and R. Hanson, *Two-photon quantum interference from separate nitrogen vacancy centers in diamond* Phys. Rev. Lett. **108**, 043604 (2012).

[291] W. Pfaff, T. H. Taminiau, L. Robledo, H. Bernien, M. L. Markham, D. J. Twitchen, and R. Hanson, *Demonstration of entanglement-by-measurement of solid state qubits* Nature Physics **9**, 29 (2013).

[292] R. Hanson, F. M. Mendoza, R. J. Epstein, and D. D. Awschalom, *Polarization and readout of coupled single spins in diamond* Phys. Rev. Lett. **97**, 087601 (2006).

[293] R. J. Epstein, F. M. Mendoza, Y. K. Kato, and D. D. Awschalom, *Anisotropic interactions of a single spin and dark-spin spectroscopy in diamond* Nature Physics **1**, 94 (2005).

[294] J. R. Rabeau, P. Reichart, G. Tamanyan, D. N. Jamieson, S. Prawer, F. Jelezko, T.Gaebel, I. Popa, M. Domhan, and J. Wrachtrup, *Implantation of labelled single nitrogen vacancy centersin diamond using* ^{15}N Appl. Phys. Lett. **88**, 023113 (2006).

[295] P. Spinicelli, A. Dréau, L. Rondin, F. Silva, J. Achard, S. Xavier, S. Bansropun, T. Debuisschert, S. Pezzagna, J. Meijer, V. Jacques, and J.-F. Roch, *Engineered arrays of nitrogen-vacancy color centers in diamond based on implantation of* CN^- *molecules through nanoapertures* New J. Phys. **13**, 025014 (2011).

[296] C. Vieu, F. Carcenac, A. Pépin, T. Chen, M. Mejias, A. Lebib, L. Manin-Ferlazzo, L. Couraud, H. Launois, *Electron beam lithography: resolution limits and applications* Appl. Surf. Sci. **164**, 111 (2000).

[297] Y. Kubo, F. R. Ong, P. Bertet, D. Vion, V. Jacques, D. Zheng, A. Dréau, J.-F. Roch, A. Auffeves, F. Jelezko, J. Wrachtrup, M. F. Barthe, P. Bergonzo, and D. Esteve, *Strong coupling of a spin ensemble to a superconducting resonator* Phys. Rev. Lett. **105**, 140502 (2010).

[298] W. Harneit, *Fullerene-based electron-spin quantum computer* Phys. Rev. A **65**, 032322 (2002).

[299] S. C. Benjamin, A. Ardavan, G. A. D. Briggs, D. A. Britz, D. Gunlycke, J. H. Jefferson, M. A. G. Jones, D. F. Leigh, B. W. Lovett, A. N. Khlobystov, S. A. Lyon, J. J. L. Morton, K. Porfyrakis, M. R. Sambrook, and A. M Tyryshkin, *Towards a fullerene-based quantum computer* J. Phys.: Condens. Matter **18**, S867 (2006).

[300] J. J. L. Morton, A. M. Tyryshkin, A. Ardavan, S. C. Benjamin, K. Porfyrakis, S. A. Lyon, and G. A. D. Briggs, *Bang-bang control of fullerene qubits using ultrafast phase gates* Nature Physics **2**, 40 (2006).

[301] J. J. L. Morton, A. M. Tyryshkin, A. Ardavan, K. Porfyrakis, S. A. Lyon, and G. A. D. Briggs, *Electron spin relaxation of $N@C_{60}$ in CS_2* J. Chem. Phys. **124**, 014508 (2006).

[302] R. M. Brown, Y. Ito, J. Warner, A. Ardavan, H. Shinohara, G. A.. D. Briggs, and J. J. L. Morton, *Electron spin coherence in metallofullerenes: Y, Sc and $La@C_{82}$* Phys. Rev. B **82**, 033410 (2010).

[303] J. J. L. Morton, A. M. Tyryshkin, A. Ardavan, K. Porfyrakis, S. A. Lyon, and G. A. D. Briggs, *High fidelity single qubit operations using pulsed electron paramagnetic resonance* Phys. Rev. Lett. **95**, 200501 (2005).

[304] R. M. Brown, A. M. Tyryshkin, K. Porfyrakis, E. M. Gauger, B. W. Lovett, A. Ardavan, S. A. Lyon, G. A. D. Briggs, and J. J. L. Morton, *Coherent state transfer between an electron and nuclear spin in $^{15}N@C_{60}$* Phys. Rev. Lett. **106**, 110504 (2011).

[305] M. Mehring, W. Scherer, and A. Weidinger, *Pseudoentanglement of spin states in the multilevel $^{15}N@C_{60}$* Phys. Rev. Lett. **93**, 206603 (2004).

[306] B. W. Smith, M. Monthioux, and D. E. Luzzi, *Encapsulated C_{60} in carbon nanotubes* Nature **396**, 323 (1998).

[307] T. A. Murphy, Th. Pawlik, A. Weidinger, M. Höhne, R. Alcala, and J.-M. Spaeth, *Observation of atomlike nitrogen in nitrogen-implanted solid C_{60}* Phys. Rev. Lett. **77**, 1075 (1996).

[308] A. N. Khlobystov, D. A. Britz, A. Ardavan, and G. A. D. Briggs, *Observation of ordered phases of fullerenes in carbon nanotubes* Phys. Rev. Lett. **92**, 245507 (2004).

[309] A. N. Khlobystov, D. A. Britz, J.-W. Wang, S. A. O'Neil, M. Poliakoff, and G. A. D. Briggs, *Low temperature assembly of fullerene arrays in single-walled carbon nanotubes using supercritical fluids* J. Mater. Chem. **14**, 2852 (2004).

[310] F. Simon, H. Kuzmany, H. Rauf, T. Pichler, J. Bernardi, H. Peterlik, L. Korecz, F. Fülöp, A. Jánossy, *Low temperature fullerene encapsulation in single*

wall carbon nanotubes: systhesis of $N@C_{60}@SWCNT$ Chem. Phys. Lett. **383**, 362 (2004).

[311] X.-S. Wang, Q.-Q. Li, J. Xie, Z. Jin, J.-Y. Wang, Y. Li, K.-L. Jiang, and S.-S. Fan *Fabrication of ultralong and electrically uniform single-walled carbon nanotubes on clean substrates* Nano Lett. **9**, 3137 (2009).

[312] L. A. W. Robinson, S.-B. Lee, K. B. K. Teo, M. Chhowalla, G. A. J. Amaratunga, W. I. Milne, D. A. Williams, D. G. Hasko, and H. Ahmed, *Fabrication of self-aligned side gates to carbon nanotubes* Nanotechnology **14**, 290 (2003).

[313] M. J. Biercuk, S. Garaj, N. Mason, J. M. Chow, and C. M. Marcus, *Gate-defined quantum dots on carbon nanotubes* Nano Lett. **5**, 1267 (2005).

[314] S. Lloyd, *A potentially realizable quantum computer* Science **261**, 1569 (1993).

[315] S. C. Benjamin, *Quantum computing without local control of qubit-qubit interactions* Phys. Rev. Lett. **88**, 017904 (2002).

[316] L. P. Kouwenhoven, A. T. Johnson, N. C. van der Vaart, and C. J. P. M. Harmans, *Quantized current in a quantum-dot turnstile using oscillating tunnel barriers* Phys. Rev. Lett. **67**, 1626 (1991).

[317] C. T. White and T. N. Todorov, *Carbon nanotubes as long ballistic conductors* Nature **393**, 240 (1998).

[318] A. Javey, J. Guo, Q. Wang, M. Lundstrom, and H.-J. Dai, *Ballistic carbon nanotube field-effect transistors* Nature **424**, 654 (2003).

[319] F. Miao, S. Wijeratne, U. Coskun, Y. Zhang, C. N. Lau, *Phase-coherent transport of charges in graphene quantum billiards* Science **317**, 1530 (2007).

[320] Y.-W. Hsu, S.-P. Chiu, A.-S. Lien, and J.-J. Lin, *Long electron dephasing length and disorder-induced spin-orbit coupling in indium tin oxide nanowires* Phys. Rev. B **82**, 195429 (2010).

[321] K. Aihara, M. Yamamoto, K. Iwadate, and T. Mizutani, *Temperature dependence of the phase coherence length of high-mobility AlGaAs/GaAs quantum-wire rings* Jpn. J. Appl. Phys. **30**, L1627 (1991).

[322] M. Ferrier, L. Angers, A. C. H. Rowe, S. Guéron, H. Bouchiat, C. Texier, G. Montambaux, and D. Mailly, *Direct measurement of the phase-coherence length in a GaAs-GaAlAs square network* Phys. Rev. Lett. **93**, 246804 (2004).

[323] A. L. Cantone, M. R. Buitelaar, C. G. Smith, D. Anderson, G. A. C. Jones, S. J. Chorley, C. Casiraghi, A. Lombardo, A. C. Ferrari, H. Shinohara, A. Ardavan, J. Warner, A. A. R. Watt, K. Porfyrakis, and G. A. D. Briggs, *Electronic transport characterization of $Sc@C_{82}$ single-wall carbon nanotube peapods* J. Appl. Phys. **104**, 083717 (2008).

[324] N. Tombros, C. Jozsa, M. Popinciuc, H. T. Jonkman, and B. J. van Wees, *Electronic spin transport and spin precession in single graphene layers at room temperature* Nature **448**, 571 (2007).

[325] A. A. Kozikov, D. W. Horsell, E. McCann, and V. I. Fal'ko, *Evidence for spin memory in the electron phase coherence in graphene* Phys. Rev. B **86**, 045436 (2012).

[326] A. Kumar and B. Ghosh, *Spin dephasing in III-V nanowires* arXiv:1106.4618 (2011).

[327] Y. Kato, R. C. Myers, A. C. Gossard, and D. D. Awschalom, *Coherent spin manipulation without magnetic fields in strained semiconductors* Nature **427**, 50 (2004).

[328] J. H. Jefferson, A. Ramšak, and T. Rejec, *Entanglement between static and flying qubits in quantum wires* Europhys. Lett. **74**, 764 (2006).

[329] D. Gunlycke, J. H. Jefferson, T. Rejec, A. Ramšak, D. G. Pettifor, and G. A. D. Briggs, *Entanglement between static and flying qubits in a semiconducting carbon nanotube* J. Phys.: Condens. Matter **18**, S851 (2006).

[330] M. Habgood, J. H. Jefferson, and G. A. D. Briggs, *Scattering-induced entanglement between spin qubits at remote two-state structures* J. Phys.: Condens. Matter **21**, 075503 (2009).

[331] L. D. Landau, *Theory of Fermi-liquids* Zh. Eksp. Teor. Fiz. **30**, 1058 (1956).

[332] A. T. Hanbicki, B. T. Jonker, G. Itskos, G. Kioseoglou, and A. Petrou, *Efficient electrical spin injection from a magnetic metal/tunnel barrier contact into a semiconductor* Appl. Phys. Lett. **80**, 1240 (2002).

[333] E. D. Fraser, S. Hegde, L. Schweidenback, A. H. Russ, A. Petrou, H. Luo, and G. Kioseoglou, *Efficient electron spin injection in MnAs-based spin-light-emitting-diodes up to room temperature* Appl. Phys. Lett. **97**, 041103 (2010).

[334] C. H. W. Barnes, J. M. Shilton, and A. M. Robinson, *Quantum computation using electrons trapped by surface acoustic waves* Phys. Rev. B **62**, 8410 (2000).

[335] P. M. Platzman and M. I. Dykman, *Quantum computing with electrons floating on liquid Helium* Science **284**, 1967 (1999).

[336] J. Clarke and F. K. Wilhelm, *Superconducting quantum bits* Nature **453**, 1031 (2008).

[337] C. Padurariu and Yu. V. Nazarov, *Theoretical proposal for superconducting spin qubits* Phys. Rev. B **81**, 144519 (2010).

[338] A. Wallraff, D. I. Schuster, A. Blais, L. Frunzio, R.-S. Huang, J. Majer, S. Kumar, S. M. Girvin, and R. J. Schoelkopf, *Strong coupling of a single photon to a superconducting qubit using circuit quantum electrodynamics* Nature **431**, 162 (2004).

[339] A. Blais, R.-S. Huang, A. Wallraff, S. M. Girvin, and R. J. Schoelkopf, *Cavity quantum electrodynamics for superconducting electrical circuits: An architecture for quantum computation* Phys. Rev. A **69**, 062320 (2004).

[340] J. Bardeen, L. N. Cooper, and J. R. Schrieffer, *Theory of superconductivity* Phys. Rev. **108**, 1175 (1957).

[341] P. Lafarge, P. Joyez, D. Esteve, C. Urbina, and M. H. Devoret, *Two-electron quantization of the charge on a superconductor* Nature **365**, 422 (1993).

[342] B. D. Josephson, *Possible new effects in superconductive tunnelling* Phys. Lett. **1**, 251 (1962).

[343] M. Büttiker, *Zero-current persistent potential drop across small-capacitance Josephson junctions* Phys. Rev. B **36**, 3548 (1987).

[344] L. J. Geerligs, V. F. Anderegg, J. Romijn, and J. E. Mooji, *Single Cooper-pair tunneling in small-capacitance junctions* Phys. Rev. Lett. **65**, 377 (1990).

[345] V. Bouchiat, D. Vion, P. Joyez, D. Esteve, and M. H. Devoret, *Quantum coherence with a single Cooper pair* Phys. Scr. **T76**, 165 (1998).

[346] Y. Nakamura, Yu. A. Pashkin, and J. S. Tsai, *Coherent control of macroscopic quantum states in a single-Cooper-pair box* Nature **398**, 786 (1999).

[347] T. Yamamoto, Yu. A. Pashkin, O. Astafiev, Y. Nakamura, and J. S. Tsai, *Demonstration of conditional gate operation using superconducting charge qubits* Nature **425**, 941 (2003).

[348] J. Majer, J. M. Chow, J. M. Gambetta, J. Koch, B. R. Johnson, J. A. Schreier, L. Frunzio, D. I. Schuster, A. A. Houck, A. Wallraff, A. Blais, M. H. Devoret, S. M. Girvin, and R. J. Schoelkopf, *Coupling superconducting qubits via a cavity bus* Nature **449**, 443 (2007).

[349] Y. Nakamura, Yu. A. Pashkin, T. Yamamoto, and J. S. Tsai, *Charge echo in a Cooper-pair box* Phys. Rev. Lett. **88**, 047901 (2002).

[350] D. Vion, A. Aassime, A. Cottet, P. Joyez, H. Pothier, C. Urbina, D. Esteve, and M. H. Devoret, *Manipulating the quantum state of an electrical circuit* Science **296**, 886 (2002).

[351] J. Koch, T. M. Yu, J. Gambetta, A. A. Houck, D. I. Schuster, J. Majer, A. Blais, M. H. Devoret, S. M. Girvin, and R. J. Schoelkopf, *Charge-insensitive qubit design derived from the Cooper pair box* Phys. Rev. A **76**, 042319 (2007).

[352] J. A. Schreier, A. A. Houck, J. Koch, D. I. Schuster, B. R. Johnson, J. M. Chow, J. M. Gambetta, J. Majer, L. Frunzio, M. H. Devoret, S. M. Girvin, and R. J. Schoelkopf, *Suppressing charge noise decoherence in superconducting charge qubits* Phys. Rev. B **77**, 180502(R) (2008).

[353] A. A. Houck, J. Koch, M. H. Devoret, S. M. Girvin, and R. J. Schoelkopf, *Life after charge noise: recent results with transmon qubits* Quantum Inf. Process. **8**, 105 (2009).

[354] D. I. Schuster, A. P. Sears, E. Ginossar, L. DiCarlo, L. Frunzio, J. J. L. Morton, H. Wu, G. A. D. Briggs, B. B. Buckley, D. D. Awschalom, and R. J. Schoelkopf, *High-cooperativity coupling of eletron-spin ensembles to superconducting cavities* Phys. Rev. Lett. **105**, 140501 (2010).

[355] J. Hubbard, *Electron correlations in narrow energy bands* Proc. Roy. Soc. (London) A **276**, 238 (1963).

[356] H. Bruus and K. Flensberg, *Many body quantum theory in condensed matter physics* (Oxford, 2004).

[357] C. Kittel, *Introduction to solid state physics, 8th edition* (Wiley, 2005).

[358] J. Spałek, *t-J model then and now: A personal perspective from the pioneering times* Acta Physica Polonica A **111**, 409 (2007).

[359] C. L. Cleveland and R. A. Medina, *Obtaining a Heisenberg Hamiltonian from the Hubbard model* Am. J. Phys. **44**, 44 (1976).

[360] G. Burkard, D. Loss, and D. P. DiVincenzo, *Coupled quantum dots as quantum gates* Phys. Rev. B **59**, 2070 (1999).

[361] H.-A. Engel, L. P. Kouwenhoven, D. Loss, and C. M. Marcus, *Controlling spin qubits in quantum dots* Quantum Inf. Process. (Springer) **3**, 115 (2004).

[362] L. Ge, B. Montanari, J. H. Jefferson, D. G. Pettifor, N. M. Harrison, and G. A. D. Briggs, *Modeling spin interactions in carbon peapods using a hybrid density functional theory* Phys. Rev. B **77**, 235416 (2008).

[363] Y. Ito, W. Fujita, T. Okazaki, T. Sugai, K. Awaga, E. Nishibori, M. Takata, M. Sakata, and H. Shinohara, *Magnetic properties and crystal structure of solvent-free $Sc@C_{82}$ metallofullerene microcrystals* Chem. Phys. Chem. **8**, 1019 (2007).

[364] M. Zaka, J. H. Warner, Y. Ito, J. J. L. Morton, M. H. Rümmeli, T. Pichler, A. Ardavan, H. Shinohara, and G. A. Briggs, *Exchange interactions of spin-active metallofullerenes in solid-state carbon networks* Phys. Rev. B **81**, 075424 (2010).

[365] H. Ebert and S. Mankovsky, *Anisotropic exchange coupling in diluted magnetic semiconductors: Ab initio spin-density functional theory* Phys. Rev. B **79**, 045209 (2009).

[366] A. Auerbach, *Interacting electrons and quantum magnetism* (Springer-Verlag, 1994).

[367] M. Greiner, O. Mandel, T. Esslinger, T. W. Hänsch, and I. Bloch, *Quantum phase transition from a superfluid to a Mott insulator in a gas of ultracold atoms* Nature **415**, 39 (2002).

[368] G. Pennington and N. Goldsman, *Semiclassical transport and phonon scattering of electrons in semiconducting carbon nanotubes* Phys. Rev. B **68**, 045426 (2003).

[369] N. Nishiguchi, *Electron scattering due to confined and extended acoustic phonons in a quantum wire* Phys. Rev. B **54**, 1494 (1996).

[370] A. Cox, M. E. Newton, and J. M. Baker, *^{13}C, ^{14}N and ^{15}N ENDOR measurements on the single substitutional nitrogen centre (Pl) in diamond* J. Phys.: Condens. Matter **6**, 551 (1994).

[371] C. Kedkaew, P. Limsuwan, K. Thongcham, and S. Meejoo, *The spin Hamiltonian parameters calculation of ^{14}N and ^{15}N in natural type I diamond* Int. J. Mod. Phys. B **22**, 4740 (2008).

[372] J. C. Cordes, *The secular approximation with dipole-dipole interaction* J. Phys. B: At. Mol. Phys. **20**, 1433 (1987).

[373] F. Ciccarello, M. Paternostro, M. S. Kim, and G. M. Palma, *Extraction of singlet states from noninteracting high-dimensional spins* Phys. Rev. Lett. **100**, 150501 (2008).

[374] F. Ciccarello, M. Paternostro, G. M. Palma, and M. Zarcone, *Reducing quantum control for spin-spin entanglement distribution* New J. Phys. **11**, 113053 (2009).

[375] N. Dupuis and K. Sengupta, *Superfluid to Mott-insulator transition of cold atoms in optical lattices* Physica B: Condens. Matter **404**, 517 (2009).

[376] V. Averbukh, S. Osovski, and N. Moiseyev, *Controlled tunneling of cold atoms: From full suppression to strong enhancement* Phys. Rev. Lett. **89**, 253201 (2002).

[377] V. V. Ivanov, A. Alberti, M. Schioppo, G. Ferrari, M. Artoni, M. L. Chiofalo, and G. M. Tino, *Coherent delocalization of atomic wave packets in driven lattice potentials* Phys. Rev. Lett. **100**, 043602 (2008).

[378] L. Förster, M. Karski, J.-M. Choi, A. Steffen, W. Alt, D. Meschede, and A. Widera, *Microwave control of atomic motion in optical lattices* Phys. Rev. Lett. **103**, 233001 (2009).

[379] Q. Beaufils, G. Tackmann, X. Wang, B. Pelle, S. Pelisson, P. Wolf, and F. Pereira dos Santos, *Lase controlled tunneling in a vertical optical lattice* Phys. Rev. Lett. **106**, 213002 (2011).

[380] D. P. Rhodes, D. M. Gherardi, J. Livesey, D. McGloin, H. Melville, T. Freegarge, and K. Dholakia, *Atom guiding along high order Laguerre-Gaussian light beams formed by spatial light modulation* J. Mod. Opt. **53**, 547 (2006).

[381] L. Brandt, C. Muldoon, T. Thiele, J. Dong, E. Brainis, and A. Kuhn, *Spatial light modulators for the manipulation of individual atoms* Appl. Phys. B **102**, 443 (2011).

[382] C. Muldoon, L. Brandt, J. Dong, D. Stuart, E. Brainis, M. Himsworth, and A. Kuhn, *Control and manipulation of cold atoms in optical tweezers* New J. Phys. **14**, 073051 (2012).

[383] S. Bose, *Quantum communication through an unmodulated spin chain* Phys. Rev. Lett. **91**, 207901 (2003).

[384] M. Christandl, N. Datta, A. Ekert, and A. J. Landahl, *Perfect state transfer in quantum spin networks* Phys. Rev. Lett. **92**, 187902 (2004).

[385] M.-H. Yung and S. Bose, *Perfect state transfer, effective gates, and entanglement generation in engineered bosonic and fermionic networks* Phys. Rev. A **71**, 032310 (2005).

[386] E. Lieb, T. Schultz, and D. Mattis, *Two soluble models of an antiferromagnetic chain* Annals Phys. **16**, 407 (1961).

[387] M. Fleischhauer, S. F. Yelin, and M. D. Lukin, *How to trap photons? Storing single-photon quantum states in collective atomic excitations* Optics Comm. **179**, 395 (2000).

[388] C. Liu, Z. Dutton, C. H. Behroozi, and L. Vestergaard, *Observation of coherent optical information storage in an atomic medium using halted light pulses* Nature **409**, 490 (2001).

[389] C. H. van der Wal, M. D. Eisaman, A. André, R. L. Walsworth, D. F. Phillips, A. S. Zibrov, and M. D. Lukin, *Atomic memory for correlated photon states* Science **301**, 196 (2003).

[390] T. Chanelière, D. N. Matsukevich, S. D. Jenkins, S.-Y. Lan, T. A. B. Kennedy, and A. Kuzmich, *Storage and retrieval of single photons transmitted between remote quantum memories* Nature **438**, 833 (2005).

[391] J. F. Sherson, H. Krauter, R. K. Olsson, B. Julsgaard, K. Hammerer, I. Cirac, and E. S. Polzik, *Quantum teleportation between light and matter* Nature **443**, 557 (2006).

[392] R. J. Schoelkopf and S. M. Girvin, *Wiring up quantum systems* Nature **451**, 664 (2008).

[393] J. Nunn, K. Reim, K. C. Lee, V. O. Lorenz, B. J. Sussman, I. A. Walmsley, and D. Jaksch. *Multimode memories in atomic ensembles* Phys. Rev. Lett. **101**, 260502 (2008).

[394] M. Afzelius, I. Usmani, A. Amari, B. Lauritzen, A. Walther, C. Simon, N. Sangouard, J. Minář, H. de Riedmatten, N. Gisin, and S. Kröll. *Demonstration of atomic frequency comb memory for light with spin-wave storage.* Phys. Rev. Lett. **104**, 040503 (2010).

[395] D. S. Saraga and D. Loss, *Spin-entangled currents created by a triple quantum dot* Phys. Rev. Lett. **90**, 166803 (2003).

[396] W. D. Oliver, F. Yamaguchi, and Y. Yamamoto, *Electron entanglement via a quantum dot* Phys. Rev. Lett. **88**, 037901 (2002).

[397] A. Kolli, S. C. Benjamin, J. G. Coello, S. Bose, and B. W. Lovett, *Large spin entangled current from a passive device* New J. Phys. **11**, 013018 (2009).

[398] P. Recher, E. V. Sukhorukov, and D. Loss, *Andreev tunneling, Coulomb blockade, and resonant transport of nonlocal spin-entangled electrons* Phys. Rev. B **63**, 165314 (2001).

[399] P. Recher and D. Loss, *Superconductor coupled to two Luttinger liquids as an entangler for electron spins* Phys. Rev. B **65**, 165327 (2002).

[400] C. Bena, S. Vishveshwara, L. Balents, and M. P. A. Fisher, *Quantum entanglement in carbon nanotubes* Phys. Rev. Lett. **89**, 037901 (2002).

[401] W. J. Munro, D. F. V. James, A. G. White, and P. G. Kwiat, *Maximizing the entanglement of two mixed qubits* Phys. Rev. A **64**, 030302 (2001).

[402] A. Kolovsky, J. Link, and S. Wimberger, *Energetically constrained cotunneling of cold atoms* New J. Phys. **14**, 075002 (2012).

[403] R. Beals and R. Wong, *Special Functions* (Cambridge, 2010).

[404] Z. Liu, *Some properties of centrosymmetric matrices* Appl. Math. Comp. **141**, 297 (2003).

[405] B. Chen, W. Fan, and Y. Xu, *Long-range adiabatic quantum state transfer through a linear array of quantum dots* Sci. China: Phys. Mech. Astron. **55**, 1635 (2012).

[406] A Wójcik,T. Łuczak, P. Kurzyński, A. Grudka T. Gdala, and M. Bednarska, *Unmodulated spin chains as universal quantum wires* Phys. Rev. A **72**, 034303 (2005).

[407] L. C. Venuti, S. M. Giampaolo, F. Illuminati, and P. Zanardi, *Long-distance entanglement and quantum teleportation in XX spin chains* Phys. Rev. A **76**, 052328 (2007).

[408] S. R. Clark, C. M. Alves, and D, Jaksch, *Efficient generation of graph states for quantum computation* New J. Phys. **7**, 124 (2005).

[409] M. Markiewicz and M. Wiesniak, *Perfect state transfer without state initialization and remote collaboration* Phys. Rev. A **79**, 054304 (2009).

[410] M. Grace, C. Brif, H. Rabitz, I. A. Walmsley, R. L. Kosut, and D. A. Lidar *Optimal control of quantum gates and suppression of decoherence in a system of interacting two-level particles* J. Phys. B: At. Mol. Opt. Phys. **40**, S103 (2007).

[411] Y. Li and S. C. Benjamin, *High threshold distributed quantum computing with three-qubit nodes* New J. Phys. **14**, 093008 (2012).

[412] K. Fujii, T. Yamamoto, M. Koashi, N. Imoto, *A distributed architecture for scalable quantum computation with realistically noisy devices* arXiv:1202.6588 (2012).

[413] J.-M. Cai, Z.-W. Zhou, and G.-C. Guo, *Decoherence effects on the quantum spin channels* Phys. Rev. A **74**, 022328 (2006).

[414] M. L. Hu and H. L. Lian, *State transfer in intrinsic decoherence spin channels* Eur. Phys. J. D **55**, 711 (2009).

[415] T.-H. Zeng, B. Shao, and J. Zou, *Effects of intrinsic decoherence on information transport in a spin chain* Chin. Phys. Lett. **26**, 020313 (2009).

[416] M.-L Hu, *State transfer in dissipative and dephasing environments* Eur. Phys. J. D **59**, 497 (2010).

[417] N. H. Nickerson, Y. Li, and S. C. Benjamin, *Topological quantum computing with a very noisy network and local error rates approaching one percent* Nature Comm. **4**, 1756 (2013).

[418] A. Wallraff, D. I. Schuster, A. Blais, L. Frunzio, J. Majer, M. H. Devoret, S. M. Girvin, and R. J. Schoelkopf, *Approaching unit visibility for control of a superconducting qubit with dispersive readout* Phys. Rev. Lett. **95**, 060501 (2005).

[419] D. I. Schuster, A. A. Houck, J. A. Schreier, A. Wallraff, J. M. Gambetta, A. Blais, L. Frunzio, J. Majer, B. Johnson, M. H. Devoret, S. M. Girvin, and R. J. Schoelkopf, *Resolving photon number states in a superconducting circuit* Nature **445**, 515 (2007).

[420] M. D. Reed, L. DiCarlo, B. R. Johnson, L. Sun, D. I. Schuster, L. Frunzio, and R. J. Schoelkopf, *High-fidelity readout in circuit quantum electrodynamics using the Jaynes-Cummings nonlinearity* Phys. Rev. Lett. **105**, 173601 (2010).

[421] M. Tiersch, S. Popescu, and H. J. Briegel. *A critical view on transport and entanglement in models of photosynthesis* Phil. Trans. R. Soc. A **370**, 3771 (2012).

[422] C. Spengler, M. Huber, and B. C. Hiesmayr, *A composite parameterization of unitary groups, density matrices and subspaces* J. Phys. A: Math. Theor. **43**, 385306 (2010).

[423] B. C. Hiesmayr and M. Huber, *Multipartite entanglement measure for all discrete systems* Phys. Rev. A **78**, 012342 (2008).